Design and development of a novel wave energy converter

by
James Rattray Joubert

Dissertation presented for the degree of *Doctor of Engineering in the Faculty of Engineering at Stellenbosch University*

Promoter: Prof J. L. van Niekerk
Co-promoter: G. de F. Retief

Declaration

By submitting this dissertation electronically, I declare that the entirety of the work contained therein is my own, original work, that I am the sole author thereof (save to the extent explicitly otherwise stated), that reproduction and publication thereof by Stellenbosch University will not infringe any third party rights and that I have not previously in its entirety or in part submitted it for obtaining any qualification.

Signature ……

J.R. Joubert

Date: .....

Abstract

Design and development of a novel wave energy converter

J.R. Joubert

2013

The design, development and evaluation of a novel wave energy converter (WEC) device, called the ShoreSWEC, in a South African port development is presented. Based on the device requirements, site selection criteria were specified and applied to identify a suitable deployment location. A wave modeling procedure was developed to determine the operational wave conditions and available wave power resource at the selected location. The site was found to have a low mean annual average resource of approximately 2.3 kilowatt per meter wave crest (kW/m) due to its relatively sheltered location. The wave model was further used to determine design storm conditions and a structural stability analysis of the device was conducted.

Experimental tests were performed to evaluate the hydrodynamic conversion efficiency of a single chamber of the device at its most conservative orientation, under a variety of wave energy conditions. The effect of a floor incline and an additional chamber on the performance of the system was investigated. The incline improved efficiency for low wave heights, making it ideal for the low wave power resource conditions of the site, whilst the multi-chamber system experienced increased performance at high wave periods. A comparison between the ShoreSWEC and a conventional oscillating water column (OWC) WEC showed that the OWC extracted 72% more energy, highlighting the sensitivity of performance on device orientation. A three-dimensional (3D) numerical model of the experimental setup was developed. The numerical model provided comparable water surface elevations inside the flume and chamber, yet predicted significantly higher internal chamber pressures and overall efficiency. The electricity generation potential of a 10 chamber ShoreSWEC at the specified location, approximated from the experimental results and 11 years of hindcast wave data, was found to be 6 kW on average for a 15 kW capacity system.

Results of this study highlighted the need for greater understanding of the hydrodynamic characteristics of a full length device. Experimental tests in a 3D wave basin on a scaled full length ShoreSWEC model are therefore recommended. Once conducted, South Africa will be one step closer to the deployment of the full scale SWEC device.

Samevatting

Ontwerp en ontwikkeling van ‘n unieke golfenergieomsetter

J.R. Joubert

2013

Die ontwerp, ontwikkeling en evaluasie van ‘n unieke golfenergieomsetter (GEO), genaamd die ShoreSWEC, in ‘n Suid-Afrikaanse haweontwikkeling word aangebied. Terrein evaluasie kriteria, gebaseer op die omsettervereistes, is ontwikkel en toegepas om die mees belowende terrein te identifiseer. ‘n Golfmodeleringsprosedure is ontwikkel om die operasionele golfkondisies en beskikbare golfdrywinghulpbron te bepaal. Daar is gevind dat die terrein ‘n lae gemiddelde golfdrywing van bykans 2.3 kilowat per meter golfkruin het as gevolg van die beskutte ligging. Die golfmodel is verder gebruik om ontwerpstormkondisies te bepaal en ‘n stabiliteitsanalise was op die toestel struktuur uitgevoer.

Eksperimentele toetse van verskeie golfenergie kondisies is gedoen om die hidrodinamiese omsettingseffektiwiteit van ‘n enkel kamer van die toestel te bepaal teen sy konserwatiefste orientasie. Die effek van ‘n vloerhelling en ‘n addisionele kamer op die uitsette van die sisteem is ondersoek. Die helling het effektiwiteit verbeter vir lae golfhoogtes wat dit ideaal maak vir die lae hulpbron by die terrein, terwyl die veelvoudige-kamer-sisteem beter gevaar het by hoë golfperiodes. ‘n Vergelyking tussen die ShoreSWEC en ‘n konvensionele ossilerende waterkolom (OWK) GEO het gewys dat die OWK 72% meer energie onttrek. Dit beklemtoon die sisteem se sensitiwiteit vir die inkomende golfrigting. ‘n Drie-dimensionele (3D) numeriese model van die eksperimentele opstelling is ontwikkel. Die numeriese model het aansienlik hoër drukke binne die kamer, en gevolglik algehele effektiwiteit, voorspel as die eksperimentele toetse. Die elektriese opwekkingskapasiteit van ‘n 10 kamer ShoreSWEC by die terrein, gebaseer op die eksperimentele resultate en 11 jaar se golfdata, is bereken as 6 kW gemiddeld vir ‘n 15 kW kapasiteit stelsel.

Die bevindinge van hierdie studie het die behoefte aan ‘n beter begrip van die hidrodinamiese eienskappe van ‘n vollengte sisteem beklemtoon. Eksperimentele toetse in ‘n 3D golfbak op ‘n geskaleerde vollengte ShoreSWEC model word dus aanbeveel. Sodra dit voltooi is, sal Suid-Afrika een stap nader wees aan die ontplooiing van ‘n volskaalse SWEC toestel.

Acknowledgements

A research project of this magnitude is never the output of one isolated individual, but rather it is the work realised by a community. To each of you I express my deepest, heartfelt gratitude.

I want to thank God for enabling me to complete this project and for creating the wonderful element of water I had the honor of studying in such great depth. Professor Wikus van Niekerk, my promoter, faithfully supported me throughout my postgraduate studies, I thank you greatly. Eddie Bosman was always willing to help and provided valuable coastal engineering insights. Deon Retief shed light on the historical development of the SWEC. The personnel of the Civil Engineering Department, Geoff Toms, and Christiaan Visser in particular, were very accommodating to experimental work performed in the wavemaking facility. The technical staff of the hydraulic laboratory (Noel, Ashley, Elian and Johan) were always willing to lend a helping hand. Oom Dries Rossouw helped me to build the experimental model.

Marius Rossouw and Padhairic O'Conner of the CSIR provided valuable coastal engineering input. I would like to thank the CSIR and the National Ports Authority (NPA) for making wave data available.

My fellow students, Felipe Guerrero, Chris Baret and Bavesh Kooiverji were always willing to help. Stephan Schmitt, Johan van der Spuy and Michael Horko provided guidance with CFD work. Cobus Zietsman helped with practical aspects of experiments. Kenny Allen conducted orifice calibration tests. Cobus Rossouw provided valuable guidance in coastal engineering and wave modeling and Albert Strasheim helped to develop a programming tool to determine the wave power resource. Warrick Pierce added some finishing touches to the final document.

The Center for Renewable and Sustainable Energy Studies (CRSES) financially supported my studies. The CRSES staff, with whom I shared an office, created a friendly and motivating work environment.

I would have not been able to complete this study without the unyielding love and support of my partner Caitlin Licina, friends and family.

Thank all of you so much.

Contents

List of Tables

List of Figures

Nomenclature

Symbols

C	wave celerity
C_g	group velocity
D_p	peak wave direction
$Dspr$	directional spreading
d	water depth measured from the still water level
E	total wave energy
E_k	kinetic energy
E_p	potential energy
$E(f)$	energy density as a function of frequency
F	frequency
F_H	horizontal force
F_U	uplift force
F_G	weight of the vertical wall structure
H	wave height
H_{design}	design significant wave height for a specified return period
H_{m0}	significant wave height
$H_{m0_{100}}$	100 year wave height
H_{RMS}	root-mean-square wave height
h_c	freeboard
h_b	distance $5H_{design}$ seawards of front wall
k	wave number
L	wavelength
m	power of the $\cos^m\theta$ function related to directional spreading around the peak direction
M_U	uplift moment
M_H	horizontal moment
M_G	resistant moment
p	wave induced pressure
SS_{100}	hundred year storm surge
T	wave period
T_p	spectral peak wave period
vt	virtual buoy
U_{F_H}	stochastic variable of bias and uncertainty related to the horizontal force
U_{F_U}	stochastic variable of bias and uncertainty related to the uplift force
U_{M_H}	stochastic variable of bias and uncertainty related to the horizontal moment

Greek symbols

α_1, α_2, α_3 and α^*	coefficients to determine wave induced pressures
β	angle of wave approach

γ	peak-enhancement factor of the JONSWAP wave spectrum
η	surface elevation
η^*	theoretical height above structure of horizontal wave pressure distribution
λ_1, λ_2, and λ_3	modification factors dependent on the structure type to determine wave induced pressures
ρ_w	density of seawater
ρ_c	density of concrete
ω	wave frequency

Subscripts

design	design parameter
e	eccentric
H	horizontal
k	kinetic energy
m0	zeroth-moment
peak	peak
p	potential energy
s	significant
u	uplift
1	At the water surface
2	Top of the structure
3	Bottom of the structure

Auxiliary symbols

$\bar{E}$	specific energy or energy density
$\bar{P}$	wave energy flux or wave power

Abbreviations

1D	one-dimensional
2D	two-dimensional
3D	three-dimensional
CD	chart datum
CFD	computational fluid dynamics
HAT	highest astronomical tide
JONSWAP	joint North Sea wave project
LAT	lowest astronomical tide
LIMPET	land installed marine energy transformer
MHWN	mean high water neap
MHWS	mean high water spring
ML	mean level
MLLW	mean lower low water
MLWN	mean low water neap
MLWS	mean low water spring
MSL	mean sea level
NCEP	National Centre for Environmental Predictions
NOAA	National Oceanic and Atmospheric Administration
NWT	Numerical wave tank
OWC	oscillating water column
PM	Pierson and Moskowitz

PRDW	Prestedge Retief Dresner Wijnberg
PTO	power takeoff
ShoreSWEC	Breakwater adaptation of the Stellenbosch wave energy converter
SWEC	Stellenbosch wave energy converter
SWL	still water level
UDF	user defined function
VOF	volume of fluid
WEC	wave energy converter
W01 to W05	wave probes 1 to 5

1 Introduction

1.1 General

The ever increasing threats of climate change, finite resources, and the human population explosion have forced governments of the world to shift their focus away from fossil fuels and towards more sustainable means of electricity generation. Renewable energy sources such as solar, wind and ocean energy, have become household terms of the twenty-first century. The world's oceans provide an abundant resource of, as yet, unutilised wave energy. Mørk et al. (2010) have estimated that the global wave energy potential at present stands at approximately 3.7 terawatt (TW) - 75% greater than the total global installed capacity in 2009 (International Energy Agency, 2011).

South Africa is the sixth largest producer of electricity from coal in the world (International Energy Agency, 2011). In an attempt to diversify the country's future energy mix, the local Department of Energy (DOE) has develop an Integrated Resource Plan (IRP) which envisions 17.8 gigawatt (GW) installed capacity of renewable energy by 2030 (Department of Energy, 2011). A local, free and world class energy resource exists on South Africa's doorstep – the south Atlantic and Indian Oceans. Utilising this could greatly assist the country in reaching its renewable energy goals.

Wave energy technology is still in the early stages of development. Two of the biggest barriers to the industry are the reliability and the cost of the technology. One of the more commonly utilised energy conversion methods in the field of ocean wave energy conversion is the Oscillating Water Column (OWC), which has proven its reliability over years of operation in real sea conditions.

1.2 Background

1.2.1 Oscillating Water Column (OWC)

An OWC essentially comprises a collector, which captures and transfers incident waves to air power; and a power takeoff (PTO) system, which converts the pneumatic power to electricity. Inside the collector, wave action causes the air pressure to increase and decrease as the water level rises and falls (refer to the schematic of Figure 1-1).

The PTO of an OWC can be a conventional unidirectional air turbine provided that the reciprocating airflow is rectified by a series of non-return valves. Some argue that the valve system is complicated and difficult to maintain. The best practical example of OWCs with rectifying valves and a conventional turbine are Masuda's navigational buoys, some of which have been operational for more than 30 years. The most commonly used PTO for OWCs however, is the self-rectifying, bidirectional Well's turbine (Raghunathan and Tan, 1982). There are some disadvantages inherent to the Well's turbine - poorer starting characteristics, higher

noise levels and lower efficiency in comparison to conventional turbines optimised for unidirectional airflow (Setoguchi, 2006).

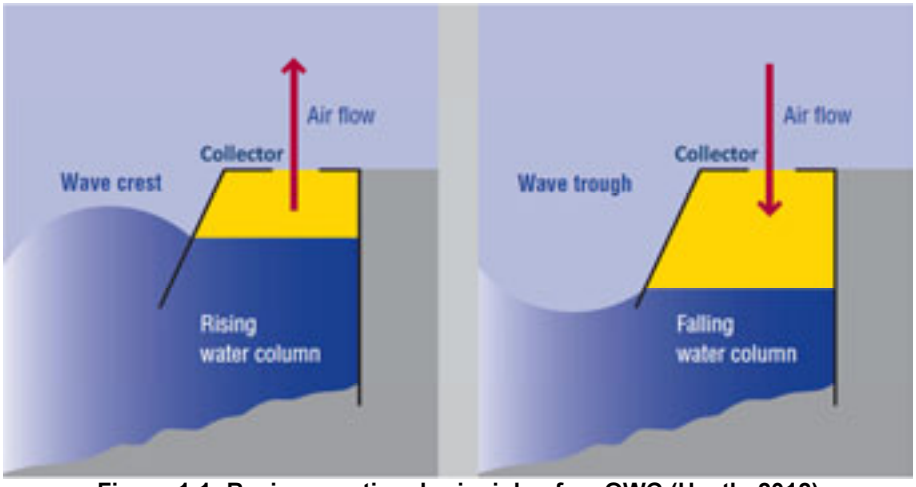

Figure 1-1: Basic operational principle of an OWC (Heath, 2012)

The world's first commercial scale wave energy plant to be connected to the grid, is an OWC called the LIMPET, commissioned in November 2000. It has survived 11 years in the demanding ocean environment off the Scottish west coast, proving the reliability of the technology and survivability of the device. During this time the LIMPET has been continuously grid connected and recently exceeded 60 000 generation hours. Today the plant serves as a demonstration facility for testing new generation Wells turbines, and although there can be no doubt as to the reliability of this device type, Heath (2011) admits it is not yet cost effective.

According to the Carbon Trust (2005) the OWC structure of the collector makes up 85% of the total cost of the project for a generic shoreline device. To improve the economic feasibility of a standalone OWC, it can be incorporated into the structure of a vertical breakwater. The total project cost is then shared between the wave energy converter (WEC) and the breakwater, effectively reducing the cost of the OWC by as much as 60% (Neumann, 2001). Examples of wave power extracting OWC breakwaters that have been successfully constructed and operated include the one built in 1989 at the Port of Sakata, Japan (Takahashi, 1992) and more recently at Mutriku on the Basque coast of Spain (Torre-Enciso et al., 2007).

This study entails the research and development of a novel OWC breakwater device based on an indigenous South African invention.

1.2.2 Stellenbosch Wave Energy Converter (SWEC)

The history of wave energy research in South Africa, and in particular at Stellenbosch University, dates back to the late seventies. The oil crisis of 1973 served as a catalyst which forced governments of the world to consider alternatives forms of energy. Looking to reduce their dependency on oil, a conglomerate of organisations including De Beers, Murray and Roberts and other Anglo American affiliated companies, began funding the Ocean Energy Research Group (OERG) at Stellenbosch University. Led by Professor Deon Retief, their aim was to identify

viable alternative sources of ocean energy and the means to harness them. Of all available marine energy resources, wave- and ocean current energy were identified as the most feasible resources for extraction in the coastal waters of South Africa. Nearshore wave energy was deemed more accessible for utilisation than the deeper water Agulhas Current, flowing offshore of the east coast.

In an attempt to quantify and characterise the available resource, an assessment of the spatial and temporal distribution of wave energy along the South African coast was conducted by Geustyn (1983) and later updated by Joubert (2008). It was found that the southwest has the greatest wave power resource of approximate 40 kilowatt (kW) per meter wave crest on average. The rest of the South African coast is exposed to an average wave power of approximately 18 kW/m to 23 kW/m.

With a clear understanding of the availability of the resource, a wave power conversion system called the Stellenbosch Wave Energy Converter or SWEC, was developed for the prevailing wave conditions on southwest coast of South Africa (Retief et al., 1982). The SWEC consists of a pair of submerged collectors (arms) coupled in a "V"-formation to a conventional unidirectional air turbine generator mounted above the water level in a tower at the apex of the V. Each collector arm is made up of a series of OWC chambers in which water level oscillations displace air via inlet and outlet non-return valves to and from low and high pressure manifold systems which are connected to the air turbine in the tower. Figure 1-2 below shows a simple depiction of the device and its working principle.

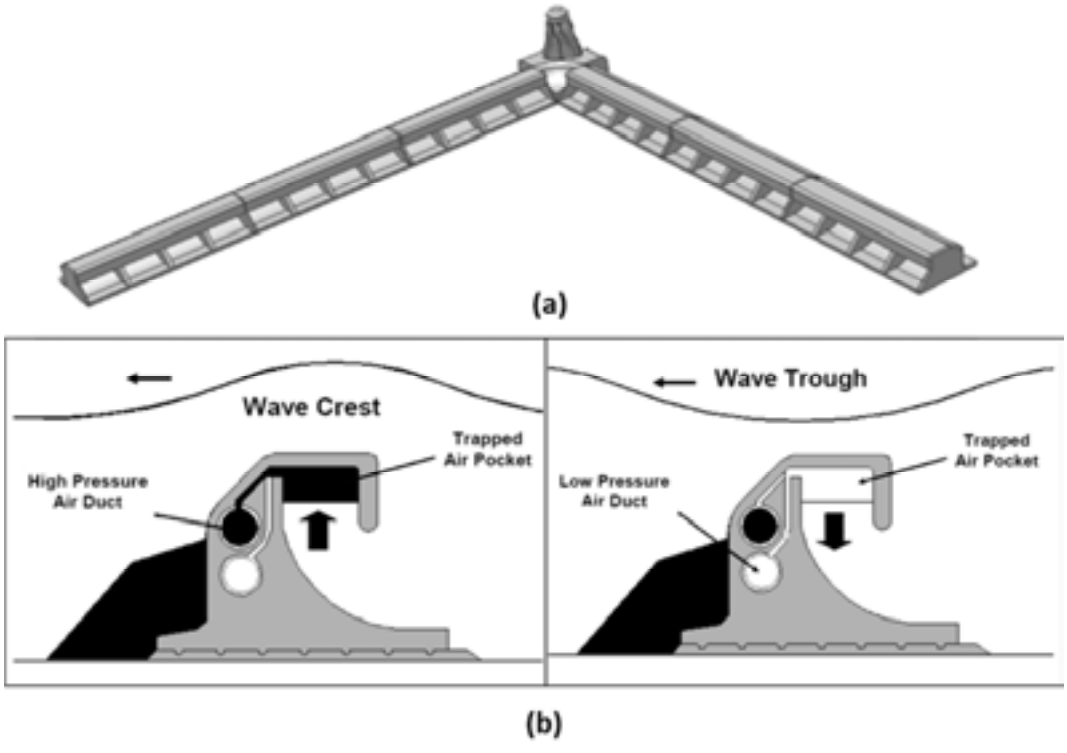

Figure 1-2: Stellenbosch Wave Energy Converter (SWEC) (a) Layout of device. (b) Working principle (Ackerman, 2009)

Key features which differentiate, and improve the utility of the SWEC from a typical OWC, include

- The collector arms of the SWEC are fully submerged, increasing its survivability.
- The SWEC is orientated at a more oblique angle to the incident waves enabling its capture chambers to be activated sequentially. This causes air to accumulate over the entire collector arm during passing waves and provides smooth, unidirectional airflow to the turbine.
- The power take-off mechanism is a single, more efficient, conventional air-turbine that can be optimised for the airflow and will reduce maintenance and manufacturing costs.

Through extensive two- and three-dimensional experimental tests in wave flume and -basin facilities, the OERG optimised the SWEC's device configuration and structure. Work was also conducted on the impact of sedimentation, structural stability, the cost, manufacture and installation of the device. A scale prototype of the SWEC has never been built in the ocean and all research and development of the project was halted in the late eighties when the oil price stabilised. Today with the oil price at an all-time high, there is renewed drive for green energy generation. The implementation of a modified version of this indigenous design is being considered as an effective means to harness wave energy.

1.2.3 ShoreSWEC

The main obstacles in the way of the SWEC's full scale deployment relate to the cost of a stand-alone system, licensing and the permit requirements for a device with such a large footprint on the seafloor. To overcome these challenges, amongst others, an adaptation of the SWEC incorporated into the structure of a coastal development breakwater, was proposed (see Figure 1-3). The purpose of this modified version of the device is to:

- demonstrate the working principle of the original device and prove its technical feasibility whilst being easily accessible for operation, maintenance and monitoring
- simplify environmental impact assessments and permit requirements due to its location inside a port development
- reduce the cost of the project by integrating the structure of the WEC into that of the breakwater.

Stellenbosch University patented this adaptation of the SWEC and named it the ShoreSWEC, due to its shoreline location (refer to patent document of Van Niekerk and Retief, 2010). The ShoreSWEC is in essence a single arm of the SWEC which protrudes above the water surface.

The ShoreSWEC's working principle makes it highly sensitive to the incident wave direction. Waves approaching the device head-on (similar to an OWC) will result in each chamber simultaneously experiencing the same pressure and therefore no differential pumping can occur between them. Waves traveling parallel to the longitudinal axis of the structure, would be optimal from an operational point of view, but less so from an energy capture perspective. At this orientation, no kinetic energy

is captured by the device and the only driving force for flow into the chamber is the potential energy due to the difference in water level outside and inside the chamber. Such conditions would result in the most conservative device performance or minimum generation capacity of the ShoreSWEC. If the device proves to be technically feasible under such conditions, a change in orientation can only increase its performance.

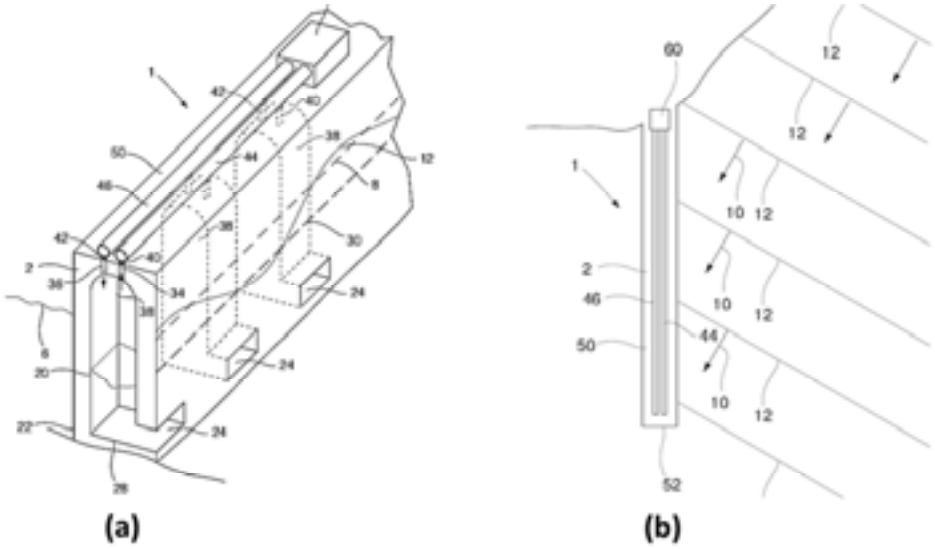

Figure 1-3: (a) Part-cross sectional view of the ShoreSWEC. (b) Top view of the ShoreSWEC depicting the relative approach angle of incident waves. Images from the patent of Van Niekerk and Retief (2010).

1.3 Objectives

This study aims to develop a preliminary design of the ShoreSWEC at its most conservative orientation for a specific location and evaluate its technical feasibility. The body of work consists of a literature review, site selection, evaluation and design, experimental and numerical tests and generation capacity estimation. The objectives of each of these subsets are discussed and presented in Figure 1-4.

Once a preliminary design of the ShoreSWEC is successfully developed, South Africa will be one step closer to the deployment of the full-scale SWEC device.

1.4 Outline of this report

Chapter 2: The results of a literature survey on OWC development using numerical models and experimental tests are discussed. Wave theory that best describes the prevailing wave conditions at the deployment location of the ShoreSWEC is highlighted and hydrodynamic conversion efficiency calculations are presented that were used to evaluate the performance of the device.

Chapters 3, 4 and 5: Site selection criteria were developed, based on the device requirements, and used to identify a suitable location for the deployment of the ShoreSWEC. A numerical wave modeling procedure to transfer 11 years of offshore

hindcast wave data to a nearshore location is discussed. The operational wave conditions and wave power resource at the site, as determined from the wave model, is presented. The wave model is furthermore used to transfer design wave conditions to the site and a stability analysis of the ShoreSWEC structure is conducted.

Chapter 6: The results of the experimental tests to evaluate the hydrodynamic efficiency of a single capture chamber of the ShoreSWEC at its most conservative orientation are presented. The device performance under a variety of wave energy conditions is discussed and the impact of a floor incline and additional chamber is quantified. A comparison is drawn between the proposed system and a conventional OWC.

Chapter 7: A commercial CFD code is used to develop a 3D numerical wave tank (NWT) and model of a single chamber of the ShoreSWEC. The output of the 3D model is compared to the experimental data.

Chapter 8: An estimate of the electricity generation potential of the device at the selected location is presented, based on the experimental results.

Chapter 9: Final conclusions on the research are drawn and recommendations for future work are made.

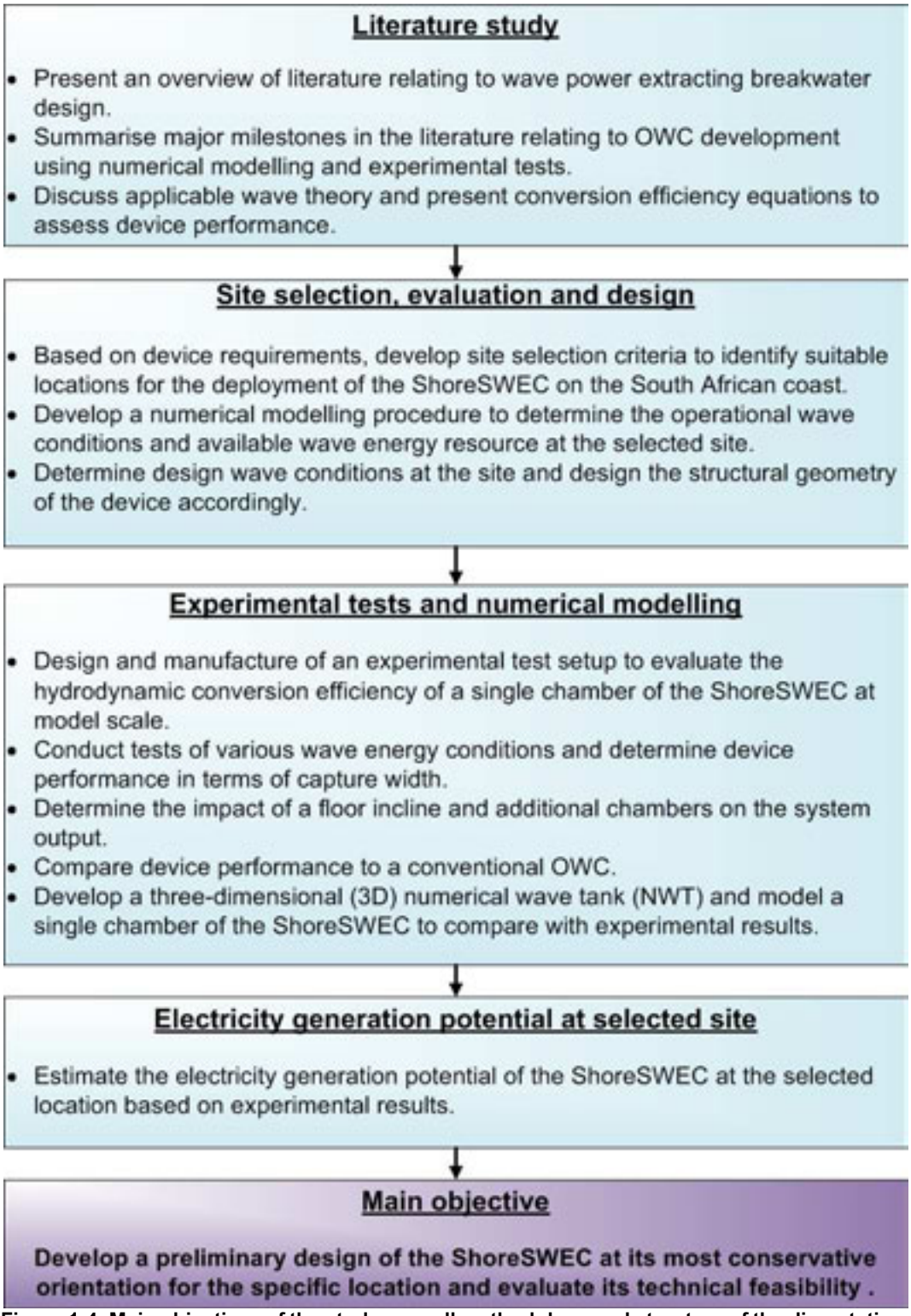

Figure 1-4: Main objectives of the study, overall methodology and structure of the dissertation

2 Literature survey

The ShoreSWEC's dual function of a vertical wall breakwater and a WEC requires that it must be designed both for stability and to optimally convert wave energy. Literature relating to these two design requirements, the relevant wave theory and hydrodynamic efficiency calculations are highlighted and presented.

2.1 Wave power caisson design

Coastal engineering design codes and manuals such as the British Standard BS 6349-7:1991 BSI (1991) and Coastal Engineering Manual (CEM) (2006c) provide design philosophies, procedures and formulae for the design of vertical wall caisson breakwaters. BSI (1991) recommends suitable return periods and methods to determine the wave climate for design. Rossouw (1989) conducted an extensive evaluation of the wave conditions off the South African coast, providing recommendations for design wave height and period conditions.

Design loading conditions caused by nonbreaking waves on a vertical wall can be analysed using Goda's (1974, 1985) prediction method as prescribed by BSI (1991) and CEM (2006c). The results from Goda's method can then be used to determine the caisson width required to resist wave induced forces and overturning moments at an acceptable factor of safety.

Takahashi (1989) included a modification factor into Goda's method to account for energy absorption from an OWC system. Recommendations were also made for the height of vertical and sloping front wall and the submergence depth of the front lip. A sloping front wall can significantly reduce the wave loads on a structure by transferring a component of the horizontally applied force downwards. Takahashi and Hosoyamada (1994) modified Goda's formulae to account for the effect of an inclined front wall.

Patterson et al. (2009) argued that Goda's methods do not take into account wave energy influx into an OWC chamber and therefore give overly conservative estimates of the stability requirements. Similar to perforated breakwaters, an OWC chamber experiences a downward force from the water volume inside which cancels the uplift pressure in the permeable foundation underneath the capture chamber. In their stability analysis, Patterson et al. assumed that the uplift pressure is only fully developed underneath the ballast chamber of the OWC breakwater.

The presented coastal engineering literature was employed to design the ShoreSWEC's structure for stability under extreme storm conditions at a selected location. Literature relating to design and development of conventional OWCs through numerical modelling and experimental tests are presented next.

2.2 Oscillating Water Column (OWC)

2.2.1 Numerical modeling and experimental tests

The hydrodynamic behavior of an OWC has traditionally been predicted by simplified analytical methods. Evans (1978) was one of the first to develop a simple OWC model based on rigid-body theory. He, and others, argued that the internal fluid motion can be assumed to act like a light, rigid piston provided that the chamber width is small in relation to the wave length. Falcão and Sarmento (1980) improved upon the rigid piston approach by allowing for the possibility of spatial variation of the internal free surface, i.e. a non-plane surface. Evans (1982) generalised this model for a number of rigid bodies with oscillating pressure distributions.

Through his experimental work, Sarmento (1992) validated the oscillating surface pressure model and investigated the effect of the power takeoff (PTO) and front wall submergence on efficiency. Sarmento (1993) went on to conduct further experimental studies to optimise the Pico OWC in terms of the most suitable location, geometric layout and available annual energy production. The LIMPET was designed, developed and successfully deployed after extensive tank testing as presented by Wavegen (2002). It was found that the water depth has a critical impact on the performance of shoreline OWCs. The non-linear flow characteristics of the LIMPET were investigated by Folley and Whittaker (2002). These non-linear conditions were mainly the result of wave reflection off the OWC's front wall.

Using the potential theory and neglecting viscous effects, Evans and Porter (1996) developed a procedure to optimise the system's efficiency with respect to the chamber width and front wall depth. Theoretical hydrodynamic efficiency of up to a 100% was found around the resonant period of the device. Clément (1997) employed a two-dimensional (2D) numerical wave tank, CANAL, to determine the non-linear radiation step response of an OWC. He analysed the influence of the front wall shape, draught and thickness on the performance of an OWC. The majority of the analytical methods developed to describe the hydrodynamic behavior of OWCs is 2D and based on first order approximations.

A simple one-dimensional (1D) analytical model of the SWEC's airflow system was developed by Ackerman (2009). From the model results, an optimal design of an air turbine and diffuser was determined. The performance and operation of the turbine was investigated under various flow conditions for constant and variable speed. It was found that a variable speed turbine improved performance at off-design conditions.

According to linear wave theory, the theoretical wave power incident on a WEC device is defined as $\overline{P} = EC_g \sin \beta$ where E is the specific energy, C_g is the wave group velocity and β is the angle of the incident waves. In this study it was assumed that the ShoreSWEC is longitudinally orientated parallel to the incident waves, therefore at a right angle to the wave fronts ($\beta = 90^o$) and the incident wave power will thus theoretically be zero. In order to investigate the wave induced flow at a right angle to the advancing waves, a 3D analysis method is required.

Lee et al. (1996) were the first to develop a low order 3D boundary element model of a generic OWC to investigate its hydrodynamic response using the radiation/diffraction code WAMIT. The model yielded accurate results through the implementation of appropriate dynamic boundary conditions on the interior free surface. Predictions published by Lee et al. was confirmed by a similar model developed by Brito-Melo et al. (1999) using an adaptation of AQUADYN to investigate the performance of an OWC system with different geometric parameters.

The effect of the incident wave direction on the entrapped water column motion was investigated by Brito-Melo et al. and also Martins-Rivas and Mei (2009). The latter developed a 3D model of the linearised problems of radiation and scattering for a hollow cylinder OWC at the tip of a long breakwater. It was found that the power capture of the cylinder is not affected by the wave direction whereas Brito-Melo et al.'s model was greatly dependent on wave direction due to the rectangular shape and orientation of the OWC.

The implementation of the above mentioned 3D boundary element models for OWC applications required extensive modification of the original source code and therefore a considerable computer programming effort. It was not developed for generic applications, making it challenging to adapt for specific OWC geometries and environmental conditions.

In recent times commercial computational fluid dynamics (CFD) codes have been successfully used in OWC applications.

2.2.2 CFD numerical models

Fluent is one of the most commonly used CFD codes for OWC modeling. It can analyse any user defined geometry and account for viscous and air compressibility effects inside the OWC chamber. Horko (2007) was one of the first to use Fluent to conduct an in depth analysis of the hydrodynamic efficiency of an OWC. By prescribing the velocity profile of the incident waves, a 2D numerical wave tank (NWT) was developed and used to optimise the front lip width and shape of an OWC chamber. It was found that a thicker or rounder front lip increased efficiency due to the less abrupt change in flow direction from external to internal flow resulting in less turbulence. The numerical estimates of hydrodynamic efficiency were however significantly higher than was found for the experimental results giving a poor overall correlation.

Using a dynamic mesh model Liu et al. (2010) and Liu et al. (2011) developed a 2D and 3D numerical wave tank (NWT) in Fluent with which to investigate the effect of various geometric parameters on device performance. Output from their 2D numerical model was validated by comparing the relative surface elevation inside the chamber with experimental results. The 3D model was also validated through the comparison with experimental values of relative surface elevation, pressure inside the chamber and airflow velocity in the outlet duct. No comparison was however drawn on the overall efficiency of the system. Using their 3D NWT Liu et al. (2010) further investigated the effect of wave focusing on the internal chamber pressure and air flow rate at the outlet. As can be expected, it was found that protruding walls at a wide angle can greatly increase the internal pressure and airflow of the device.

The effect of wave direction on the OWC performance was recently investigated by Jin et al. (2012) using the 3D NWT of Liu et al. (2011). Jin et al. found that the system response, in terms of relative wave height and outlet airflow rate, decreases for decreasing incident wave direction. The numerical model was validated through the comparison with experimental results of relative wave heights. This study lacks a detailed analysis of the overall hydrodynamic efficiency of the system as a function of wave direction.

OWC efficiency is a function of its geometry, the incident wave direction and the level of applied damping. The effect of each of these parameters on the performance of the ShoreSWEC will be investigated.

2.2.3 Turbine design

Various studies have been conducted on the OWC's PTO and the Well's turbine in particular. Tindall and Xu (1996) and Curran et al. (1997) developed mathematical models of the Islay wave power system in an attempt to optimise the Well's turbine. From the studies, an optimal turbine design was determined and the damping applied by the turbine yielding the greatest efficiency was evaluated. The main focus of the proposed study is the hydrodynamic characteristics of the ShoreSWEC's capture chamber and its PTO was therefore not studied in great detail.

In order to determine the incident wave energy on the ShoreSWEC and evaluate its hydrodynamic efficiency, relevant wave theory and equations are required.

2.3 Relevant wave theory

In this section the relevant theory required to describe wave conditions is discussed. Linear wave theory is firstly presented and later extended to higher order wave theories. Irregular sea states and spectral analysis are also described. Lastly, equations to evaluate the conversion efficiency of an OWC are presented.

2.3.1 Linear wave theory

Linear, first-order or Airy wave theory (Airy, 1845) has been the basic theory to describe small-amplitude surface gravity waves for about 150 years. The small-amplitude approximation implies that the amplitude of a linear wave is small in comparison to its wavelength and the water depth. Linear theory is based on various assumptions - one of which includes that the motion of water particles is irrotational (particles do not rotate about their own axes). This allows the use of a mathematical function called the velocity potential equation to describe particle velocity in the water. The velocity potential equation and its stream functions can be solved using the equation of Laplace and Bernoulli in combination with suitable boundary conditions as presented by Holthuijsen (2007).

A simple harmonic wave is best described in terms of its parameters such as wavelength, L (horizontal distance between two successive wave troughs or crests), wave period, T (time it takes a wavelength to pass a given point), wave height, H (vertical distance between the trough and succeeding crest) and water depth, d (vertical distance from the seafloor to still water level (SWL). These parameters are presented for a progressive linear wave in terms of its phase (θ) in Figure 2-1.

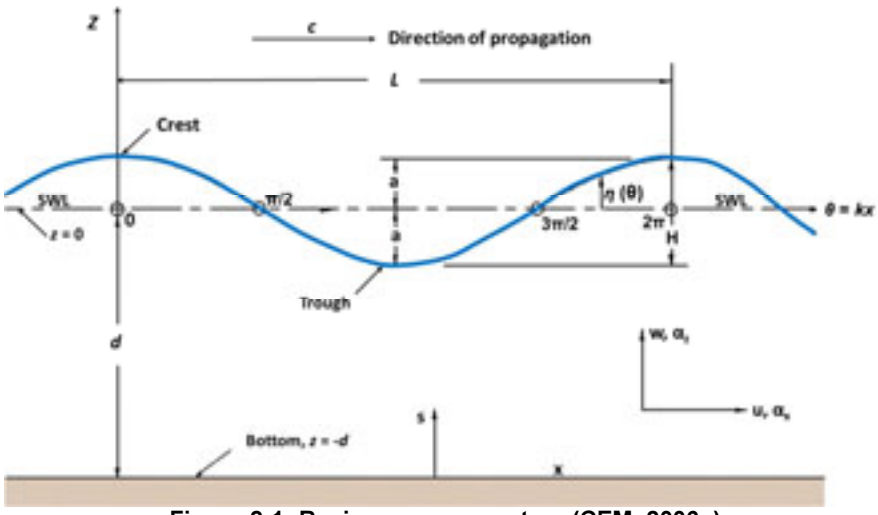

Figure 2-1: Basic wave parameters (CEM, 2006a)

Other important wave parameters include the wave number $k = 2\pi/L$ and the angular or radian frequency $\omega = 2\pi/T$.

Surface elevation

The surface elevation, relative to SWL, of a sinusoidal wave as a function of time *t* and horizontal distance *x* can be described as:

$$\eta = \frac{H}{2}\cos(\frac{2\pi x}{L} - \frac{2\pi t}{T}) = \frac{H}{2}\cos(kx - \omega t) \quad (1)$$

Particle velocities

Using the surface elevation and velocity potential equation, the horizontal-, *u*, and vertical-, *w*, component of the fluid velocity can be shown to be:

$$u = \frac{H}{2}\frac{gk}{\omega}\frac{\cosh k(d+z)}{\cosh kd}\cos(kx - \omega t) \quad (2)$$

$$w = \frac{H}{2}\frac{gk}{\omega}\frac{\sinh k(d+z)}{\cosh kd}\sin(kx - \omega t) \quad (3)$$

Wavelength

The wavelength (*L*) of a regular wave in any water depth is defined as:

$$L = \frac{gT^2}{2\pi}\tanh(\frac{2\pi d}{L}) \quad (4)$$

Waves can be classified according to the relative depth (*d*/*L*) criteria. Where:

- Deep water *d*/*L* > ½
- Transitional depth 1/20 < *d*/*L* < ½
- Shallow water *d*/*L*< 1/20

Celerity

The propagation speed of an individual regular wave is called the wave celerity or phase velocity, as defined by:

$$C = \frac{L}{T} = \frac{gT}{2\pi}\tanh(2\pi d/L) \quad (5)$$

Group velocity

Waves mainly travel in groups from the same direction as a collection of sinusoids with different periods. This is an important concept, because it directly determines the rate at which wave energy propagates in space and time. The propagation velocity of the wave group is called the group velocity (C_g) and is defined as:

$$C_g = \frac{1}{2}\left[1 + \frac{4\pi d/L}{\sinh(4\pi d/L)}\right]C \quad (6)$$

Specific energy

The total energy of a progressive, linear wave is the sum of its kinetic and potential energy. The kinetic energy is associated with the water particle velocities and the potential energy is due to the absolute elevation of the fluid mass above and below the SWL. The total energy is given by:

$$E = E_k + E_p = \int_x^{x+L}\int_{-d}^{\eta} \rho\frac{u^2 + w^2}{2}\,dz\,dx + \int_x^{x+L} \rho g\left[\frac{(\eta + d)^2}{2} - \frac{d^2}{2}\right]dx \quad (7)$$

where the subscript k and p refer to the kinetic and potential energy. After integration it can be seen that the kinetic and potential energy components are equal, provided that the potential energy is relative to SWL and that the waves propagate in the same direction. The total average wave energy per surface area, known as the specific energy or energy density is given by:

$$\overline{E} = \frac{\rho g H^2}{8} \quad (8)$$

Refer to Joubert (2008) for the derivation of Equation (8) from first principles.

Wave power

The rate at which wave energy is transmitted through a vertical plane perpendicular to the direction of the wave advance is known as the wave energy flux or wave power. This is given by:

$$\overline{P} = \frac{1}{T}\int_t^{t+r}\int_{-d}^{\eta} pu\,dz\,dt \quad (9)$$

where p is the gauge pressure, t and r are the start and end time respectively.

After integration:

$$\overline{P} = \overline{E}C_g \quad (10)$$

If a vertical plane is taken at an angle other than perpendicular to the wave direction, then $\overline{P} = EC_g sin\theta$, where θ is the angle between the plane over which the energy is transmitted and the wave direction. It is important to note that theoretically zero energy is transmitted through a vertical plane in the direction of wave advance.

To summarise: the total incident wave power per unit width of a linear wave at any water depth is given by:

$$\overline{P} = \frac{\rho g H^2}{8}\frac{1}{2}\left[1+\frac{4\pi d/L}{\sinh(4\pi d/L)}\right]\frac{gT}{2\pi}\tanh(2\pi d/L) \quad (11)$$

From Equation (11), it can be seen that wave power is a function of *H*, *T* and *d*.

As waves propagate into shallower water, the wave steepness (*H*/*d*) can increase to such an extent that the small-amplitude approximation of linear theory is no longer valid. In this case, higher order non-linear wave theories are required to describe wave conditions. Wave parameters (*H*, *T* and *d*) as functions of the suitable linear and higher order wave theories are presented in Figure 2-2.

From Figure 2-2 it can be seen that a portion of the wave conditions of interest for this study can be described by linear theory, but the majority is best represented by 2nd order Stokes wave theory. A discussion of this higher order theory is presented in the following section.

2.3.2 2nd Order Stokes wave theory

To better approximate the non-linearity of ocean waves, higher order corrections can be added in the form of perturbation expansions to the harmonic wave profile as prescribed by Stokes (1847). An example of a linear profile with a 2nd order correction and the resulting 2nd order Stokes wave is shown in Figure 2-3.

From Figure 2-3 it can be seen that the 2nd order Stokes wave has a flatter trough and higher crest in comparison to the linear profile.

Surface elevation

Dean and Dalrymple (1992) showed that the surface elevation of the 2nd order Stokes is composed of the linear component and the 2nd order correction:

$$\eta = \frac{H}{2}\cos(kx-\omega t)+\frac{H^2 k}{16}\frac{\cosh(kd)}{\sinh^3(kd)}(2+\cosh(2kd)\cos 2(kx-\omega t)) \quad (12)$$

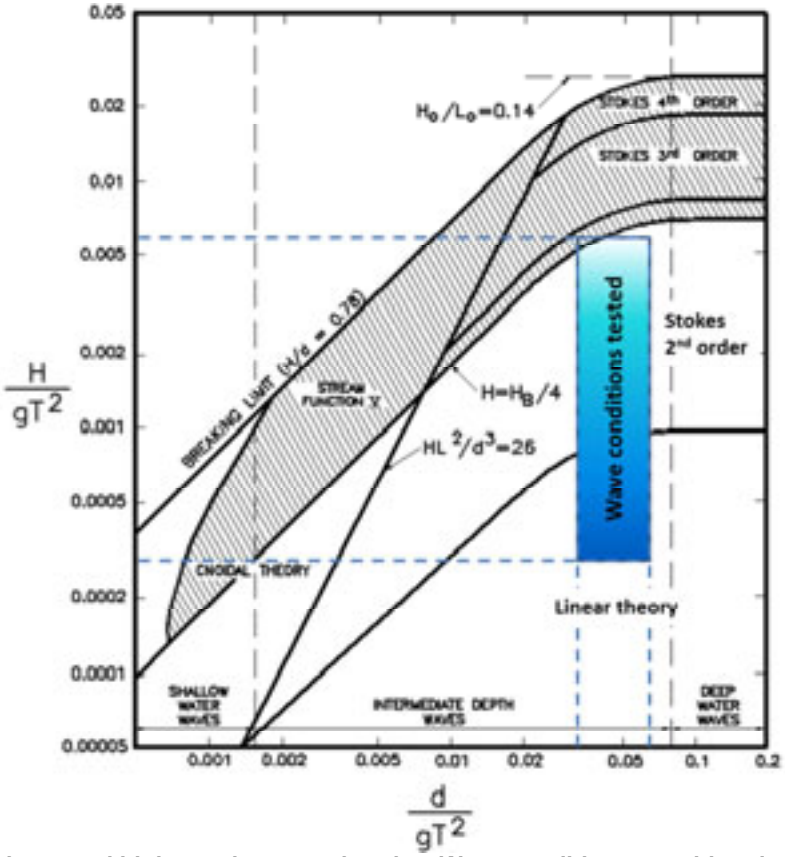

Figure 2-2: Linear and higher order wave theories. Wave conditions considered are shown in blue (CEM, 2006a)

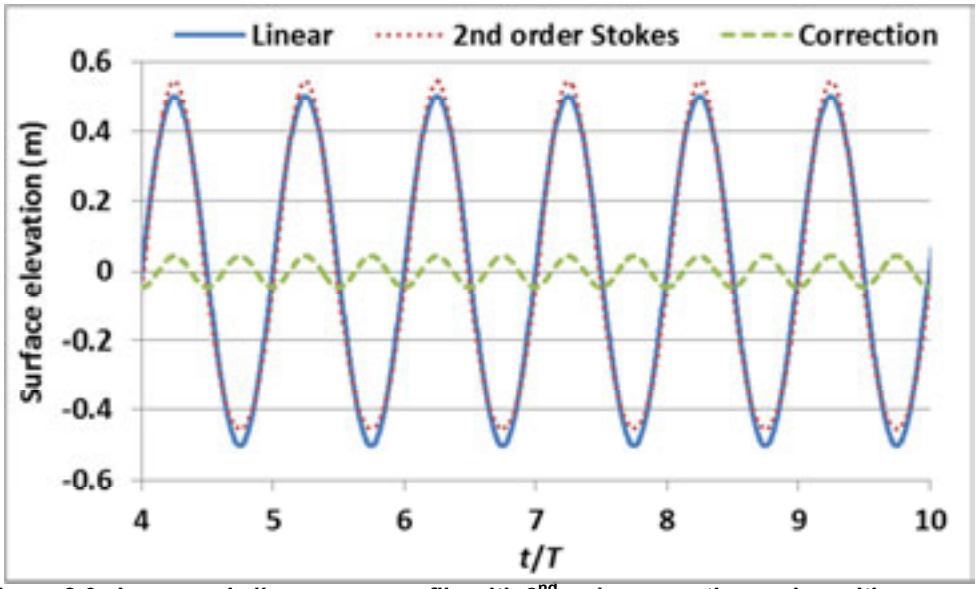

Figure 2-3: An example linear wave profile with 2nd order correction and resulting second order Stoke wave for *H* = 1 m and *T* = 10 s

Particle velocities

In the same way, the orbital velocity of the water particles of the 2nd order Stokes wave can be shown to be:

$$u = \frac{H}{2}\frac{gk}{\omega}\frac{\cosh k(d+z)}{\cosh kd}\cos(kx-\omega t) + \frac{3H^2\omega k}{16}\frac{\cosh 2k(d+z)}{\sinh^4(kd)}\cos 2(kx-\omega t) \quad (13)$$

$$w = \frac{H}{2}\frac{gk}{\omega}\frac{\sinh k(d+z)}{\cosh kd}\sin(kx-\omega t) + \frac{3H^2\omega k}{16}\frac{\sinh 2k(d+z)}{\sinh^4(kd)}\sin 2(kx-\omega t) \quad (14)$$

Linear theory does not describe wave kinematics above the SWL due to its small-amplitude approximation. To better describe the near surface kinematics, linear theory is often used in combination with empirical stretching techniques such as wheeler-, delta- and vertical stretching (Couch and Conte, 1997). Even though it is not necessarily the most accurate method, the vertical stretching technique was used in this study due to its computational simplicity compared to the other techniques. Vertical stretching essentially sets the particles velocities above the SWL equal to that calculated at SWL.

Specific energy

The rate of energy transport for a 2nd order Stokes wave is the same as for a linear wave, but McCormick (1982) showed that the specific energy or energy density of the 2nd order wave has an added component as shown by:

$$\overline{E} = \frac{\rho g H^2}{8}\left[1 + \frac{9}{64}\frac{H^2}{k^4 d^6}\right] \quad (15)$$

Wave power

The total incident wave power per unit width of a 2nd order Stokes wave at any water depth is given by:

$$\overline{P} = \frac{\rho g H^2}{8}\left[1 + \frac{9}{64}\frac{H^2}{k^4 d^6}\right]\frac{1}{2}\left[1 + \frac{4\pi d/L}{\sinh(4\pi d/L)}\right]\frac{gT}{2\pi}\tanh(2\pi d/L) \quad (16)$$

In the experimental section of this study the incident wave power was calculated for both the linear and 2nd order Stokes waves using Equation (11) and Equation (16) respectively. The operational, design conditions and resource assessment of this study were conducted for irregular waves using spectral analysis.

2.3.3 Spectral analysis

The wave theory discussed thus far has mainly been concerned with monochromatic waves which are nearly sinusoidal with a constant height, period and direction. However, real sea states are randomly distributed, irregular waves that are best described statistically. An example of a typical measured wave record is presented in the bottom left-hand corner of Figure 2-4(a).

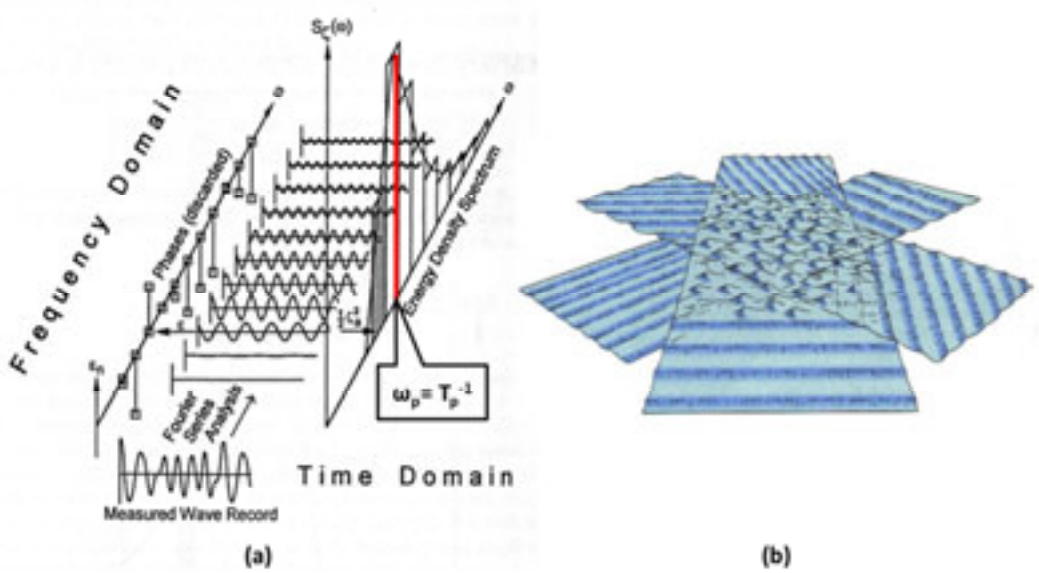

Figure 2-4: (a) Irregular sea state in the time and frequency domain. (b) Directional components of real sea states.

Figure 2-4(a) further shows that the randomly distributed surface elevation of the measured record can be deconstructed with Fourier series analysis into a collection of linear wave components, each with its own unique height and period. The amplitude and frequency of each linear component is used to produce a distribution of wave energy density as a function of frequency called a 1D or frequency spectrum ($E(f)$).

The inverse of the frequency at which the maximum energy density occurs is known as the peak wave period (T_p) of the record, an important parameter in coastal engineering applications. Another key wave parameter is the significant wave height (H_s). H_s or $H_{1/3}$ was traditionally defined as the average wave height of the highest third wave heights in a record. H_s can also be derived from the variance of the spectrum (m_0, zeroth-moment), and is then denoted as H_{m0}. It is generally assumed that $H_s \approx H_{m0}$ therefore:

$$H_s \approx H_{m0} = 4\sqrt{m_0} = \sqrt{\int_0^\infty E(f)df} \qquad (17)$$

Where $m_i = \int_0^\infty f^i E(f)df$ is the i^{th} moment of the spectral distribution.

The root-mean-square wave height (H_{RMS}) has been found to best represent the equivalent energy density of an irregular wave record and can be derived from:

$$H_{RMS} = \frac{H_s}{\sqrt{2}} \qquad (18)$$

In a similar way, the representative wave period containing the same energy as the irregular wave record is known as the energy period, T_e which is defined as:

$$T_e = \frac{m_{-1}}{m_0} \quad (19)$$

From Equation (19) it is clear that T_e is dependent on the energy density spectrum. It is often difficult to accurately recreate a spectrum from only its measured wave parameters and it is therefore necessary to assume a linear relationship between T_e and T_p (Cornett, 2008) such as:

$$T_e = \alpha T_p \quad (20)$$

The shape of a 1D spectrum is generally prescribed in terms of its peak-enhancement factor (γ). Analysis of measured wave spectra off the South African southwest coast indicated that the average γ-value was approximately 1.5 which gives an α value of 0.877. This is considered to be a conservative value of α and was used in the resource assessment of this study.

Typical spectra shapes and peak-enhancement factor

Two of the most common empirical spectral shapes are that of Pierson-Moskowitz (PM) and JONSWAP as shown in Figure 2-5(a). As mentioned in the previous section, the spectrum shape is described in terms of its peak-enhancement factor (γ). The value of γ is defined as the ratio of the maximum energy density of the JONSWAP and PM spectrum. A PM spectrum is therefore a JONSWAP distribution with a γ-value of 1.

The PM spectrum describes a wave-field that has reached equilibrium for a given wind speed, i.e. no more wind energy is transferred to the wave-field and it is therefore a fully developed sea. It assumes that both the fetch and wind duration is infinite. It has a low γ-value of 1 indicating that the energy density is spread over a large range of frequencies around the peak frequency. The JONSWAP on the other hand has a high, narrow peak around the maximum energy density. JONSWAP is fetch-limited.

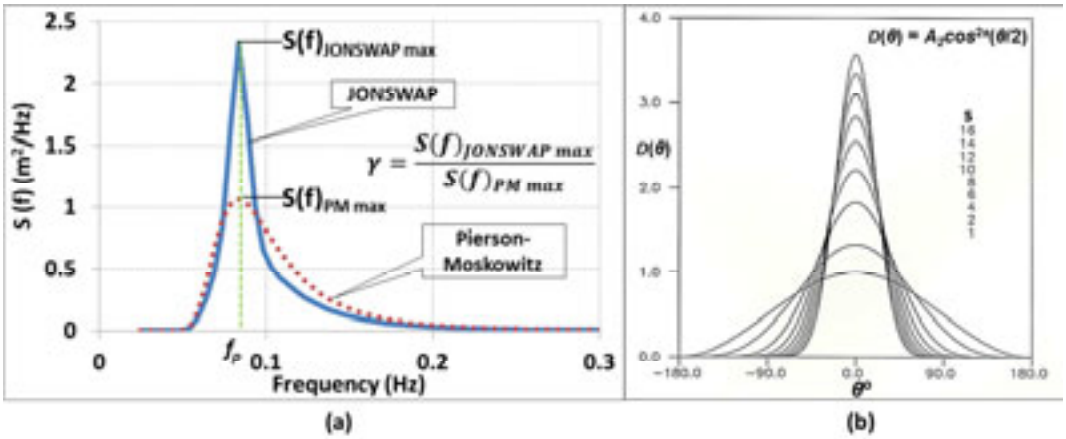

Figure 2-5: (a) 1D energy density spectrum. (b) Directional energy distribution

Two dimensional (2D) wave energy density spectrum

Each sinusoid of an irregular sea state has a propagation direction as shown in Figure 2-4(b). Energy density is therefore also a function of direction. Wave energy density as a function of direction and frequency is known as a 2D spectrum $E(f, \theta)$ (refer to Figure 2-6 for an example 2D spectrum). A model for directional distribution is:

$$D(\theta) = A_2 \cos^{2s}(\frac{\theta}{2}) \text{ for } -180° < \theta \leq 180° \quad \textbf{(21)}$$

where $D(\theta)$ is the normalised distribution of the wave energy density over directions at one frequency, $A_2 = \Gamma(s+1)/\left[\Gamma\left(s+\frac{1}{2}\right)2\sqrt{\pi}\right]$ and s controls the width of the distribution. $\Gamma(.)$ in the A_2 equation above is the gamma function. The direction distribution is presented in Figure 2-5(b) for different s-values. For this study however, the generalised $\cos^m\theta$ model was used, where m controls the width of the distribution.

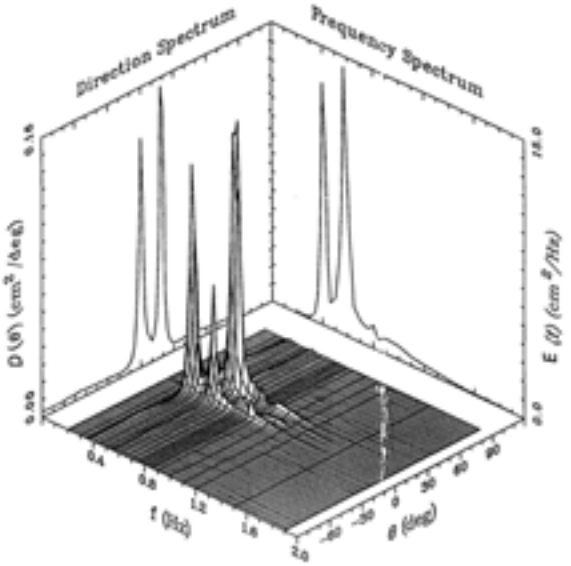

Figure 2-6: Example of 2D spectrum (CEM, 2006a)

2.3.4 Wave energy conversion efficiency

The power capture of the ShoreSWEC was investigated in terms of hydrodynamic and pneumatic efficiency. Equations to determine these quantities are presented in the following sections.

Hydrodynamic power

The motion of an oscillating water column can be considered similar to that of a rigid piston provided that the interior water surface heaves as a horizontal plane area. The dimension of the chamber in the direction of the incident waves therefore has to be small relative to the typical wave length conditions. Brendmo (1996) found that this heaving body analogy is acceptable for long period waves. Assuming the interior

water surface acts as piston, the hydrodynamic power input to the air chamber can be defined as the product of the net wave force acting on the inner water surface and the vertical velocity of this surface. The wave force can furthermore be derived from the product of the air pressure inside the chamber and the area of the inner water surface. The instantaneous hydrodynamic power absorbed by the OWC is defined as:

$$P_{hyd_i} = p_i A v_i \quad \textbf{(22)}$$

where p_i is the air pressure inside the chamber, A is the area of the inner water surface and v_i is the instantaneous vertical velocity of inner water surface. v_i can be determined from:

$$v_i = \frac{\eta_i - \eta_{i-1}}{\Delta t} \quad \textbf{(23)}$$

where η_i is the water surface elevation inside the chamber at the ith instant, η_{i-1} is the water surface elevation inside the chamber at the $(i-1)$th instant and Δt is the sampling interval. The mean hydrodynamic power absorbed by the OWC, P_{hyd} is:

$$P_{hyd} = \frac{1}{T}\int_0^T p_i A v_i \, dt \quad \textbf{(24)}$$

The integration can be done by numerical summation considering the sampling interval is Δt.

$$P_{hyd} = \frac{1}{T}\sum_{i=1}^{n} p_i A v_i \Delta t \quad \textbf{(25)}$$

where, $n = \frac{T}{\Delta t}$

This formulation neglects the impact of compressibility.

In the next stage the hydrodynamic power captured by the chamber is converted to pneumatic power in the entrapped air volume.

Pneumatic power

The pneumatic power absorbed by the OWC is effectively the power available to the air turbine for conversion. The PTO of an OWC is typically not modeled in great detail. In this study a simple orifice was used to provide a similar level of applied damping as a turbine. This has been successfully done in various other OWC studies. Refer to Sarmento (1992), Thiruvenkatasamy and Neelamani (1997), and Folley and Whittaker (2002).

The pneumatic power capture of the OWC is calculated in a similar way to the hydrodynamic power as presented in the previous section, the only difference being that the volume rate through the orifice instead of inside the chamber is used. Through calibration, the relationship between the pressure drop over the orifice (effectively the internal chamber pressure) and volume flow through the orifice can be determined (Sarmento, 1992). The mean absorbed pneumatic power is then be given by:

$$P_{ab} = \frac{1}{T}\int_0^T p(t)Q(t)\,dt \qquad (26)$$

where p is the internal chamber pressure relative to atmosphere and Q is the volume flow rate as determined from the calibration equation. Refer to the definition sketch presented in Figure 2-7.

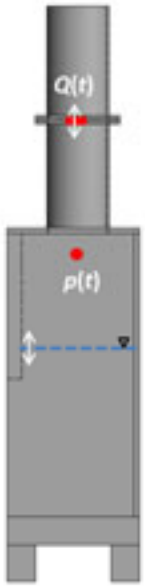

Figure 2-7: Definition sketch for pneumatic power calculation

Capture width

The performance of a WEC device is determined by the level at which it absorbs and converts incident wave energy. In 2D applications a WEC's performance is defined in terms of its efficiency, which is defined as the ratio of output power to input power, with a unit width of the device able to extract power from only a unit width of the incident wavefront. In three dimensions however the device is permitted to absorb power from the total wavefront incident to the device, not just the wavefront with the same width as the device (Cruz, 2008). It is therefore more suitable to characterise the performance of a device in terms of its capture width which Price (2009) defines as the width of the wavefront (assuming uni-directional waves) that contains the same amount of power as that absorbed by the WEC. The capture width describes the performance of a linearised WEC model in a sinusoidal sea.

In this study the incident wave power and the mean pneumatic power absorbed by the ShoreSWEC was calculated by Equation (11), Equation (16) and Equation (26) respectively. The system's overall efficiency was expressed in terms of its capture width, the ratio of these two quantities.

2.3.5 Resonance

An OWC system will perform optimally if the natural period of its heave motion matches the excitation period of the incident waves. The resonant period of an OWC is essentially a function of its geometry which determines its added mass, the surrounding water excited by the water column motion. The depth of submergence of the front lip is the main geometric parameter influencing the natural period of the system. Increasing it will increase the natural period, but will reduce the kinetic energy capture of the system, which is greatest on the water surface. Numerous studies have been conducted on the effect of front lip submergence depth on the resonant response and efficiency of OWCs. Refer to Sarmento (1992) and Evans and Porter (1996). It is important to determine the efficiency of the ShoreSWEC over a variety of wave periods to ensure it matches the prevailing period conditions of the deployment location. The level of damping applied by the PTO to the water column motion is another control mechanism which can be used to induce resonance and must be considered in the ShoreSWEC design.

The selection of a suitable deployment site for the ShoreSWEC is discussed next.

3 Site selection

To identify sites best suited for the deployment of the ShoreSWEC, preliminary selection criteria were developed for locations along the South African coast, based on the site requirements of the device. The ShoreSWEC is in principle a wave-power-extracting caisson breakwater as termed by Takahashi (1989). Suitable locations will therefore be new port developments which require vertical breakwaters, or existing port developments with the potential for expansion, or those which can be retrofitted to facilitate the ShoreSWEC. The evaluation criteria are discussed in the following sections.

3.1 Evaluation criteria

South Africa's entire 2800 km coastline stretching from the Namibian border on the west coast to the border with Mozambique on the east coast was studied in the preliminary site selection procedure using Google Earth TM. Sites were evaluated and ranked according to the following criteria based on the work of Hagerman and Bedard (2003):

- Port development and breakwater
- Wave power resource
- Environmental impact and regulatory requirements
- Power purchaser
- Infrastructure
- Grid connection

Each of these will be discussed in greater detail.

3.1.1 Port development and breakwater

Newly planned and existing port developments with breakwater structures were considered. From Google Earth's satellite images (and other sources where available) the breakwater type and orientation of existing developments were determined. The ShoreSWEC's operational principle dictates that the longitudinal axis of the device must be orientated parallel to the dominant angle of wave attack. Sites with inadequately orientated breakwaters were not evaluated further and were omitted from the selection process. Water depth at the site was then considered. Bathymetry on the southwest coast was based on the South African naval chart INT 2670 SAN 79. Water depth was approximated where no data was available. Vertical breakwaters are mostly constructed beyond the breaker zone, in water depth typically greater than 10 m, to avoid excessive wave loading from the dominant conditions. South Africa has a relatively low tidal range (average of 1.05 m) and this therefore did not influence the site evaluation process.

3.1.2 Wave power resource

The energy conversion capacity of the ShoreSWEC at a particular location depends on the available wave power resource. This resource was calculated from measured and modeled wave data (where available) at each site. Assessments of the

South African wave power resource have been conducted by Geustyn (1983) and more recently by Joubert (2008), who specifically focused on the spatial distribution of wave power off the southwest coast. The nearshore annual average wave power resource off the South African coast ranges from 15 kW/m to 40 kW/m based on measured wave data as shown in Figure 3-1. The annual average wave power distribution of the southwest coast is presented in Figure 3-2, based on 10 years of hindcast wave data. At locations where no data was available, the resource was linearly approximated from available data. Once a final site was selected, a detailed resource assessment was conducted to determine the site's generation potential.

Figure 3-1: Nearshore wave power levels based on measured wave data (Retief, 2007) and (Joubert, 2008)

3.1.3 Environmental impact and regulatory requirements

For the ShoreSWEC to be deployed off the South African coast it will have to adhere to various regulations, laws (environmental and other), conventions and policies.

The Environmental Management Act (Act 107 of 1998) states a full environmental impact assessment (EIA) is required for "construction or earth moving activities in the sea or within 100 meters inland of the highwater mark of the sea, in respect of: buildings or infrastructure". Incorporating the WEC device inside a breakwater greatly increases the likelihood of EIA approval compared to a stand-alone system. In a lecture presented by Rossouw (2008), he discussed the potential environmental impacts of a wave plant that must be assessed. These include: visual impact, shoreline accretion/erosion, impact on fishing, military practice areas, commercial shipping, the impact of electromagnetic fields on marine mammals and sharks, impact on seabirds and their nesting, potential for marine mammals to become entangled or hauled out of the sea and the impact of pressurised water and water quality on marine larvae. The following South African laws must be adhered to in the case of a port development as outlined in the presentation by Rossouw (2008):

- National Environment Management Act (Act 107 of 1998) (NEMA)
- Integrated Coastal Management Act (2008)

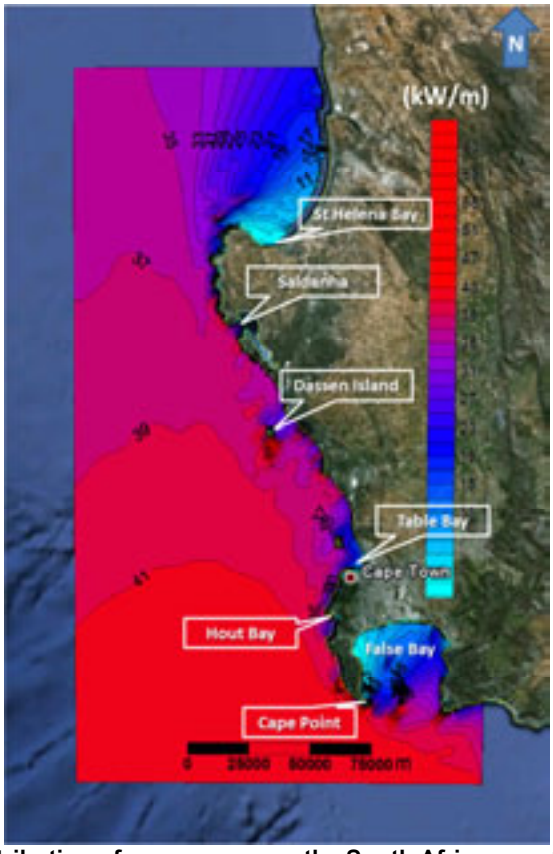

Figure 3-2: Spatial distribution of wave power on the South African southwest coast based on 10 years of hindcast wave data (Joubert, 2008)

- Sea-shore Act (Act 21 of 1935)
- Marine Living Resources Act (Act 18 of 1998)
- Sea Birds and Seals Protection Act (Act 46 of 1973)
- Maritime Zones Act (Act 15 of 1994)
- Marine Pollution (Control and Civil Liability) Act (Act 6 of 1981)
- National Monuments Act (Act 28 of 1969)
- The South African Marine Safety Authority (1998)

In addition the following convention and policies must also be considered:

- White Paper on the Renewable Energy Policy of the RSA (2004)
- Draft Western Cape Integrated Energy Strategy (2007)
- United National Convention on the Law of the Sea (1982)
- Convention on the Prevention of Marine Pollution by Dumping of Wastes and Other Matter (1972)
- Convention on Biological Diversity (1992)
- Conservation of Biological Diversity White Paper (1997)

Generating electricity from ocean waves falls under the Electricity Regulation Act of 2006 as outlined in the Government Gazette of 5 August 2009. A generation permit must be obtained from the National Energy Regulator of South Africa (NERSA). NERSA requires general information such as: the name of the project, its location,

type, capacity, energy efficiency and expected lifespan. More detailed information on the following must also be provided: maintenance/decommissioning costs and schedule, expansion/modifications planned during lifespan, customer profile and financial information of the project (Rossouw, 2008).

Lastly, the Sea-shore Act and Integrated Coastal Management Act state that land use permission is required for onshore development below the high water mark.

3.1.4 Power purchaser

The ShoreSWEC must be deployed near a populated coastal area to ensure a market for its generated electricity. Potential power purchasers include the port development, an electricity distributor such as Eskom or the nearest municipality. Distributors will in turn sell the generated electricity to willing buyers. In order to sell the electricity a Power Purchase Agreement (PPA) is required. A PPA is a legal contract between the generator and the electricity purchaser. The PPA can be used to obtain financing for the project provided that electricity outputs and associated revenue are clearly defined.

South Africa's first commercial wind farm, the Darling Wind Farm, signed a private PPA with the City of Cape Town in 2006 for 20 years. The city sells the electricity generated as "green electricity certificates" to willing buyers, at a premium of 25c/kWh above the current electricity rates (SEA and REEP 2009). The City of Cape Town has set itself a target that 10% of electricity generated must be from renewable energy sources by 2020. Deploying the ShoreSWEC in close proximity to Cape Town and signing a PPA will assist the city in reaching its renewable energy goal. Selling the electricity generated by the ShoreSWEC to the port development in which it is deployed will help create an environmentally conscientious image for the port, which can increase tourism and attract investment.

The South African Department of Energy published a request for proposals for renewable energy projects from Independent Power Producers, based on competitive price bidding, in August 2011. The bids were evaluated and awarded according to price and a tariff cap was put in place for each of the renewable technologies (ocean energy was unfortunately not included). This bidding method is called the "Rebid" process. Wave energy technology can be included in the Rebid process once it has proved its reliability and has reached maturity.

3.1.5 Infrastructure

A site's relative proximity to fabrication facilities and the available coastal infrastructure greatly influences its suitability for the deployment of the ShoreSWEC. The device is composed of structural-, airflow- and PTO components. The majority of these components must be custom manufactured and deployed using available manufacturing facilities and coastal infrastructure.

The structure of the device is mainly made up of steel reinforced concrete units which will be fabricated in the dry using a casting basin close to the site (provided there is space available) or in a port development. The units will be floated to the deployment location and provision must therefore be made to temporarily seal the chamber openings. Transporting the units from the fabrication facility into the water entails flooding the casting basin and floating the units out, or in a port development

using a synchrolift to lower the units into the water. Tugs are used to tow the units to the prepared stone foundation bed where each unit is sunk into its final position with the help of divers.

The airflow system of the ShoreSWEC consists of high and low pressure conduits and unidirectional valves. The piping and valves will be manufactured from stainless steel, aluminum or polyvinyl chloride (PVC) to ensure that they are corrosion resistant. These will be transported to the site for assemblage either by ship or road, since the device is shore connected.

The turbine/generator set in its housing, together with transmission cabling, form the PTO of the device. Once manufactured, the PTO will be incorporated into the device by connecting it to the completed airflow system.

3.1.6 Grid connection

The electricity generated by the ShoreSWEC will be fed into the national utility's distribution network and it is therefore important to consider a site's proximity to a grid connection point with suitable capacity. According to a report compiled by Queen's University of Belfast, an 11 kV capacity grid connection point is sufficient to accept the 500 kW generation capacity of LIMPET (Wavegen, 2002). The energy conversion capacity of the ShoreSWEC is expected to be less than, or comparable to, that of the LIMPET and therefore grid connections with a minimum of 11 kilovolt capacity were considered in the site evaluation process.

The above mentioned site selection criteria were used to evaluate 20 potential sites off the South Africa coast. Each site was ranked according to suitability with A = well suited, B = moderately suited and C = not suited. Of the 20 sites, 5 were ranked as well suited and best met the selection criteria. These 5 sites were considered for further investigation and include: Saldanha, Koeberg, Granger Bay, Hermanus and Coega. Refer to Table A-1 for all the 20 sites evaluated.

3.2 Potential sites

The evaluation of the five most promising sites is presented in Table 3-1. Figure 3-3 to Figure 3-7 are satellite images, orientated northwards, showing the layout of each site relative to the dominant wave direction (indicated by the white arrow).

Table 3-1: Site evaluation of the five most promising locations

Site	Coastal structures	Resource	Environment	Power purchaser	Fabrication and infrastructure	Grid	Rating
Saldanha 33°2'50.31"S 17°58'9.29"E	A half-moon shaped artificial beach curved towards the dominant SW wave direction and a 990 m long, sheltered jetty orientated towards SSW both of which can potentially be retrofitted to facilitate the ShoreSWEC.	Saldanha has an mean annual average wave power resource of approximately 30 kW/m.	The port has EIAs in place. Langebaan Lagoon is ecologically sensitive. Potential impact on commercial shipping, fishing and sedimentation processes.	Population of Saldanha is 75 000. Mittal Steel Mill. Ferromarine Africa.	Manufacturing facilities for structural caisson units. Mittal Steel Mill can supply structural steel and piping. Tugs, cranes and divers available.	11 kV, 66 kV and 132 kV Eskom lines available	**A**
Koeberg 33°40'43.1"S 18°25'31.1"E	Rubble mound breakwater. Primary breakwater 900 m long longitudinally orientated towards NW and W. Secondary breakwater 500 m long, SW orientated. Water depth equal to or less than 10 m	Substantial resource of approximately 35 kW/m mean annual average	Located in UNEP Cape Floristic Region. Potential security issues. Potential impact on sedimentation.	Koeberg, Melkbos-strand, City of Cape Town.	Permission required to manufacture units on site. Coastal infrastructure available at port of Cape Town 30 km south.	11 kV, 66 kV and 132 kV Eskom lines available	**A**
Granger Bay 33°53'56.95"S 18°24'54.58"E	220 m long dolos breakwater orientated ENE. Wave refracted into Table Bay approach site from NW.	Site sheltered by Mouille Point reducing resource available to less than 5 kW/m	Close proximity to Port of Cape Town that has EIAs in place. Potential impact on commercial shipping.	Port of Cape Town. V and A Waterfront. City of Cape Town.	Units can be manufactured on site or in Cape Town port. Coastal infrastructure such as tugs, floating and mobile cranes and divers available.	11 kV, 66 kV and 132 kV Eskom lines available	**A**
Hermanus 34°26'0.48"S 19°13'40.46"E	270 m long breakwater with 20 t concrete cubes and Toskane armourment. Orientated towards NE. Refracted waves propagate along breakwater. Deep water location.	Resource approximately 35 kW/m.	Potential impact on fishing activities, whales and other marine mammals.	Overstrand Municipality. Population 50 000	Port of Cape Town approximately 150 km west. Limited infrastructure available.	11 kV and 132 kV	**A**
Port of Ngqura 33°49'5.78"S 25°41'37.01"E	Approximately 2.5 km composite vertical breakwater orientated SSW. One caisson left open for potential OWC application.	Relatively sheltered in Algoa Bay, but resource approximately 20 kW/m.	Potential impact on commercial shipping, sedimentation and marine protected areas such as Jahleel Island.	Coega Industrial Development Zone (IDZ).	Manufacturing facilities and infrastructure available.	11 kV and 134 kV substations	**A**

Figure 3-3: Layout of the port of Saldanha relative to the dominant wave direction

Figure 3-4: Layout of Koeberg nuclear power station relative to the dominant wave direction

Figure 3-5: Layout of Granger Bay small vessel harbor relative to the dominant wave direction

Figure 3-6: Layout of Hermanus small vessel harbor relative to the dominant wave direction

Figure 3-7: Layout of the port of Ngqura, Coega IDZ, relative to the dominant wave direction

3.3 Final site selection

All the promising sites identified from the evaluation are port developments with existing coastal structures which could potentially be retrofitted to facilitate the ShoreSWEC. However, it would be ideal if the ShoreSWEC device could be designed for and built into a vertical breakwater of a new port development. The master plan for the expansion of the Victoria and Alfred (V and A) Waterfront in Cape Town includes the possibility of expanding the current development to the northwest of the area currently occupied by the Oceana Power Boat Club. A local coastal engineering consultancy, Prestedge Retief Dresner Wijnberg (Pty) Ltd (PRDW), proposed a breakwater layout for the new development, similar to that shown in Figure 3-8. The breakwater will require caissons from at least 10 m water depth to the head of the structure and is ideally orientated to incorporate the ShoreSWEC device (as indicated by the red portion of the conceptual layout in Figure 3-8).

Another main advantage of deploying the ShoreSWEC at Granger Bay is its close proximity to the Cape Town port with all its available coastal infrastructure and manufacturing facilities. In general Granger Bay is located in a sheltered part of Table Bay, but the ShoreSWEC is still expected to fulfil is primary objective which is to serve as a technology demonstrator and working prototype of a full scale SWEC.

The next phase of the study was to conduct a detailed evaluation of the wave conditions at the Granger Bay site and to determine the wave power available for conversion.

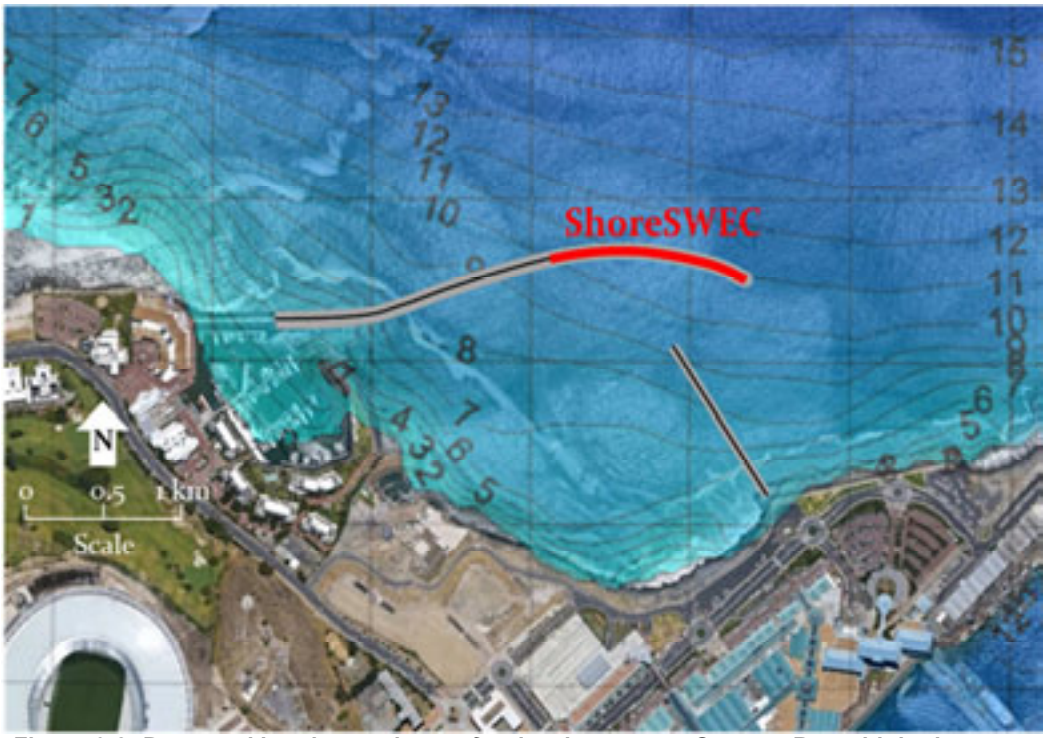

Figure 3-8: Proposed breakwater layout for development at Granger Bay with bathymetry contours. Potential location for the ShoreSWEC indicated in red.

4 Wave conditions and energy resource at Granger Bay

From the site identification and selection procedure outlined in Chapter 3, Granger Bay was selected as the most suitable location for the deployment of the ShoreSWEC prototype. In order to effectively design the ShoreSWEC for deployment at Granger Bay, statistics of local short-term and long-term sea states are required. Due to the lack of sufficient measured wave data at or near the site of interest, the development of a numerical wave modelling procedure was required to simulate wave propagation from a deep sea location with known wave conditions into Table Bay. Once validated, the model was employed to transfer the dominant (operational) wave conditions and extreme storm events from offshore to the deployment location.

The ShoreSWEC was designed to optimally both convert wave energy from the most frequently occurring wave conditions, and to remain stable during design load conditions of extreme storms (refer to Chapter 5 for the ShoreSWEC design conditions). In order to determine the energy conversion capacity of the deployed device at Granger Bay, an assessment of the available wave power resource is required which was derived from the transferred wave data.

The objective for this portion of the study, the employed methodology and desired output are presented in Figure 4-1. The Granger Bay site shown in Figure 4-1 is at the head of proposed breakwater (refer to Figure 3-8 for a more detailed diagram).

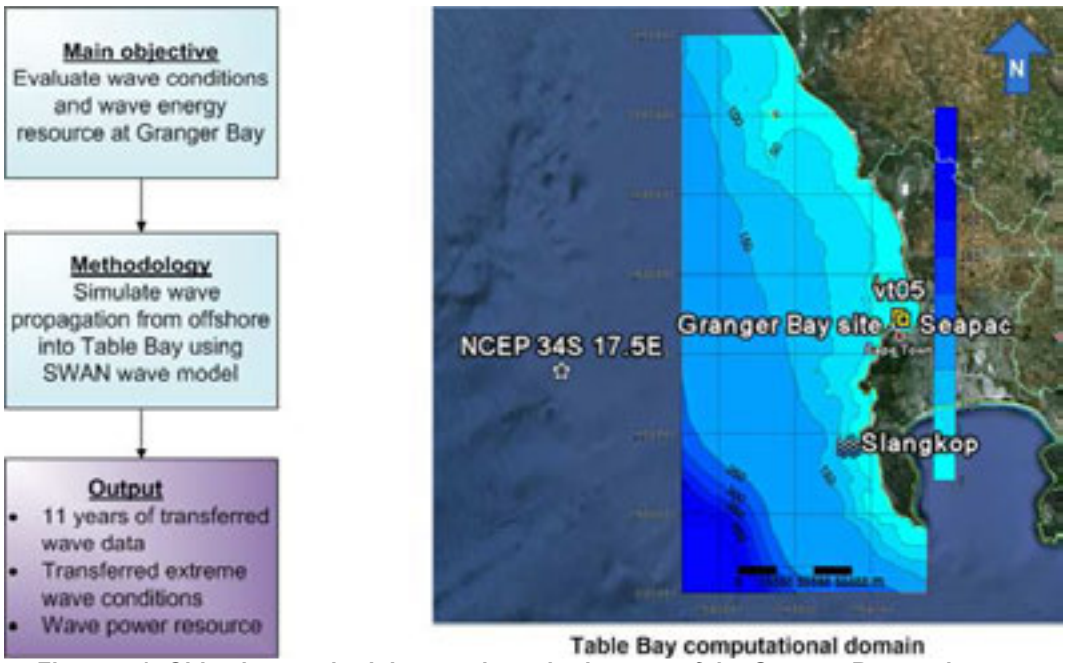

Figure 4-1: Objective, methodology and required output of the Granger Bay study area.

4.1 Offshore wave data used in the study

The input offshore wave data used for the wave data analysis at Granger Bay was obtained from the National Centers for Environmental Prediction (NCEP). NCEP is a department of the National Oceanic and Atmospheric Administration (NOAA) which is an agency of the United States federal government responsible for monitoring the global climate and environment. NCEP comprises nine centers, including the Environmental Modelling Center, which develops, improves and monitors data assimilation systems and models of the atmosphere, ocean and coupled system. (NCEP Internet team, 2007). NCEP provides operational ocean wave predictions using the wave model Wave Watch III with operational NCEP products as input. Wave Watch III is a third generation wave model developed by NCEP based on the WAM wave model.

Tolman (2006), a developer of WAVEWATCH III, describes the wave model's functionality as follows:

> "WAVEWATCH III solves the spectral action density balance equation for wavenumber-direction spectra. The implicit assumption of this equation is that properties of medium (water depth and current) as well as the wave field itself vary on time and space scales that are much larger than the variation scales of a single wave. A constraint is that the parameterisations of physical processes included in the model do not address conditions where the waves are strongly depth-limited. These two basic assumptions imply that the model can generally be applied on spatial scales (grid increments) larger than 1 to 10 km, and outside the surf zone."
> (NOAA: Marine modeling and analysis branch, 2012)

Considering Granger Bay's nearshore location, further numerical wave modeling is required to simulate wave propagation from the deep sea NCEP location into Table Bay. The NCEP global model output is calibrated and validated with buoy data and with European Remote-Sensing Satellites (ERS2) fast-delivery altimeter (measures altitude above a certain datum) and scatterometer (measures scatter from the ocean surface) data. An analysis of the NCEP data is presented in the following section.

4.2 Analysis of offshore NCEP wave data

The offshore NCEP wave data used as input to the nearshore wave model is located approximately 85 km west of Granger Bay at 34ºS 17.5ºE in approximately 500 m water depth (refer to "NCEP 34S 17.5E" in Figure 4-1 and Figure 4-2). The hindcast wave data set was obtained for February 1997 to August 2008, just more than 11 years. The wave data is available in three hourly intervals and each record consists of the date- and time of recording, significant wave height (H_{m0}), peak wave period (T_p), and peak wave direction (D_p). The wave data is a 100% complete set, consisting of 33 857 records. As a quality assurance measure, the NCEP wave parameters were compared to wave data recorded by the Slangkop wave measuring buoy for the period the two data sets overlap, which was July 2000 to July 2006. Slangkop is located 5 km offshore in 70 m water depth as shown in Figure 4-2. It is expected that the NCEP wave heights will be greater than Slangkop's due to the energy losses occurring as waves propagate to the shallower water location. Slangkop was deployed and operated by CSIR on behalf of the National Port Authority who made the data available for this study.

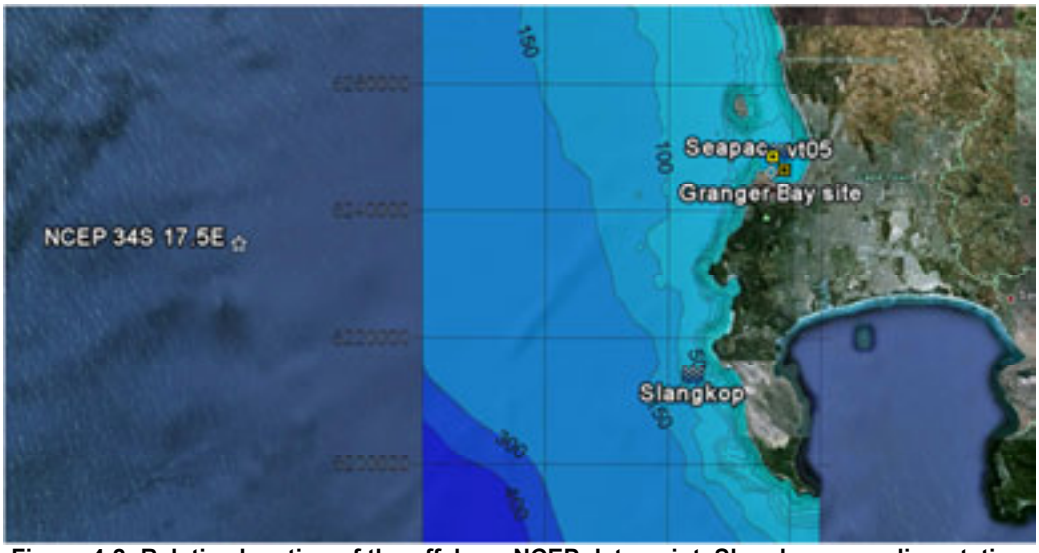

Figure 4-2: Relative location of the offshore NCEP data point, Slangkop recording station and CSIR's virtual wave buoys (vt05) and Seapac current meter in Table Bay

The NCEP wave parameters were analysed and compared to Slangkop measured data. The results of the data analysis are presented in the following sections.

4.2.1 Wave height distribution

Wave height is a very important wave parameter not only to determine the available resource, but also for design purposes. It is therefore imperative that the input NCEP wave height data is of an acceptable standard and compares well to the measured wave data of Slangkop.

The probability of exceedance curves of wave height in Figure 4-3(a) show that the NCEP wave heights are on average 0.3 m greater than Slangkop's. This reduction in wave height occurs as waves travel to the shallower water of the Slangkop location, and can be ascribed to energy losses caused by bottom friction. In general the NCEP wave height data has a similar probability of exceedance distribution compared to the Slangkop data and therefore appears to be of acceptable quality.

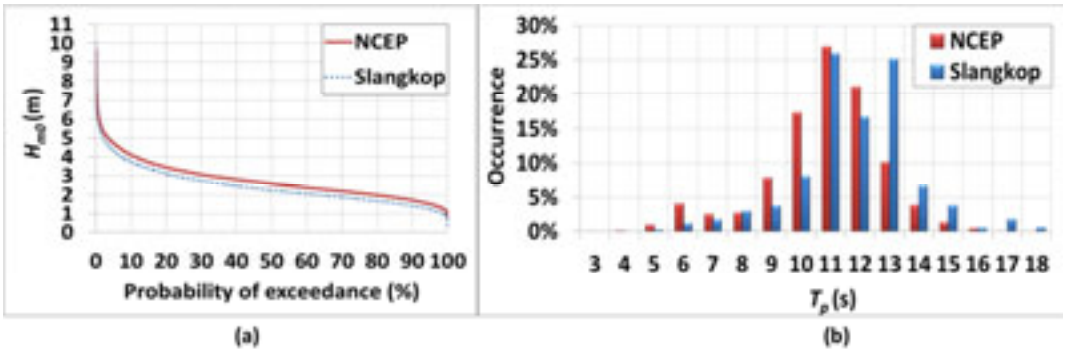

Figure 4-3: (a) Probability of exceedance of wave height at NCEP 34ºS 17.5ºE and measured at Slangkop wave recording station. (b) Frequency of occurrence of wave period at NCEP 34S 17.4E and measured at Slangkop wave recording station July 2000 to July 2006

A comparison of the NCEP and Slangkop wave period data is presented in the next section.

4.2.2 Wave period

The frequency of occurrence of wave period bar graphs for NCEP and Slangkop presented in Figure 4-3(b) show that both data sets' most frequently occurring wave period is 11 s for approximately 25% of the six year period. In general the Slangkop data contains higher values of wave period occurring more frequently than the NCEP data, indicating that the NCEP data might slightly underestimate the wave period conditions off the South African coast. This could be due to local effects not included in the NCEP model or the Slangkop buoy's recording frequency bins. In general the frequency of occurrence graphs of the two data sets correlate sufficiently to warrant the use of the NCEP wave period data.

4.2.3 Directional distribution

The CSIR replaced the non-directional buoy at Slangkop with a directional Datawell Waverider in 2001, but unfortunately none of this directional wave data was available for comparison with the NCEP directional data. The frequency of occurrence of NCEP's peak wave direction data plotted on the contour graph in Figure 4-4 confirms the predominant southwesterly direction of approaching waves as stated by Rossouw (1989).

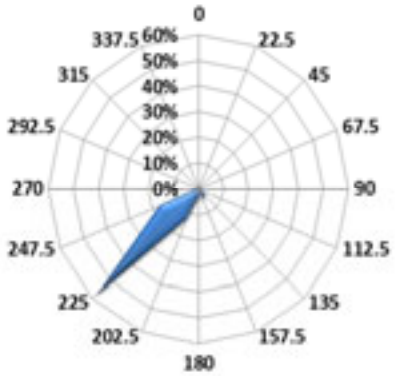

Figure 4-4: Directional wave rose showing the frequency of occurrence of peak wave direction NCEP 34°S 17.5°E

The accuracy of the NCEP data and the output of the nearshore wave model will be validated through further comparison with CSIR recorded wave data as presented in section (§)4.5.2. A discussion of the SWAN wave model used to simulate the propagation of waves from the NCEP offshore location to Granger Bay is presented in the following sections.

4.3 Background of the SWAN wave model

SWAN, an acronym for **S**imulating **WA**ves **N**earshore, is a third-generation wave model to obtain estimates of wave parameters in coastal areas, lakes and estuaries from given wind, bottom and current conditions according to the user manual of SWAN Cycle III version 40.85. SWAN was developed at the Delft University of Technology and is continuously improved. Unlike most other coastal wave models, SWAN is freely available and open-source. It is described in peer-reviewed literature and is used by more than 250 institutions (Allard and Rogers, 2004). The SWAN model solves spectral action balance equations and accounts for shoaling and refraction (depth and current induced), wave generation due to wind, energy dissipation due to whitecapping, bottom friction and depth-induced wave breaking, as well as nonlinear wave-wave interactions (quadruplets and triads).

4.4 Wave transfer methodology

As stated earlier, the objective of this part of the study was to transfer NCEP's 11 years of wave data from offshore to Granger Bay to enable the investigation of the ocean conditions at the proposed breakwater. The most direct way to achieve this would be to do a SWAN simulation for each of the 33857 NCEP records. Such an operation would have been very computationally intensive making it impractical.

To simplify the computational effort NCEP wave direction and period data were divided into bins (3 s to 19 s in 1s intervals and 0º to 337.5º in 22.5º intervals) and the average wave height for each combination of direction and period was determined (refer to Table B-4). A SWAN simulation was done for each combination of offshore wave direction, period and its average wave height. The 16 directional and 17 period bins equates to a total of 272 simulations which took approximately 16 hours in parallel sessions on a quad core processor. SWAN output includes the variation in wave direction and wave height over the computational area for each offshore wave period and direction combination. The wave height variation, expressed as a percentage of the offshore input wave height, is used to determine the wave height at the site of interest. The methodology used to transfer the offshore NCEP data into Table Bay and an example record is presented diagrammatically in Figure 4-5.

The wave modelling procedure outlined in Figure 4-5 is based on the assumption that the wave height variation is relative to the average offshore wave height. Energy dissipation processes such as bottom friction greatly influence the resulting wave heights in shallow water and are also a function of wave height. In an attempt to determine the sensitivity of wave height variation to the input offshore wave heights, SWAN simulations were conducted for offshore wave heights of less than and greater than the average wave heights. It was found that the model overestimates dissipation for smaller wave heights and underestimates dissipation for larger waves in shallow water. However, the discrepancies are marginal and are shown to not greatly influence the accuracy of the model (refer to the model validation in §4.5.2).

4.5 SWAN input requirements

The operational wave parameters give a general description of the expected wave conditions at the Granger Bay site of interest within Table Bay. Time dependency, wind and current inputs were deemed unnecessary for this purpose and are more applicable to site specific designs and real time simulations. It was therefore not included in the simulations. For SWAN to model wave propagation from the input boundary conditions, a computational domain and associated bathymetric grid must be defined.

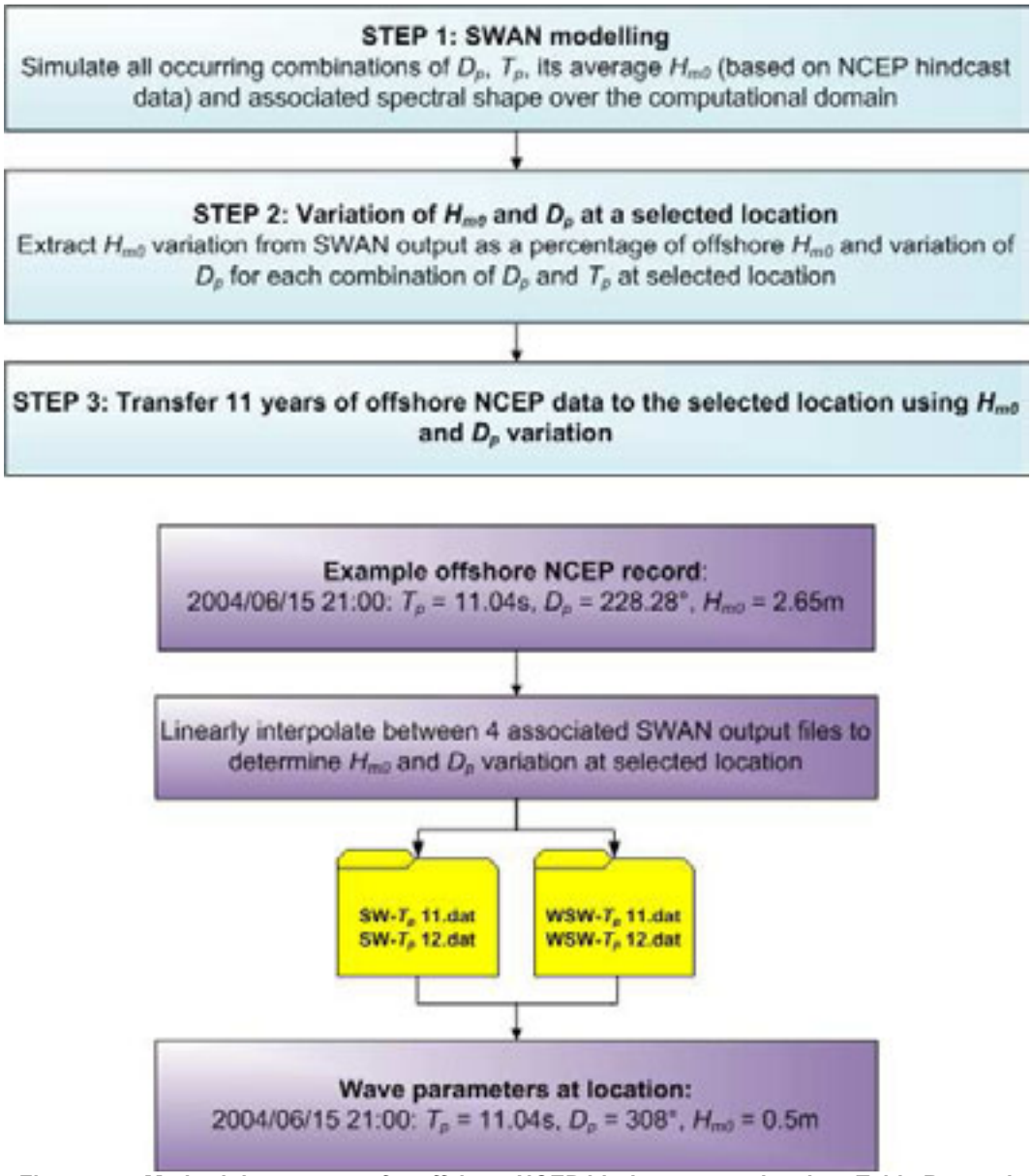

Figure 4-5: Methodology to transfer offshore NCEP hindcast wave data into Table Bay and example output

4.5.1 Computational and bathymetric grids

A uniform, rectangular computational grid covering an area of 65 km by 140 km was specified for the initial SWAN simulations (refer to "Grid 1" shown in Figure 4-6). Grid 1 has a 250 m by 250 m cell resolution and it was assumed that the offshore NCEP wave conditions apply to each gridpoint of Grid 1's boundaries. In reality the wave conditions on the boundaries will vary, but as waves propagate away from the boundaries the influence of the seafloor on the wave parameters will rectify this assumption. A second computational grid with a 50 m by 50 m cell resolution was specified a sufficient distance away from the Grid 1 boundaries. SWAN was used to simulate waves from Grid 1's boundaries to the boundaries of Grid 2. Through

interpolation SWAN calculated the wave conditions on Grid 2's finer resolution boundary. In order to determine the spatial distribution of wave power at a minimum of 10 grid points along the breakwater structure an even finer resolution computational grid of 10 m by 10 m cells was defined. Figure 4-6 shows the three computational grids used for the wave simulations.

The bathymetric grids were derived from naval charts of the southwest coast and Table Bay (provided courtesy of C. Rossouw). The water level over the domain was based on the Mean High Water Spring (MHWS) for Table Bay of 1.74 m (South African Navy Hydrographic Office). Sea level rise was also included in the water level values used based on the predictions of The Copenhagen Diagnosis (2009) of 0.27 m for 2035 as outlined by PRDW (2010).

4.5.1.1 Boundary conditions

The computational Grid 1 shown in Figure 4-6 has three water boundaries (south, west and north) and the remaining boundary (east) is mainly land except for a small water portion. This implies only a small water boundary is available for waves to enter the domain from the east. The wave fields on the model boundaries were prescribed as energy density spectra defined by shape, directional distribution, significant wave height, peak wave period and peak wave direction. A discussion of these parameters follows.

Peak enhancement factor (γ)

The shape of the energy density spectrum was prescribed in terms of its peak enhancement factor (γ). Refer to §2.3.3 for a detail discussion of spectral shapes. The γ-values recorded at the Slangkop measuring station, over a six year period, were analysed to determine the shape of the input energy density spectrum on the model boundary The γ-values were divided into directional bins and a linear relationship between γ and wave height and γ and wave period was determined. The average γ-values as prescribed by the two linear relationships were used as input into the wave model. Refer to Table B-5.

Directional spreading (m)

The directional distribution of energy density on the model boundaries was prescribed in terms its directional spreading. Refer to §2.3.3 for a detail discussion of directional distributions. In order to determine the values for directional spreading best suited for South African wave conditions, spreading values recorded at Slangkop station over a six year period were analysed. A similar analysis to that conducted on the γ-values was done for the measured spreading values. The most probable spreading values as a function of wave height and wave period were determined. Refer to Table B-6.

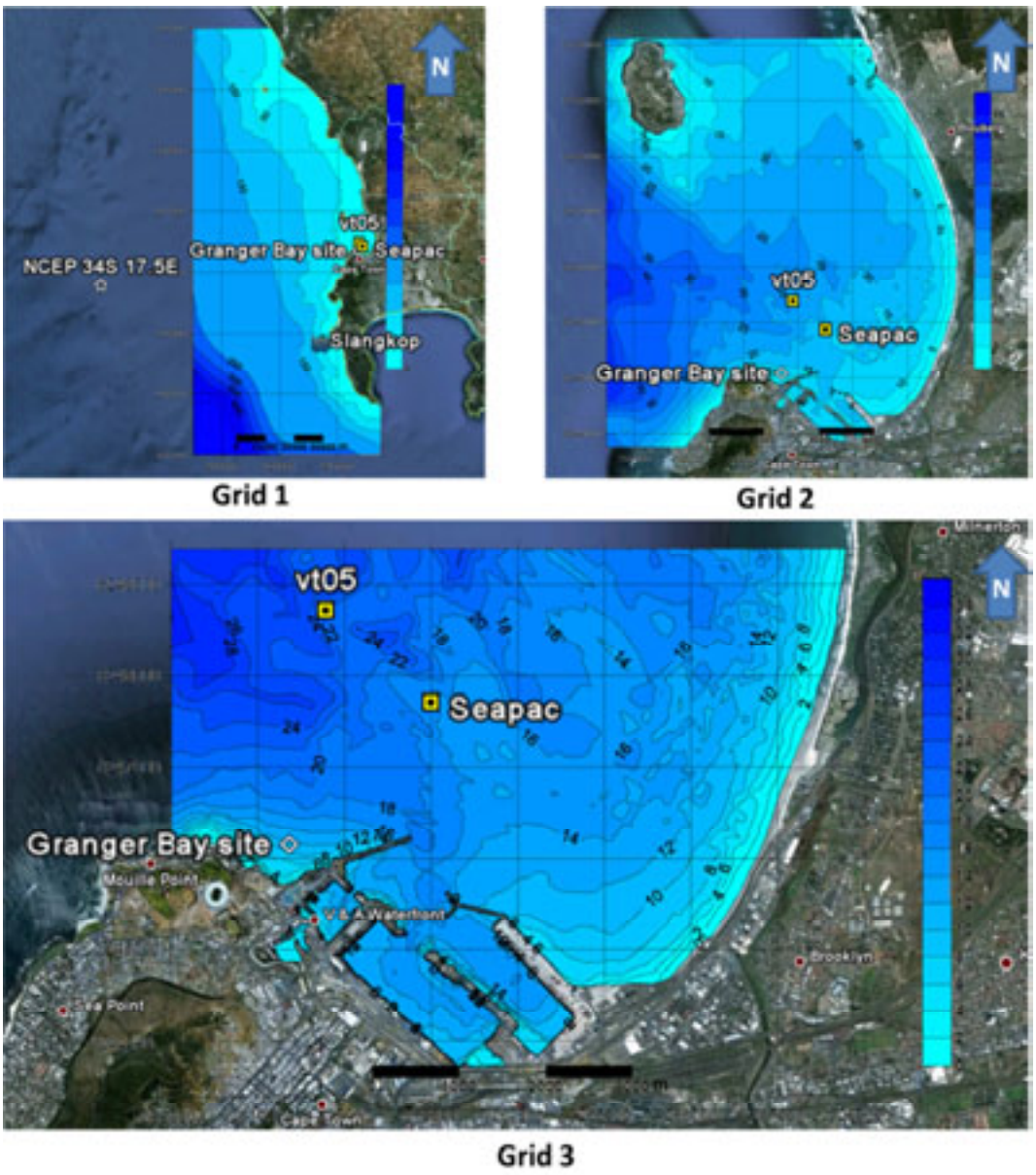

Figure 4-6: Computational and bathymetric grids of Table Bay

Wave height

As stated in §4.4, SWAN simulations were done for the average wave height of each occurring combination of wave period and wave direction (see Table B-4). The variation in wave height as determined by SWAN was expressed as a percentage of the input offshore wave height.

Wave period

Wave periods from 3 s to 19 s in 1 s intervals were modelled as discussed previously.

Wave direction

The entire directional spectrum from 0º to 337.5º in 22.5º intervals was simulated. The frequency of occurrence of combinations of wave height, period and direction for the NCEP data is presented in Table B-1, Table B-2 and Table B-3.

This concludes the discussion of the input boundary conditions required for SWAN. Simulations were conducted over the three computational domains and the output was validated through comparison with CSIR wave data, as presented and discussed in the following section.

4.5.2 Validation through comparison with measured CSIR data transferred to Table Bay

Rossouw et.al. (2005) developed a real-time wave model for the National Ports Authority of Cape Town to determine wave conditions at selected locations in Table Bay, known as "virtual wave buoys". SWAN is used to simulate waves propagating from Slangkop wave recording station (refer to Figure 4-2 that shows Slangkop's location relative to the NCEP offshore data point and the virtual buoys in Table Bay). Rossouw's model was calibrated with measured data from a Seapac electromagnetic current meter deployed 1.6 km north of the entrance to the Port of Cape Town in 17 m water depth (refer to Figure 4-7). The Seapac was operational for the relatively short period of 1 February to 28 March 2002. The measured Seapac and modeled virtual wave buoy data was made available by National Port Authority to validate the Granger Bay model output.

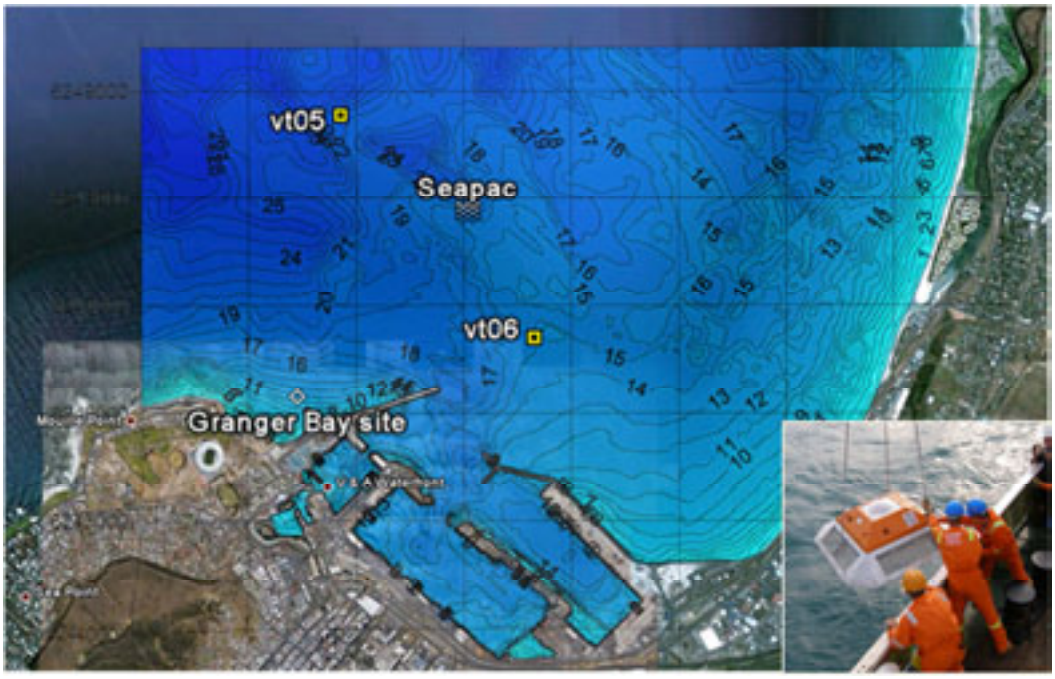

Figure 4-7: Location of two virtual wave buoys (vt05 and vt06) and Seapac relative to the Granger Bay site. Seapac current meter deployment (image courtesy of CSIR)

The measured Seapac wave height data was directly compared to the modelled wave height data. Figure 4-8 shows that the model's values of wave height

compares favourably to the Seapac data, but the model does give wave heights which are virtually zero on a few occasions. Upon closer inspection it was found that the model underestimates the wave height conditions in Table Bay for waves approaching from the southeast to southerly direction. This can be due to the relatively small water area on the model's eastern boundary from which these easterly waves must enter the computational domain.

It is expected to not greatly influence the operational conditions at Granger Bay, due to the relatively low occurrence of these directional conditions (10% frequency of occurrence refer to Table B-2 and Table B-3) and the small wave height it produces in Table Bay.

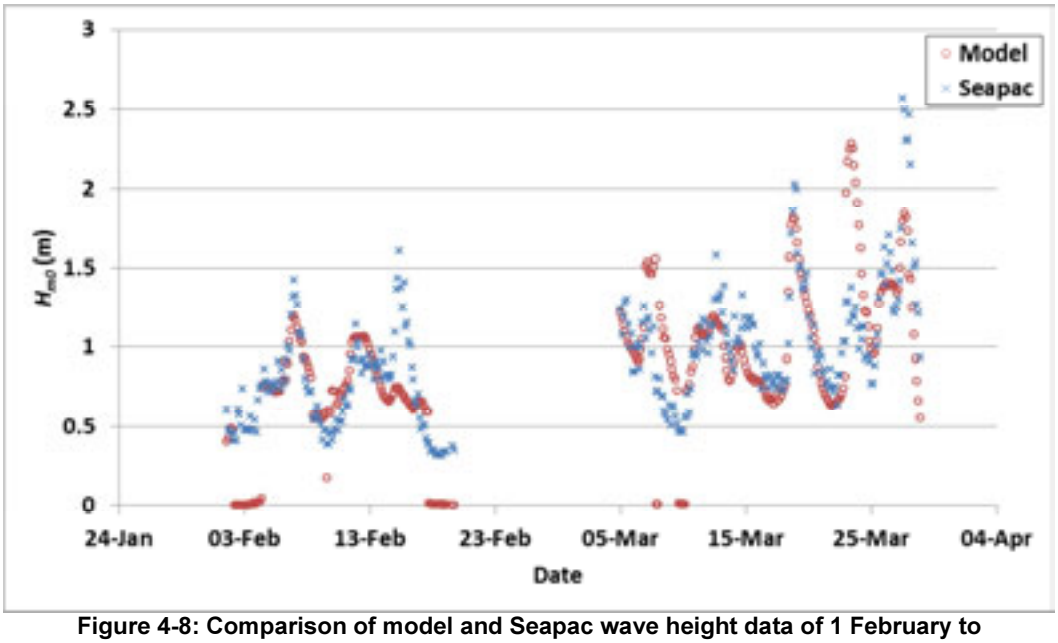

Figure 4-8: Comparison of model and Seapac wave height data of 1 February to 28 March 2002

The correlation between the model and Seapac wave height data was found to have a coefficient of determination, R^2, of 0.55 indicating that 55% of the model wave height data correlates well with the Seapac data over the recording period. This relatively low correlation could be ascribed to the short recording period. Similar correlation analyses with the longer virtual wave buoy data sets (four year overlapping period) showed that the model wave height correlates with 75% of the virtual buoy data (refer to Figure B-2 and Figure B-4).

The probability of exceedance curves of the model and Seapac wave heights presented in Figure 4-9 show that the model wave height's probability of exceedance agrees reasonably well with that of Seapac, except for the very low values of wave heights from the southeast as discussed previously. The probability of exceedance of wave height curves of the model and the virtual buoy data, presented in Appendix B, compare favourably and have a similar distribution to that shown in Figure 4-9.

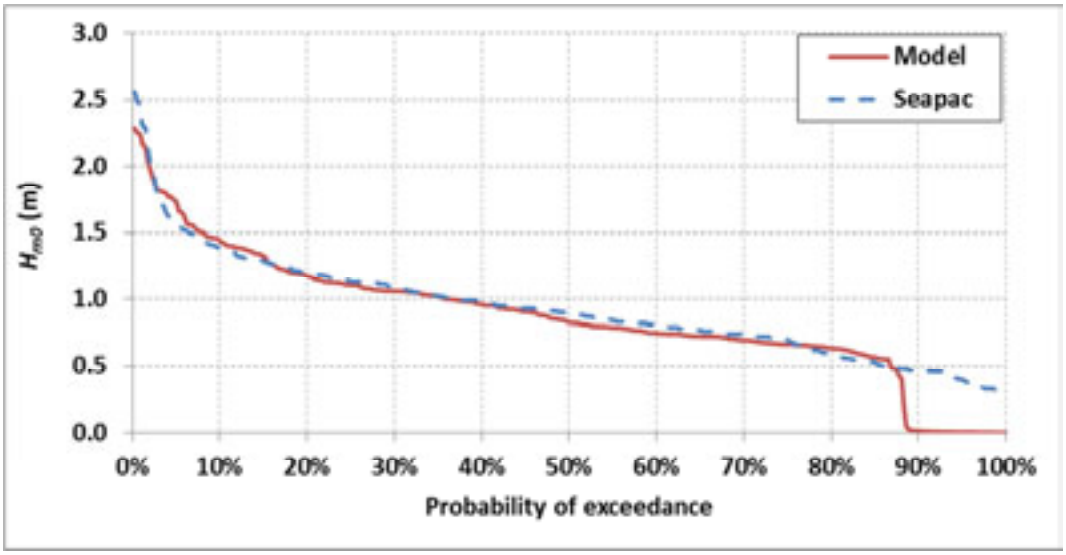

Figure 4-9: Probability of exceedance of model and Seapac wave height data February to March 2002

From the comparison of the model output, measured Seapac data, and virtual buoy data (based on recorded Slangkop data), it can be concluded that the model will give acceptably accurate wave conditions in Table Bay.

4.6 Results of model study

An example of the model output is presented in Figure 4-10 as a contour and vector plot of the spatial distribution of wave height and direction for the most frequently occurring combination of offshore wave direction (southwest) and wave period (11 s) with an average offshore wave height of 2.65 m. The resulting wave height at Granger Bay is 0.5 m and refracted waves approach the site from the northwest (refer to Figure 4-11). This is an 80% reduction in wave height as waves propagate from offshore to Granger Bay due to energy losses caused by wave-bottom interaction and the sheltering effect of Mouille Point. The reduced wave height conditions will result in a low wave power resource available for utilisation by the ShoreSWEC.

The main objective of this part of the study is to determine the operational wave conditions at Granger Bay for which to evaluate the hydrodynamic conversion efficiency of the ShoreSWEC. The operational wave parameters derived from 11 years of hindcast NCEP data is presented in the following section.

4.6.1 Operational wave conditions

The operational wave parameters were extracted at the head of the breakwater proposed by PRDW for the Granger Bay development as shown in Figure 4-12. The site is located at 33.898ºS 18.42ºE in 11 m water depth (indicated by the yellow star).

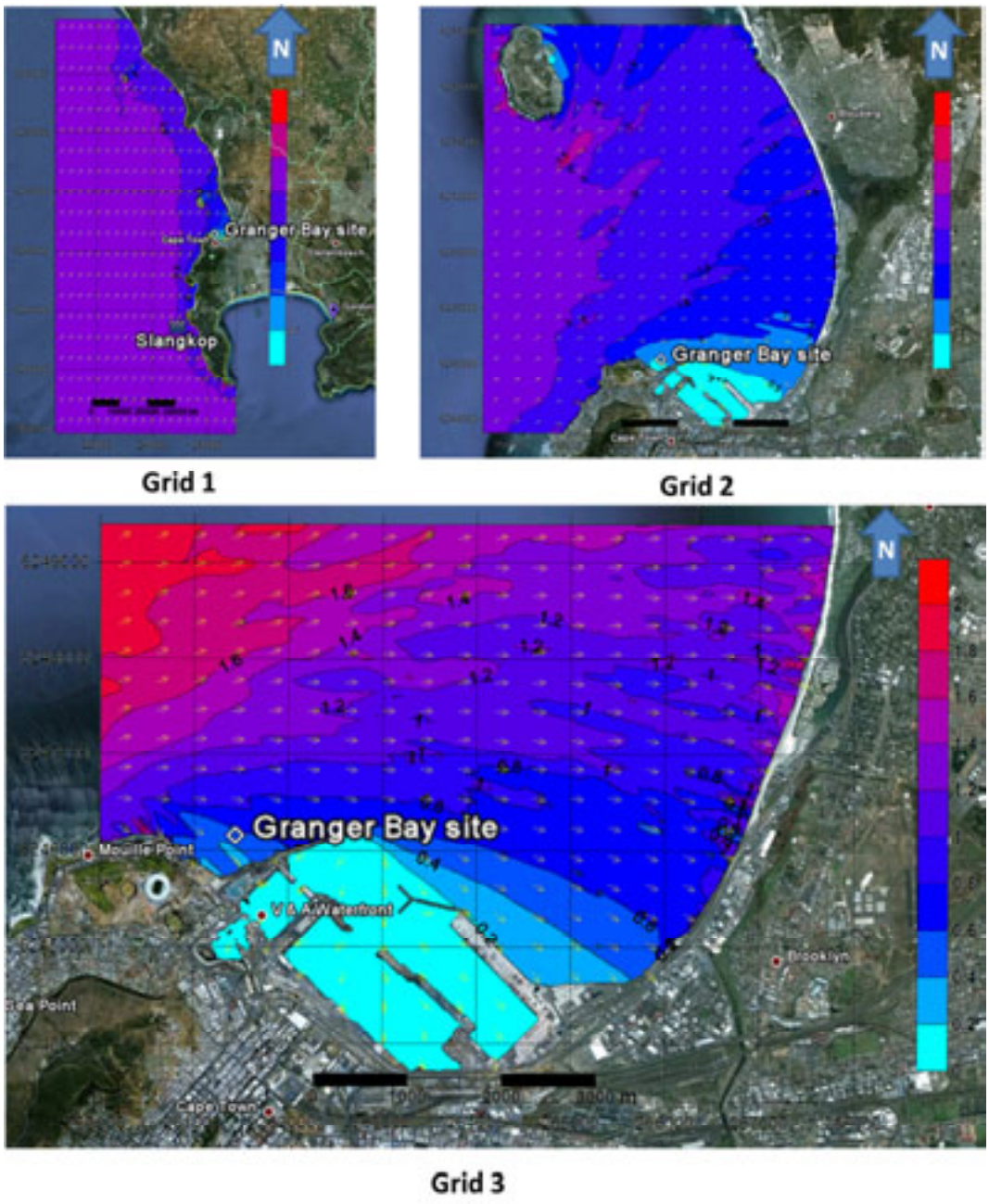

Figure 4-10: Operational wave conditions in Table Bay. Offshore wave conditions: D_p = 225º, T_p = 11 s and H_{m0} = 2.65 m

Wave height

The operational conditions, as presented in Figure 4-13, show that 96% of the wave height values range from 0 m to 1.5 m which will result in a relatively low wave power resource of roughly 0 kW/m to 12 kW/m. In the experimental test component of this study, the conversion efficiency of the ShoreSWEC was evaluated to determine if its production from these operational wave height conditions would be sufficient to justify its deployment at Granger Bay.

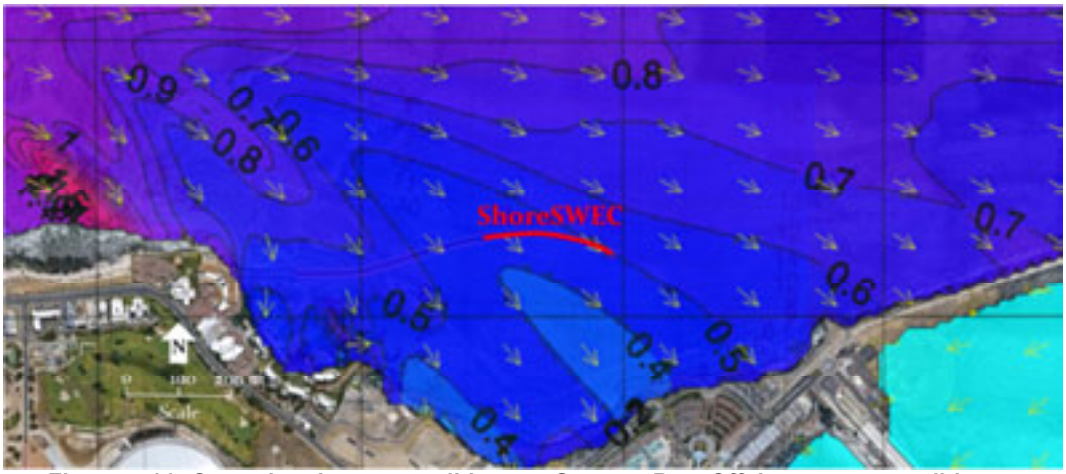

Figure 4-11: Operational wave conditions at Granger Bay. Offshore wave conditions: D_p = 225°, T_p = 11 s and H_{m0} = 2.65 m

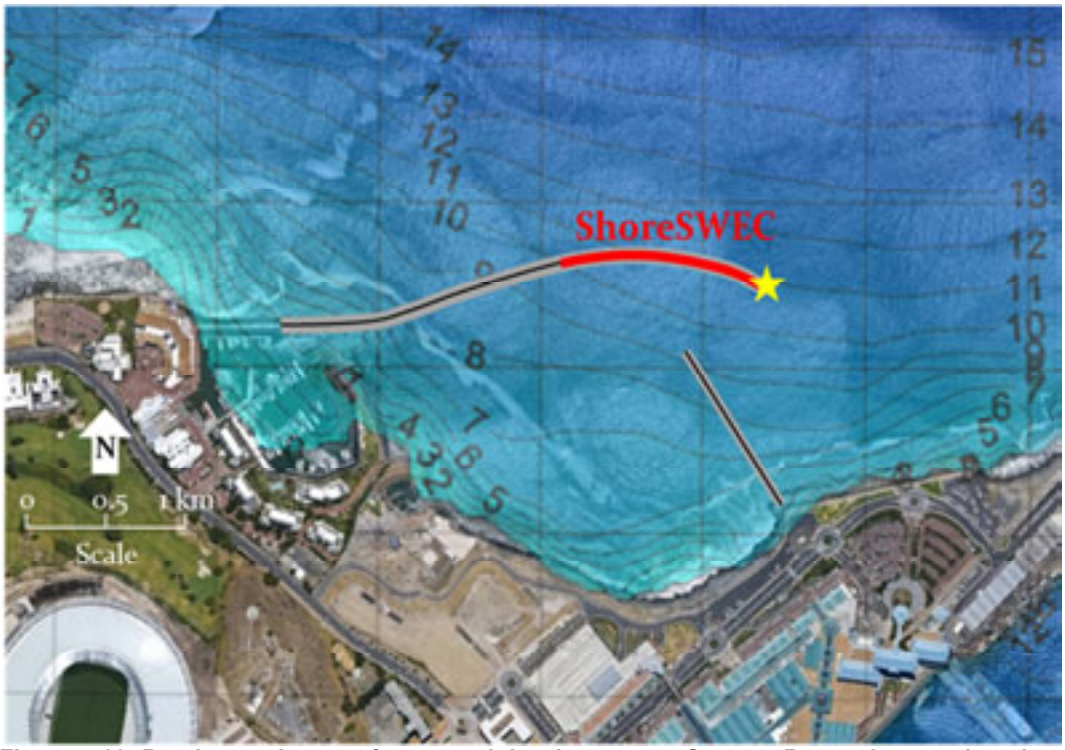

Figure 4-12: Breakwater layout of proposed development at Granger Bay and output location (indicated by the yellow star)

Wave period

The wave period remains constant as waves propagate into shallower water from deep sea and therefore the NCEP wave period conditions were assumed at Granger Bay (refer to §4.2.2). The operational values of wave period, 9 s to 13 s, will result in wave lengths of 85 m to 130 m in the 11 m water depth of the Granger Bay site. The total length of the ShoreSWEC must be greater than the typical wave length at the site to ensure differential pressures between the chambers.

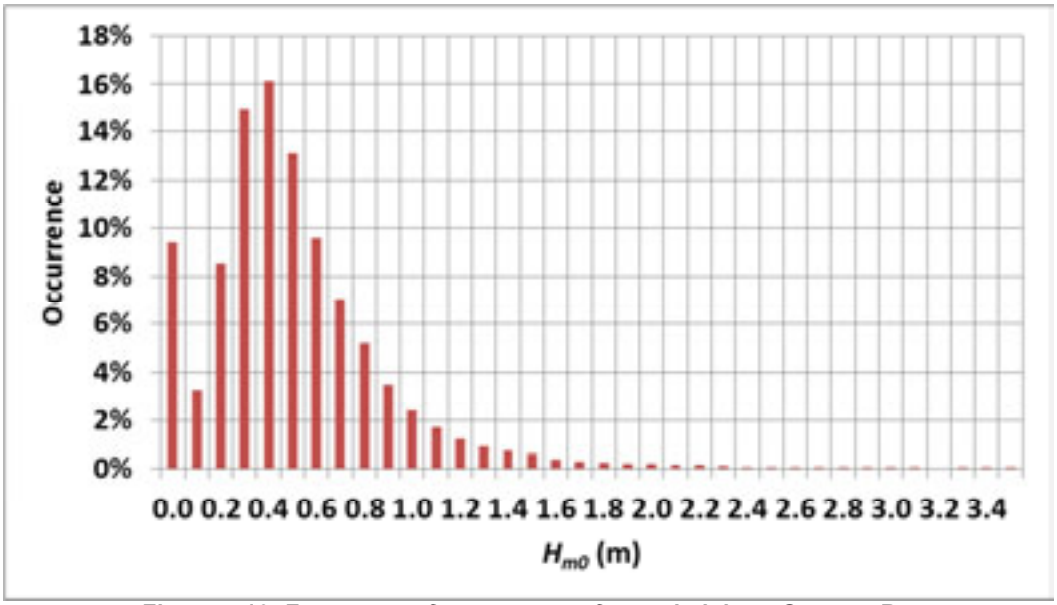

Figure 4-13: Frequency of occurrence of wave height at Granger Bay

Wave direction

Due to refraction 93% of the incident waves at Granger Bay approach from the northwest. Orientating the ShoreSWEC longitudinally towards the northwest will ensure that its chambers are activated sequentially for the majority of its design life.

Wave energy scatter

A wave energy scatter analysis, as presented by Hagerman and Bedard (2003), was conducted on the operational data. A wave energy scatter diagram is a surface contour graph of the annual wave energy (expressed in megawatthours, MWh) available from each combination of wave height and wave period. The wave energy scatter diagram of Granger Bay presented in Figure 4-14 shows that the most frequently occurring and energetic combinations of wave height and wave period range from 0.5 m to 1.5 m and 10 s to 14 s respectively, and produce between 1 MWh to 3 MWh per year per meter wave crest. A wave energy scatter analysis does not take wave direction into account, but this is not expected to influence the results due to the low variability of wave direction at Granger Bay. Refer to Chapter 8 for a more detailed discussion of the wave energy scatter at Granger Bay.

4.6.2 Mean annual average wave power distribution in Table Bay

The annual average distribution of wave power in Table Bay based on 11 years of hindcast wave data is presented as a contour map in Figure 4-15. Figure 4-15 shows that the wave power resource in Table Bay is greatest north of Cape Town harbour due to the waves penetrating into the bay from the dominant southwest. There is a concentration of wave power (and wave height, refer to Figure 4-10) approximately 2 km south of Robben Island caused by the 11 m deep reef known as Whale Rock. Although not suitable for the ShoreSWEC this might prove to be an ideal location for other types of WEC devices. The port of Cape Town, and Granger Bay especially, lie in the shadow of Mouille Point which greatly reduces the incident wave power resource.

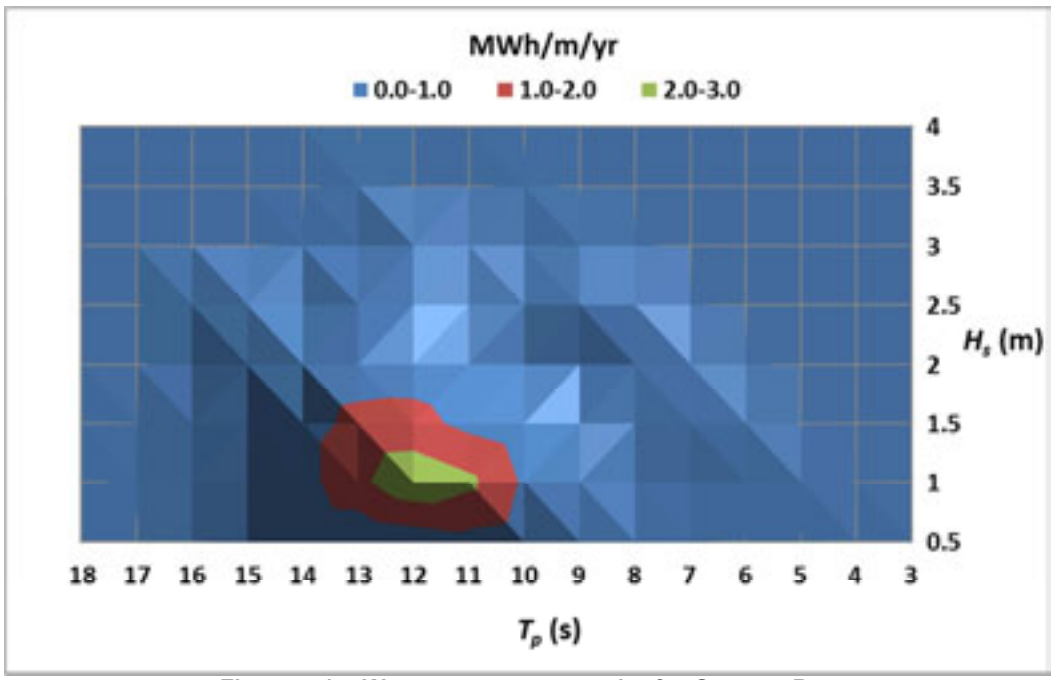

Figure 4-14: Wave energy scatter plot for Granger Bay

4.6.3 Mean annual average wave power distribution at Granger Bay

The spatial distribution of mean annual average wave power based on NCEP hindcast wave data is presented in Figure 4-16 as a contour map overlaid on the proposed development area at Granger Bay.

The average wave power at the head of the breakwater is approximately 2.3 kW/m. One of the main objectives of the study is to determine the length of the wave crest, i.e. amount of resource available, the ShoreSWEC can utilise for energy generation. With the available resource known, the next step is to determine the conversion efficiency of the device and the consequent output potential. The hydrodynamic efficiency of the ShoreSWEC was investigated in greater detail through the physical and numerical tests as presented in Chapter 6 and 7.

For future work it is recommended that a detailed analysis be conducted on the effect of the ShoreSWEC on the local wave and resource conditions in Table Bay. The ShoreSWEC breakwater structure can be represented by a line obstacle with a prescribed transmission coefficient in SWAN similar to the study of Smith et al. (2012). From such an analysis the impact on sedimentation and shipping can also be determined.

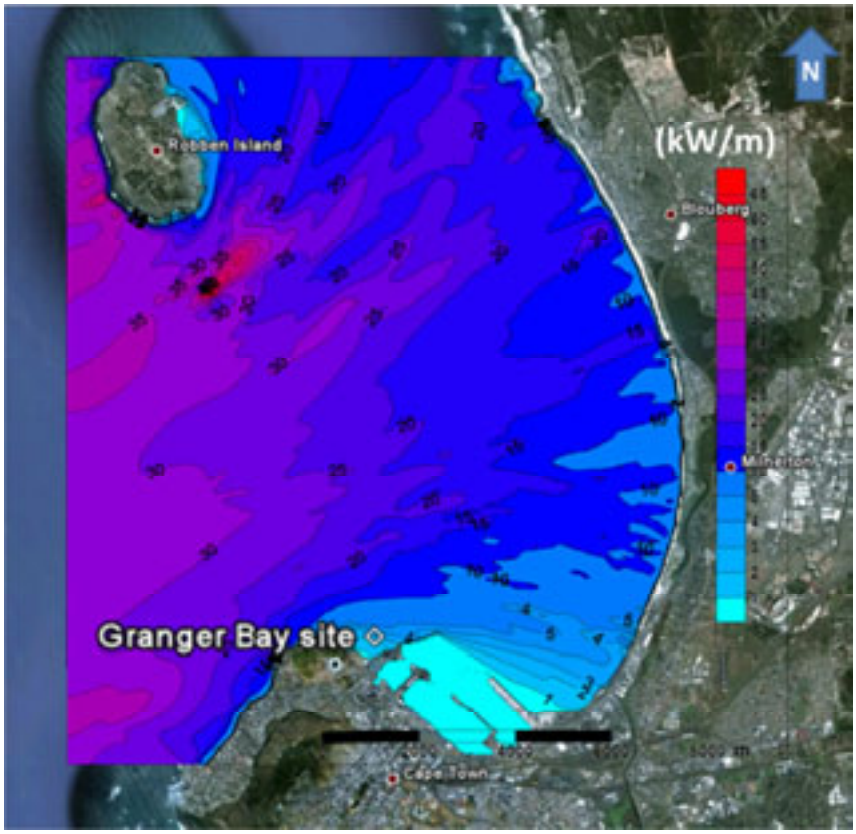

Figure 4-15: Mean annual average wave power distribution (kW/m) of Table Bay based on 11 years of hindcast NCEP wave data

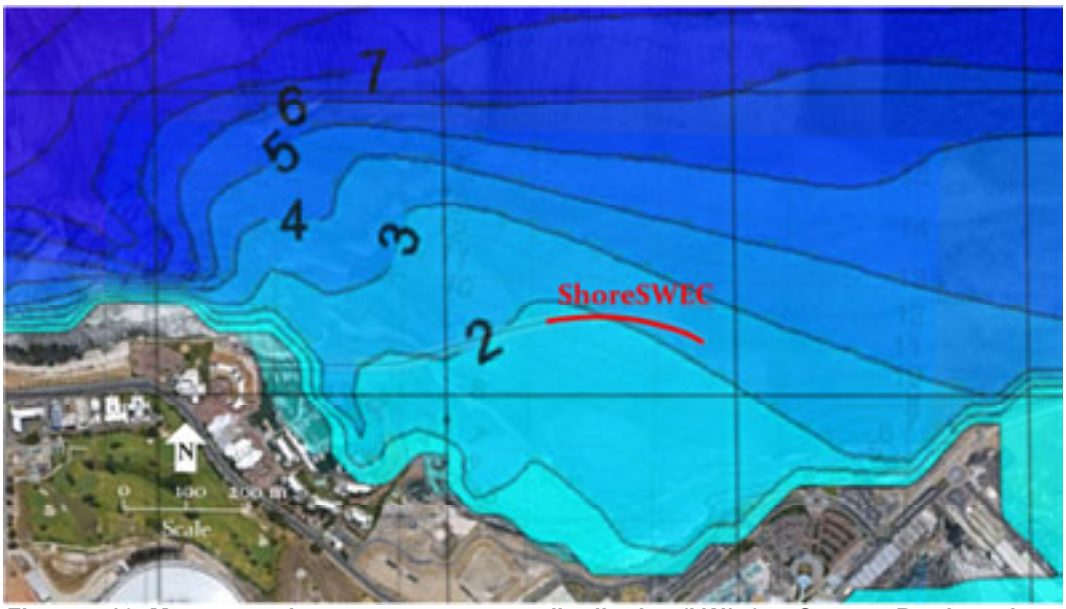

Figure 4-16: Mean annual average wave power distribution (kW/m) at Granger Bay based on 11 years of hindcast NCEP wave data

4.6.4 Mean seasonal average wave power distribution at Granger Bay

The mean seasonal average wave power at Granger Bay is presented in Figure 4-17. As expected the maximum average wave power of 4.2 kW/m occurs in winter while the summer months have the lowest average wave power of 1.1 kW/m. Autumn and spring have similar average values of wave power of 1.9 and 2.1 kW/m respectively. The seasonal variability index (SV) is an indication of the level of seasonal variability defined by Cornett (2008) as:

$$SV = \frac{P_{s1} - P_{s4}}{P_{year}}$$

where P_{s1} and P_{s4} are the mean wave power of the most and least energetic seasons respectively. P_{year} is the mean wave power of the entire data series. The value of SV for Granger Bay was found to be 1.3 which is the same order magnitude as Cornett found for the offshore wave power resource of the South African coast. The seasonal probability of exceedance curves of wave power at the site are shown in Figure 4-18. Values of wave power greater than 20 kW/m were excluded to better compare the seasonal distributions. The exceedance curves of autumn, spring and mean annual are very similar while summer and winter are again the least and most powerful seasons respectively. The monthly wave power distribution and its variability at Granger Bay are discussed next.

4.6.5 Mean monthly wave power distribution at Granger Bay

The spatial distribution of mean monthly average wave power at Granger Bay for January, April, July and October, which are representative of summer, autumn, winter and spring respectively, is presented in Figure 4-19. The monthly values of wave power are very similar to that of the seasons they represent indicating that the shorter term monthly variability is the same as the seasonal variability.

Figure 4-20 shows statistical parameters (median, 5%- and 90% probability of exceedance) of mean monthly wave power at the site in Table Bay. The 5% probability of exceedance curve shows the high likelihood of powerful storm events in the winter months and highlights the importance of a proper device design to ensure survivability during these events. The next step is to conduct a thorough structural stability analysis of the device under design storm conditions.

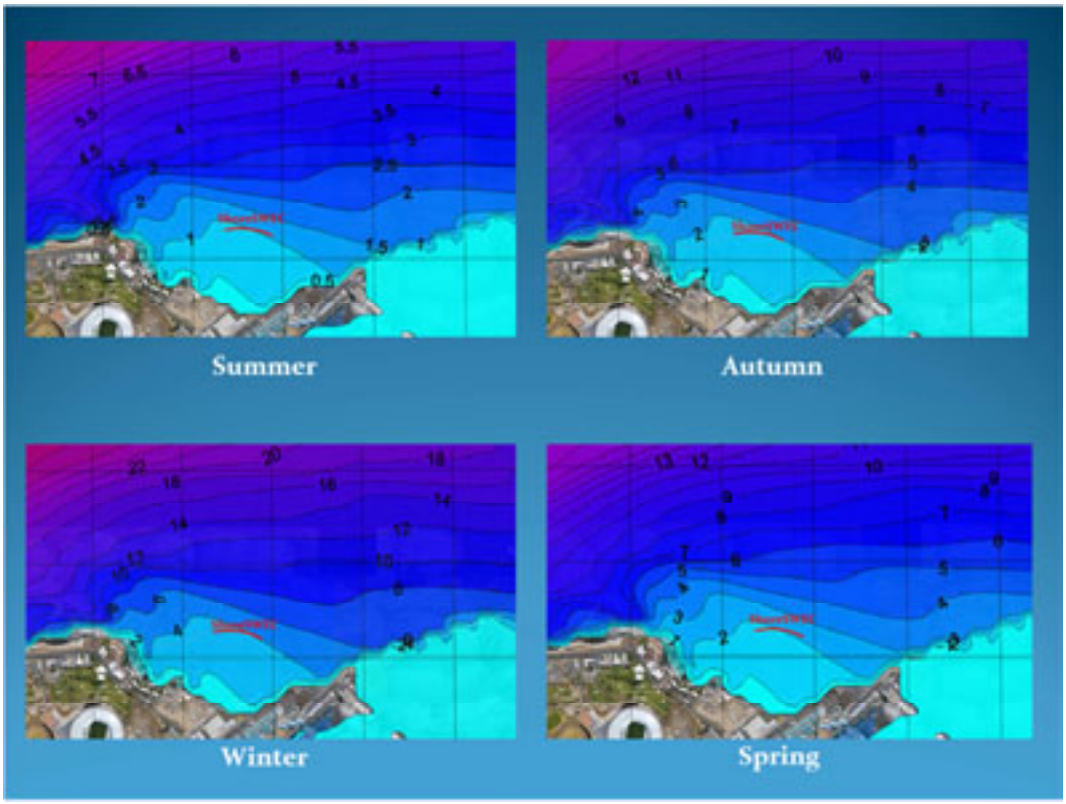

Figure 4-17: Mean seasonal average wave power distribution at Granger Bay based on 11 years of hindcast NCEP wave data

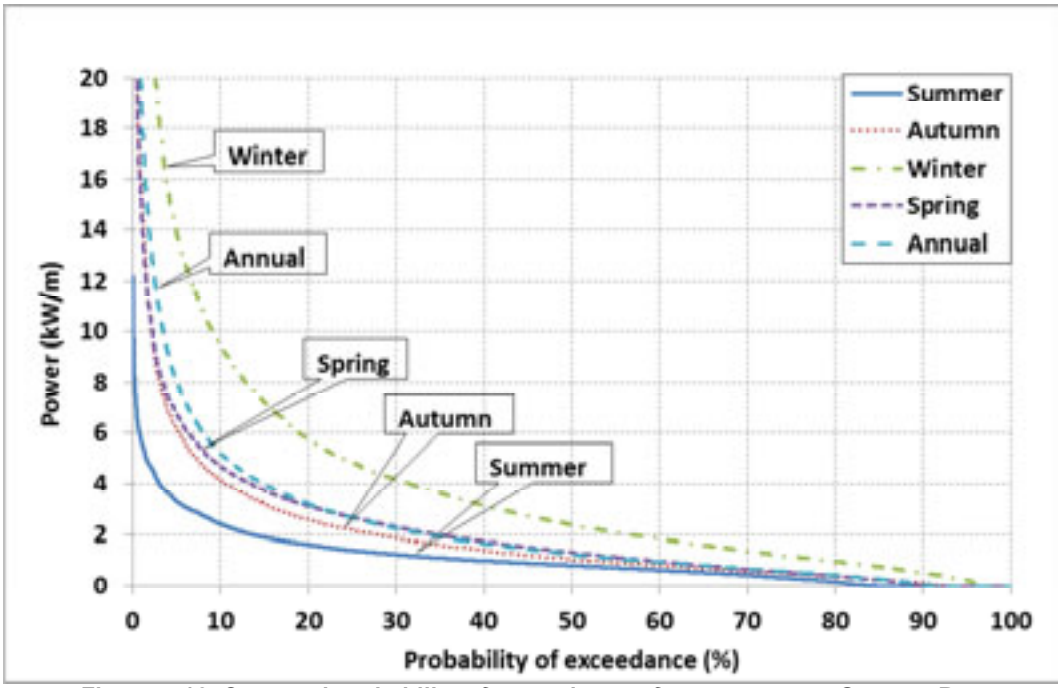

Figure 4-18: Seasonal probability of exceedance of wave power at Granger Bay

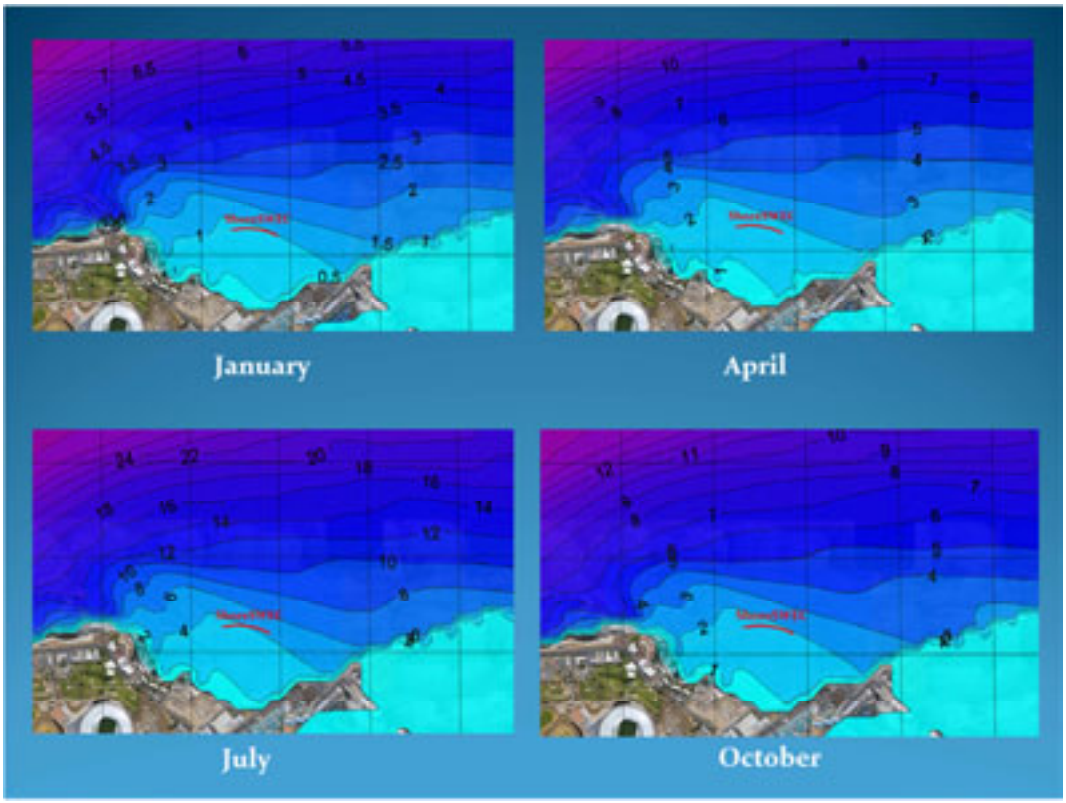

Figure 4-19: Mean monthly average wave power distribution at Granger Bay based on 11 years of hindcast NCEP data

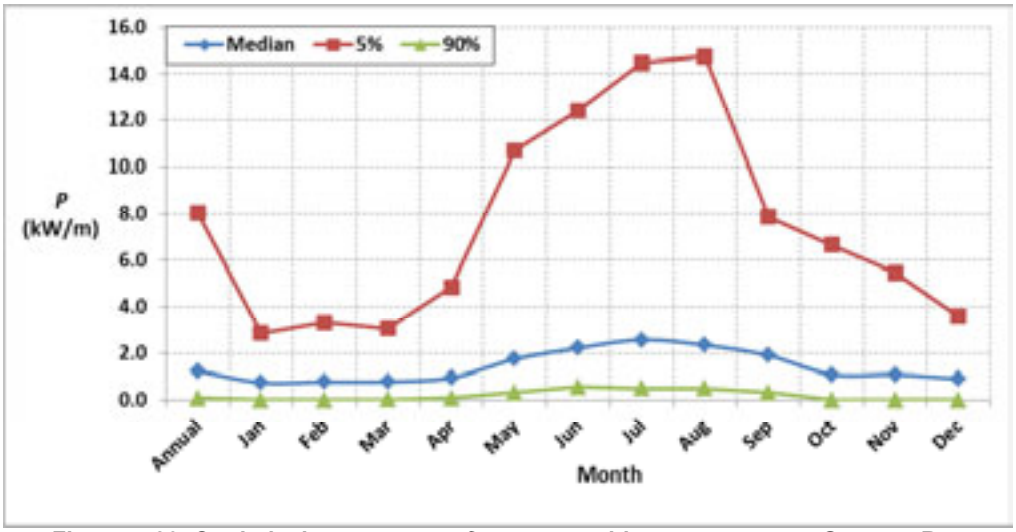

Figure 4-20: Statistical parameters of mean monthly wave power at Granger Bay

4.7 Conclusions

A spectral wave model was developed to transfer 11 years of hindcast NCEP wave data to a site near Granger Bay selected from the site evaluation of Chapter 3. The operational wave conditions at the site were derived from the transferred wave data

and are typically a wave height of 0.5 m with an 11 s wave period from predominately the northwest direction. The transferred wave data was also used to determine the wave power resource at the site. The mean annual average wave power was found to be approximately 2.3 kW/m. This is considerably less than the wave power resource of 12 kW/m measured at the site of the LIMPET (Carbon Trust, 2005). Once the conversion efficiency of the device has been established its output potential from this available wave power resource will be determined.

5 Design conditions and breakwater design for Granger Bay

In this chapter the design wave and water level conditions at the proposed location of the ShoreSWEC are discussed. This was used as input into Goda's (1974, 1985) formulae and the resulting pressures, loads and movements of the structure were evaluated. Suitable dimensions of the device structure were selected to ensure stability during extreme wave conditions.

5.1 Design conditions

5.1.1 Design life, return period and probability of exceedance

There are very few wave devices that have been operational in the ocean for extended periods of time. The LIMPET, commissioned in 2000, is the longest operating WEC device. It was assumed that the ShoreSWEC has a design life/operational period (*N*) of 25 years, as suggested by the Carbon Trust (2005) for OWC's. The stability of the structure must be evaluated for a specified design storm with a certain return period (*T*). This extreme event must have an acceptable probability of being exceeded in the design life of the device. From Equation (27) (BSI, 1991) it can be shown that the one in a hundred (1:100) year storm has a 22% probability of exceedance (*P*) in the ShoreSWEC's 25 year design life.

$$T = \frac{1}{1 - \sqrt[N]{1 - \frac{P}{100}}} \qquad (27)$$

This probability and risk of damage and/or failure of the structure and the consequences thereof on the port development were deemed acceptable in comparison to the cost required to reduce this probability.

The design conditions are specified for installation at the head of the breakwater of the proposed development at Granger Bay (see Figure 4-12).

5.1.2 Hydrographic conditions

The surface elevation at the structure is an important design criterion greatly influenced by the wave conditions for which the geometric layout of the ShoreSWEC will be designed. The total surface elevation for design is determined by the water depth, tidal level and the storm surge. All water levels are relative to chart datum (CD) which is based on the Lowest Astronomical Tide (LAT).

5.1.3 Water depth

From the Granger Bay bathymetry, presented in Figure 4-12, it can be seen that the water depth at the head of the breakwater is 11 m below CD.

5.1.4 Tidal levels

The tidal levels at Cape Town for 2011, as predicted by the South African Navy Hydrographic Office, are:

Table 5-1: Predicted tidal levels for Cape Town

Tidal parameter	Level (m CD)
Highest Astronomical Tide (HAT)	2.02
Mean High Water Springs (MHWS)	1.74
Mean High Water Neap (MHWN)	1.26
Mean Level (ML)	0.98
Mean Low Water Neap (MLWN)	0.7
Mean Low Water Spring (MLWS)	0.25
Lowest Astronomical Tide (LAT)	0.0

The crown height of the structure and the lip submergence depth will be defined relative to MHWS and MLWS respectively, ensuring the most critical water level conditions are considered.

5.1.5 Storm surge

The CEM (2003) defines storm surge as a rise above normal water level on the open coast due to the action of wind stress on the water surface. Generally, joint probability methods are used to determine the correlation between wave height and total water level, but for this application it will conservatively be assumed that the hundred year storm surge (SS_{100}) condition will occur concurrently with the hundred year design wave. Prestedge Retief Dresner Wijnberg (Pty) Ltd (PRDW) consulting port and coastal engineers were contracted by the City of Cape Town to investigate the effect of climate change on the sea level of the city (refer to (PRDW, 2010)). Using an extreme value analysis of hourly tidal measurements at Granger Bay, it was showed that the 1:100 year storm surge is 0.74 m.

5.1.6 Sea level rise

Sea level rise due to climate change affects water levels and wave conditions at Cape Town and therefore must be included in the design of the ShoreSWEC. Assuming the device is built 10 years from now, it is necessary that it be designed for the predicted sea level at half its design life, approximately 2035. In their study, PRDW concluded that the sea-level will have risen 0.27 m by 2035. They further predict that the storm surge will decrease by 3% due to a reduction in local onshore winds and that offshore wave heights will increase by 1%. Incorporating sea-level rise and the impact of climate change on storm surge, the total design depth at the structure is estimated to be 13.73 m.

5.2 Offshore design wave conditions

5.2.1 Significant wave height

The stability of the ShoreSWEC device must be analysed for the design wave load conditions. To determine the most critical design parameters SWAN was used to simulate the propagation of various design storms from offshore to Granger Bay over the computational grids discussed in §4.5.1.

The maximum occurring wave height in each directional bin, as derived from NCEP data, was used to evaluate the directional distribution of extreme storm events. It is shown as a wave height and direction rose in Figure 5-1. From Figure 5-1 it can be seen that the maximum wave height in the 11 year period is 10.31 m from the west-southwest direction.

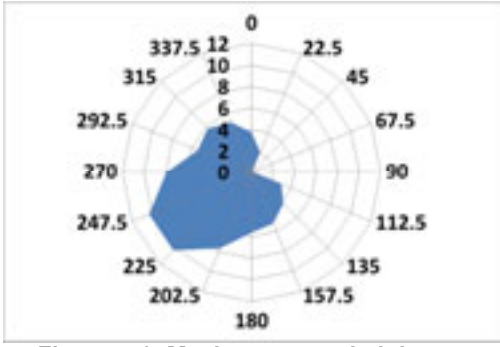

Figure 5-1: Maximum wave height per direction for the 11 year NCEP data

It is expected that westerly storms will generate the most critical design conditions due to the fact that Table Bay is relatively exposed to the west. As previously stated the device will be designed for the hundred year storm. In his dissertation Rossouw (1989) recommends an offshore hundred year wave height ($H_{m0_{100}}$) of 12m for South Africa. Climate change will eventually affect the local wind regime as well as offshore wave heights: an increase of 0.1 m was therefore assumed as proposed by PRDW (2010). To determine the hundred year wave height for each direction, it was assumed that $H_{m0_{100}}$ of 12.1 m is from west-southwest, as indicated by the NCEP data, and the wave heights for the remaining directions were determined relative to this value (refer to Table 5-2).

5.2.2 Peak wave period

The design peak wave period was calculated according to the upper range of periods presented by Del Norske Veritas (1977) as:

$$3.6\sqrt{H_{m0}} < T_p < 5.5\sqrt{H_{m0}}$$

Rossouw (1989) found that this relationship between T_p and H_{m0} agrees favourably with measured wave data off South Africa's coast.

5.2.3 Peak-enhancement factor

For this extreme analysis it was assumed that the wave energy density spectrum had a Pierson-Moskowitz (PM) shape, i.e. the wave-field is a fully developed sea. In storm conditions the energy density is spread over a broad range of frequencies around the peak frequency.

5.2.4 Directional spreading

The spreading of energy density around the peak wave direction (D_p) was assumed to be 19º (power *m* of approximately 8, refer to Table B-6) which corresponds to values of directional spreading measured during storm events at Slangkop wave recording station.

SWAN simulations were conducted for the hundred year storms from each wave direction and the resulting wave conditions at the Granger Bay site are presented in the following section.

5.3 Nearshore design wave conditions

The SWAN output presented in Table 5-2 shows that the hundred year design storm from the west gives the greatest wave height of 4.94 m at the site. Other important design wave parameters at Granger Bay for the westerly storm include: T_p of 17 s, D_p of 317.5º and the individual maximum wave height (H_{max}) of 8.89 m as calculated from 1.8*H_{m0} (Goda 1983).

Table 5-2: 100 year offshore and nearshore wave conditions

Offshore			Granger Bay		
D_p(º)	H_{m0}(m)	T_p(s)	H_{m0}(m)	H_{max}(m)	D_p (º)
0	4.41	11	1.02	1.83	302.5
22.5	2.41	8	0.13	0.24	302.5
45	0.00	0	0.00	0.00	0
67.5	0.00	0	0.00	0.00	0
90	0.00	0	0.00	0.00	0
112.5	3.50	10	0.01	0.01	322.5
135	4.90	12	0.03	0.06	322.5
157.5	6.11	14	0.16	0.29	322.5
180	6.63	14	0.38	0.69	322.5
202.5	9.02	16	1.22	2.19	322.5
225	12.10	19	3.06	5.50	317.5
247.5	12.12	19	4.25	7.66	317.5
270	**9.29**	**17**	**4.94**	**8.89**	**317.5**
292.5	6.37	14	4.39	7.90	312.5
315	6.79	14	4.73	8.52	307.5
337.5	5.96	13	3.03	5.46	307.5

SWAN generated spatial distribution of the H_{m0} and D_p over the computational domains for the westerly hundred year design storm is presented in Figure 5-2 on the next page.

The design wave conditions at the head of the proposed wave power breakwater are presented in Table 5-3.

Table 5-3: Design criteria for the ShoreSWEC at Granger Bay

Design parameters					
H_{m0}	H_{max}	T_p	D_p	*Dspr*	Water depth
4.94 m	8.89 m	17 s	135º, Northwest	12º	13.73 m

From Figure 5-2 it can be seen that the design waves approach the head of the breakwater from the northwest almost parallel to the longitudinal axis of the device. To account for the 12^0 directional spreading it is assumed that the angle of approach (β) relative to a line normal to the structure is 70^0.

The stability of the ShoreSWEC structure was evaluated under wave loads caused by these design wave and water level conditions.

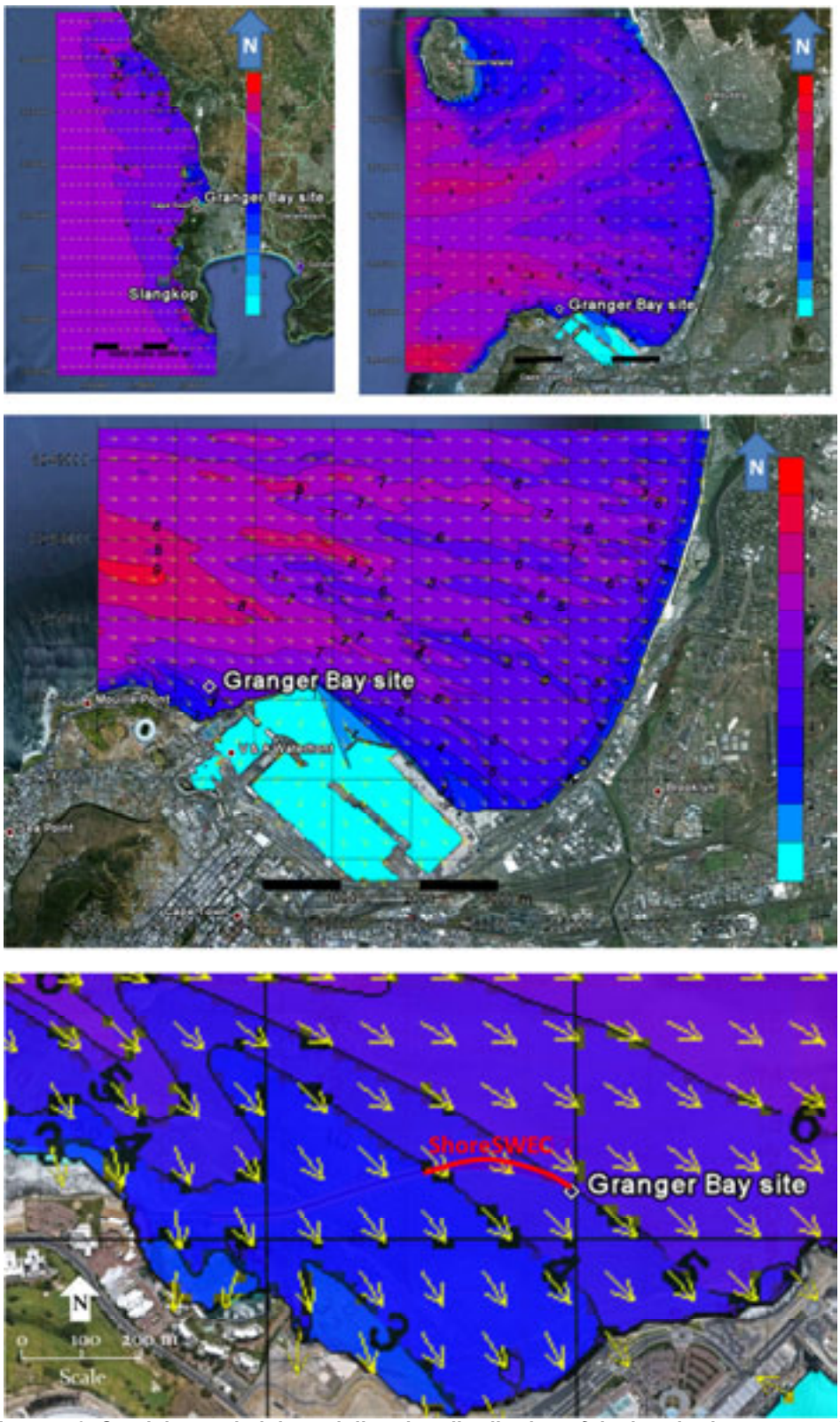

Figure 5-2: Spatial wave height and direction distribution of the hundred year westerly design storm. Offshore wave conditions T_p = 17 s and H_{m0} = 9.29 m

5.4 Design wave loading and dimensional requirements

The design of vertical breakwaters is primarily influenced by wave loading and foundation conditions. Vertical breakwaters are typically large structures that resist wave loading by gravity and friction forces as well as the bearing capacity of the rubble foundation. In the preliminary design process, assuming a rigid structure, a quasi-static analysis and developed formulae can be used to determine the applied wave pressure, loads, moments and movements of the structure during extreme storms. To resist these applied loadings, structural dimensions are assumed and its stability is assessed to ensure a suitable factor of safety is maintained.

5.4.1 Type of wave forces

Wave-loadings on structures are complicated functions of wave conditions and the structure's geometry. It is therefore recommended that in the final stages of design (which is beyond the focus of this study), experimental tests be conducted in hydraulic laboratories on unconventional structural geometries such as that of the ShoreSWEC. This will give greater insight into the wave-structure interaction and the device design can be adapted accordingly.

Wave loads on vertical walls can be categorised as pulsating, impact or broken. Nonbreaking waves cause pulsating or quasi-static loads on structures. This can be considered a static load in stability calculations due to its longer duration (typically ¼ or ½ of a wave period) relative to the natural period of oscillation of the structure. There are well-established formulae to determine pressure, forces and moments caused by pulsating loads that will be discussed in detail later.

Plunging waves that break directly onto a vertical wall result in very high, short duration (0.1 to 1 s) impact loads, giving peak pressures of 10 or more times greater than pulsating waves with the same wave height. It is best to avoid frequent wave breaking on the structure by orientating it at an oblique angle to the design wave direction greater than 20^0 from normal incidence. The mild slope of 1 in 100 at the deployment location will also ensure a reduced probability of wave breaking. The decision tree of Goda (1985) and Allsop et al. (1996) shows that by avoiding breaking waves, the stability analysis of the ShoreSWEC is greatly simplified in that only pulsating or broken wave loads need to be considered. A conventional OWC, that faces into the incident waves, will experience significantly greater wave forces and must be designed for breaking waves.

Waves that break offshore due to depth-limitation result in waves that are well aerated and loads significantly less than impact or even pulsating loads. Broken wave loads will not be included in this preliminary design procedure.

To better understand the stability requirements of the ShoreSWEC device the potential failure modes are presented.

5.4.2 Failure modes

Failure or ultimate limit state is defined as: "Damage resulting in the structure performance and functionality below the minimum anticipated by design and the cost of damage repair, including interference with commercial operation, is unacceptable." CEM (2006c) and BSI (1991). Possible failure modes for a typical vertical wall structure are shown in Figure 5-3.

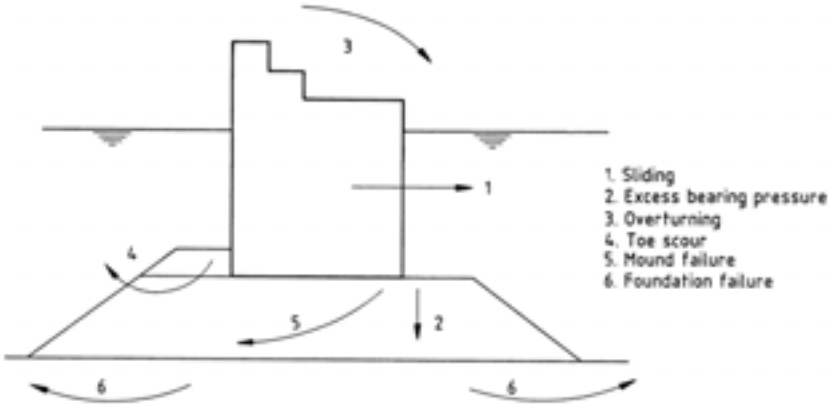

Figure 5-3: Failure modes for a vertical breakwater (BSI, 1991)

The main causes of failure are scour of the rubble foundation and extreme wave loads that cause displacement of the vertical wall structure. In the preliminary design of the ShoreSWEC, a suitable safety factor is ensured against the failure modes presented above by analysing the stability of the device during extreme wave loading.

5.4.3 Foundation design

The foundation of the ShoreSWEC was designed against toe scour, mound and foundation failure. The foundation design methodology presented in CEM (2006c) was applied. In the absence of geotechnical information on the soil conditions at Granger Bay, it was assumed that the seafloor would be able to support the weight of the structure and all wave-induced transmitted loads. The device will be placed on a suitable, granular bedding (core layer) with an assumed thickness of 15% of the water depth at the site. This is similar to the caisson design example in CEM (2006d) which is also in the same order of magnitude as the wave power caisson of Takahashi (1992). Patterson et al. (2009) proposed the use of a concrete mattress to contain the granular material and grouting to form a seal between the foundation and the OWC unit.

The toe of the structure will be protected by a single armour layer or two layers of quarrystone with toe protection blocks adjacent to the base of the device. Using formulae of Tanimoto et. al. (1982) and Takahashi et. al. (1990), as presented in CEM (2006c), it was found that a double layer of 2.5 tonne quarrystone and 0.74 m high concrete toe protection blocks (refer to Takahashi (1996)) would provide sufficient protection to the toe of the structure. The core material of the bedding layer will be made up of 0.25 tonne rock assuming a one in ten weight ratio between the armour and core layer, similar to rubble mound breakwaters prescribed in CEM (2006b). The rock berm width was assumed to be a multiplier of the armour layer thickness (refer to CEM (2006d)). Foundation elements that could potentially obstruct flow entering the OWC chamber were minimised to ensure optimal utilisation of the available water depth. This foundation design will ensure a reduced likelihood of toe scour, mound and foundation failure. The foundation layout is presented in Figure 5-4.

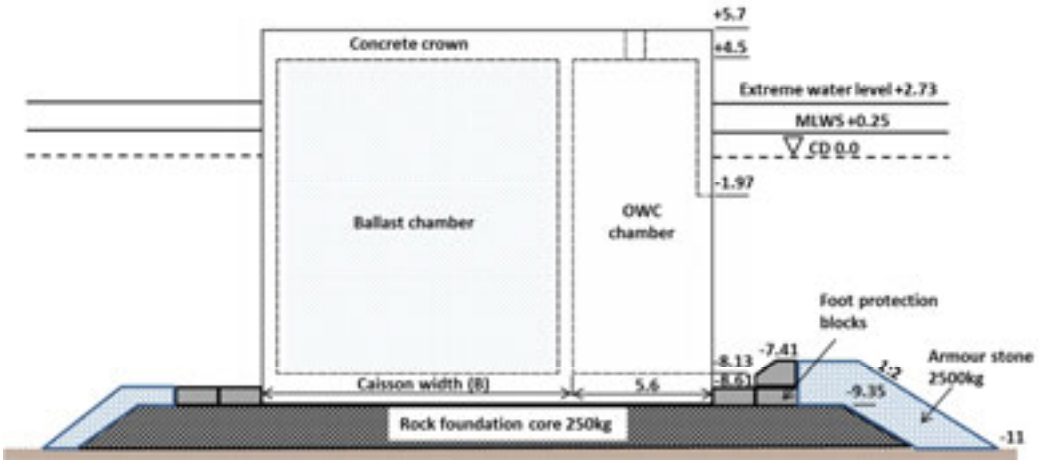

Figure 5-4: Cross section of ShoreSWEC structure and its foundation with elevations relative to chart datum (CD, units in meters)

5.4.4 Material

The ShoreSWEC structure will be manufactured from steel-reinforced concrete. To ensure sufficient protection of the steel reinforcing bars against the corrosive sea spray in the splash zone, a minimum concrete cover of 65 mm is recommended by CEM (2006b). ASTM Type V Portland cement will be used due to its resistance to the sulphates in seawater and high compressive strength (typically 46 MPa after five years) (CEM, 2006b). To ensure the durability of the concrete and reduce the likelihood of chloride ingress, Patterson et al. (2009) recommends the use of low porosity concrete. This is achieved by a low water/cement ratio combined with Ground Granulate Blast Furnace Slag (GGBFS) cement replacement or blended concrete mix (Pulverised Fuel Ash (PFA)).

5.4.5 Wall thickness and structural height

The selection of the front and side walls, floor and crown capping thickness of the device was based on existing OWC structures, OWC breakwaters and conventional caisson breakwaters (refer to Wavegen (2002), Torre-Enciso et al. (2007) and Takahashi (2002)). These parameters will be analysed in depth using Finite Element Methods (FEM) in the detailed design of the device, which is beyond the focus of this study. A front and side wall thickness of 0.6 m was assumed which is believed to be sufficient to accommodate steel reinforcement and to provide adequate structural strength. A concrete cap and floor thickness of twice the wall thickness (1.2 m) was assumed which is in the same order of magnitude as similar structures.

The height of the structure influences its hydraulic response such as overtopping and wave reflection. To ensure an acceptable level of overtopping is maintained, Takahashi (1989) recommends a structure crest elevation (crown height) of 0.6 H_{design} above the extreme water level for a vertical front wall and 1 H_{design} for a sloped front wall. As an added safety measure against overtopping, some caisson breakwaters have splash walls which further extend the height. The final design of the ShoreSWEC may very well include a splash wall and a PTO (including inlet and outlet piping and turbo-generator) integrated into the structure of the device. The

effect of these components on the stability of the device was not included in this analysis.

The ShoreSWEC's front wall submergence depth was designed as 25% of the maximum wave height expected to occur at the deployment location as recommended by Takahashi (1989). Due to the orientation and the effect of energy absorption, wave reflection is not expected to be a problem. Refer to Figure 5-4 to see the layout and elevations (relative to chart datum) of key features of the structure and its foundation.

5.4.6 Pulsating wave loads

The main focus of the initial design is to determine the dimensions of the ShoreSWEC's ballast chamber, which is required to resist the design wave loads. The challenge is to design the main structure big enough to resist sliding and overturning forces whilst also being small enough to ensure a cost effective design. As discussed in §5.4.1 only nonbreaking, pulsating wave loads need to be considered in the stability analysis. Coastal engineering design codes and manuals such as the British Standard BSI (1991) and Coastal Engineering Manual (CEM) (2006c) recommend the use of Goda's (1974, 1985) prediction method of wave forces for nonbreaking waves on vertical walls. Goda's prediction method is the most well established and widely accepted, and therefore will be used to determine the wave loadings on the ShoreSWEC.

Two designs were considered for the stability analysis of the ShoreSWEC, yielding different dimensional requirements. These include a vertical- and inclined front wall structure. The stability analysis used was based on Goda's method and a modification thereof.

5.4.7 Vertical wall structure

For nonbreaking waves on a vertical wall, the total hydrodynamic pressure distribution consists of two time-varying components. The hydrostatic pressure due to instantaneous water depth and the dynamic pressure caused by the accelerations of the water particles. The hydrostatic pressure below SWL on the front and leeside of a structure is equal and in opposite direction therefore it cancels each other out, leaving only the wave-induced hydrodynamic pressure to consider in stability analyses.

Goda (1974) developed formulae for estimating the pressure distribution, corresponding forces and overturning moments on vertical walls due to irregular nonbreaking waves. Figure 5-5 shows the horizontal and uplift pressure distribution on the ShoreSWEC's ballast and capture chamber.

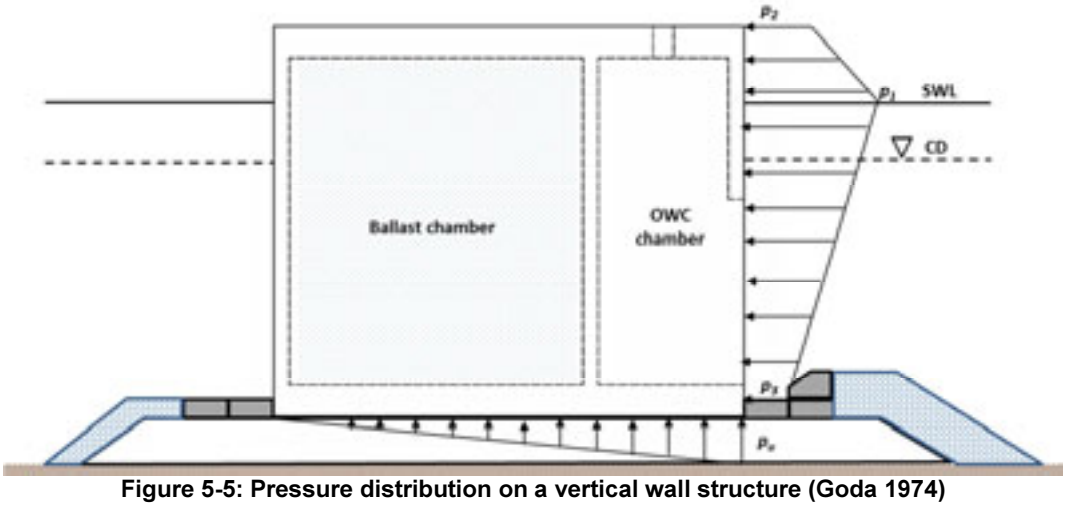

Figure 5-5: Pressure distribution on a vertical wall structure (Goda 1974)

Pressures

From Figure 5-5 it can be seen that the horizontal pressure distribution on the front face has a trapezoidal shape. The pressure at the seafloor, still water level (SWL) and top of the structure is defined by p_3, p_1 and p_2 respectively. The orbital particle velocity and resulting dynamic pressure is greatest at the SWL and decreases linearly above and below this point. The distributed horizontal pressure theoretically extends beyond the top of the structure due to the standing wave formed by wave reflection.

The vertical wall structure acts as an impermeable barrier to incident waves and causes a pressure increase on the seaward face. Dispersing waves will seek passage through the permeable rock foundation causing an increased water pressure in the bedding layer, represented by the linear uplift pressure distribution p_u as shown in Figure 5-5. Goda (1974) provides formulae to calculate p_1, p_2, p_3 and p_u from coefficients α_1, α_2, α_3 and α^* which depend on the wavelength (L), the water depth a distance five times H_{design} seaward of the front wall of the structure and the bottom slope.

The pressures are furthermore highly dependent on the incident wave direction (β) and modification factors λ_1, λ_2, and λ_3. The factors depend on the structure type which can be vertical, inclined, curved or energy absorbent. For a conventional vertical structure the modification factors are all equal to one. Takahashi (1989) recommends that λ_2 equals zero for energy absorbing structures, but this was found to not greatly reduce the required width of the structure for stability.

Forces

The total horizontal applied force can be calculated by integrating the pressure distribution with added uncertainty and bias for the horizontal force, uplift force, horizontal moment and uplift moment as prescribed by CEM (2006c). The vertical forces acting on the device consist of the uplift force and its submerged weight (weight of the concrete and sand minus the effect of buoyancy) which are both dependent on the width of the structure. A caisson width is therefore assumed and

the stability of the structure is evaluated and adjusted if the selected width does not provide satisfactory safety against failure.

Moments
The horizontal and uplift force both create an overturning moment about the heel of the device which is resisted by the moment of the net structural weight.

Stability
In order to avoid the device sliding between its base and the rubble foundation, the net vertical force (difference between the structure's submerged weight and the uplift force) multiplied by the prescribed frictional coefficient of 0.6 must be greater than the applied horizontal load. A conservative safety factor of 1.5 against sliding and overturning was used as recommended by BSI (1991). Stability against overturning is ensured if the resisting moment caused by the structure's weight is greater than the horizontal and uplift force moment. The heel bearing pressure for eccentric, inclined loadings was evaluated as prescribed by Goda (1985).

A summary of the wave induced pressures, forces, moments and safety factors against sliding and overturning for a caisson width of 12.4 m is presented in Table 5-4.

Table 5-4: Design wave generated pressures, forces and moments for a vertical wall device

Pressure	kPa	Forces	kN/m	Moments	kNm/m
p_1	59.6	*FH*	754.2	*MH*	5033.3
p_2	39.9	*FU*	376.3	*MU*	4222.2
p_3	54.8	*FG*	2529.5	*MG*	18233.9
p_u	54.3	**Safety factor**	**1.5**	**Safety factor**	**2.0**

Refer to Appendix C for a detailed calculation example of the vertical wall stability analysis.

One of the main advantages of the ShoreSWEC, in comparison with a conventional OWC, is that it experiences significantly lower storm wave loading due to its orientation. An OWC, orientated to face into the design wave conditions, would require a 60% wider ballast chamber than the ShoreSWEC to remain stable. The OWC structure will comprise 68% more steel-reinforced concrete which significantly increases the capital cost of the project in comparison with the ShoreSWEC.

To reduce wave loading, a vertical wall structure is often designed with a sloping front face. The effect of a sloping wall on the stability of the ShoreSWEC is investigated in the following section.

5.4.8 Sloped face structure

Adding an incline to the seafront face of the device ensures that a portion of the wave induced load is transmitted vertically downwards, effectively reducing the applied horizontal loading and overturning moment, but increasing the potential for overtopping when compared with a vertical wall structure. As mentioned in §5.4.5 Takahashi (1989) recommends that the crest height of a sloping wall structure be increased from 0.6 H_{design} to 1 H_{design} to account for the greater likelihood of overtopping. Takahashi and Hosoyamada (1994) extended Goda's formulae to

incorporate the effect of the incline on the pressure distribution. These formulae, as presented in CEM (2006c), were used to determine the ballast chamber width required for device stability.

Pressures

The pressure distribution on the ShoreSWEC with a front wall sloping at 56º is presented in Figure 5-6. The pressure at the seafloor-, SWL on the vertical section, SWL on the sloped section and at the top of the sloped section is represented by p'_3, p''_1, p'_1, and p'_2 respectively. These values are calculated using p_1, p_2, p_3 for a conventional vertical structure and modified using the factors λ_{SL} and λ_V which are dependent on the front wall slope, H_{design} and wavelength (L). The uplift pressure, p_u, is unaffected by the incline and the energy capture of the device. Some believe this to be an overly conservative approach (refer to Patterson et al. 2009).

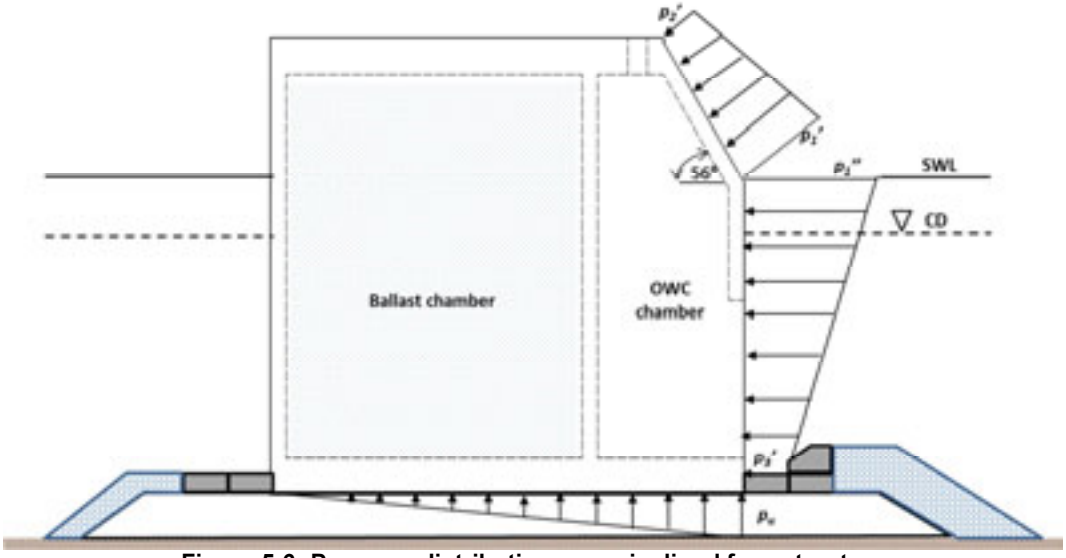

Figure 5-6: Pressure distribution on an inclined face structure (Takahashi and Hosoyamada, 1994)

Forces

The horizontal wave force acting on the structure was determined by integrating the pressure distributions on the vertical and sloped front wall. Vertical forces consist of the downward load component as transferred by the slope, the uplift force and the submerged weight of the structure.

Moments

The overturning moments about the heel of the structure caused by the horizontal and uplift forces were resisted by the submerged weight and vertically transmitted slope force.

Stability

Similarly to the vertical wall structure design, the stability of the inclined structure against sliding, overturning and heel bearing failure was evaluated. The computed

wave induced-pressures, forces, moments and safety factors for a 10 m wide caisson section are presented in Table 5-5.

Table 5-5: Design wave generated pressures, forces and moments on an inclined structure

Pressure	kPa	Forces	kN/m	Moments	kNm/m
p''_1	57.9	*FH*	795.2	*MH*	6478.3
p'_1	25.9	*FU*	230.2	*MU*	1827.7
p'_2	51.4	*FG*	2439.0	*MG*	13937.7
p'_3	47.2	**Safety factor**	**1.5**	**Safety factor**	**1.7**
p_u	54.3				

The results of Table 5-5 show that the higher crest height of the incline face increases the total horizontal force compared to the vertical wall. The slope however reduces the uplift force by approximately 40% due to the transmitted downward force and smaller width of the ballast chamber. The smaller width also reduces the weight of concrete required for stability by 7%. From a structural and economic point of view a sloped front wall seems to be a good option, but its effect on the wave energy capture of the ShoreSWEC is unknown.

Goda's method to predict the horizontal and vertical wave forces was developed for vertical impermeable structures, which does not take into account wave energy entering the capture chamber. Adjusting the modification factor (λ_2), as recommended by Takahashi (1989), was found to have a very small impact, reducing the required width by only 0.1 m. Patterson et al. (2009) argued this is an overly conservative approach and suggested a modification to the traditional pressure distribution. The effect of Patterson et al.'s modified pressure distribution on the stability and required width of the structure will be assessed in the following section.

5.4.9 Effect of capture chamber

In their modified pressure distribution model, Patterson et al. (2009) accounted for waves entering the capture chamber and applying a horizontal load on the chamber's rear wall (refer to Figure 5-7). It was conservatively assumed that there will be no momentum loss due to turbulence and mixing as wave energy enters the chamber.

The uplift pressure on the base of the structure arising in the permeable foundation due to the incompressibility of water at the toe will be significantly reduced by the pressure release caused by the capture chamber. Wave energy entering the OWC chamber will also exert a downward force on the chamber's base similar to perforated breakwaters (refer to CEM 2006c). Due to these factors Patterson et al. (2009) argued that the uplift pressure distribution would only be fully developed under the base of the ballast chamber (see Figure 5-7). Assuming a reduced uplift force it was found that an 11.6 m wide ballast chamber provided sufficient stability to the ShoreSWEC. The resulting pressures, forces and moments are presented in Table 5-6.

Table 5-6: Design wave generated pressures, forces and moments assuming a reduced uplift force.

Pressure	kPa	Forces	kN/m	Moments	kNm/m
p_1	59.1	*FH*	746.5	*MH*	1281.5
p_2	39.5	*FU*	242.5	*MU*	1753.5
p_3	54.3	*FG*	2385.8	*MG*	16282.1
p_u	54.3	**Safety factor**	**1.5**	**Safety factor**	**5.4**

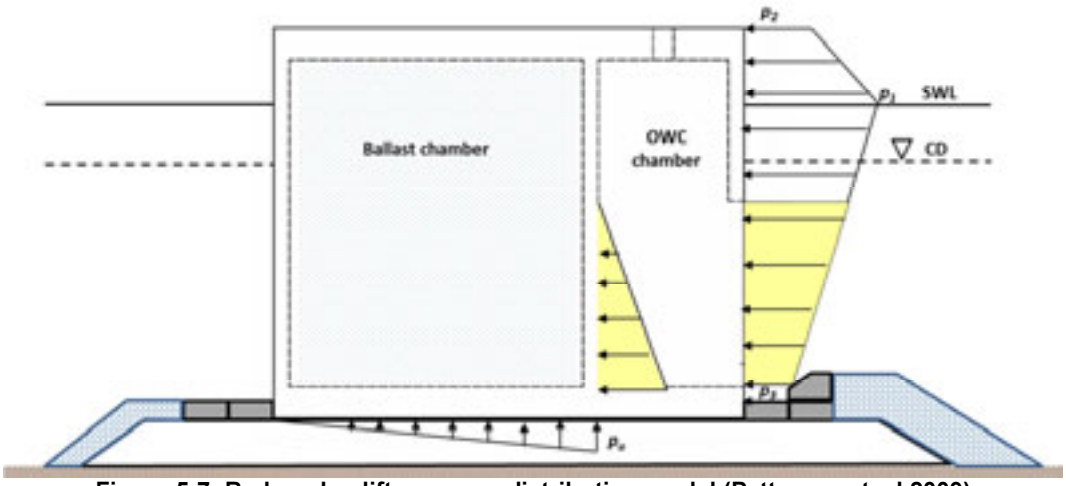

Figure 5-7: Reduced uplift pressure distribution model (Patterson et. al 2009)

The wave generated pressures shown in Table 5-6 is slightly less than that predicted by the conventional Goda (1974) formulae, refer to Table 5-4, due to the effect of setting the modification factor (λ_2) equal to zero. The uplift force was reduced by 35%, which greatly increased device stability against overturning.

This concludes the stability analysis of the ShoreSWEC. Two designs and two design approaches were considered, yielding different dimensional requirements to resist wave loads. The inclined front wall significantly reduced the required width of the ballast chamber, but due to the greater likelihood of overtopping and the uncertainty regarding its effect on conversion efficiency, a vertical wall structure was selected in the final design. It was also decided to follow the more conservative, traditional approach of Goda with regards to stability requirements. The final geometric layout is presented in the next section.

5.5 Final geometric layout

A 3D representation of the final preliminary design of the ShoreSWEC's caisson, OWC chamber and foundation (consisting of the core foundation layer, foot protection armour and blocks) is presented in Figure 5-8. Each unit is 18 m wide (5.6 m OWC and 12.4 m ballast chamber), 13.2 m long and 15.1 m high. The system consists of ten units in total ensuring that the overall length of the device is longer than the dominant wave lengths occurring off the South African coast (a typical long period wave shown in Figure 5-8). As discussed earlier, the PTO of the system is not shown, yet it will most likely be incorporated into the device structure's final design.

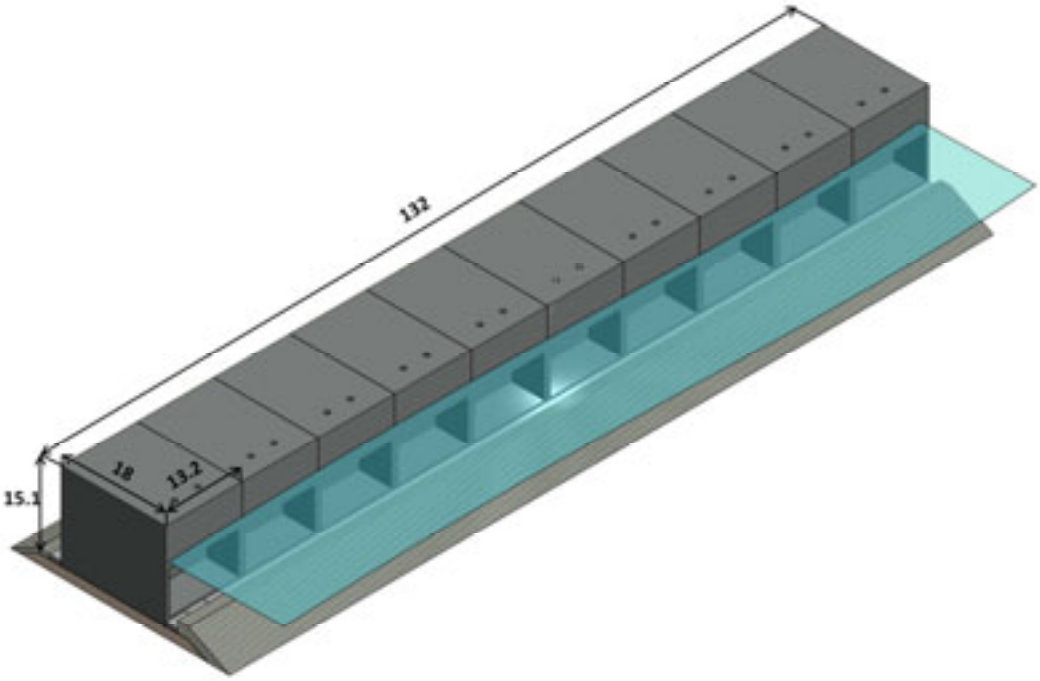

Figure 5-8: Final geometric layout based on design stability analysis (Autodesk, 2011)

6 Experimental testing

Experimental wave tank testing on a WEC device at model scale plays a pivotal role in the overall design and development process. Through tank testing the working principle of the concept can be demonstrated and verified. It can provide valuable information on the power capture, hydrodynamics and overall performance of the device. Experimental results are typically used to validate and calibrate numerical models. Certain wave phenomenon like extreme waves and wave breaking are not well understood theoretically and is best investigated experimentally. The impact of a device on the surrounding environment (such as sedimentation processes and shipping) can also be quantified through experiments. Physical model testing is however a costly exercise, requiring substantial infrastructure such as wave flumes, basins and monitoring equipment.

In this study an experimental campaign was conducted to demonstrate the concept and evaluate the hydrodynamic efficiency of the ShoreSWEC with a single and double capture chamber at model scale. Geometric configurations, under a variety of wave energy conditions were tested and, from the experimental results, an estimate of the ShoreSWEC's energy conversion capacity at Granger Bay was made (refer to Chapter 8). This objective and the breakdown of the test program are presented in the schematic of Figure 6-1.

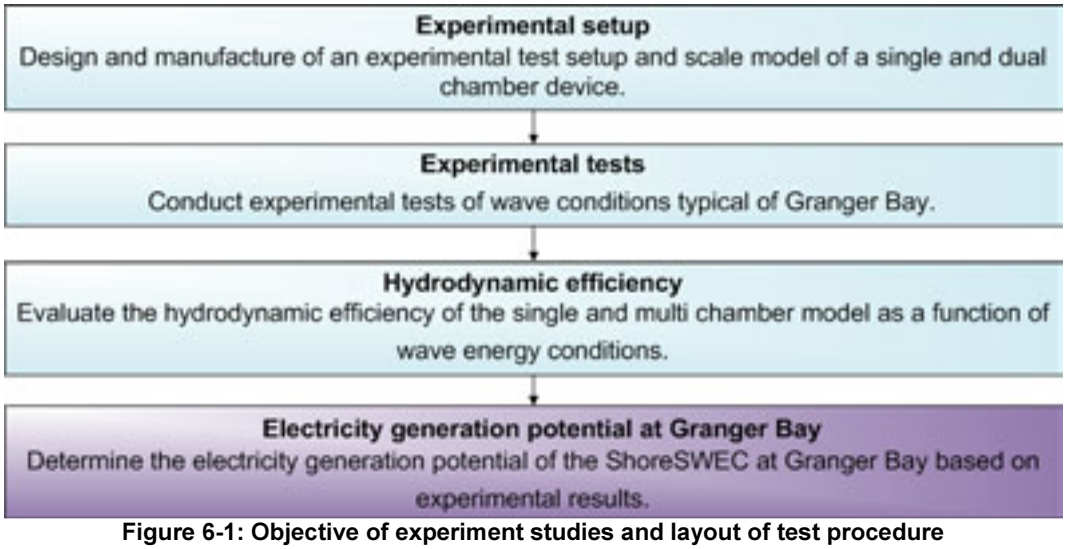

Figure 6-1: Objective of experiment studies and layout of test procedure

6.1 Model scale

The experimental tests were conducted in a glass wave flume at the University of Stellenbosch's hydraulic laboratory. The physical model was orientated with its longitudinal axis parallel to the direction of wave propagation, this ensures that the operational conditions of the device are met. At this orientation wave-induced flow enters the chamber at a right angle relative to the advancing waves, thus presenting

the most conservative estimate of the efficiency of the device. The ballast chamber of the ShoreSWEC, as designed in Chapter 5, was not included in the experimental tests due to the limited flume width available. It is not expected to greatly influence the power capture characteristics of the system.

The installation method initially considered was to remove a side panel of the flume to accommodate the experimental model. This approach would provide a simplified configuration, with no installation inside the actual flume. However, this had to be reconsidered due to the cost and time required to remove and replace the three-layered glass panel. Instead an artificial channel was constructed inside the flume consisting of two wave guides, one before and after the model. The upwave guide was filled with absorption material to reduce the reflection caused by model's side wall and the downwave guide ensured that diffracted waves did not affect the performance of the device. Refer to Figure 6-3 and Figure D-3.

The selected model scale (s) of 1:25 was based primarily on the available width of the flume. It was decided that at least three quarters should be available for waves to pass down the artificial channel, whilst still providing sufficient space to accommodate the capture width of the device. The model scale used is in the same order of magnitude as the first choice scale for validation of numerical models and optimisation suggested by Sarmento and Thomas in Cruz (2008).

The compressibility of air is often inaccurately reproduced in small scale models, but this can be accounted for. One approach to address this issue is to use two different scales for the air and water portions of the model. From the results of their experimental tests, Wavegen (2002) found that using an airbox at a different scale to the OWC chamber, did not greatly influence the overall power capture of their device. Sarmento (1992) suggests that in some cases the air compressibility effect can be ignored for small models. Thakker et. al. (2003) found that air compressibility can reduce wave energy conversion efficiency by 5% in comparison with incompressible flow. This was deemed acceptably accurate for the purpose of this study which is to investigate the power capture of the ShoreSWEC, a single scale was used which greatly simplified implementation.

Froude scaling laws were applied to the basic quantities of interest for the experiments as shown in Table 6-1.

Table 6-1: Quantity and scale factor

Quantity	Scale factor
Device dimension	s
Wave height and length	s
Wave period	$s^{0.5}$
Pressure	s
Wave power	$s^{3.5}$

All measured and derived quantities and results, such as water level, velocity, pressure, pneumatic power and capture width are presented in terms of the full scale device.

6.2 Experimental setup

The ShoreSWEC's capture chamber dimensions were based on that of the original SWEC design as outlined by Ackerman (2009) and specified by the stability analysis of §5.5. Refer to Table 6-2 for a summary of the device dimensions.

Table 6-2: Typical dimensions of the SWEC and ShoreSWEC's capture chamber

	Full scale		Model
Dimension	**SWEC (m)**	**ShoreSWEC (m)**	**ShoreSWEC (m)**
Chamber width	6.0	5.0	0.2
Chamber length	12.0	12.0	0.48
Chamber height relative to CD	-5.5	5.7	0.228
Lip submergence depth	N/A	-2.0	-0.08
Lip thickness	1.0	0.6	0.25
Device total length	160	130	5.2

The physical model of the chamber was mostly manufactured from 25 mm clear Perspex sheets, allowing visibility of water level oscillations within the chamber. To best utilise the available width of the flume the back wall's thickness was not to scale, neither was the roof of the device. These parameters were not expected to impact on the performance of the system. The model was slightly raised from the floor to accommodate flow through its foundations and a geometric variation of the chamber was explored by way of a sloped floor to investigate its impact on the efficiency of the system. The outlet of the device consisted of an orifice plate housed in a chimney extension centrally located in the roof of the structure (see §6.4.3 for a detailed discussion of the device outlet). The main features of the physical model's basic (or Base) configuration and its elevation relative to chart datum are presented in Figure 6-2.

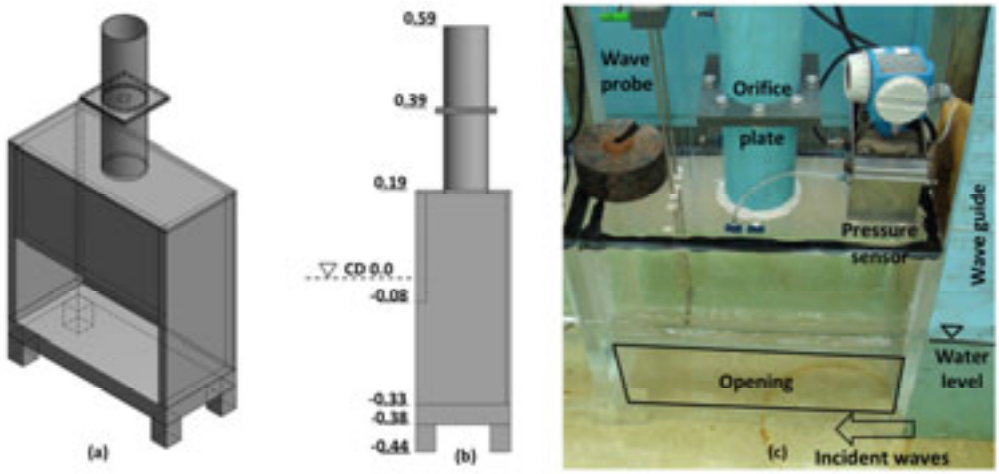

Figure 6-2: (a) Isometric view of the ShoreSWEC's capture chamber. (b) Side view of the model with elevations relative to chart datum, units in meters. (Autodesk, 2011) (c) Experimental model with monitoring equipment in the wave flume.

6.3 Wave testing facility and monitoring equipment

The University's flume is 1 m wide, 1.245 m deep (maximum water depth of 0.8 m), approximately 30 m long, and equipped with a HR piston wavemaker driven by an

electric actuator with a rack and pinion. Dynamic wave absorption enables the wavemaker to absorb waves reflected back towards the paddle, helping to calm the water in the flume after each test. An absorption “beach” consisting of rubble, model armor units and hollow bricks was built with a slope of approximately 1 in 15 at the far end of the flume, minimising wave reflection back towards the model (refer to Figure D-1, Figure D-2 and Figure D-3).

The water level elevation was measured by five standard capacitive wave probes. Probes were placed before and after the model to measure the incident and transmitted waves. One probe measured the water level inside the model and the remaining two probes were positioned in line with the model - refer to Figure 6-3 for relative positions of the wave probes. The probes were calibrated twice daily with a minimum correlation coefficient of 0.99. Measuring the change in output voltage when the probe is raised and lowered by a known amount in still water, defines the relationship of wave height and output voltage.

The air pressure fluctuations inside the capture chamber were monitored by two pressure sensors with a measuring range of 0 kPa to 2.5 kPa at 0.2% accuracy. One sensor measured the compression air pressure and the other the expansion air pressure in the chamber. Both the sensors and wave probes sampled data at 100Hz which was fed to a WaveDaq system in the control hut. The pressure sensors and WaveDaq system were calibrated with a Betz micromanometer to correlate output voltage to pressure.

A schematic showing the experimental setup and the relative position of the monitoring equipment in the flume is presented in Figure 6-3. The model was positioned away from the wavemaker a minimum distance of two of the longest wave lengths tested, to ensure that generated waves develop fully before reaching the model.

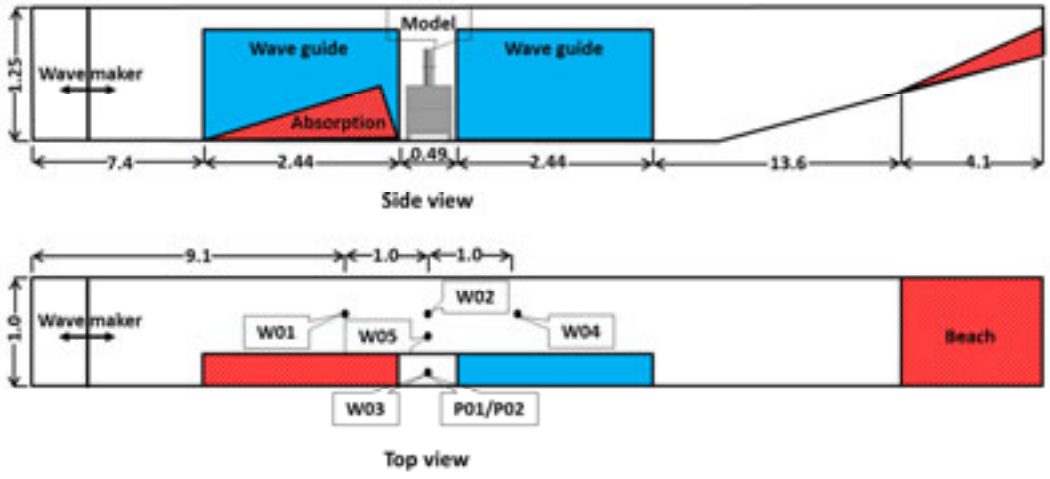

Figure 6-3: Experimental setup in the wave flume which includes the model, wave gauges (W01 to W05), pressure sensors (P01 and P02), wave guides and the absorption beach (distances in meters, drawing not to scale)

6.4 Preliminary experimental tests

The experimental campaign comprised of a preliminary and detailed test program. The objectives of the preliminary tests were to evaluate the accuracy of wave conditions generated in the flume in the absence of the model, determine the PTO damping level which delivers the greatest efficiency and to tune the device's response by adjusting the front lip submergence.

Based on these initial findings a more detailed experimental program was conducted to determine the energy conversion capacity of the system.

6.4.1 Test procedure

The conversion efficiency (refer to §2.3.4) of the ShoreSWEC scale model was evaluated over a series of regular and 2nd order Stokes wave conditions. Monochromatic wave conditions were considered to give a general idea of the response characteristics of the device at this early design stage, but device performance must be analysed under more realistic, irregular wave conditions in the future detailed design.

Device performance was evaluated by experimental tests of 25 s duration. This test duration was deemed acceptably long to ensure a sufficient amount of waves passed the model, while avoiding wave reflection off the "beach" contaminating the recording sample. Thus, there was no need to account for wave reflection which greatly simplified the post-processing analysis. The system response proved to be stable within the test duration with low variability between incident waves. The model performance was assessed according to its response averaged over six wave lengths.

6.4.2 Generated wave conditions

To evaluate the accuracy of the wave profiles generated by the wavemaker, the majority of the test conditions discussed in §4.6.1, were created in the flume without the experimental setup. The generated surface elevations measured by the wave probes at the locations shown in Figure 6-3 were compared to the target conditions. A comparison was also drawn between the generated and theoretical 1st and 2nd order Stokes profile to evaluate the suitability of these theories to describe the wave conditions.

Wave heights

Incident wave energy is highly dependent on wave height. It is therefore important to ensure that the generated wave heights are acceptably accurate compared to the required input values of wave height and period. Representative wave heights and periods were extracted from measured data records for the first six fully developed, monochromatic waves. It was found that the generated wave heights were mostly within 10% of the input wave heights, with the exception of 3 of all the conditions tested (see Figure 6-4). Results showed that the generated wave heights are smaller for lower wave periods and higher for higher wave periods compared to the target values. The higher wave heights also diverged further from the input values due to the increased non-linearity of these conditions.

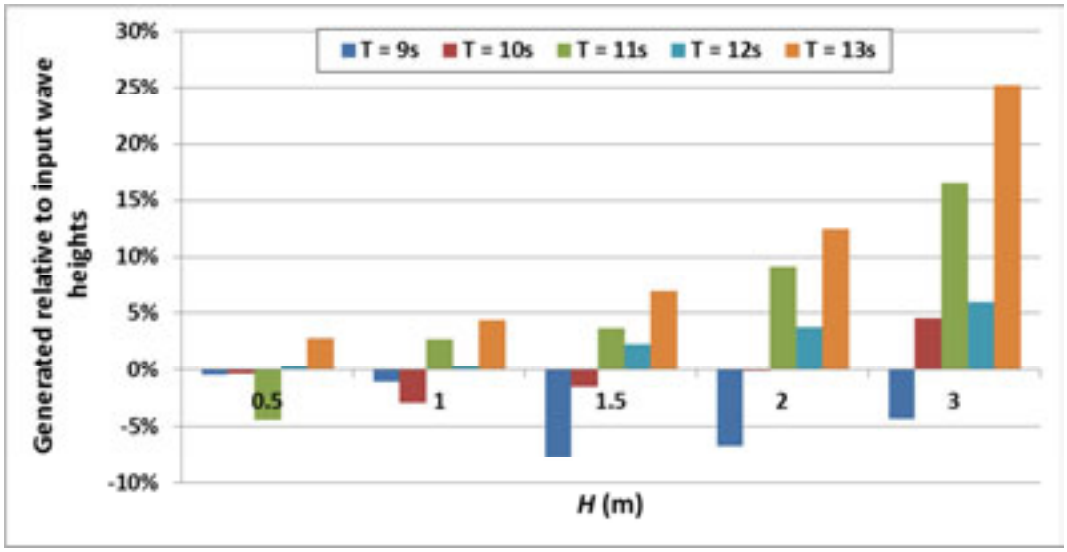

Figure 6-4: A comparison of input and resulting generated wave heights

Wave period

The wave periods of the all the test conditions generated in the flume compared reasonably well with the input wave period conditions (within approximately -3% and 4%).

Wave profile

The incident wave profile measured at the wave probe closest to the wavemaker (W01) was compared to linear and 2nd order Stokes theoretical profiles to evaluate the suitability of these theories to describe the wave conditions. The measured experimental and theoretical surface elevations are presented in Figure 6-5. The measured profile better follows the theoretical 2nd order Stokes profile compared to the linear wave, indicating that the higher order theory is a better approximation for this wave condition.

The wave conditions generated in the wave flume compared reasonably well with input and theoretical conditions. The next main objective of the preliminary experimental procedure was to determine the optimal damping level of the system.

6.4.3 Optimal damping

The main focus of these experimental tests was to investigate the energy capture of the ShoreSWEC at model scale. The air turbine used to convert pneumatic to electric power was therefore not modelled in great detail. The PTO mechanism of the device was represented by a simple orifice plate to dissipate this pneumatic energy generated inside the chamber. The pressure drop over an orifice is non-linear and is proportional to approximately the flow rate squared. An orifice outlet is easy to implement and provides a damping load similar to that of a turbine. It has been successfully used in many other studies on OWC's. Refer to Sarmento (1992), Thiruvenkatasamy and Neelamani (1997), and Folley and Whittaker (2002).

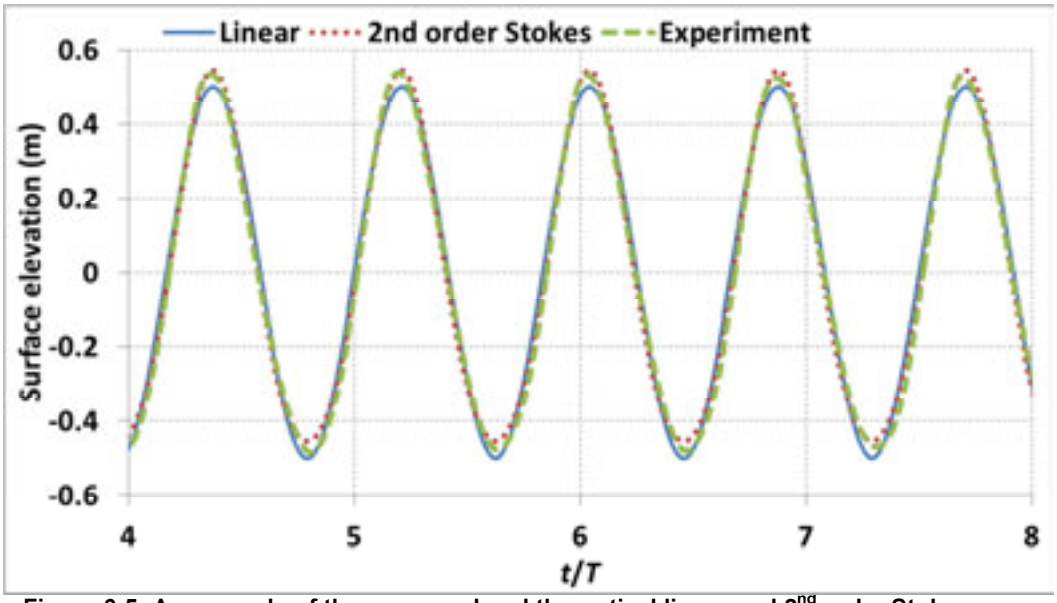

Figure 6-5: An example of the measured and theoretical linear and 2nd order Stokes wave profiles for H = 1 m, T = 12 s

The PTO mechanism and its applied damping greatly influence the conversion efficiency of OWC devices. It is therefore very important to apply damping that will ensure maximum efficiency over the greatest range of wave conditions. To identify the optimal damping level, a comparison was made between the hydrodynamic capture width of the system, as calculated by Equation 25, for various orifice sizes. The pressure sensor's lowest measurement range determined the largest orifice size that could be tested. Larger orifices did not generate sufficient pressure inside the chamber.

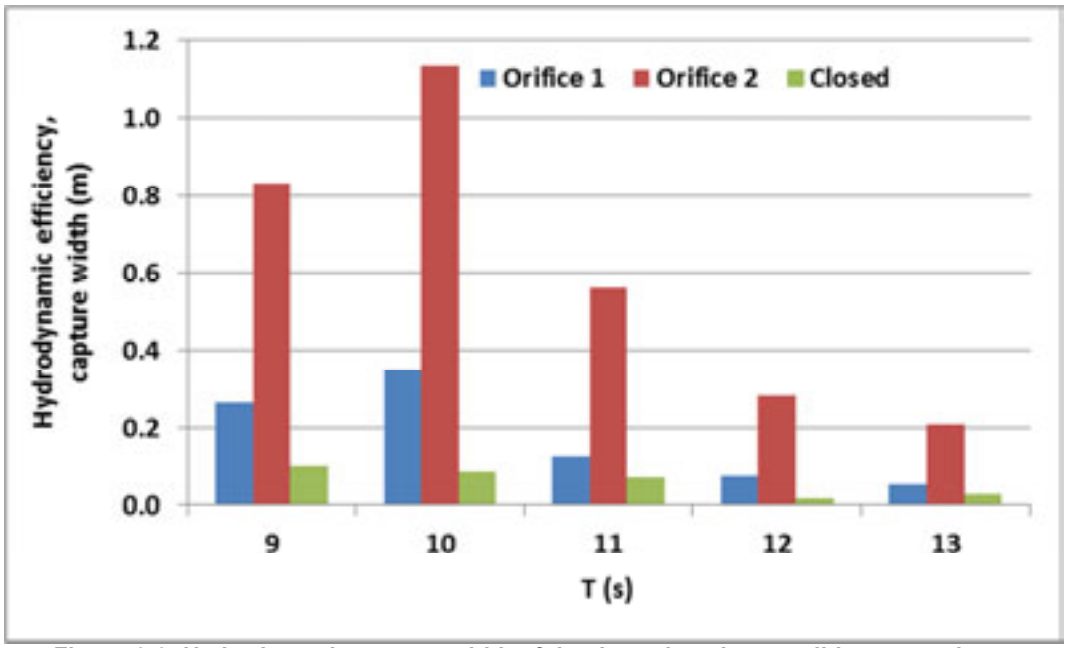

Figure 6-6: Hydrodynamic capture width of the three damping conditions tested as a function of incident wave period with a constant wave height of H = 1.5 m

Two orifice sizes and a closed roof were tested. As would be expected the closed roof produced the highest pressures inside the model, but the lowest internal water surface velocity resulting in the lowest overall efficiency of the three damping scenarios tested. From Figure 6-6 it can be seen that an area ratio of 0.7% produced the greatest efficiency for the wave period conditions at constant wave height of 1.5 m and was also the most efficient for the other 20 wave conditions tested. The area ratio is the orifice opening area to the water column area, which at full scale is a 0.75 m diameter orifice. This area ratio corresponds to the optimal condition used by Takahashi (1989), Thiruvenkatasamy and Neelamani (1997) and Horko (2007). There is however no single damping level which ensures maximum efficiency over all occurring sea conditions, but Curran et al. (1997) recommends highly damped system to maximise output in mixed frequency seas.

Once identified, the optimal orifice and its chimney structure were calibrated in the high and low flow wind tunnel at Mechanical and Mechatronic Engineering to determine the volume flow rate as a function of the pressure measured inside the chamber (refer to Equation (28) and Figure E-1). Flow in both directions through the orifice was tested to ensure its symmetry and ability to account for the bidirectional airflow of the system.

$$Q = 0.000887\Delta p^{0.46939} / 1.2 \qquad (28)$$

where Q is the volume flow rate in m^3/s and Δp is the difference between the internal chamber pressure and atmosphere in Pascal.

The above relationship was used in the detailed experimental tests to determine the pneumatic power captured by the device.

6.4.4 Device tuning through front lip submergence

The process of tuning a device to the incident wave conditions entails altering its response through geometric or damping level (as discussed in §6.4.3) adjustments in an attempt to induce resonance. The effect of the front lip submergence depth on OWC performance is one of the most common geometric parameters investigated in the literature. Sarmento (1992) and Evans and Porter (1996) found that deeper front lip submergence increases the natural period of the OWC. In order for the ShoreSWEC to perform optimally in South Africa's long period waves a deep front lip is therefore required, while still allowing sufficient wave induced flow to enter its capture chamber. Two front lip configurations were tested in the experimental model to determine its effect on the system's performance.

The deeper front lip model was an average of 8% more efficient than the shallower lip version over all the conditions tested, but did not significantly increase the natural period of the model. This submergence depth was equivalent to 25% of the maximum wave height expected to occur at the deployment location as recommended by Takahashi (1989). This model configuration was used in the detailed experimental tests. In general however, the front lip depth cannot be increased sufficiently to match the natural period of the device to the long period conditions at the nearshore deployment location. For example, the natural period of the LIMPET, due to its front lip depth, is only 5 s while the dominant wave period it is

exposed to is 10.5 s, refer to (Carbon Trust, 2005). Other geometric features that affect the response and natural period of the device include its length and width. The effect of these parameters was not investigated in this study.

6.5 Detailed experimental tests

The main objective of this experimental campaign was to quantify the energy conversion capacity of the ShoreSWEC at Granger Bay under a variety of wave energy conditions, which include the prevailing wave height, period and water depth. The impact of an inclined floor and dual chambers on the performance of the system were also investigated. Lastly the power capture of the ShoreSWEC was compared to that of a conventional OWC system. Results from the experimental tests were used to determine a conservative, rough estimate of the annual output potential of the device at the selected site in Chapter 8.

The initial objectives of the detail experimental tests were to investigate the stability and repeatability of the tests and also to determine the effect of the wave guides on the generated wave conditions.

6.5.1 Test repeatability

Tests were repeated several times under the “same” input conditions. Wave heights inside the chamber and the wave period varied by 2% and 0% respectively averaged over ten tests.

6.5.2 Effect of wave guides

The effect of the experimental setup, and the wave guides in particular, on the incident waves were investigated through the comparison of wave parameters measured with and without the model at W01 (see Figure 6-3). It was found that the wave guides generally focused the generated waves and increased wave heights by 19% on average. The 3D CFD model developed in this study, as discussed in Chapter 7, did not include wave guides and showed a reasonable correlation to the experimentally generated waves, refer to Figure 7-11 and Figure 7-12. It was therefore assumed that, for the purpose of this study, the effect of the wave guides on the experimental results was negligible.

6.5.3 Wave and water level conditions

The energy available for power capture is dependent on water depth, wave height and period.

Water depth

Water depth greatly influences wave height, wavelength and direction, yet does not affect the period. As waves travel towards the ShoreSWEC at its shallow water location, the seafloor will affect the conditions and therefore the wave energy incident on the system. To determine the effect of water depth on the efficiency of the device two water levels were tested in the wave flume. The first was 11 m (relative to Chart Datum (CD) as shown in Figure 4-12), the typical water depth for a caisson breakwater, as seen at the site of Granger Bay. The second was the Mean Sea Level (MSL) of +0.98 m for Table Bay, as discussed in §5.1.2, to evaluate the effect of tides on efficiency.

Wave height
To determine the effect of wave height on the performance of the device the range of tests included the relatively low wave height distribution at Granger Bay as well as greater wave heights of up to 2m. This upper limit of wave height has occurred very infrequently over the past ten years at Granger Bay, but this testing ensures that the analysis is of a more generic nature, thus allowing a design suitable for a greater range of local conditions. With an increase in wave height, the conversion efficiency of the device was expected to decrease, due to viscous losses at the entrance and orifice outlet of the chamber.

Wave period
Similar to wave height, the device performance was expected to be dependent on wave periods. The geometry of the chamber dictates its natural period; this should match the prevailing wave periods of the site, ensuring that resonance of the water column occurs. The wave period conditions as outlined in §4.6.1 are independent of water depth and are typical of South Africa's southwest and south coasts. Wavelength is a function of wave period and water depth, also influencing the system's response. In order to keep the water surface within the chamber plane, thus rendering a piston effect, the length of a single capture chamber must be significantly smaller than the predominant wavelength conditions.

Wave heights of 0.5 m to 2 m in 0.5 m intervals and wave periods of 6 s to 13 s in 1 s intervals were tested. This gave a test condition matrix of four wave heights by eight wave periods to isolate the influence of wave height and period on the efficiency of the device, similar to the study of Folley and Whittaker (2002). These test conditions represent 92% of the conditions over 11 years of wave data at Granger Bay. All results presented are in terms of full-scale dimensions. Refer to Table D-1 for all real and scaled experimental test conditions.

6.5.4 Capture width
The performance of WEC devices are generally described in terms of hydrodynamic efficiency which is defined as the ratio of power output to incident power. In the case of the ShoreSWEC it is difficult to determine the length of wave crest and resulting incident power available for extraction. Its efficiency was therefore rather expressed in terms of capture width similar to the optimisation study conducted by Sarmento (1993). The capture width of the ShoreSWEC model for each of the wave period and height test conditions was determined from measured data using the post processing procedure outlined in Figure 6-7.

6.5.5 Test results of the Base configuration
From initial observations it was clear that the system is highly dependent on wave period. For short period waves (6 s to 8 s) slight sloshing occurred in the chamber due to the larger ratio of chamber opening to wave length. The internal water level oscillations were perfectly monochromatic for wave periods of 9 s to 11 s (refer to Figure 6-8), but the water level rose discontinuously for the remaining longer periods of 12 s and 13 s (refer to Figure 6-9). To better understand the hydrodynamic characteristics of the device in longer period waves example output is presented for a 10 s and 12 s wave with a 1 m wave height in Figure 6-8, Figure 6-9, Figure 6-10 and Figure 6-11.

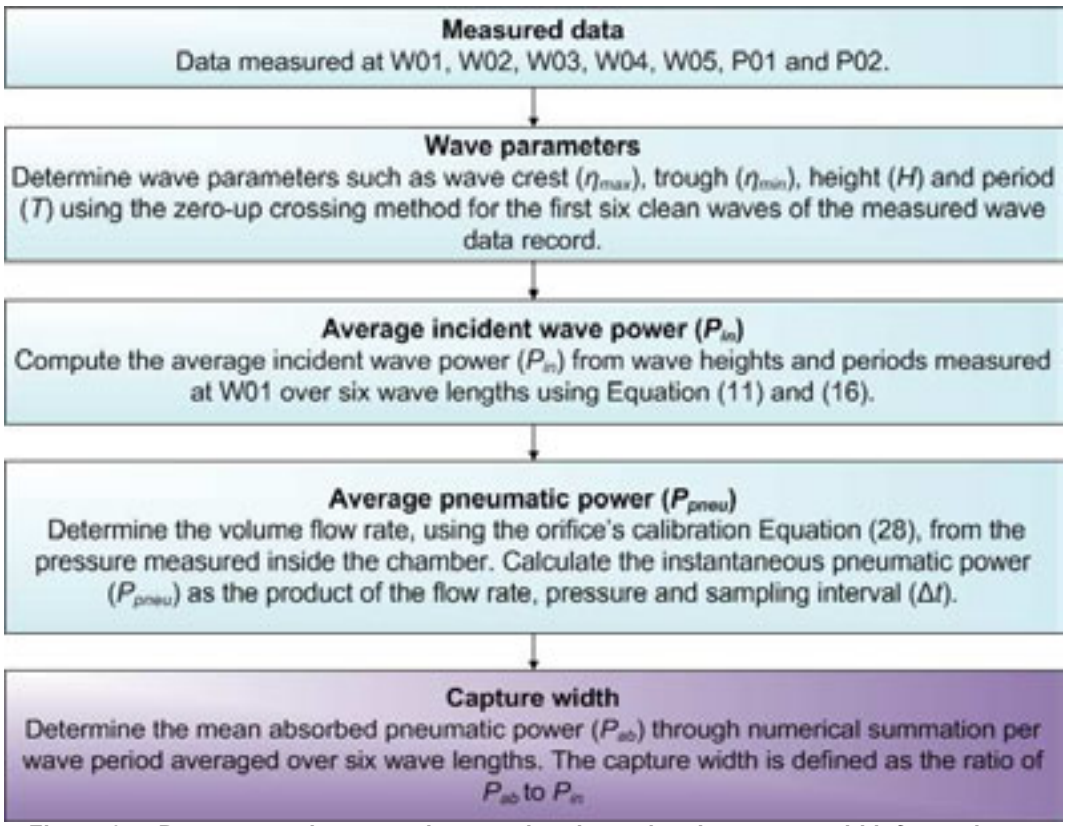

Figure 6-7: Post processing procedure used to determine the capture width for each test condition.

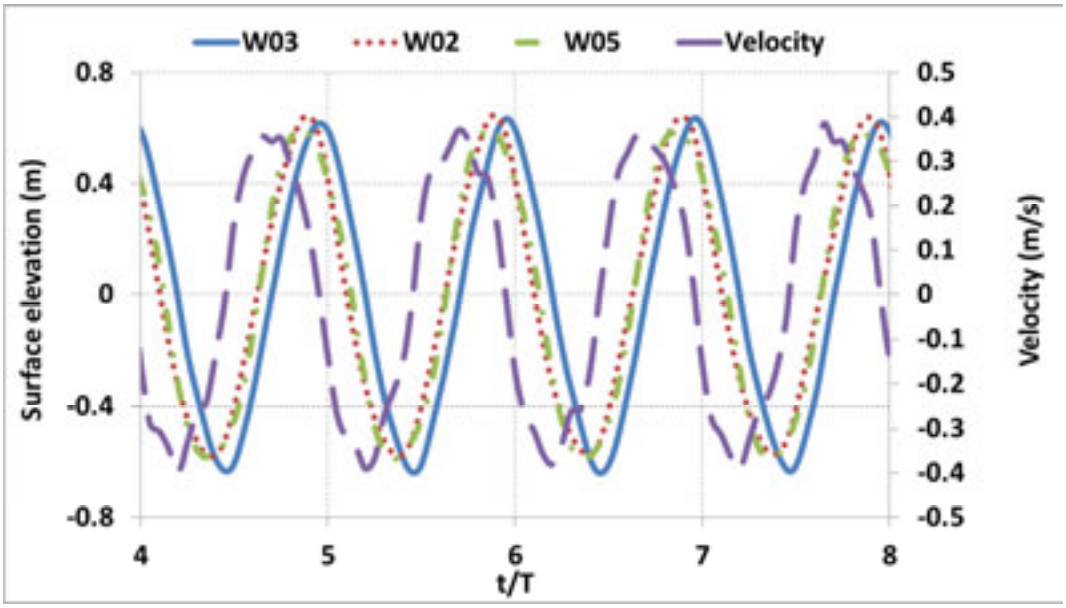

Figure 6-8: Surface elevation at W03, W02, W05 and internal surface velocity for test example H = 1 m and T = 10 s

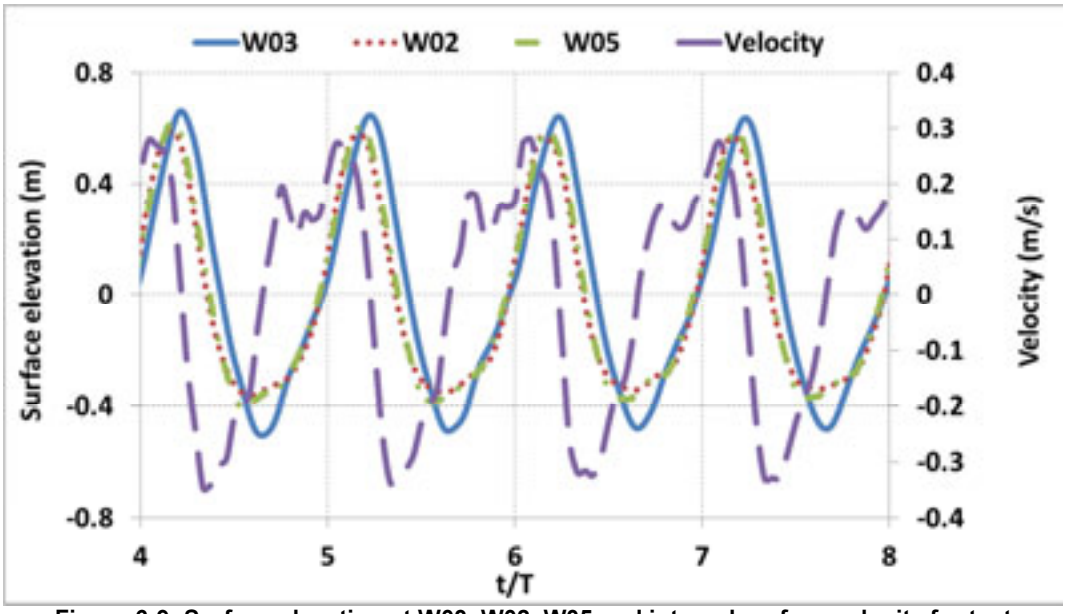

Figure 6-9: Surface elevation at W03, W02, W05 and internal surface velocity for test example H = 1 m and T = 12 s

Figure 6-8 shows the steady oscillations of the water level inside the chamber, measured at W03, for the 10 s wave in contrast to the irregular rise of the water column for the 12 s wave presented in Figure 6-9. For the longer period wave, the water level inside the chamber fell, under gravity, well below that measured at W05 and W02 just outside the model in the flume. The velocity of the internal water surface, as calculated using Euler differentiation over 10 time steps, shows that the difference in water level was quickly accounted for, but the system's response was slightly out of phase with the incident wave crest. This discontinuous rise in water level disrupted the gradual pressure build up inside the chamber and reduced the overall energy capture of the system (refer to Figure 6-9).

The resulting internal chamber pressure and instantaneous pneumatic power for the two example tests are presented in Figure 6-10 and Figure 6-11.

Figure 6-10 shows that the chamber pressure and pneumatic power are approximately of similar magnitude in compression and expansion for the 10 s wave while the power generated for the 12 s wave, as shown in Figure 6-11, is considerably less in compression than expansion. This is a result of the irregular pressure build up in the chamber. The total absorbed pneumatic power averaged over six wave lengths is 8.3 kW and 4.6 kW. The overall efficiency of the system in terms of capture width is 0.72 m and 0.24 m for the 10 s and 12 s wave respectively, as calculated in the post processing procedure outlined in Figure 6-7.

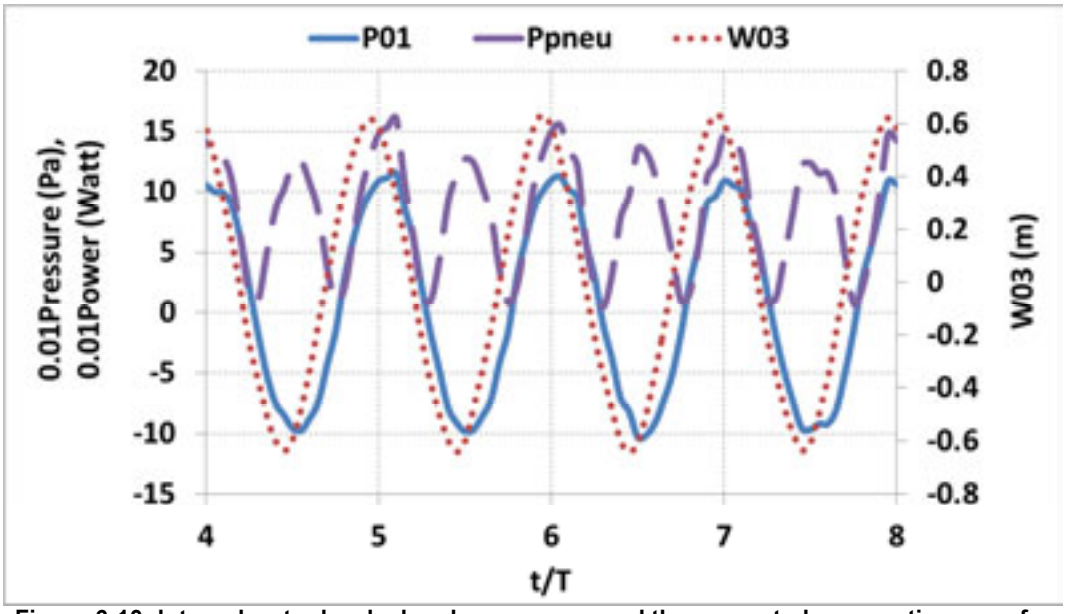

Figure 6-10: Internal water level, chamber pressure and the generated pneumatic power for test example H = 1 m and T = 10 s

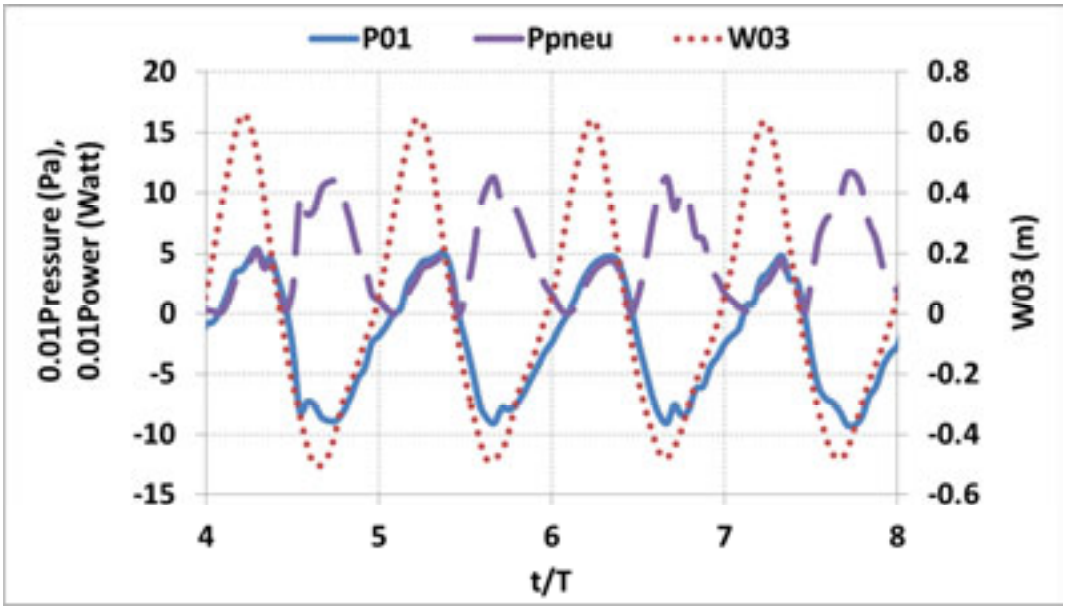

Figure 6-11: Internal water level, chamber pressure and the generated pneumatic power for test example H = 1 m and T = 12 s

The mean absorbed pneumatic power and capture width of the device for all the wave conditions tested, shown in Figure 6-12 and Figure 6-13 respectively, again highlights the device's sensitivity to the incident wave period.

The results presented in Figure 6-12 show that the maximum mean absorbed pneumatic power occurs at 10 s followed by 11 s, 9 s and 13 s. As expected the system absorbs more pneumatic power with increasing wave height confirming it will

have a greater energy conversion capacity at more energetic deployment locations compared to the sheltered site at Granger Bay.

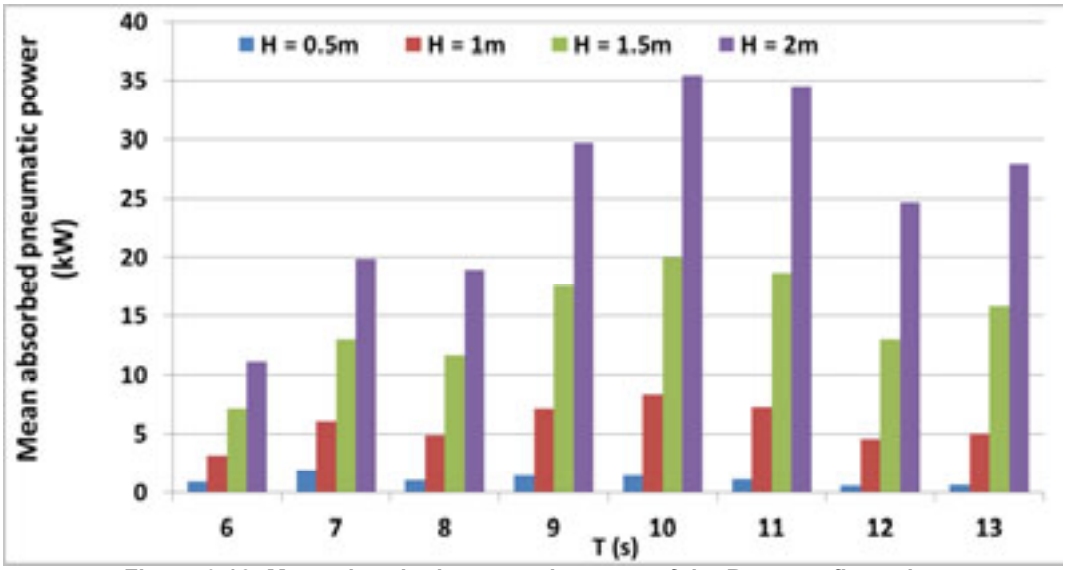

Figure 6-12: Mean absorbed pneumatic power of the Base configuration

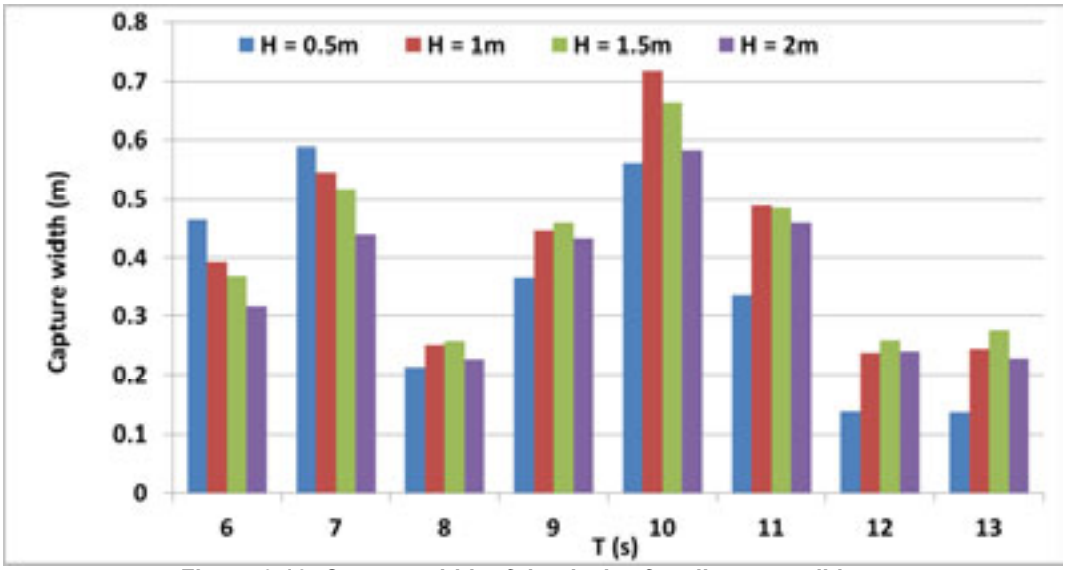

Figure 6-13: Capture width of the device for all test conditions

To determine the overall efficiency of the system the incident wave energy is taken into account and expressed in terms of the device's capture width as shown in Figure 6-13. The maximum efficiency occurs at 10 s, followed by 7 s, 11 s, 9 s and 6 s. As discussed earlier, the conversion efficiency of the model is low for the longer periods of 12 s and 13 s. This capture width comparison shows that the efficiency of the system is relatively insensitive to wave height. The average absorbed pneumatic power and capture width of the device is 11.7 kW and 0.39 m respectively over the 32 test conditions.

In the next phase of the experimental program the effect of water depth on the conversion efficiency of the model was investigated.

6.5.6 Effect of water depth on device efficiency

Water depth and tidal variation can potentially have an impact on the performance of the system. Deeper water influences the incident waves at the device due to wave-bottom interaction processes such as bottom friction, and reduces the entrapped air volume inside the chamber. It also increases the front lip submergence and natural period of the system, forcing water particles to travel further to enter the model. To determine the impact of water depth on the ShoreSWEC's power capture the test conditions were generated at a water depth increased from chart datum (CD) to mean sea level (MSL) and the conversion efficiency was calculated.

The mean pneumatic power absorbed by the system and its efficiency in terms of capture width are presented in Figure 6-14 and Figure 6-15 respectively, for all the test conditions at MSL. The capture width of the device relative to chart datum, presented in Figure 6-16, shows that the deeper water increases efficiency at 10 s and 9 s especially and reduces performance at 6 s, 11 s and 13 s. The average percentage difference of capture width between CD and MSL is 3% for the 32 test conditions which shows that water depth has a small net effect on the overall efficiency of the system.

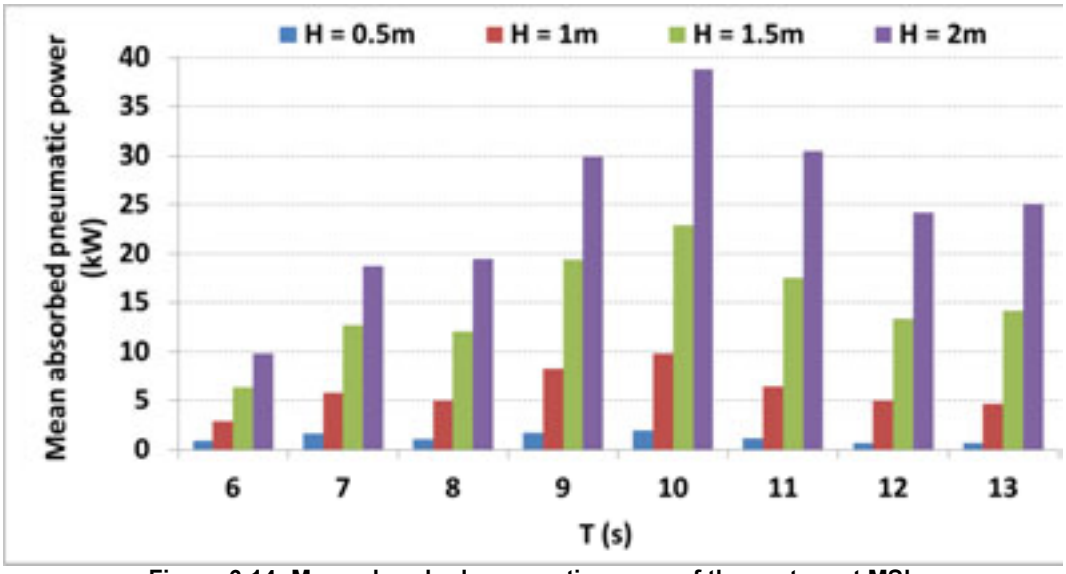

Figure 6-14: Mean absorbed pneumatic power of the system at MSL

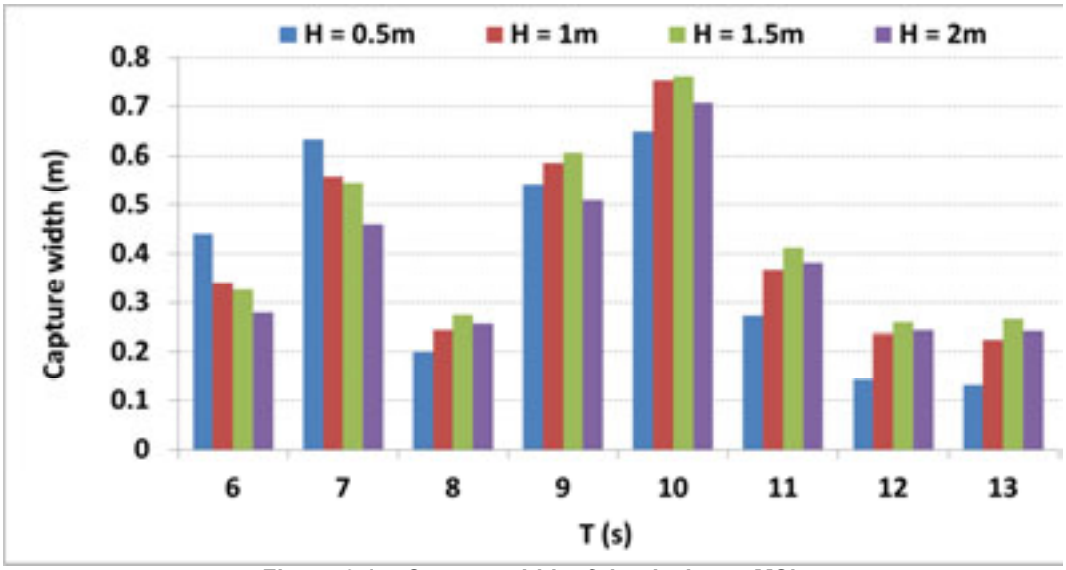

Figure 6-15: Capture width of the device at MSL

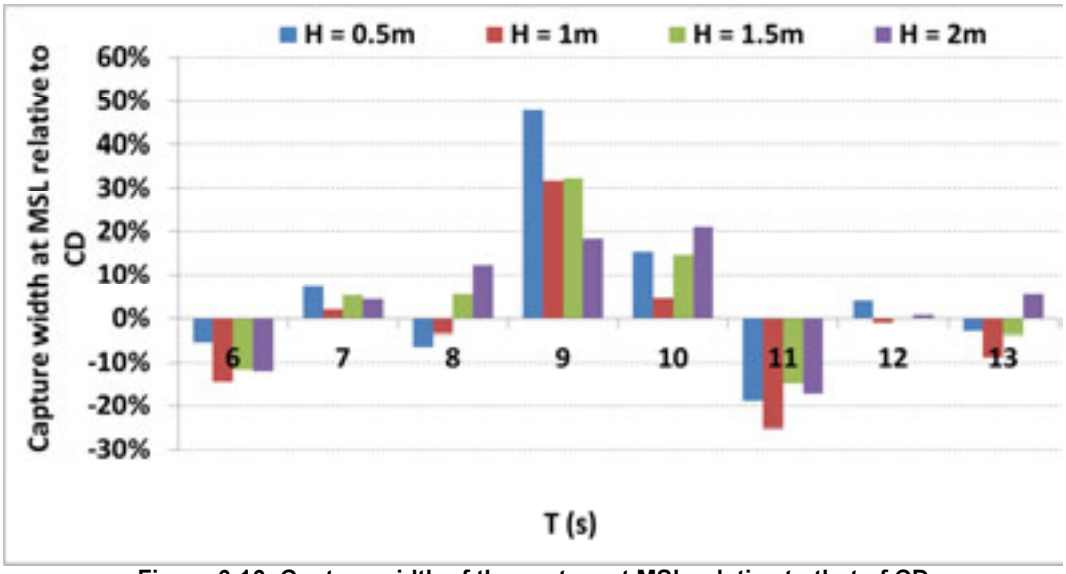

Figure 6-16: Capture width of the system at MSL relative to that of CD

The effect of water depth on the incident waves was investigated by comparing the waves measured at W01 for CD and MSL as shown in Figure 6-17. There is an inverse relationship between the difference in wave height and device output in deeper water as shown in Figure 6-16. This would suggest that the difference in incident wave height is the direct cause of the difference in device performance in comparison to that of CD. It is however difficult to make any foregone conclusions on the effect of water depth on the efficiency of the system, due to the relatively small tidal range of South Africa.

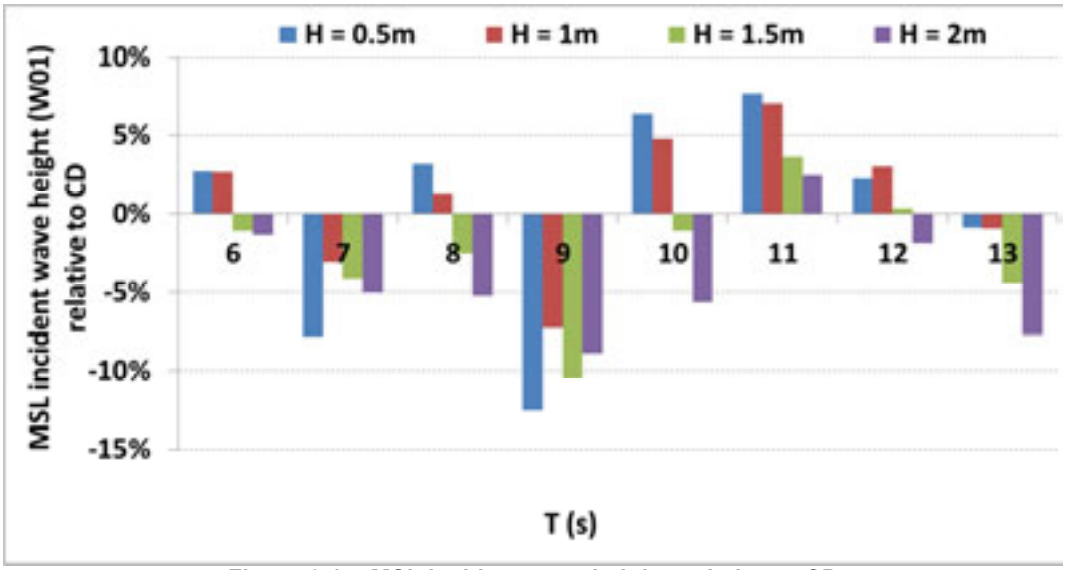

Figure 6-17: MSL incident wave heights relative to CD

Output of example test conditions (H = 1 m and T = 9 s), presented in Figure 6-18(a), shows that the water level oscillations inside the chamber (relative to still water level) is virtually identical for CD and MSL. In the presence of wave troughs the water surface velocity (see Figure 6-18(b)) is slightly lower for MSL which result in lower internal pressure (refer to Figure 6-18(c)) compared to CD. The generated pneumatic power (see Figure 6-18(d)) is slightly more at MSL compared to CD for the inhale cycle. For this particular test condition the output of the system was 30% greater at MSL than CD.

This concludes the analysis of the system's performance as a function of wave energy conditions. In the next phase of testing the effect of a geometric alteration was evaluated.

6.5.7 Floor incline

Wave-induced flow enters the capture chamber horizontally and must turn 90º to displace the entrapped air vertically through the outlet. Inclining the floor of the device not only accelerates the incident fluid flow, but assists it to turn and reduces losses due to vortices formed in the lower rear corner of the chamber. Examples of inclined OWC chambers include the designs of Liu et al. (2010a, 2010b and 2011) and the most well-known example the LIMPET. The effect of an inclined floor on the power capture of the ShoreSWEC was investigated by installing a 50º Perspex slope into the model, see Figure 6-19.

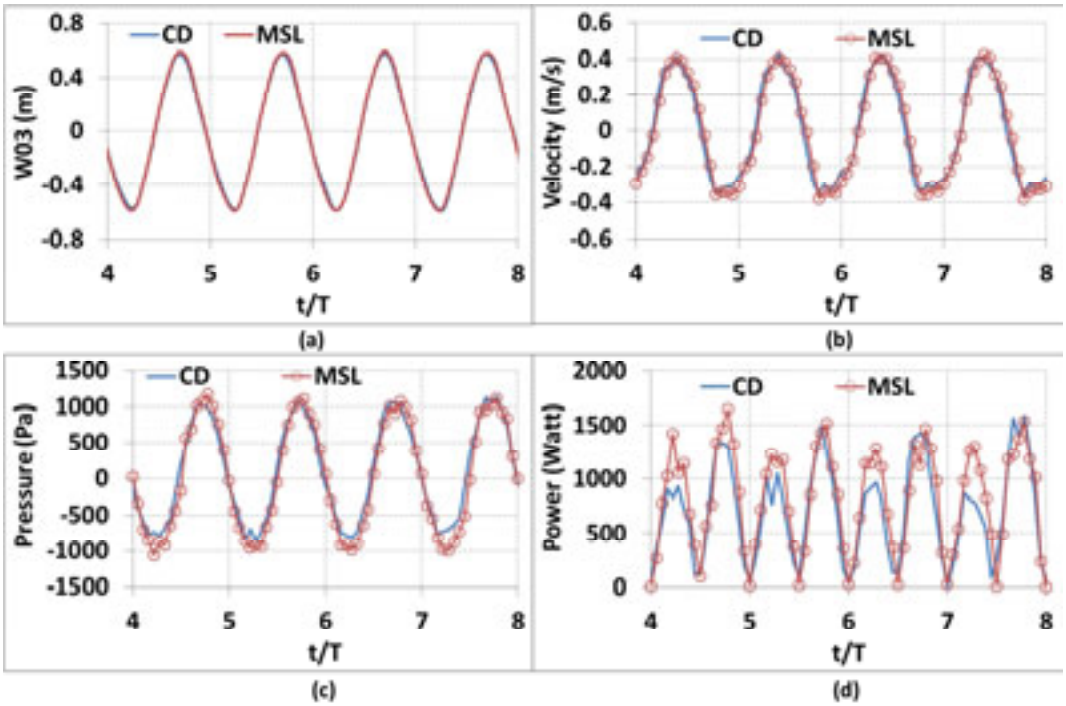

Figure 6-18: Test example, *H* = 1 m and *T* = 9 s, of model at MSL showing resulting: (a) Internal water level (b) Surface velocity (c) Chamber pressure and (d) Pneumatic power

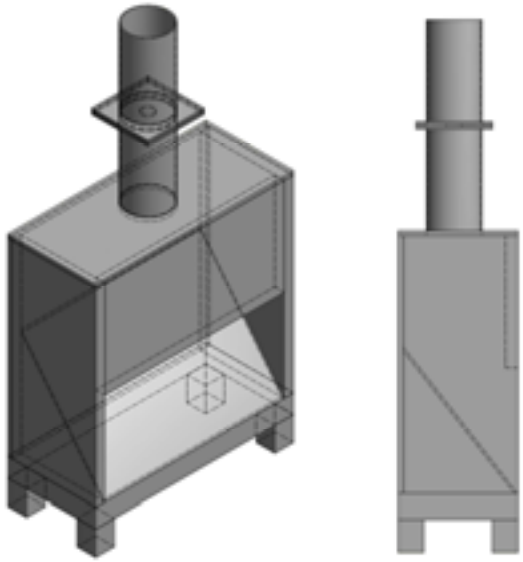

Figure 6-19: Isometric and side view of scale model with floor incline

The mean absorbed pneumatic power and capture width of the sloped floor model for all the test conditions are presented in Figure 6-20 and Figure 6-21 respectively. The capture width of the sloped model relative to the Base configuration in Figure 6-22 shows that the gradient improved efficiency for 26 of the 32 tests by an overall average increase of 11%. Greatest gains were achieved for the lowest wave heights tested making it an ideal modification of the ShoreSWEC design for the small wave

heights of Granger Bay. Minor reduction in performance (maximum 5%) occurred mainly for the biggest wave height tested which suggests that this alteration is less suited for more energetic locations.

For the majority of the test conditions the water level oscillations inside the chamber were visibly less plane in comparison with the Base configuration. This is due to the reflection caused by the slope - refer to the surface elevation graph (W03) of the output example in Figure 6-23(a). The increased velocity of the water surface (Figure 6-23(b)) during water ingress and resulting gain in pressure and power (Figure 6-23(c) and (d)) highlights the advantage of using a floor incline. For this example test condition the slope improved the efficiency of the model by 15% compared to the Base model.

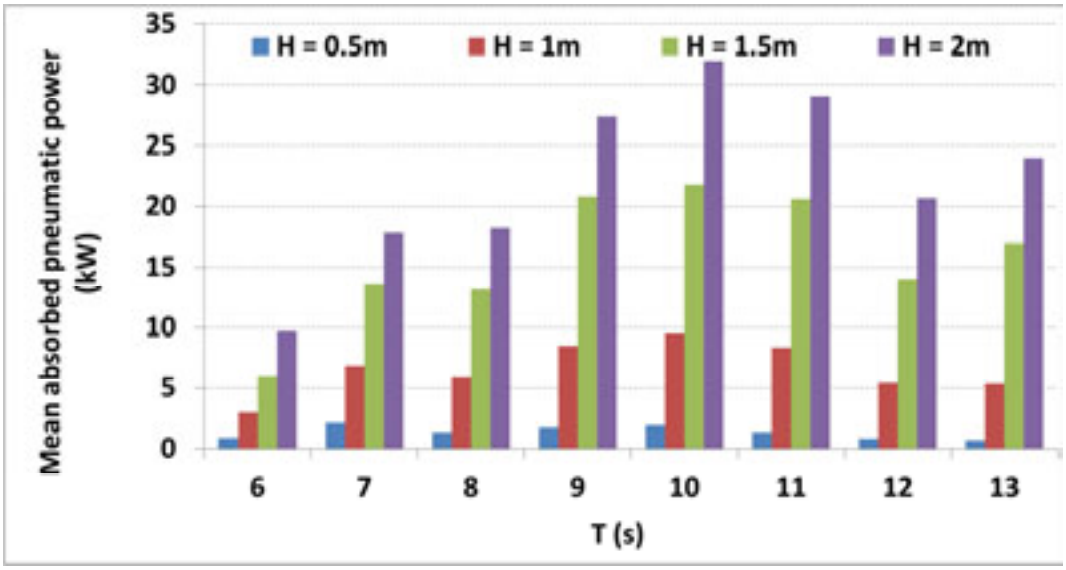

Figure 6-20: Mean absorbed pneumatic power of inclined floor model

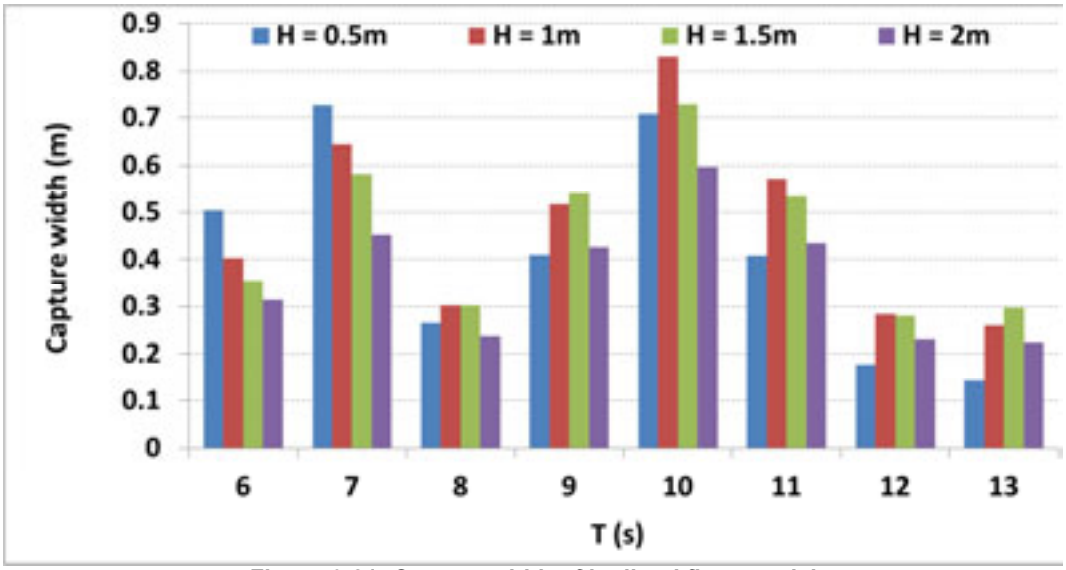

Figure 6-21: Capture width of inclined floor model

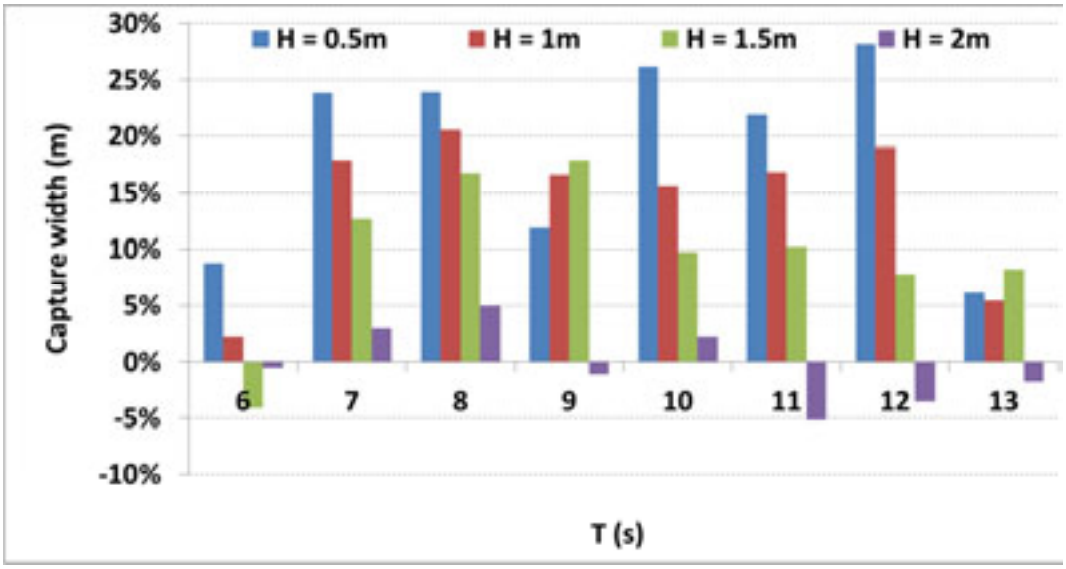

Figure 6-22: Output of inclined floor model relative to the Base configuration

The inclined model was also tested at MSL and showed increased efficiency at 9 s and 10 s and reduced output at 11 s, similar to the Base model at MSL.

The experimental testing of a single chamber of the ShoreSWEC provided valuable insights into its hydrodynamic energy conversion characteristics. In the next stage of experimental tests the performance of a dual chamber system was investigated.

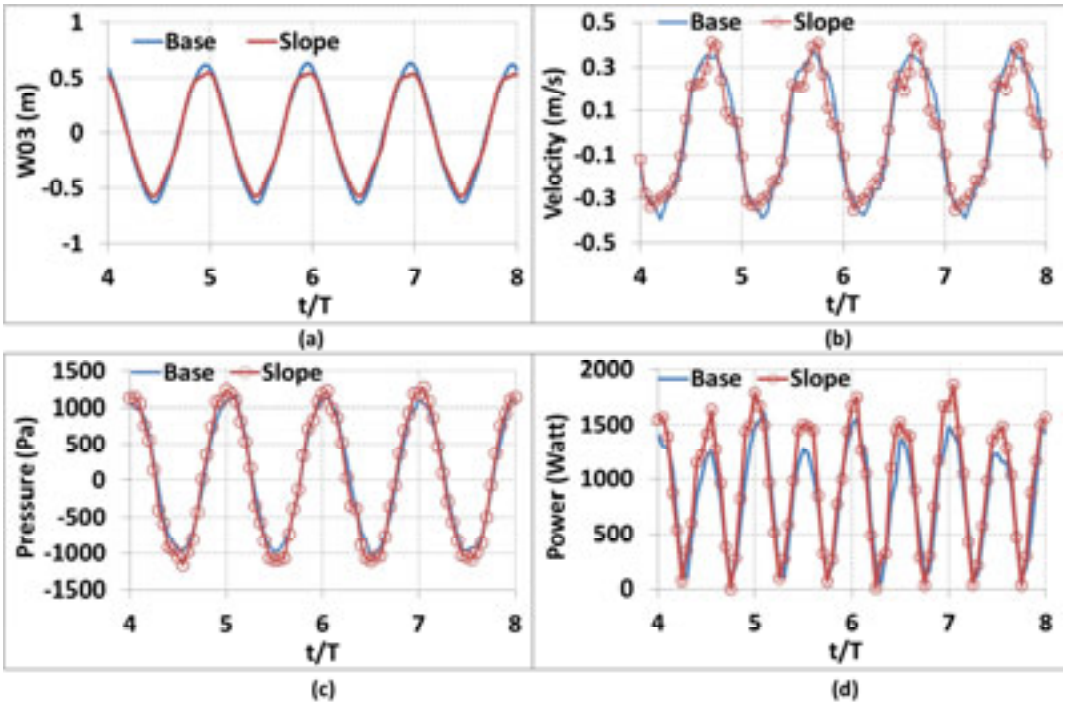

Figure 6-23: Output example, *H* = 1 m and *T* = 10 s, of the sloped floor model which include: (a) Internal water level (b) Surface velocity (c) Chamber pressure and (d) Pneumatic power

6.5.8 Multiple chambers

The ShoreSWEC is a multi-chamber device which will ideally consist of at least 10 chambers. In an attempt to characterise the energy capture of multiple chambers an additional box model was added to the experimental setup (Figure 6-24). Only wave heights of 0.5 m and 1 m were tested due to the limited amount of pressure sensors available for this study. The conversion efficiency of the model has been shown to be relatively insensitive to wave height, therefore two wave height conditions were considered adequate to evaluate the performance of the system.

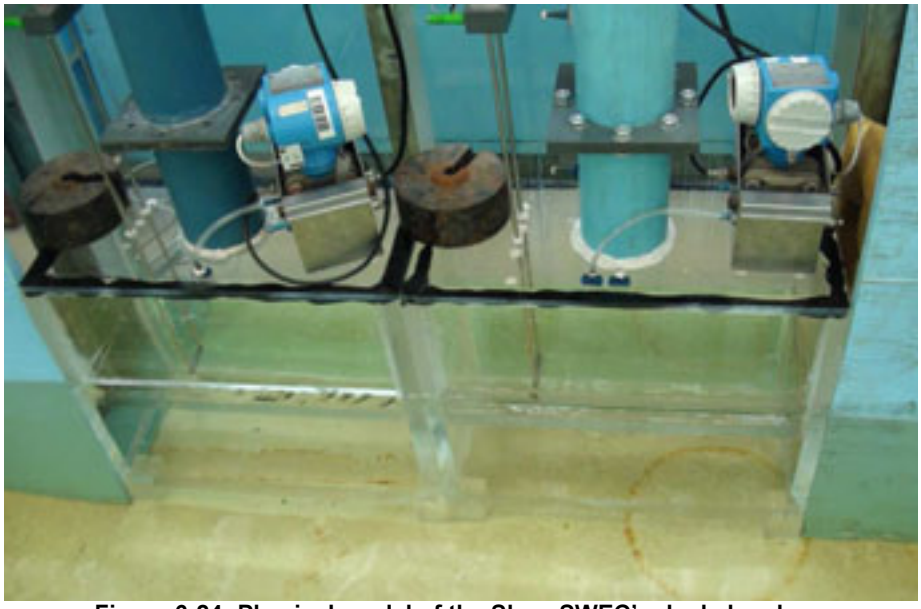

Figure 6-24: Physical model of the ShoreSWEC's dual chambers

The mean pneumatic power absorbed by the first of the two chambers and its conversion efficiency, in terms of the capture width, is presented in Figure 6-25 and Figure 6-26 respectively.

Figure 6-27 shows that the additional chamber reduces the efficiency in comparison with a standalone chamber at 9 s and 10 s, periods of maximum performance of the single chamber system, and 7 s. There is a substantial increase in capture width at 8 s and a promising increase for the longer period waves of 11 s, 12 s and 13 s.

Example output for the first of the two chambers (1Box2) is presented in Figure 6-28 for H = 1 m and T = 12 s in comparison with the Base configuration output. From the results it can be seen that the additional chamber greatly improves the expansion and especially the compression cycle of the first chamber. This leads to an overall increase in capture width of 80% compared to the Base configuration.

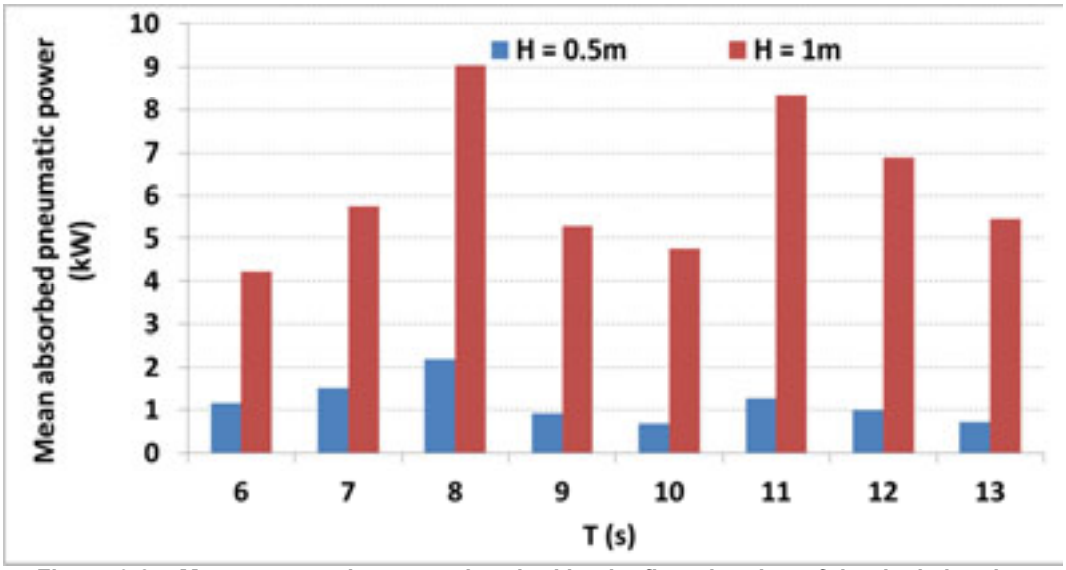

Figure 6-25: Mean pneumatic power absorbed by the first chamber of the dual chamber system

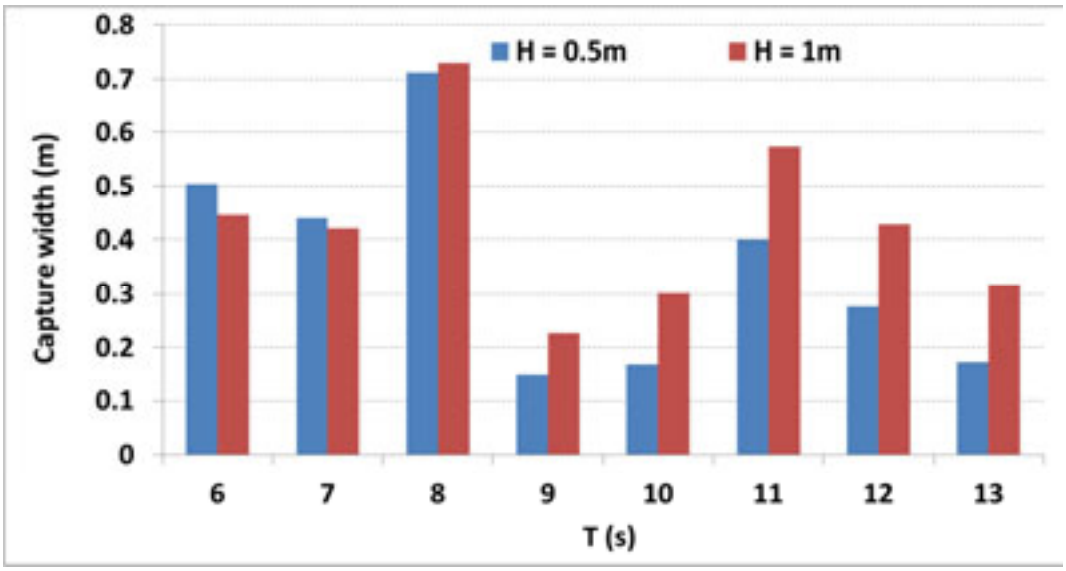

Figure 6-26: Capture width of the first chamber of the dual chamber system

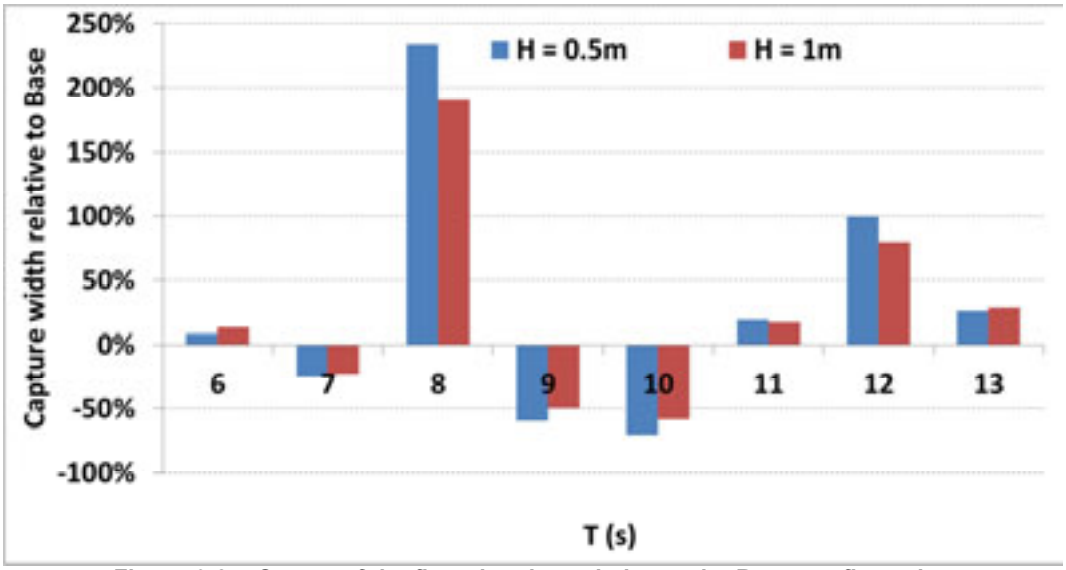

Figure 6-27: Output of the first chamber relative to the Base configuration

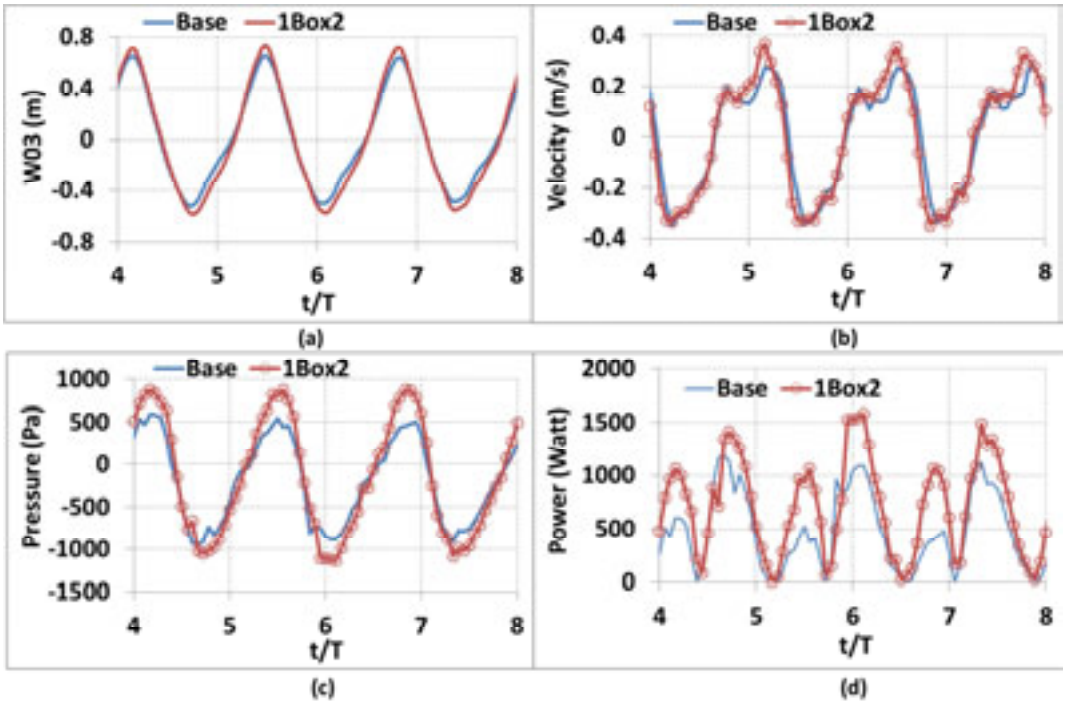

Figure 6-28: Example output of the first of two capture chambers for *H* = 1 m and T = 12 s which include: (a) Internal water elevation (b) Water column surface velocity (c) Chamber pressure and (d) Pneumatic power

The mean pneumatic power absorbed by the second of the two chambers and its conversion efficiency, in terms of the capture width, is presented in Figure 6-29 and Figure 6-30 respectively. The average pneumatic power absorbed and capture width of the second chamber equals that of the first chamber. The effect of water depth on the performance of the dual chamber system was also investigated and it was found to slightly increase the average capture width of the first chamber compared to CD.

The multi-chamber system cumulatively captures and converts energy as incident waves propagates along its length. The total mean pneumatic power absorbed and the capture width of the dual chamber model are presented in Figure 6-31 and Figure 6-32 respectively. The average capture width of the dual chamber model is 0.78 m and its peak efficiency is no longer at 10 s, as was the case for the Base configuration, but rather at 11 s and 8 s. The multi chamber system has greater efficiency at 11 s, 12 s and 13 s in comparison to the single chamber model.

These results would suggest that the multi-chamber device is better suited to the longer period wave regime of South Africa compared to an isolated, single chamber device. For future work it is recommended that experimental tests be conducted on a system with a minimum of ten capture chambers, to fully understand the hydrodynamic characteristics of a large scale device. This was not possible in this experimental campaign due to scale and spatial constraints. A 3D basin must also be used to determine the performance of a multi-chamber system less obliquely orientated that can better capture the kinetic wave energy.

The last set of experimental tests focused on the evaluation of the generated output of an OWC in comparison with a single chamber ShoreSWEC.

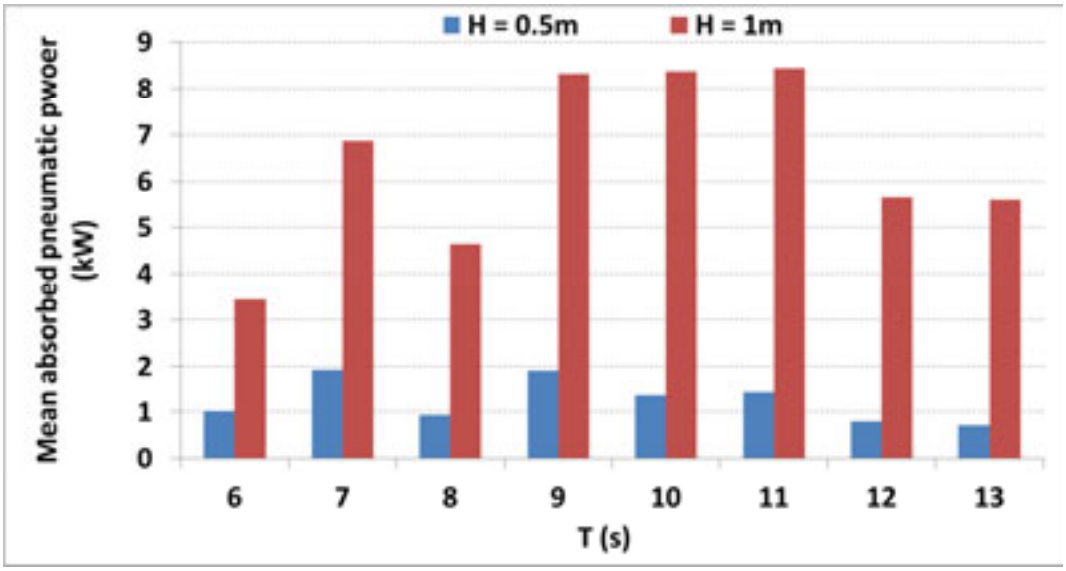

Figure 6-29: Mean pneumatic power absorbed by the second chamber of the dual chamber system

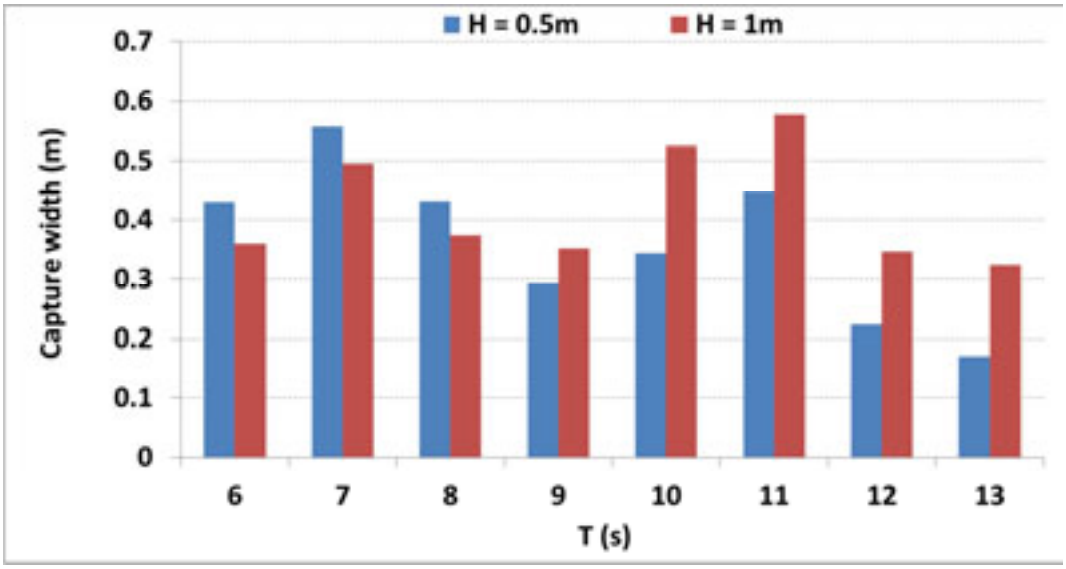

Figure 6-30: Capture width of the second chamber of the dual chamber system

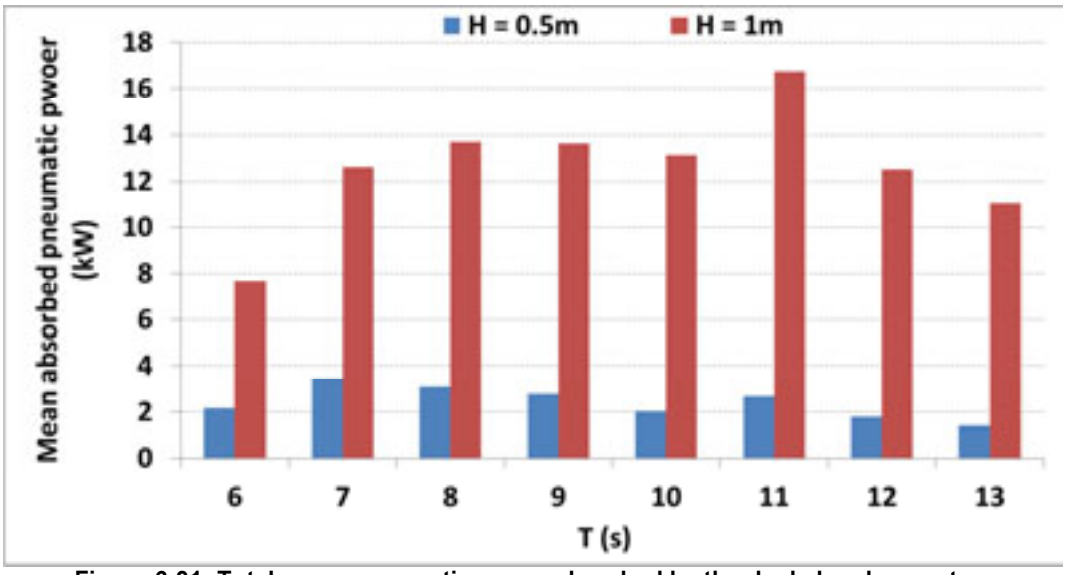

Figure 6-31: Total mean pneumatic power absorbed by the dual chamber system

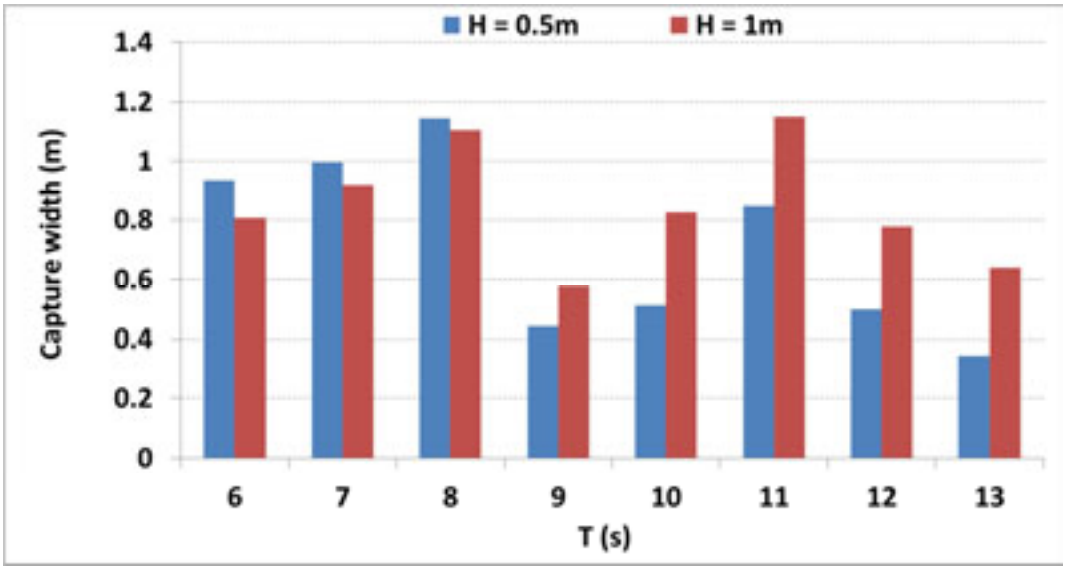

Figure 6-32: Total capture width of the dual chamber model

6.5.9 OWC

The essential difference between the ShoreSWEC and a conventional OWC is its orientation relative to the dominant wave direction. In order to investigate the power capture of an OWC of the same size and dimensions as the ShoreSWEC the scale model was rotated by 90^0 to face into the incident waves (refer to Figure 6-33). The OWC caused significant wave reflection inside the flume and experienced substantial wave loading, as would be expected.

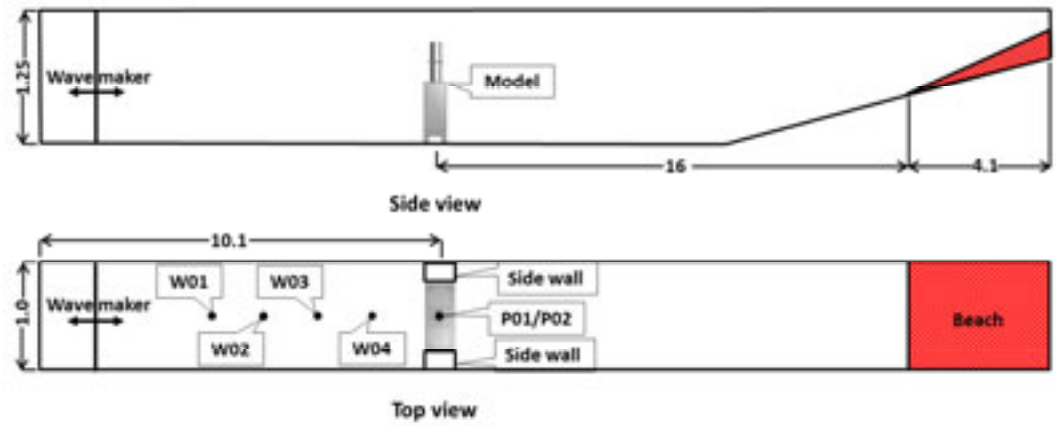

Figure 6-33: OWC experimental test setup (distances in meters, drawing not to scale)

The mean absorbed pneumatic power output of the Base configuration and OWC is presented in Figure 6-34 and Figure 6-35 respectively.

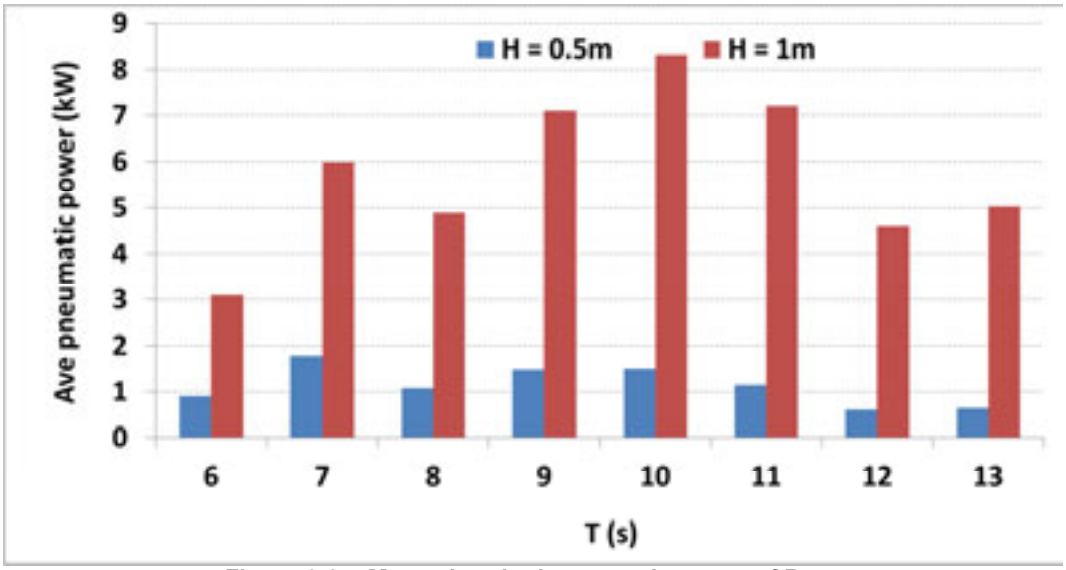

Figure 6-34: Mean absorbed pneumatic power of Base

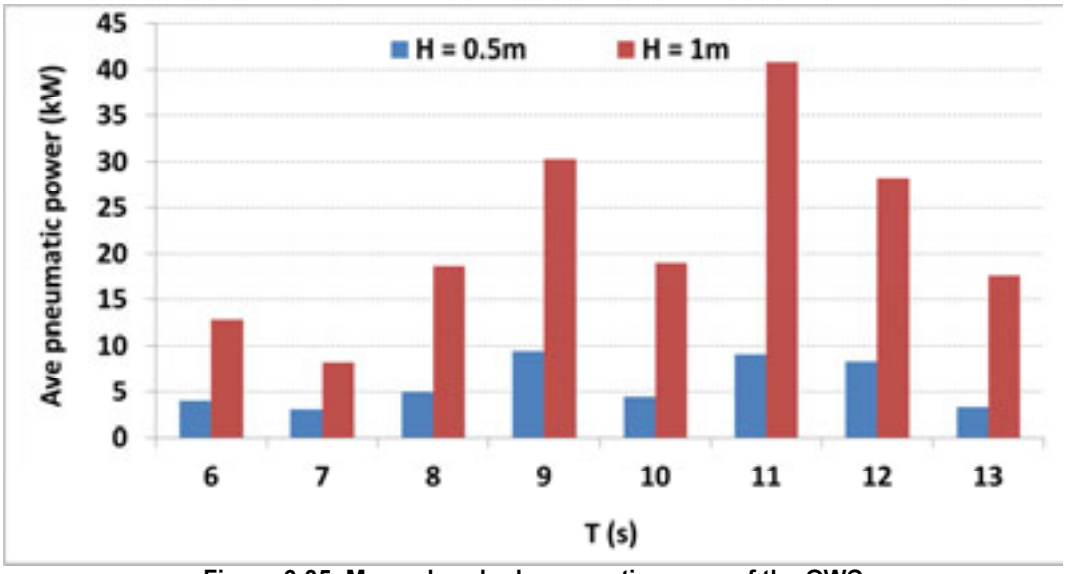

Figure 6-35: Mean absorbed pneumatic power of the OWC

The pneumatic power output of the Base configuration presented in Figure 6-35 is very similar to its capture width with maximum output at 10 s. There is however an increased pneumatic power output compared to the capture width analysis at 11, 12 and 13 s due to the fact that the incident wave energy is not accounted for.

The OWC's pneumatic output is 72% greater, averaged over all test conditions, than that of the ShoreSWEC (refer to Figure 6-12). It's interesting to note that the OWC's maximum output is at 11 s and not at 10 s as was the case for the ShoreSWEC model. These results demonstrate the sensitivity of OWCs to incident wave direction, as also demonstrated by Jin et al. (2012).

6.6 Summary and conclusions

The hydrodynamic efficiency of a single chamber ShoreSWEC was investigated by means of a detailed experimental test program. The performance of the system under various wave energy conditions with an optimal PTO was studied. It was found that the conversion efficiency of the device is highly dependent on wave period and to a lesser extent wave height. The model was most efficient at 10 s with low efficiency at higher wave periods typical of the South African wave regime.

Water depth affected device efficiency for particular wave conditions, but the average impact over all the test conditions was insignificant. A floor incline improved the efficiency of the device for low wave heights, making it an ideal design alteration for locations with small wave height distribution such as Granger Bay. A dual chamber model was tested to better understand the behaviour of a multi-chamber system and it was found that the added chamber increased efficiency at high periods for the first and second chamber. Lastly, an OWC was tested which generated 72% more pneumatic power (averaged over all the test conditions) than the ShoreSWEC, highlighting the sensitivity of the system to incident wave direction.

A summary of the average capture width of the system and its various variables tested for wave heights and periods of 0.5 m, 1 m and 6 s to 13 s respectively is presented in Figure 6-36.

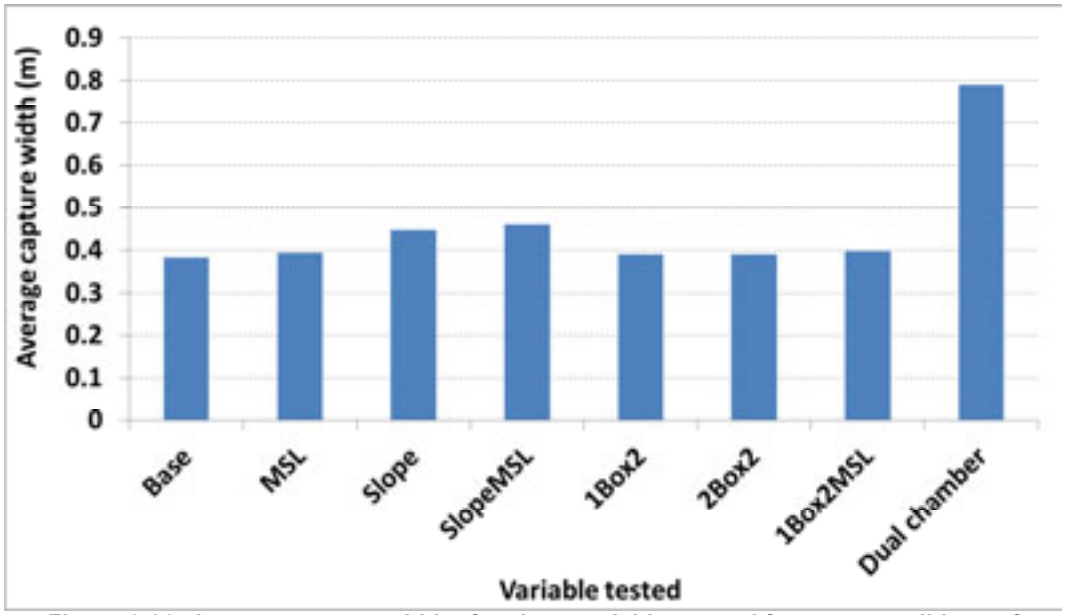

Figure 6-36: Average capture width of various variables tested for wave conditions of H = 0.5 m, 1 m and T = 6 s to 13 s.

In Figure 6-36 “2Box2”, “1Box2MSL” and “Dual chamber” represent the second chamber of the dual chamber system, the first chamber of the dual chamber system at MSL and the combined capture width of the two chambers respectively. Figure 6-36 highlights the improvement in capture width of the sloped floor model at CD and MSL compared to the Base configuration. The total capture width of the dual system shows how energy capture is accumulated for a multi-chamber system.

Some of the main conclusions that can be drawn from the experimental test results are:

- The ShoreSWEC successfully captures and converts incident wave energy to pneumatic power at its most conservative orientation.
- Additional chambers greatly affect the performance of the system, compared to a single chamber device. A better understanding of the hydrodynamic characteristics of a full length device is required.
- Device performance is highly dependent on wave direction.

7 Computational Fluid Dynamics (CFD) study

Computational Fluid Dynamics (CFD) is a numerical simulation tool that solves the fundamental Navier-Stokes fluid flow equations. The CFD code used in this thesis solve the Navier-Stokes equations using the finite volume method over a specified domain. Two commercial CFD codes, ANSYS Fluent and Star CCM+, were considered for this study. Fluent proved to be the more computational efficient in solving the specific research problem and was therefore used. It has the capability to simulate and track the water-air interface using its volume of fluid (VOF) method. Wave surfaces can therefore be modeled and the water-air interaction inside the OWC chamber can be simulated.

The main objective of this section was to develop a 3D CFD model of the experimental test setup to compare results. In order to achieve this, a 2D numerical wave tank (NWT) was first developed, based on the work of Horko (2005). After the accuracy of the 2D NWT was confirmed, it was extended into the third dimension. A model of a single chamber of the ShoreSWEC was incorporated into the 3D NWT and tests were conducted. Lastly, the numerical and experimental test results were compared.

7.1 Two-dimensional (2D) numerical wave tank (NWT)

The main input requirements for the 2D NWT include its layout and boundary conditions, mesh, and wave generation functionality.

7.1.1 Layout

The computational domain of the 2D numerical wave tank was 21 m long and 1 m high, as shown in the schematic of Figure 7-1. This is in the same order of magnitude as the physical wave flume dimensions used in the experimental tests to ensure results are comparable. Waves entered the domain from the wave generation boundary on the left (“velocity inlet”) and propagated along the wall boundary at the bottom towards the wall at the far end of the domain. The system was open to atmosphere, similar to an open channel flow problem, and a pressure inlet boundary was therefore specified at the top. Only the first five fully developed, monochromatic waves were considered for analysis to avoid wave reflection off the end wall contaminating the data record, similar to the experimental tests. The domain was divided into various regions according to cell size using ANSYS Designmodeller version 13.0.

7.1.2 Mesh

For Fluent to solve the governing equations, the computational domain must be divided into a series of elements or cells. The regions of the domain, specified in Designmodeller, were assigned cell sizes and a mesh of uniform quadrilateral cells, covering the entire domain, was generated using various controls and algorithms in the Mesher module of ANSYS 13.0. A high concentration of cells was specified in the region of the wavemaker, ensuring that the wave velocity profiles are accurately generated into the domain. Other areas of high cell resolution included the water-

bottom wall boundary and the water-air interface to ensure that the wave profile was sufficiently defined. The main area of interest however, was at the location where the single chamber was to be included. The wave profiles in this area were monitored to ensure accurate wave conditions at the converter.

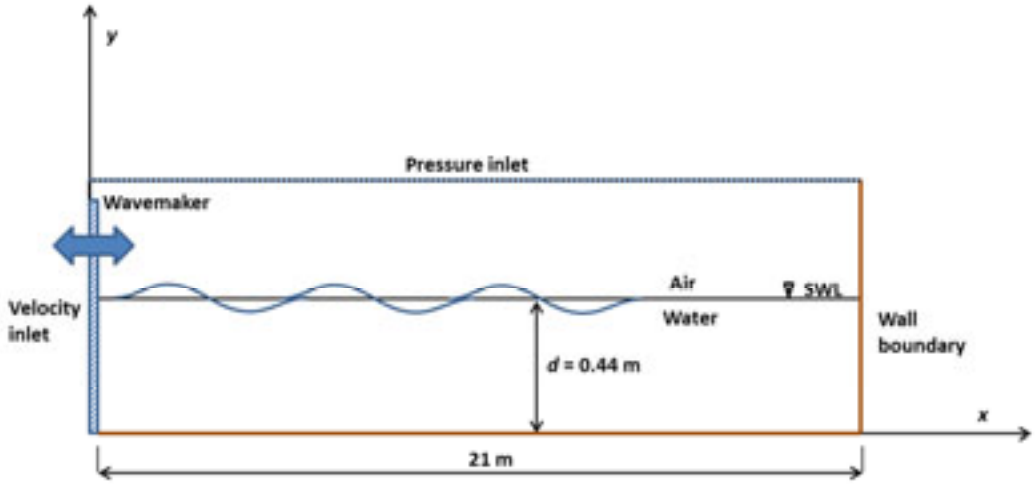

Figure 7-1: Schematic of the 2D numerical wave tank

Once the waves pass the area of interest they no longer affect the conditions at the device. A very low cell resolution was therefore specified for the remaining section of the domain which minimised computational time and promoted wave absorption through numerical diffusion. The various regions of the 2D NWT mesh are presented in Figure 7-2.

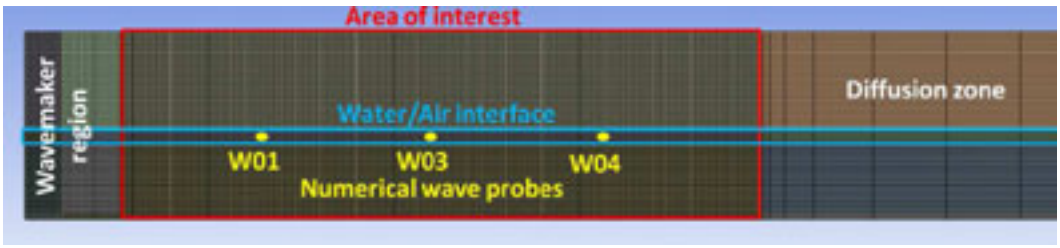

Figure 7-2: 2D NWT mesh showing the wavemaker boundary, area of interest with numerical wave probes and diffusion zone

The quality of a mesh is defined in terms of the skewness of its elements. Skewness is a measure of distortion of a cell relative to its ideal shape and is scaled from 0 (excellent) to 1 (unacceptable). The block-like domain of the model meant that the mesh used for the 2D NWT had a maximum skewness of close to zero, indicating it was of excellent quality.

7.1.3 Wave generation

There are various ways to generate waves in a numerical wave tank. Fluent has a built-in open channel wave boundary condition that is designed to generate regular waves. However, in initial investigations it was found that this function did not generate sufficiently accurate regular wave profiles and could not be readily adjusted to create 2nd order Stokes waves. Other wave generation methods include

implementing user defined functions (UDF). One of the most common of these is the moving wall boundary method as used by Liu et al. (2010). In this method the motion of a wall boundary is prescribed similar to a piston type wavemaker in an experimental wave flume. At each time step the model mesh is regenerated, making it computationally intensive. To overcome this, Horko (2007) demonstrated that regular and 2nd order Stokes waves can be generated by prescribing the incident wave *x*- and *y*-velocity profile with a UDF using Equations (13) to (14). In this study Horko's method was used to generate 2nd order Stokes waves in the NWT.

7.2 Model setup

For this type of incompressible, transient, multi-phase flow problem Fluent uses a segregated pressure-based solver which solves the governing equations separately and sequentially. The VOF model (Hirt and Nicols, 1980) was used to simulate two-phase flow and track the water-air interface (water level) throughout the domain by solving a single set of momentum equations. The VOF formulation is based on the assumption that the two fluids are immiscible, i.e. not interpenetrating. The VOF method tracks the free surface by monitoring the cells that are partially filled with water. The fluxes between computational cell faces near the interface of the two fluids are determined using geometric reconstruction with a piecewise-linear approach (Young, 1982). This assumes a linear slope between the two fluids and gives a more accurate approximation of the interface in comparison with the donor-acceptor scheme (refer to (Fluent, 2006)).

Fluent has various solvers, discretisation schemes and input variables which can influence the quality, duration and convergence of the solution. Refer to the User Manual (Fluent, 2006) for more detailed information and see Appendix G for example input parameters of this study.

7.2.1 Under-relaxation factors

Fluent's pressure-based solver uses a process called under-relaxation to control the change of each variable, ϕ, in order to help stabilise the solution and aid convergence. The change in variable is reduced by an under-relaxation factor, α, which is added to the variable of the previous iteration, ϕ_{old}.

$$\boldsymbol{\phi = \phi_{old} + \alpha \Delta \phi} \qquad (29)$$

In this 2D numerical study the default under-relaxation values were used for all the wave conditions tested.

All the output from the numerical model presented was scaled to real conditions similar to the experimental results discussed in Chapter 6. This enables a comparison of tangible quantities.

7.3 Grid dependency and the effect of timestep

It is of prime importance to ensure that the wave profiles generated by the NWT are acceptably accurate. In this section, the effect of the number of cells in the mesh and the timestep size on the model solution was investigated. An optimal ratio between solution accuracy and the computational time needed to solve higher cell resolution meshes at smaller timestep sizes is required.

Liu (2011a) recommends a minimum element size in the x-direction (Δx) and y-direction (Δy) of $L/20$ and $d/20$ respectively and a minimum timestep size of $T/100$. The basic mesh of the 2D NWT and its timestep size were selected to be well below these minimum values, shown as case 1 in Table 7-1. Two higher cell resolution meshes and two smaller timestep conditions were tested to determine their impact on generated wave profile accuracy and computational time. A typical wave condition of H = 1 m, T = 10 s and L = 96.2 m was used for this analysis.

Table 7-1: Cases of varying mesh and timestep sizes

Case	Timestep, Δt (s)	$T/\Delta t$	Typical grid size (m)	$L/\Delta x$	$d/\Delta y$
1	0.05	T/200	0.25	L/385	d/44
2	0.025	T/400	0.25	L/385	d/44
3	0.0125	T/800	0.25	L/385	d/44
4	0.05	T/200	0.125	L/770	d/88
5	0.05	T/200	0.0625	L/1540	d/176

An example wave profile generated by the basic model setup of case 1 is presented in comparison with the 2nd order Stokes and experimental profile in Figure 7-3. The numerically generated profile closely follows the theoretical and experimental profile.

The difference in wave height, wave period, crest and trough elevation averaged over 5 wavelengths for the different mesh and timestep cases are presented in Figure 7-4. The results show that the generated wave parameters are within 2% of the theoretical input conditions for case 1 and no significant increase in accuracy is gained for higher resolution meshes or smaller timesteps. Computational time increased a maximum of fivefold for the higher resolution cases.

7.4 Wave conditions

The accuracy of the case 1 model when generating various wave period conditions at a constant wave height of 1 m was investigated. The results of the analysis in Figure 7-5 shows that the generated wave heights are within 5% of the input conditions. The greatest deviation of the model from the input conditions was found at the low periods of 7 s, 8 s and the highest period of 13 s.

This analysis showed that the 2D NWT will generate sufficiently accurate wave conditions. The development of a 3D model of a single chamber of the ShoreSWEC is discussed in the next section.

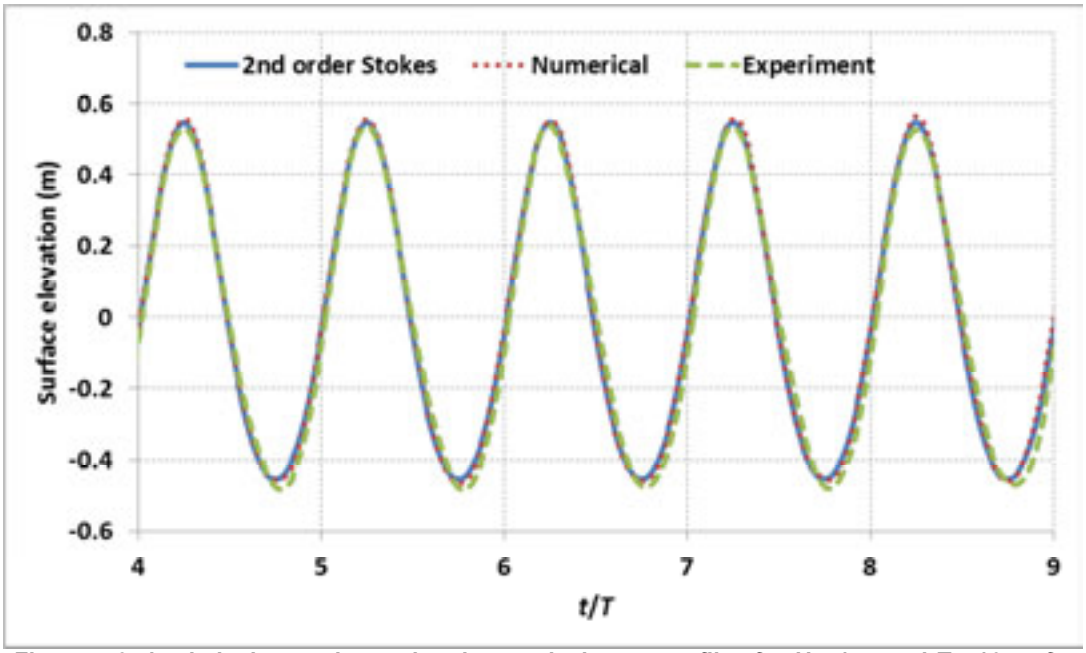

Figure 7-3: Analytical, experimental and numerical wave profiles for *H* = 1 m and *T* = 10 s of case 1.

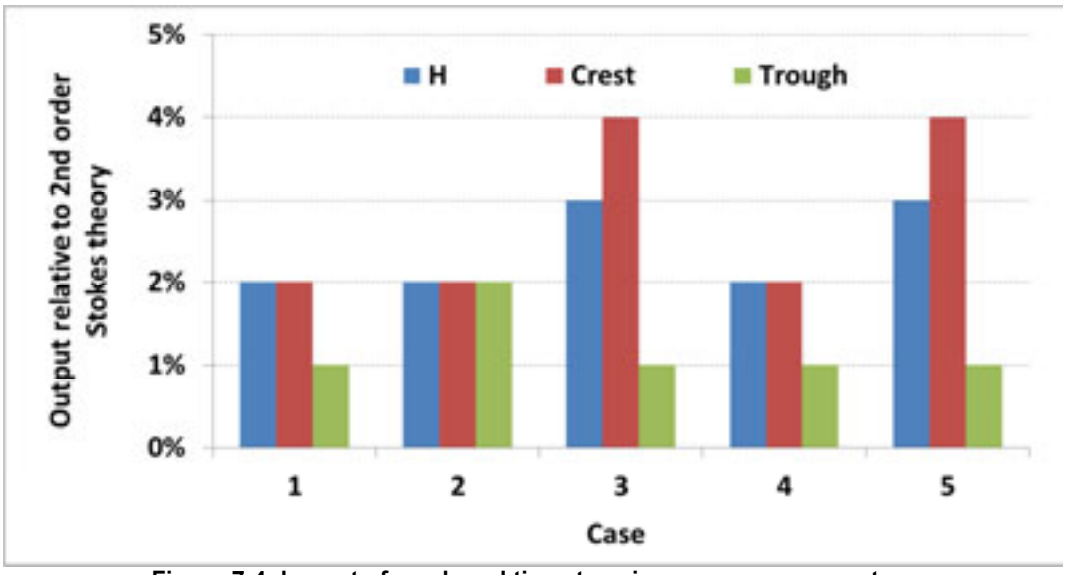

Figure 7-4: Impact of mesh and timestep sizes on wave parameters

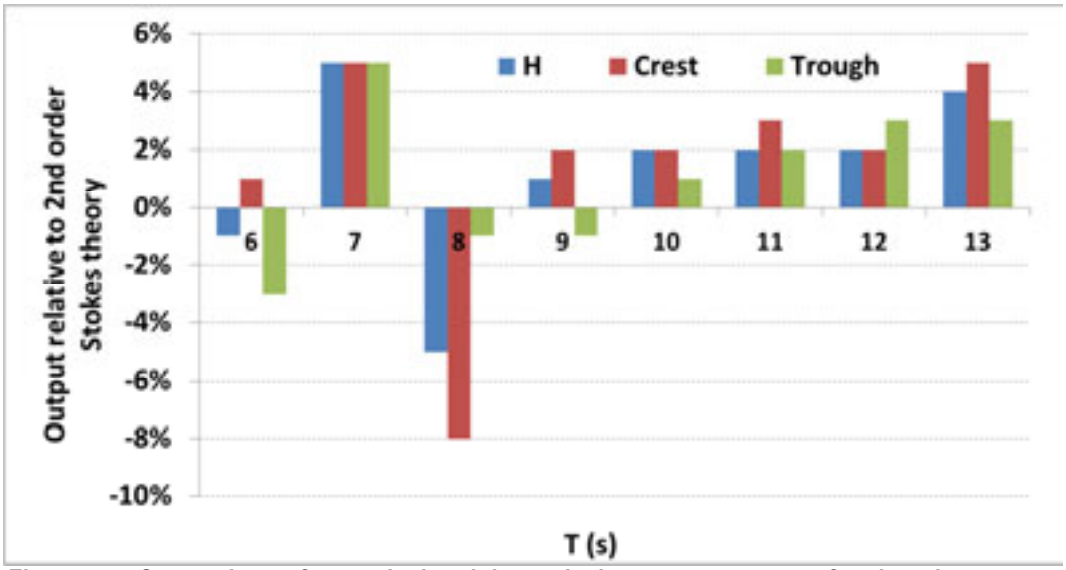

Figure 7-5: Comparison of numerical and theoretical wave parameters of various input wave periods for case 1

7.5 3D NWT and model of ShoreSWEC

A 3D NWT and model of a single chamber of the ShoreSWEC were developed to investigate the hydrodynamic characteristics of the system and verify the experimental results. The domain, grid and turbulence method of this model are discussed.

7.5.1 Domain

The same computational domain was used for the 3D as the 2D model. The 3D domain was extruded in the z-direction a distance equivalent to the available width of the physical wave tank. The same boundary conditions as the 2D model were also used with the addition of wall boundaries on the sides of the tank and chamber. A pressure outlet boundary was specified at the top of the chimney structure in which the orifice is housed.

7.5.2 Grid

The 3D mesh consisted of approximately 1 million hexahedron (prism with a quadrilateral base) and wedge (prism with a triangular base) elements. This ensured a plane water surface instead of an uneven one, which would be the case if tetrahedral cells were used. Areas of interest include the orifice outlet and the entrance to the chamber. The orifice was made up of elements with a typical size of a tenth of its diameter. The chamber opening was divided into 25 and 48 cells in the vertical and horizontal direction respectively. The quality of the 3D mesh was good with a maximum skewness of 0.55. The 3D mesh is presented in Figure 7-6(a) to (c).

7.5.3 Turbulence model

Wave induced oscillations inside the chamber, and the resulting high airflow velocities through the orifice outlet, cause turbulent flow conditions. These conditions must be accurately represented by a suitable turbulence model. The standard k-ω

model which solves the kinetic energy k and turbulent frequency ω was used for this purpose (Wilcox, 1998). It is one of the most commonly used turbulence models and is known for its robustness. The k-ω model proved to be more stable than the k-ε model provided that reduced under-relaxation factors were prescribed.

7.6 Results

Simulations were run on a 2.93 GHz Intel Core i7 processor with 16 GB of RAM. Computational time was typically 13 hours for 20 s of simulated waves. In order to test a wide variety of incident wave conditions and geometries, similar to the physical tests, considerable computational time would be required. Due to time constraints, only a limited number of test conditions was simulated. The OWC response has been shown to be highly dependent on the wave period and less so on wave height. Therefore, a constant wave height of 1 m and 8 wave periods of 6 s to 13 s in 1 s intervals were simulated.

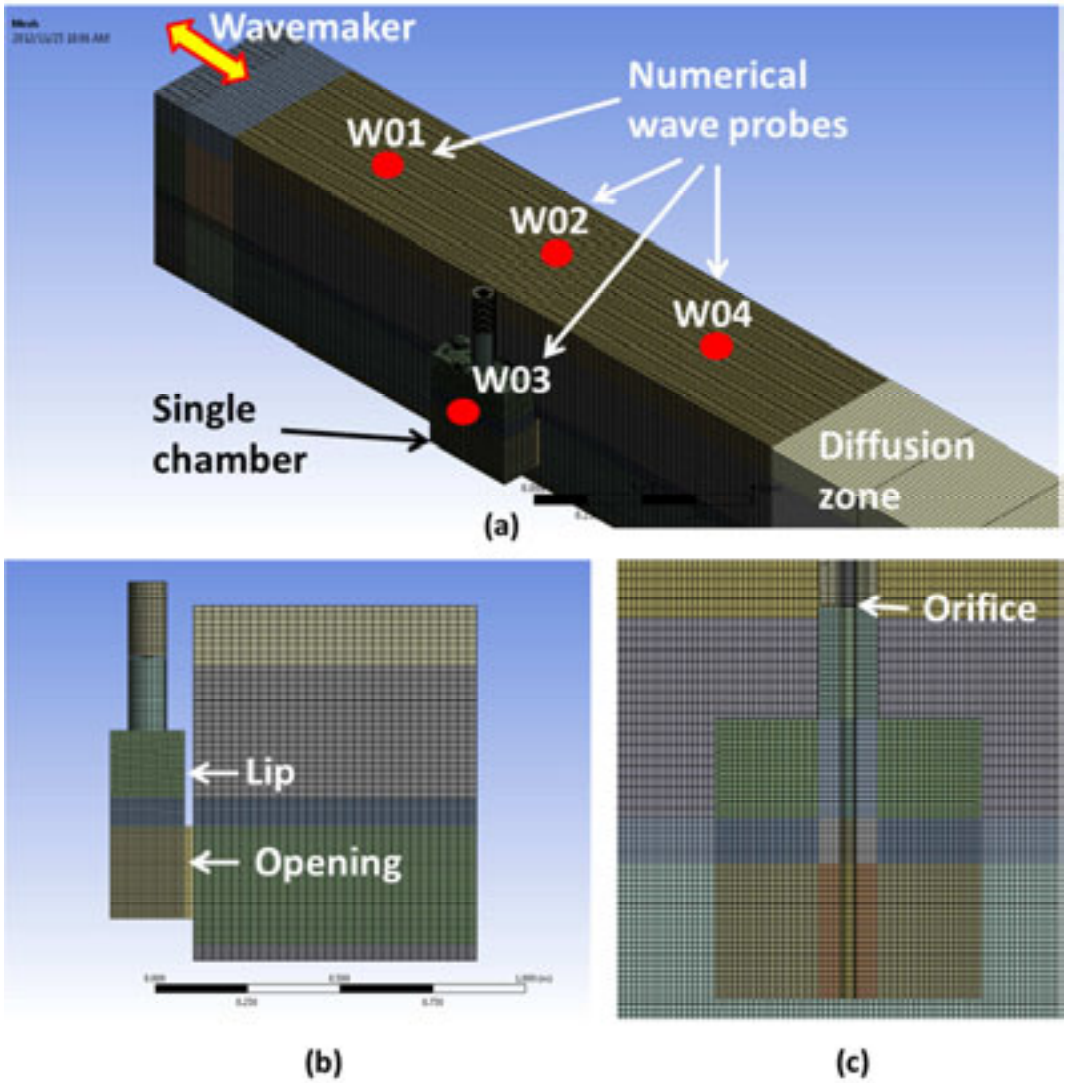

Figure 7-6: (a) Isometric view of 3D NWT, single capture chamber and surface monitors. (b) Side view showing the lip and chamber opening. (c) Cross-sectional view of the chamber mesh and orifice outlet.

7.6.1 Example output

A visual representation of example output from the model is presented. The water level inside the NWT and the resulting airflow velocity through the orifice over a typical wave cycle is shown in Figure 7-9. The model predicted velocities of up to 8 m/s in the chimney outlet due to the flow contraction caused by the orifice.

In order to gain insight into this complex 3D fluid flow problem, the pathline functionality of Fluent was employed. Pathlines are the lines travelled by naturally buoyant particles in equilibrium with the fluid motion released from specified surfaces (refer to (Fluent, 2006)). Studying the pathline of particles released from the opening of the chamber provided valuable information about the flow from the tank into the chamber and vice versa. An example of a pathline plot is shown in Figure 7-7.

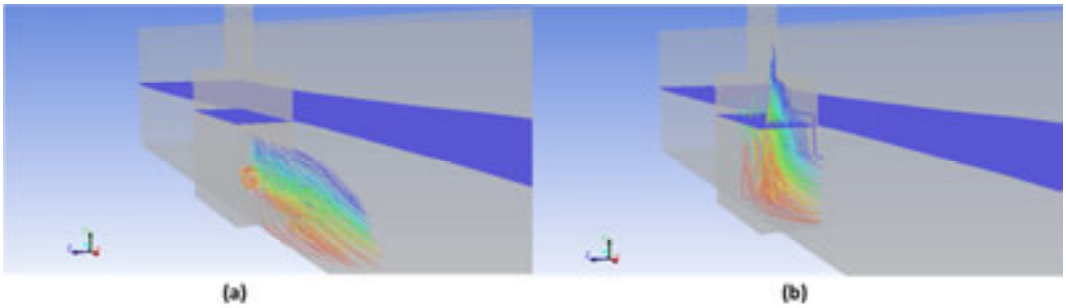

Figure 7-7: Pathlines of water and air particles to and from the chamber opening. (a) From the opening to the NWT. (b) From the air volume to opening.

The additional example output of flow velocity into the chamber presented in Appendix F suggests that a smoother chamber entrance will reduce viscous losses, improving the energy capture of the system. A future extension of this work could include the use of the presented CFD model to optimise the ShoreSWEC's capture chamber geometry.

7.6.2 Initial observations

Initial observations of the numerically generated water level motion inside the chamber mostly matched those of the experimental tests. Monochromatic oscillations were observed for wave periods of 9 s to 11 s and the irregular step motion was present for the higher periods of 12 s and 13 s. There was a clear slosh motion component for the remaining lowest period simulated - 6 s to 8 s. It had a destabilising effect on the propagating waves in the numerical wave tank which was not present in the experiments.

7.6.3 Orifice calibration

The 3D model was used to validate the orifice flow rate calibration equation, as determined in the wind tunnel testing. Figure E-2 shows the volume flow rate over the orifice determined directly by the model and calculated using the calibration equation with the pressure inside the chamber.

7.6.4 Effect of outlet duct

The effect of the outlet duct was investigated by simulating an orifice directly in the chamber roof with the 3D model. It was found that the duct does not significantly influence the pressure inside the chamber. The outlet configuration of the orifice leading into the duct is similar to that of the Helmholtz resonance phenomena (Helmholtz, 1885) where a neck leads into an air cavity. The frequency of resonance is given by:

$$f_H = \frac{v}{2\pi}\sqrt{\frac{A}{V_0 L}}$$

Where, v is the speed of sound in air = 346.1 m/s, $A = \frac{V_n}{L}$, where V_n is the volume of air in the neck, L is the length of the neck and V_0 is the static volume of the cavity. The neck and cavity is equivalent to the orifice and duct respectively.

From the above equation it was found that the Helmholtz resonance period is well below the wave period conditions tested and will therefore not result in misleading pressure readings.

7.6.5 Comparison with experimental results

Test example

Example output from the numerical model in comparison with the experimental results are shown for test condition H = 1 m and T = 11 s in Figure 7-8 and Figure 7-10. Figure 7-8(a) and (b) indicate that the model predicts lower water level elevations inside the tank and the chamber compared to the experiments, for this test condition.

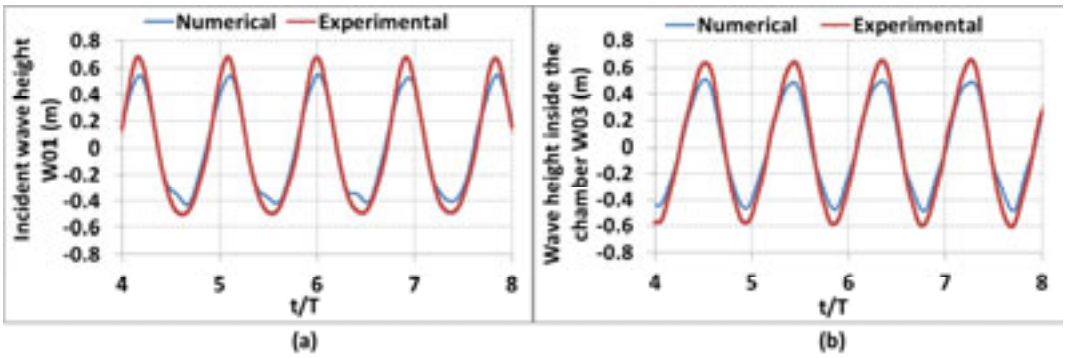

Figure 7-8: Numerical and experimental values of surface elevation: (a) At the incident wave location W01 (b) Inside the chamber W03

The velocity of the water level inside the chamber for the two test methods compare reasonably well as shown in Figure 7-10(a). Figure 7-10(b) shows that the numerically simulated internal chamber pressure was significantly greater than the experiments, nearly double on the inhale cycle. This difference in pressure could be ascribed to erroneous readings of the low pressures (typically 20 Pa at model scale) generated in the physical tests, or to air leakage, although great care was taken to ensure that the Perspex model was well sealed.

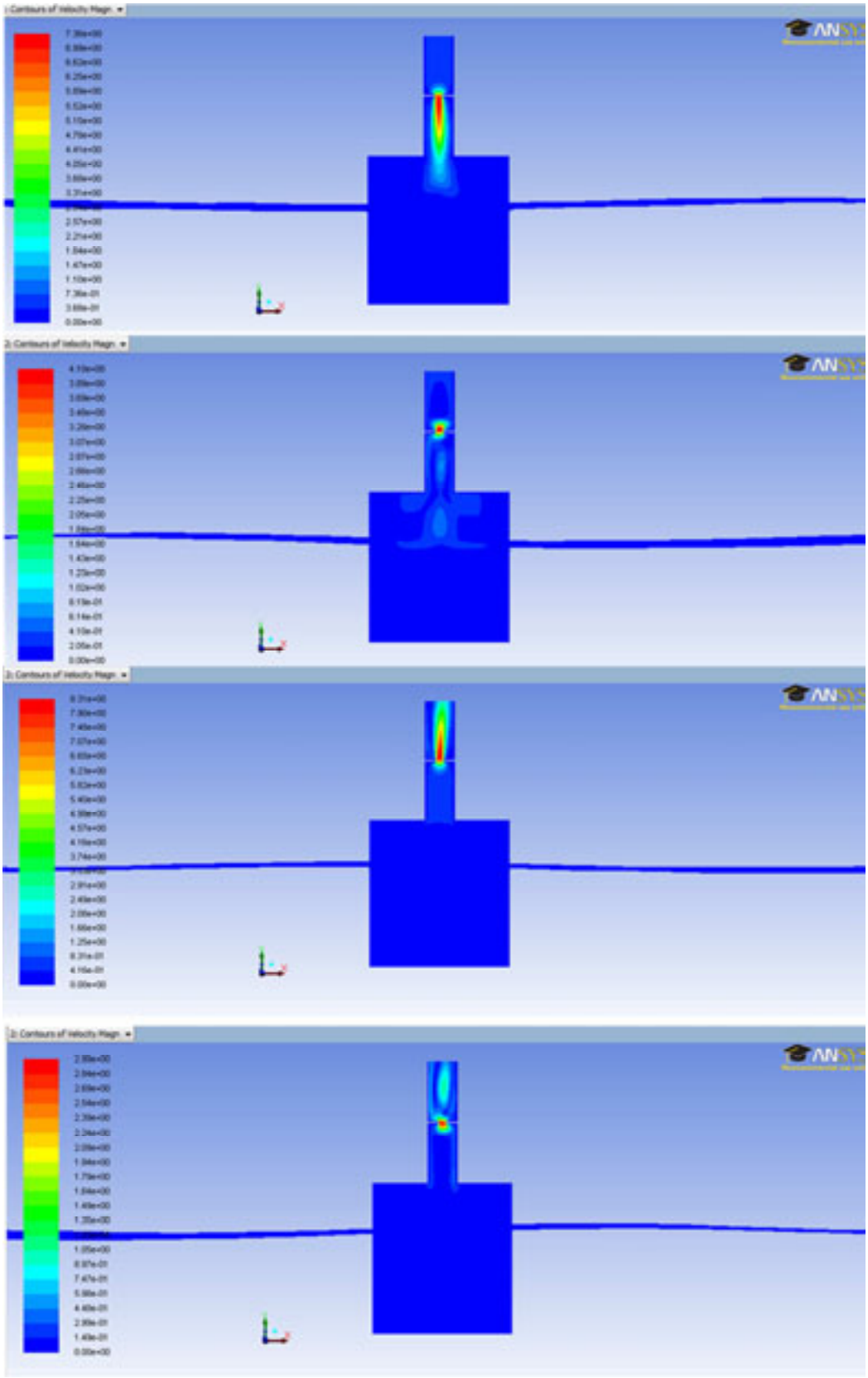

Figure 7-9: Water level inside the 3D model and the resulting airflow velocity through the orifice over a wave cycle for H = 1 m and T = 10 s.

The discrepancy in pressure could also be due to the model's inaccurate representation of the incompressible fluid flow problem, but in general the internal chamber pressure is low therefore compressibility ought to not be a problem. Losses through the model's outlet boundary could also be an inaccurate representation of reality. Additional air volumes were added to the domain at the duct outlet to investigate its effect on the chamber pressure, but did not provide further insights. Losses in the system are approximated by the turbulence model which uses average solutions of the governing equations. Other turbulence models could perhaps have provided a better approximation of the losses, but the one used was the only one that delivered stable solutions. Various domain setups, grid variations and solver settings of the CFD model were investigated in an attempt to identify other possible causes for these discrepancies.

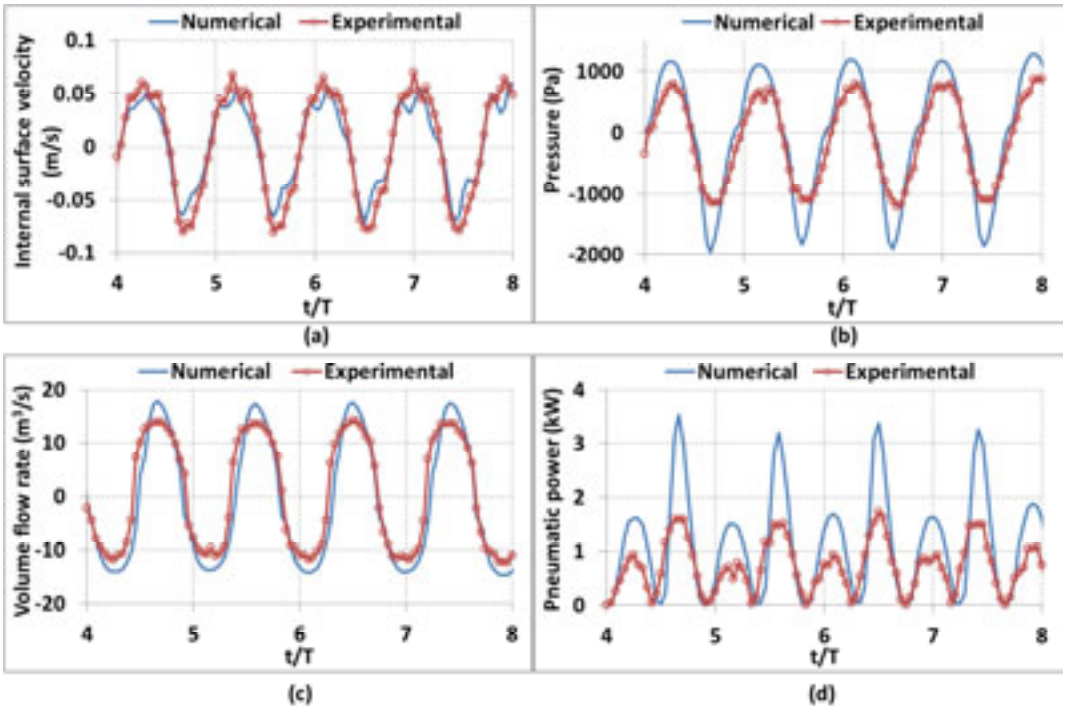

Figure 7-10: Numerical and experimental parameters: (a) Velocity of internal water surface. (b) Pressure inside the chamber. (c) Volume flow rate through the orifice. (d) Generated pneumatic power for test example *H* = 1 m, *T* = 11 s

The higher internal pressure of the model resulted in slightly greater volume flow rate through the orifice and instantaneous pneumatic power as shown in Figure 7-10(c) and Figure 7-10(d). The mean pneumatic absorbed power of the model was 36% greater than that of the experiments.

A summary of all the numerical test results is presented next.

Wave height comparison

The wave heights generated in the numerical and experimental wave tank of 1 m upwave of the model were averaged over five wavelengths are shown in Figure 7-11. The model closely matches experimental wave heights for two conditions and

is of the same order of magnitude for the remaining tests. The difference in wave conditions in the physical and numerical flume could be due to the wave guides which weren't included in the NWT. The water column motion inside the chamber of the model compares well with that of the experiments for half of the conditions tested, as shown in Figure 7-12. The model predicts lower wave heights for the remaining tests. In general it can be concluded that the model provides reasonable predictions of the water level oscillating inside the chamber compared to the physical tests.

The simulated internal chamber pressure was significantly greater than the experimental results over all tests performed, as was shown in the example output of §7.6.5. This directly impacts the numerically determined volume flow rate and overall efficiency of the system.

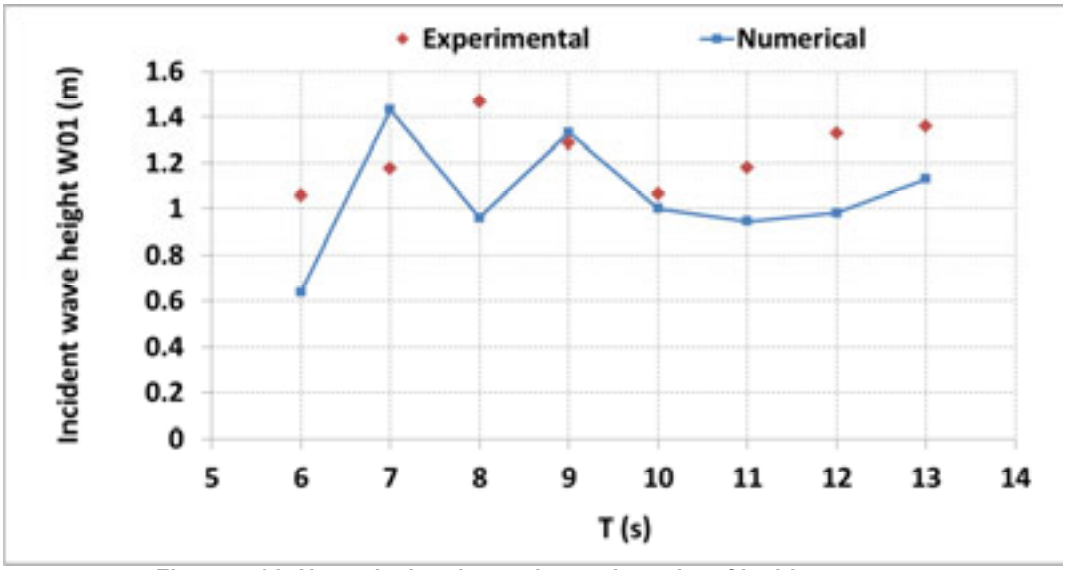

Figure 7-11: Numerical and experimental results of incident waves

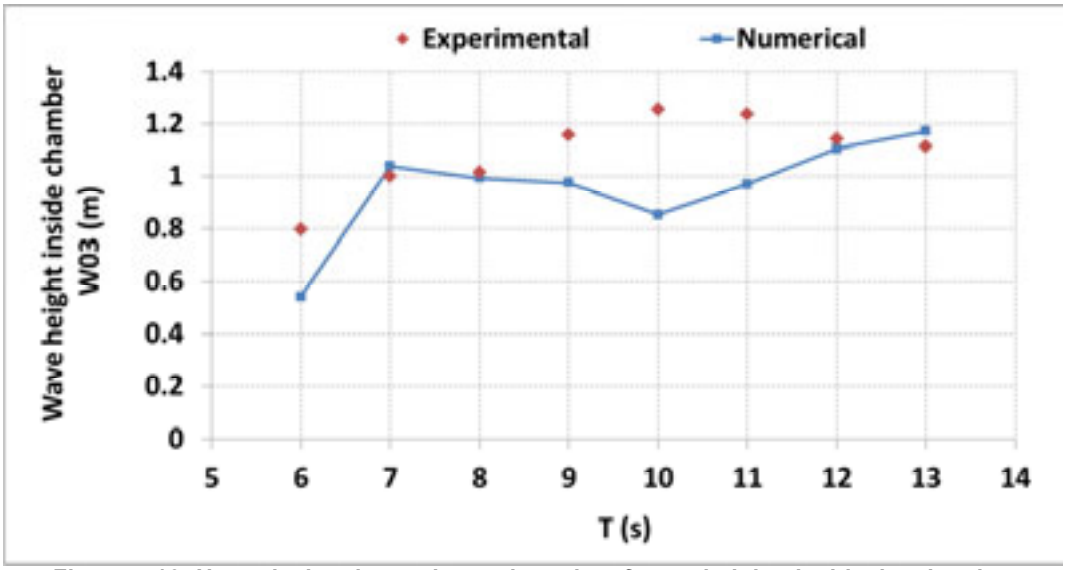

Figure 7-12: Numerical and experimental results of wave heights inside the chamber

Mean absorbed pneumatic power and capture width

The predicted mean absorbed pneumatic power of the model (Figure 7-13) greatly exceeds that of the physical tests over all test conditions especially that of the lowest wave periods due to destabilising slosh motion inside the chamber. The generated wave profiles of these low periods also deviated the furthest from the theoretical input parameters, refer to Figure 7-5.

The overall efficiency of the system, in terms of capture width, is significantly greater for the numerical model compared to the experiments. Similar results were found for the Fluent model of Horko (2007).

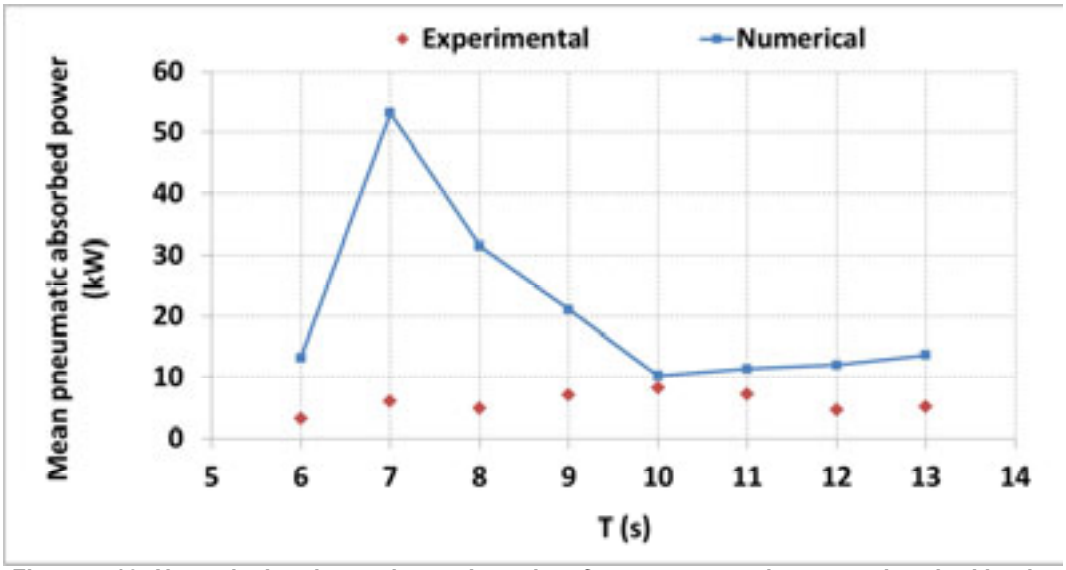

Figure 7-13: Numerical and experimental results of mean pneumatic power absorbed by the chamber

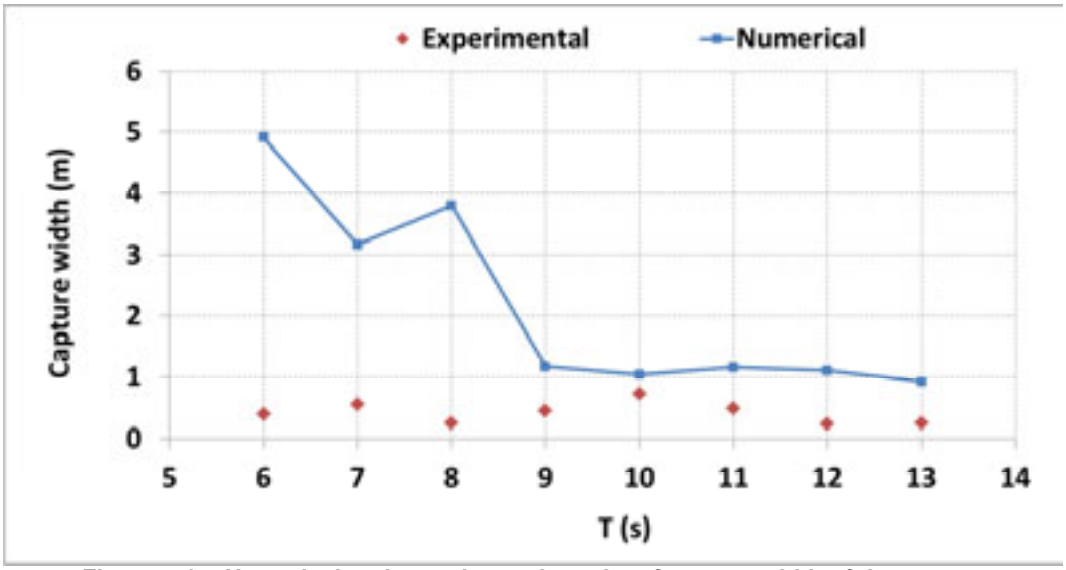

Figure 7-14: Numerical and experimental results of capture width of the system

For comparison purposes, the low period outliers were excluded from the analysis. Only the capture width of the operational periods for Granger Bay of 9 s to 13 s (occurs 83% of the 11 year period) were considered in Figure 7-15. The simulated values of capture width are still significantly greatly than the experimental values, but the general trend is similar, with the exception of the value at 10 s.

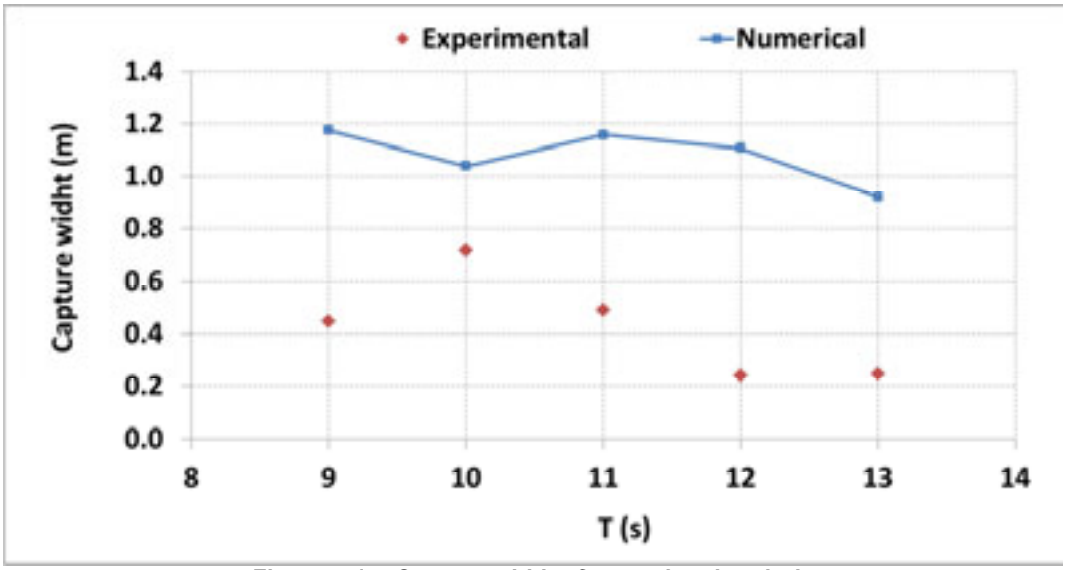

Figure 7-15: Capture width of operational periods

In this analysis it was shown that the 3D numerical model provided a reasonable approximation of the waves inside the wave tank and chamber in comparison to the experimental results. The model however, predicted significantly greater pressures and resulting pneumatic power inside the chamber. Therefore, a relatively poor correlation of overall efficiency was found. Possible reasons for these discrepancies could be ascribed to:

- Faulty readings by the pressure sensor of the low generated pressures.
- Air leakage from the experimental model.
- Inaccurate outlet boundary conditions of the CFD model.
- Incorrect representation of the incompressible fluid flow problem.
- An unsuitable turbulence model.
- Inadequate grid resolution and/or solver settings.

The more conservative experimental values of capture width for the ShoreSWEC were used to estimate its electricity generation potential at Granger Bay.

8 Electricity generation potential of the ShoreSWEC at Granger Bay

One of the main objectives of this study was to determine a minimum (conservative) rough estimate of the ShoreSWEC's electricity generation potential at the selected location in Table Bay. The mean annual average electricity generation potential of the ShoreSWEC at Granger Bay was determined as the product of the available mean annual average wave energy, derived from a wave energy scatter analysis, and the experimental capture width data. All the results presented are based on regular wave conditions. For future work the analysis of device performance under irregular waves is recommended to determine a more realistic estimate of the electricity output potential of the ShoreSWEC.

8.1 Wave energy scatter

A wave energy scatter analysis, as presented by Hagerman and Bedard (2003), was conducted to determine the available mean annual average wave energy at Granger Bay based on the 11 years of hindcast NCEP wave data. A wave energy scatter analysis comprises the following calculation procedure:

- Determination of the frequency of occurrence of all combinations of wave height and period.
- Conversion of occurrence into equivalent hours per year.
- Calculation of the average amount of wave power generated by each combination of wave height and period.
- Determination of the mean annual average wave energy (MWh/m) per year per combination of wave height and period.

The frequency of occurrence of wave height and period at Granger Bay based on 11 years of hindcast wave data is presented in Table 8-1. The most frequently occurring wave heights and periods range from 0 m to 1 m and 9 s to 13 s respectively, as was also presented in the operational wave conditions §4.6.1. The experimental tests conducted comprise 92% of the 11 year data set, refer to yellow highlighted block in Table 8-1.

The frequency of occurrence data was converted to equivalent hours per year and the average wave power generated by each combination of wave height and period was determined. The mean annual average wave energy scatter was then calculated as the product of these two data sets, see Table 8-2.

Table 8-1: Frequency of occurrence of wave height and period at Granger Bay based on 11 years of hindcast wave data

T (s) \ H (m)	0.5	1	1.5	2	2.5	3	3.5	4	Total
3	0%	0%							0%
4	0%	0%							0%
5	1%	0%	0%						1%
6	3%	0%	0%	0%					4%
7	2%	0%	0%	0%	0%				3%
8	2%	1%	0%	0%	0%	0%	0%		3%
9	3%	4%	0%	0%	0%	0%			7%
10	3%	12%	1%	0%	0%	0%	0%		16%
11	2%	20%	3%	0%	0%	0%	0%		26%
12	0%	16%	5%	1%	0%	0%	0%		22%
13	0%	7%	4%	1%	0%	0%	0%	0%	12%
14	0%	2%	2%	1%	0%	0%	0%	0%	4%
15	0%	1%	1%	0%	0%	0%	0%		1%
16	0%	0%	0%	0%	0%	0%			0%
17		0%	0%	0%					0%
18		0%	0%						0%
Total	16%	63%	17%	3%	1%	0%	0%	0%	

Table 8-2: Mean annual wave energy scatter (MWh/m/yr) at Granger Bay

T (s) \ H (m)	0.5	1	1.5	2	2.5	3	3.5	4	Total
3	0.00	0.00	0.00	0.00	0.00	0.00	0.00	0.00	0.00
4	0.00	0.00	0.00	0.00	0.00	0.00	0.00	0.00	0.00
5	0.00	0.02	0.02	0.00	0.00	0.00	0.00	0.00	0.03
6	0.00	0.01	0.08	0.03	0.00	0.00	0.00	0.00	0.12
7	0.00	0.02	0.07	0.12	0.02	0.00	0.00	0.00	0.22
8	0.01	0.05	0.07	0.09	0.17	0.02	0.01	0.00	0.42
9	0.03	0.30	0.18	0.11	0.10	0.14	0.00	0.00	0.85
10	0.04	1.00	0.49	0.13	0.08	0.08	0.04	0.00	1.86
11	0.03	2.19	1.26	0.41	0.13	0.10	0.04	0.00	4.17
12	0.01	2.12	2.00	0.70	0.42	0.22	0.02	0.00	5.49
13	0.00	1.10	1.66	0.79	0.37	0.12	0.03	0.02	4.09
14	0.00	0.31	0.74	0.58	0.18	0.04	0.05	0.06	1.97
15	0.00	0.09	0.28	0.28	0.21	0.07	0.01	0.00	0.94
16	0.00	0.03	0.10	0.10	0.03	0.03	0.00	0.00	0.30
17	0.00	0.00	0.01	0.01	0.00	0.00	0.00	0.00	0.02
18	0.00	0.01	0.00	0.00	0.00	0.00	0.00	0.00	0.01
Total	0.11	7.25	6.96	3.35	1.71	0.83	0.20	0.07	

The most energetic and frequently occurring wave height and period of 1 m and 11 s generate a total mean annual average energy of 7.25 MWh/m (summed over all occurring periods) and 4.17 MWh/m (summed over all occurring wave heights) respectively. The total mean annual average energy available over all the occurring wave periods and heights is 20.5 MWh/m. To determine the mean annual average electrical generation capacity of the ShoreSWEC from this available resource the experimental capture width data was used.

8.2 Electrical generation capacity

The electrical generation capacity of the single, dual and 10 chamber ShoreSWEC device was estimated using the experimental and wave energy scatter data.

8.2.1 Single chamber

All experimental results are based on the pneumatic power captured by the device. In order to determine the electric energy generated conversion efficiency assumptions are required. The pneumatic energy generated inside the chamber will be pumped through the valve and airflow system to the turbine. It is assumed that 5% of the energy will be lost due to pipe bends, wall friction and valves ect. Ackerman (2009) found that the unidirectional turbine and diffuser of the SWEC has an efficiency of 91% for a 2 m wave. The mechanical energy at the turbine shaft is converted into electrical energy at the generator with an assumed efficiency of 91%. The total combined pneumatic-to-electric efficiency is therefore assumed to be 79%.

The capture width of the single chamber ShoreSWEC, based on experimental results, is presented in Table 8-3. The capture width of the system at untested wave conditions, which have a small 8% occurrence over the 11 year period, was linearly and second orderly extrapolated from experimental results.

Table 8-3: Experimental capture width (m) of a single chamber of the ShoreSWEC

T (s) \ H (m)	0.5	1	1.5	2	2.5	3	3.5	4
3	0.66	0.66	0.49	0.42	0.37	0.38	0.28	0.22
4	0.61	0.61	0.48	0.42	0.35	0.34	0.24	0.19
5	0.56	0.56	0.47	0.41	0.34	0.30	0.21	0.17
6	**0.46**	**0.39**	**0.37**	**0.32**	0.27	0.22	0.18	0.13
7	**0.59**	**0.55**	**0.52**	**0.44**	0.40	0.36	0.31	0.26
8	**0.21**	**0.25**	**0.26**	**0.23**	0.16	0.07	0.00	0.00
9	**0.37**	**0.44**	**0.46**	**0.43**	0.35	0.21	0.02	0.00
10	**0.56**	**0.72**	**0.66**	**0.58**	0.34	0.00	0.00	0.00
11	**0.34**	**0.49**	**0.48**	**0.46**	0.31	0.08	0.00	0.00
12	**0.14**	**0.24**	**0.26**	**0.24**	0.18	0.03	0.00	0.00
13	**0.14**	**0.25**	**0.27**	**0.23**	0.20	0.00	0.00	0.00
14	0.14	0.14	0.35	0.33	0.21	0.00	0.00	0.00
15	0.09	0.09	0.34	0.32	0.20	0.00	0.00	0.00
16	0.04	0.04	0.33	0.31	0.19	0.00	0.00	0.00
17	0.00	0.00	0.32	0.30	0.17	0.00	0.00	0.00
18	0.00	0.00	0.30	0.29	0.16	0.00	0.00	0.00

The product of mean annual average wave energy scatter (Table 8-2), capture width (Table 8-3) and the pneumatic-to-electric efficiency is equal to the mean annual average electrical energy, presented in Table 8-4.

The capture width of the single chamber is a maximum at 9 s to 10 s, while the peak energy scatter occurs at 11 s to 13 s. Therefore great gains in electrical output can be achieved if the device performance can be increased at high periods. The total annual electric energy generated by the single chamber ShoreSWEC, calculated through the summation of the values in Table 8-4, was found to be 5.4 MWh. To put this figure into perspective, a 2.77 kW solar water heater system with a gross solar surface area of 4 m^2 deployed in a sunny location of South Africa will have total annual energy saving of approximately 4.5 MWh.

Table 8-4: Mean annual electric energy (MWh/yr) generated by the single chamber ShoreSWEC at Granger Bay

T (s) \ H (m)	0.5	1	1.5	2	2.5	3	3.5	4	Total
3	0.00	0.00	0.00	0.00	0.00	0.00	0.00	0.00	**0.00**
4	0.00	0.00	0.00	0.00	0.00	0.00	0.00	0.00	**0.00**
5	0.00	0.01	0.01	0.00	0.00	0.00	0.00	0.00	**0.01**
6	**0.00**	**0.00**	**0.02**	**0.01**	0.00	0.00	0.00	0.00	**0.03**
7	**0.00**	**0.01**	**0.03**	**0.04**	0.01	0.00	0.00	0.00	**0.08**
8	**0.00**	**0.01**	**0.01**	**0.02**	0.02	0.00	0.00	0.00	**0.06**
9	**0.01**	**0.10**	**0.06**	**0.04**	0.03	0.02	0.00	0.00	**0.26**
10	**0.02**	**0.57**	**0.26**	**0.06**	0.02	0.00	0.00	0.00	**0.93**
11	**0.01**	**0.85**	**0.48**	**0.15**	0.03	0.01	0.00	0.00	**1.52**
12	**0.00**	**0.40**	**0.41**	**0.13**	0.06	0.01	0.00	0.00	**1.01**
13	**0.00**	**0.21**	**0.36**	**0.14**	0.06	0.00	0.00	0.00	**0.78**
14	0.00	0.03	0.21	0.15	0.03	0.00	0.00	0.00	**0.42**
15	0.00	0.01	0.07	0.07	0.03	0.00	0.00	0.00	**0.18**
16	0.00	0.00	0.03	0.02	0.00	0.00	0.00	0.00	**0.06**
17	0.00	0.00	0.00	0.00	0.00	0.00	0.00	0.00	**0.00**
18	0.00	0.00	0.00	0.00	0.00	0.00	0.00	0.00	**0.00**
Total	**0.04**	**2.20**	**1.96**	**0.83**	**0.29**	**0.04**	**0.00**	**0.00**	**5.36**

8.2.2 Dual chamber

The experimental capture width of the dual chamber system, based on experimental results, is presented in Table 8-5. The performance of the system at untested wave conditions was again extrapolated from experimental results.

Table 8-5: Total capture width of the dual chamber system

T (s) \ H (m)	0.5	1	1.5	2	2.5	3	3.5	4
3	1.20	0.81	0.86	0.89	0.88	0.94	0.76	0.71
4	1.13	0.81	0.86	0.88	0.84	0.84	0.68	0.63
5	1.07	0.81	0.86	0.86	0.79	0.75	0.59	0.55
6	**0.99**	**0.79**	0.72	0.63	0.54	0.44	0.35	0.26
7	**0.93**	**0.82**	1.00	0.90	0.81	0.71	0.62	0.52
8	**0.99**	**0.93**	0.51	0.80	0.74	0.65	0.59	0.59
9	**0.58**	**0.60**	0.92	0.86	0.69	0.41	0.03	0.00
10	**0.87**	**0.95**	1.38	1.15	0.68	0.00	0.00	0.00
11	**0.88**	**0.95**	1.01	0.90	0.62	0.16	0.00	0.00
12	**0.56**	**0.76**	0.58	0.53	0.36	0.06	0.00	0.00
13	**0.51**	**0.80**	0.75	0.65	0.40	0.00	0.00	0.00
14	0.50	0.84	0.86	0.74	0.41	0.00	0.00	0.00
15	0.44	0.84	0.86	0.73	0.37	0.00	0.00	0.00
16	0.38	0.85	0.86	0.72	0.33	0.00	0.00	0.00
17	0.32	0.85	0.86	0.70	0.28	0.00	0.00	0.00
18	0.30	0.85	0.86	0.69	0.24	0.00	0.00	0.00

The mean annual electric energy generated by the dual chamber ShoreSWEC is presented in Table 8-6. The system generates a total of 12.1 MWh per year. This is greater than double that of an isolated single chamber due to the increased efficiency at high periods caused by the additional chamber.

Table 8-6: Mean annual electric energy (MWh/yr) generated by the dual chamber ShoreSWEC at Granger Bay

T (s) \ H (m)	0.5	1	1.5	2	2.5	3	3.5	4	Total
3	0.00	0.00	0.00	0.00	0.00	0.00	0.00	0.00	**0.00**
4	0.00	0.00	0.00	0.00	0.00	0.00	0.00	0.00	**0.00**
5	0.00	0.01	0.01	0.00	0.00	0.00	0.00	0.00	**0.02**
6	**0.00**	**0.01**	0.05	0.02	0.00	0.00	0.00	0.00	**0.07**
7	**0.00**	**0.01**	0.05	0.08	0.01	0.00	0.00	0.00	**0.16**
8	**0.01**	**0.04**	0.03	0.06	0.10	0.01	0.00	0.00	**0.24**
9	**0.01**	**0.14**	0.13	0.07	0.05	0.04	0.00	0.00	**0.46**
10	**0.03**	**0.75**	0.54	0.12	0.04	0.00	0.00	0.00	**1.48**
11	**0.02**	**1.65**	1.00	0.29	0.06	0.01	0.00	0.00	**3.04**
12	**0.00**	**1.28**	0.92	0.29	0.12	0.01	0.00	0.00	**2.62**
13	**0.00**	**0.70**	0.98	0.41	0.12	0.00	0.00	0.00	**2.20**
14	0.00	0.21	0.51	0.34	0.06	0.00	0.00	0.00	**1.12**
15	0.00	0.06	0.19	0.16	0.06	0.00	0.00	0.00	**0.47**
16	0.00	0.02	0.07	0.06	0.01	0.00	0.00	0.00	**0.15**
17	0.00	0.00	0.01	0.00	0.00	0.00	0.00	0.00	**0.02**
18	0.00	0.00	0.00	0.00	0.00	0.00	0.00	0.00	**0.01**
Total	**0.07**	**4.88**	**4.48**	**1.91**	**0.64**	**0.08**	**0.00**	**0.00**	**12.1**

8.2.3 Ten chamber device

One of the primary objectives of this study was to determine the generation potential of a full length, 10 chamber ShoreSWEC device at Granger Bay. In the absence of experimental data of the performance of a full length device, it was assumed that its efficiency would be similar to that of the dual chamber system. It was therefore assumed that the full length device will comprise 5 dual chambers with a total capture width as presented in Table 8-7.

Table 8-7: Total capture width of a 10 chamber ShoreSWEC device

T (s) \ H (m)	0.5	1	1.5	2	2.5	3	3.5	4
3	5.98	4.03	4.29	4.45	4.40	4.71	3.82	3.53
4	5.66	4.05	4.29	4.38	4.19	4.22	3.39	3.13
5	5.35	4.06	4.29	4.32	3.97	3.73	2.95	2.73
6	4.96	3.93	3.62	3.15	2.69	2.22	1.75	1.28
7	4.63	4.10	4.98	4.51	4.03	3.55	3.08	2.60
8	4.95	4.63	2.57	4.00	3.71	3.24	2.93	2.95
9	2.90	3.01	4.62	4.31	3.45	2.07	0.16	0.00
10	4.34	4.76	6.91	5.74	3.39	0.00	0.00	0.00
11	4.38	4.76	5.05	4.52	3.10	0.78	0.00	0.00
12	2.78	3.81	2.91	2.65	1.78	0.32	0.00	0.00
13	2.56	4.01	3.73	3.26	2.01	0.00	0.00	0.00
14	2.52	4.20	4.31	3.72	2.06	0.00	0.00	0.00
15	2.21	4.21	4.31	3.66	1.85	0.00	0.00	0.00
16	1.90	4.23	4.31	3.59	1.64	0.00	0.00	0.00
17	1.58	4.24	4.32	3.52	1.42	0.00	0.00	0.00
18	1.51	4.26	4.32	3.46	1.21	0.00	0.00	0.00

The mean annual average electric energy generated by the 10 chamber device is presented in Table 8-8. The full length ShoreSWEC was found to generate 60.3 MWh electrical energy per year, equivalent to the electricity saving of 13 solar water heaters (refer to §8.2.1).

Table 8-8: Mean annual electric energy (MWh/yr) generated by the ten chamber ShoreSWEC at Granger Bay

T (s) / H (m)	0.5	1	1.5	2	2.5	3	3.5	4	Total
3	0.00	0.00	0.00	0.00	0.00	0.00	0.00	0.00	**0.00**
4	0.00	0.01	0.00	0.00	0.00	0.00	0.00	0.00	**0.01**
5	0.00	0.05	0.06	0.00	0.00	0.00	0.00	0.00	**0.11**
6	0.00	0.03	0.23	0.08	0.00	0.00	0.00	0.00	**0.34**
7	0.01	0.05	0.26	0.42	0.06	0.00	0.00	0.00	**0.79**
8	0.03	0.18	0.15	0.28	0.50	0.06	0.02	0.00	**1.19**
9	0.07	0.71	0.65	0.37	0.27	0.22	0.00	0.00	**2.22**
10	0.14	3.77	2.68	0.59	0.22	0.00	0.00	0.00	**7.27**
11	0.09	8.25	5.01	1.47	0.32	0.06	0.00	0.00	**15.12**
12	0.01	6.39	4.59	1.47	0.58	0.06	0.00	0.00	**13.09**
13	0.00	3.48	4.91	2.03	0.59	0.00	0.00	0.00	**11.01**
14	0.00	1.03	2.53	1.72	0.29	0.00	0.00	0.00	**5.58**
15	0.00	0.29	0.94	0.81	0.31	0.00	0.00	0.00	**2.35**
16	0.00	0.11	0.33	0.28	0.04	0.00	0.00	0.00	**0.76**
17	0.00	0.01	0.04	0.02	0.00	0.00	0.00	0.00	**0.08**
18	0.00	0.02	0.01	0.00	0.00	0.00	0.00	0.00	**0.03**
Total	**0.35**	**24.39**	**22.41**	**9.54**	**3.19**	**0.40**	**0.02**	**0.00**	**60.31**

In order to determine the electric power generated by the ShoreSWEC over the 11 year period, the capture width data presented in Table 8-7 was used with an assumed pneumatic-to-electric efficiency of 79%. It was found that the ShoreSWEC will generate 7 kW of electric power on average. In the final design of the device, an optimal turbine generator size must be specified to ensure the most economical design while the system utilises the majority of the available resource. This will however impose a limit on the generation capacity of the system. Using the frequency of occurrence of electric power generated presented in Figure 8-1, a 15 kW system was specified which has a 12% probability of exceedance over the 11 years. In other words, for 12% of 11 years the system will capture a maximum of 15 kW only even though more power is available. The average power generated by the 15 kW system was reduced to 6 kW due to the generation capacity of the turbine generator.

From these results it can be concluded that the generation output of the 10 chamber ShoreSWEC at Granger Bay is low due to the low wave power resource available, but the device will still fulfil its primary function which is to serve as a technology demonstrator of a full scale SWEC device. For future work it is recommended that a full cost analysis of the ShoreSWEC be conducted to determine the cost of electricity of the project and evaluate its overall economic viability.

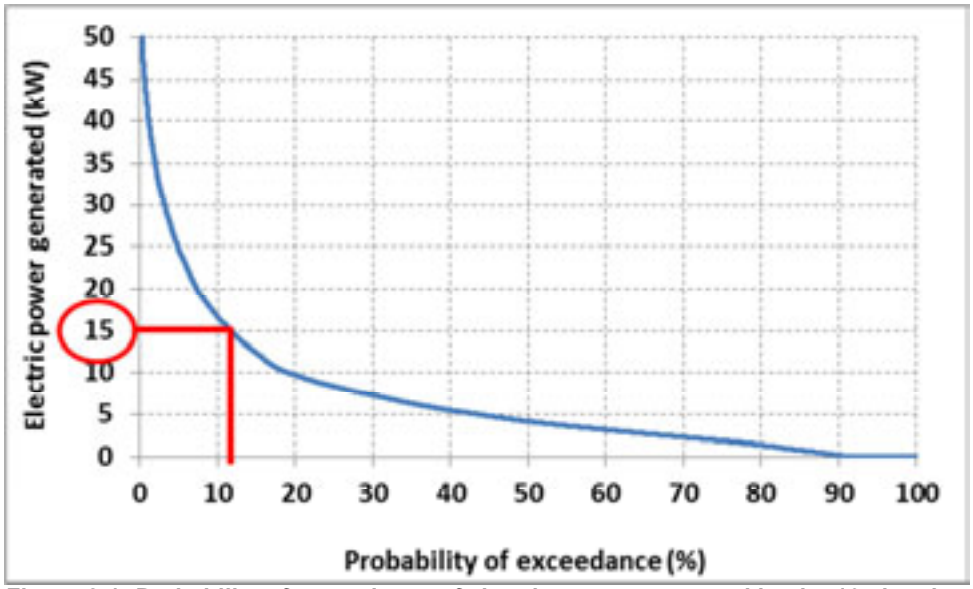

Figure 8-1: Probability of exceedance of electric power generated by the 10 chamber ShoreSWEC device at Granger Bay

9 Conclusions and Recommendations

The main objective of this study was to design, develop and evaluate a novel wave energy converter, called the ShoreSWEC, for a selected location on the South African coast. The study objective was achieved by firstly giving an overview of coastal engineering design manuals and codes required to address the device's role as a vertical breakwater structure. Literature relating to OWC development using numerical and experimental tests was highlighted, then suitable theory to describe the prevailing wave conditions and determine the available wave power resource was presented. Hydrodynamic conversion efficiency equations were presented to evaluate the performance of the device.

Site selection criteria were developed and applied to identify the best location in a South African port. Five locations were identified of which Granger Bay in Table Bay off the southwest coast proved to be the most suitable, mainly due to the orientation of the proposed breakwater structure. The operational wave conditions and available wave power resource were assessed at the site through a numerical wave simulation procedure using SWAN spectral wave model and 11 years of hindcast wave data. The results of this assessment at the head of the proposed wave power breakwater can be summarised as follows:

Table 9-1: Operational conditions at Granger Bay

H_{m0}	T_p	D_p	P_{ave} (annual)	P_{ave} (summer)	P_{ave} (winter)
0 m - 1 m	9 s - 13 s	135º, Northwest	2.3 kW/m	1 kW/m	4 kW/m

Table 9-1 shows the wave heights and resulting wave power resource is fairly low at Granger Bay mainly due to its sheltered location. An interesting finding of the Table Bay resource assessment was the identification of a wave power focal zone south of Robben Island at Whale Rock (refer to Figure 4-15). Although not suitable for the ShoreSWEC this might prove to be an ideal location for other types of WEC devices.

The same numerical wave modeling procedure outlined in Chapter 4 was used to determine design wave conditions for the ShoreSWEC structure at the site (presented in Chapter 5). The design conditions were found to be:

Table 9-2: Design wave conditions at Granger Bay

H_{m0}	H_{max}	T_p	D_p	*Dspr*	Water depth
4.94 m	8.89 m	17 s	135º, Northwest	12º	13.73 m

The stability was assessed under these conditions, with an incline variation on the front wall of the structure, and it was found that different design methods yielded different requirements to resist wave loads. A vertical wall structure in combination with the most conservative design method was finally selected. The single ballast and capture chamber of the ShoreSWEC dimensions of 13.2 m width, 17.9 m length

and 15.1 m height provided sufficient stability under design storm conditions. In order to ensure differential pumping between the chambers, the device was designed to be a total length of 132 m (10 chambers), greater than the typical wavelength. An OWC, orientated to face into the same design wave conditions, would require a 60% wider ballast chamber and 67% more steel-reinforced concrete to remain stable. This will greatly increase the OWC's capital cost in comparison with the ShoreSWEC.

A detailed experimental test program was used to determine the hydrodynamic efficiency of the ShoreSWEC, in terms of capture width, at its most conservative orientation. Some of the main findings and conclusions are:

- The physical model of the ShoreSWEC successfully captured and converted incident wave energy to pneumatic power.
- The system proved to be highly dependent on wave period with peak efficiency at 10 s followed by 7 s, 11 s, 9 s and 6 s. The device performed poorly in high wave periods (12 s and 13 s) due to discontinuous pressure buildup inside the chamber. Conversion efficiency of the device slightly decreased with increasing wave height due to greater viscous losses, but in general proved to be fairly insensitive to wave height.
- Water depth affected performance at certain periods, but on average had an insignificant effect overall. The relatively low tidal variation of South Africa is therefore not expected to adversely impact the performance of the ShoreSWEC.
- A sloped floor increased the efficiency by 12% on average, in comparison with a conventional rectangular chamber. The incline accelerated fluid flowing into the chamber and reduced losses caused by vortices formed in the rear lower corner of the model. The final design of the ShoreSWEC capture chamber at Granger Bay will include a sloped floor due to the greater efficiency it provides at low wave heights.
- The dual chamber ShoreSWEC model outperformed the single chamber system, as it achieved greater efficiency at high wave periods. This suggests that the multi-chamber full scale ShoreSWEC is better suited to the longer period wave regime of South Africa. The accumulated energy captured by the two chambers, expressed in terms of total capture width, was found to be greater than double that of the single chamber, mainly due to the increased efficiency at higher periods.
- A conventional OWC absorbed 72% more mean pneumatic power than the ShoreSWEC model due to the greater amount of kinetic energy captured. The OWC caused significant wave reflection inside the flume and experienced greater wave loading on its structure.

A 3D CFD numerical model of a single chamber ShoreSWEC in a NWT was developed. The model provided comparable water surface elevations inside the flume and chamber, yet predicted significantly higher internal chamber pressures and overall efficiency. This could be due to faulty readings by the pressure sensors in the experimental tests, or air leakage from the Perspex model. The overestimation of internal chamber pressure could also be due to the inability of the CFD code to accurately model this complex fluid flow phenomenon. The model output correlated

well with the experimental results of the orifice calibration and provided valuable insight into the hydrodynamic characteristics of the system through its visual output.

The electricity generation potential of the ShoreSWEC at Granger Bay was determined using the experimental values of capture width and the available wave energy scatter, based on 11 years of hindcast wave data. The mean annual average electric energy generated by a single chamber ShoreSWEC was found to be 5.4 MWh. A dual chamber system with a combined capture width of two chambers generated 12.1 MWh per year. A full length 10 chamber system, with an assumed efficiency similar to that of a dual chamber system, generated 60.3 MWh per year. Based on the generated power of the 10 chamber device a 15 kW turbine generator was specified which would generate 6 kW of electric power on average over the 11 year period.

The ShoreSWEC will have a low electricity generation capacity at Granger Bay due to the low resource available, but will still fulfil its primary function which is to serve as a technology demonstrator of the full scale SWEC device.

Through the completion of this work, the main objective of the study was successfully achieved. Based on the study's findings the following recommendations for future work are suggested.

Future work

The results of this study have highlighted three main areas to consider which are pivotal to the successful development of the ShoreSWEC device:

1. The need to understand the hydrodynamic characteristics of a full length ShoreSWEC device with a minimum of 10 chambers under a variety of wave conditions.
2. Experimental tests must be conducted on a scaled, full length physical model in a 3D wave basin. The wider area of the basin will allow more realistic waves to be generated and the flow of energy along a wave crest can be investigated in detail The performance of the system under real, irregular waves must be assessed.
3. Evaluation of device performance as a function of incident wave direction. Great gains in efficiency are expected for a system orientated at a more acute angle relative to the dominant wave direction.

10 References

Ackerman, P. H. 2009. *Air turbine design study for a wave energy conversion system*. MSc thesis, Stellenbosch University.

Airy, G. B. 1845. Tides and waves. *Encyclopaedia Metropolitana.* London, Scientific Department, 241 – 396.

Allard, R. Rogers, W.E. 2004. *Validation Test Report for the Simulating Waves Nearshore Model (SWAN): Cycle III, Version 40.11*. Technical report for the Naval Research Laboratory of the United States Navy.

Allison, I. Bindoff, N. Bindschadler, R. et al. 2009. *The Copenhagen Diagnosis. Updating the world on the latest climate science*.

Allsop, N. McKenna, J. Vicinanza, D. Wittaker, T. 1996. New design methods for wave impact loading on vertical breakwaters and seawalls. *Proceedings of the 25th International conference on coastal engineering*.

Booij, N. Haagsma, I.J.G. Holthuijsen, L.H. Kieftenburg, A.T.M.M. Ris, R.C. van der Westhuysen, A.J. Zijlema, M. 2009. *SWAN Cycle III version 40.72AB User Manual* Delft University

Brendmo, A. Falnes, J. Lillebekken, P.M. 1996. Linear modelling of oscillating water columns including viscous loss. *Applied Ocean Research* 18: 65 – 75

British Standards Institution. 1991. *BS: 6349-7:1991: Maritime structures – Part 7: Guide to the design and construction of breakwaters*. London, BSI.

Brito-Melo, A. Sarmento, A.J.N.A. Clément, A.H. Delhommeau, G. 1999. A 3D boundary element code for the analysis of OWC wave-power plans. *Proceedings of the 9th International Offshore and Polar Engineering Conference* 188–195.

Carbon Trust. 2005. *Marine Energy Challenge: Oscillating water column wave energy converter evaluation report*.

CEM. 2003. Coastal Engineering Manual. US Army Corps, Appendix A: Glossary of coastal terminology.

CEM. 2006a. Coastal Engineering Manual. US Army Corps, Part II Chapter 1: Water wave mechanics.

CEM. 2006b. Coastal Engineering Manual. US Army Corps, Part VI Chapter 4: Materials and construction aspects.

CEM. 2006c. Coastal Engineering Manual. US Army Corps, Part VI Chapter 5: Fundamentals of Design.

CEM. 2006d. Coastal Engineering Manual. US Army Corps, Part VI Chapter 7: Example problems.

Clément, A. H. 1997. Dynamic Nonlinear Response of OWC Wave Energy Devices. *International Journal of Offshore and Polar Engineering*. 7.2. 91 - 96.

Cornett, A. M. 2008. A global wave energy resource assessment. *International Offshore and Polar Engineering Conference* paper number 579

Couch, A.T. and Conte, J.P. 1997. Field Verification of Linear and Non-Linear Hybrid Wave Models for Offshore Tower Response Prediction. *Journal of Offshore Mechanics and Arctic Engineering* 119: 158-165.

Cruz, J. 2008. *Ocean wave energy: Current status and future perspectives*. Bristol: Springer.

Curran, R. Stewart, T.P. and Whittaker, T.J.T. 1997. Design synthesis of oscillating water column wave energy converters: performance matching. *Proceedings of the Institution of Mechanical Engineers, Part A: Journal of Power and Energy* 211: 489 – 505.

Dean, R. G. and Dalrymple, R. A. 1991. *Water Wave Mechanics for Engineers and Scientists*, New Jersey: World Scientific Publishing Company.

Department of Energy, 2011. Integrated Resource Plan for electricity 2010 - 2030

Evans, D. V. 1978. The oscillating water column wave-energy device. *Journal of the Institute of Mathematics and its Application* 22: 423 – 433.

Evans, D.V. 1982. Wave-power absorption by systems of oscillating surface pressure distributions. *Journal of Fluid Mechanics* 114: 481 – 499.

Evans, D.V. Porter R. 1995. Hydrodynamic characteristics of an oscillating water column device. *Applied Ocean Research* 17: 155 – 164

Falcão, J. and Sarmento, A.J.N.A. 1980. Wave generation by a periodic surface pressure and its application in wave-energy extraction. *15th International Congress of Theoretical Applied Mechanics*, Toronto.

FLUENT Incorporated. 2006. Fluent 6.3 User's Guide. User manual for Fluent 6.3

Folley, M. Whittaker, T.J. 2002. Identification of non-linear flow characteristics of the LIMPET shoreline OWC. *International Society of Offshore and Polar Engineering Conference* 12: 541 - 546.

Geustyn, L. 1983. *Seegolfenergie langs die Suid-Afrikaanse kus: 'n Evaluasie van die tyd en ruimtelike verspreiding*. M.Sc thesis, Stellenbosch University. (in Afrikaans).

Goda, Y. 1974. New wave pressure formulae for composite breakwaters.

Proceedings of the 14th International Coastal Engineering Conference 3: 1702-1720.

Goda, Y. 1985. *Random seas and maritime structures*. University of Tokyo Press, Tokyo.

Hagerman, G. Bedard, R. 2003. *E2I EPRI specifications: Guidelines for preliminary estimation of power production by offshore wave energy conversion devices*.

Heath, T.V. 2011. A review of oscillating water columns. *Philosophical Transaction of the Royal Society A* 370: 235–245.

Helmholtz, H. V. 1885. *On the sensations of tone as a physiological basis for the theory of music.* 2nd English Edition, translated by Alexander J. Ellis. London: Longmans, Green, and Co., p. 44. Retrieved 2010-10-12

Hirt, C. W. Nichols, B. D. 1981. Volume of fluid (VOF) methods for the dynamics of free boundaries, *Journal of Computational Physics* 39: 201–225.

Holthuijsen L.H. 2007. *Waves in oceanic and coastal waters.* New York: Cambridge University Press.

Horko, M. 2007. *CFD optimisation of an oscillating water column wave energy converter*. MSc thesis. University of Western Australia.

International Energy Agency, 2011. Key world energy statistics

Jin, J. Liu, Z. Hyun, B.-S. Hong, K. 2012. Effects of wave direction on performance of oscillating water column type wave energy convertor. *22nd International offshore and polar engineering conference* 582 – 587.

Joubert, J.R. Van Niekerk, J. L. 2009. Recent developments in wave energy along the coast of southern Africa. *European wave and tidal energy conference*.

Joubert, J.R. 2008. *An investigation of the wave energy resource on the South African coast, focusing on the spatial distribution of the southwest coast.* MSc thesis, Stellenbosch University.

Lee, C.-H., Newman, J.N. and Nielsen, F.G. 1996. Wave Interactions with an Oscillating Water Column. Proceedings of the 6th *International Offshore and Polar Engineering Conference* 1: 82-90.

Liu, Z. Hyun, B.-S. Shi, H. and Hong K. 2010a. Practical simulation of oscillating water column chamber for energy conversion. *International journal of green energy* 7: 337 – 346.

Liu, Z. Hyun, B.-S. Shi, H. and Hong K. 2010b. Effects of wave focusing device on performance of OWC chamber. *Journal of the Korean Society for Marine Environmental Engineering* 13.1: 12 – 17.

Liu, Z. Hyun, B.-S. Shi, H. and Hong K. 2011. Numerical study of air chamber for oscillating water column wave energy converter. *China ocean engineering society*. 25.1: 169 – 178.

Martins-Rivas, H. Mei, C.C. 2009. Wave power extraction from an oscillating water column at the tip of a breakwater. *Journal of Fluid Mechanics*. 626: 395 - 414

McCormick, M. E. 1981. *Ocean wave energy conversion*. New York: John Wiley and Son.

Mørk, G. Barstow, S. Kabuth A. Pontes M.T. 2010. Assessing the global wave energy potential. *29th International Conference on Ocean, Offshore Mechanics and Artic Engineering.*

NCEP Internet services team. 2007. *About NCEP*. [Online]. Available: www.ncep.noaa.gov/about/. [2012, November 12].

Neumann, F. Sarmento, A.J.N.A. 2001. OWC-Caisson economy and its dependency on breaking wave design loads. *11th International Offshore and Polar Engineering Conference*. 1: 561 – 566

NOAA: Marine Modeling and Analysis branch. 2012. *WAVEWATCH III® Model*. [Online]. Available: http://polar.ncep.noaa.gov/waves/wavewatch/wavewatch.shtml. [2012, November 12].

Patterson, C. Dunsire, R. Hillier, S. 2009. Development of wave energy breakwater at Siadar, Isle of Lewis. *Proceedings of the Coasts, Marine Structures and Breakwaters Conference*. Edinburgh, Scotland.

PRDW (PTY) LTD. 2010. *City of Cape Town: Climate change think tank. Marine/freshwater theme. Marine inputs to Salt River Flood model*. Study results presented by Stephan Luger at Setback lines coastal engineering conference 2010 hosted by Stellenbosch University.

Price, A.A.E. Dent, C.J. Wallace, A.R. 2009. On the capture of wave energy converters. *Applied ocean research* 31. 251 – 259.

Raghunathan, S. Tan, C. P. 1982. Aerodynamic Performance of the Wells Air Turbine. *Journal of Energy* 7. 226-236.

Retief, G. de F. 2007. Wave power seminar. *Ocean energy South Africa*. 8 June. [Presentation]. Cape Town.

Retief, G. de F. Prestedge, G.K. Müller, F.P.J. 1982. A proposal for wave energy conversion near Cape Town. *International Conference on Coastal Engineering.* 1: 245 – 260

Rossouw, C. 2008. Ocean energy workshop. *Permitting and EIA's for wave energy projects*. 11 March. [Presentation]. Stellenbosch.

Rossouw, J. 1989. *Design waves for the South African coastline*. PhD dissertation, Stellenbosch University.

Rossouw, M. Luger, S. Kuipers, J. Patel, S. 2005. Development of a virtual buoy system for the Port of Cape Town, South Africa. *5th International Symposium on Ocean Wave Measurement and Analysis.*

Sarmento, A. J. N. A. 1992. Wave flume experiments on two-dimensional oscillating water column wave energy devices. *Experiments in fluids* 12: 286 – 292.

Sarmento, A. J. N. A. 1993. Model-test optimization of an OWC wave power plant. International journal of offshore and polar engineering 3.1: 66 – 72.

Setoguchi, T. Takao, M. 2006. Current status of self-rectifying air turbines for wave energy conversion. *Energy conversion and management* 47: 2382 – 2396.

Smith, C.M. Pearce, C. Millar D. L. 2012. Further analysis of change in nearshore wave climate due to an offshore wave farm: An enhanced case study for the Wave Hub site. *Renewable Energy* 40:51 – 64.

Stokes, G. G. 1847. On the Theory of Oscillatory Waves. *Trans. Camb. Phil. Soc.*, 8: 441 - 455.

Sustainable Energy Africa (SEA) and Renewable Energy and Energy Efficiency Partnership (REEP). 2009. *How to implement renewable energy and energy efficiency options: Support for South African local government*.

Takahashi, S. 1989. Hydrodynamic characteristics of wave-power-extracting caisson breakwater. *21st International Coastal Engineering Conference.* 1 – 3: 2489 – 2501

Takahashi, S. Tanimoto, K. and Shimosako, K. 1990. Wave and Block Forces on a Caisson Covered With Wave Dissipating Blocks. Report of Port and Harbour Research Institute, Yokosuka, Japan, 30.4: 3-34 (in Japanese).

Takahashi, S. and Hosoyamada, S. 1994. Hydrodynamic characteristics of sloping top caissons. *Proceedings of International Conference on Hydro-Technical Engineering for Port and Harbour Construction,* Port and Harbour Research Institute, Japan, 1: 733-746.

Takahashi, S. Nakada, H. Ohneda H. 1992. Wave power conversion by a prototype wave power extracting caisson Sakata Port. *Coastal Engineering*: 3440 - 3453

Takao, M. Setoguchi, T. Kinoue Y. et al. 2006. Improvement of Wells turbine performance by means of end plate. *16th International Offshore and Polar Engineering Conference*.

Tanimoto, T. Yagyu, T. and Goda, Y. 1982. Irregular Wave Tests for Composite Breakwater Foundations. *Proceedings of the 18th International Coastal Engineering Conference, American Society of Civil Engineers* 3: 2144-2163.

Thakker, A. Dhanasekaran, T. S. Takao M. and Setoguchi, T. 2003. Effects of compressibility on the performance of a wave-energy conversion device with an impulse turbine using a numerical simulation technique. *International Journal of Rotating Machinery* 9: 443 – 450.

Thiruvenkatasamy, K. Neelamani, S. 1997. On the efficiency of wave energy caissons in array. *Applied ocean research* 19: 61 – 72.

Tindall, C.E. Xu, M. 1996. Optimising a Well's-turbine-type wave energy system. *IEEE Transactions on Energy Conversion* 11.3: 631 – 635.

Torre-Enciso, Y. Ortubia, I. López de Aguileta, L.I. and Marqués, J. 2007. Mutriku wave power plant: from the thinking out to the reality. *Proceedings of the European Wave and Tidal Energy Conference*.

Van Niekerk, J.L. Retief, G. d. F. 2010. Wave energy converter. Patent IB2009/007682.

Wavegen, 2002, *Islay LIMPET monitoring final report*. Technical report for DTI Sustainable Energy Programmes.

Wilcox, D. C. 1998. *Turbulence Modeling for CFD*. DCW Industries, Inc., La Canada, California.

Youngs, D. L. 1982. Time-dependent multi-material flow with large fluid distortion, *Numerical Methods for Fluid Dynamics*, Academic Press, New York, 273–285.

Appendix A: Site selection

The 25 sites considered in the site selection procedure are presented in Table A-1.

Table A-1: Sites evaluated in selection procedure

Site	Comments	Rating
Port Nolloth 29°15'50"S 16°52'5.4"E	Incorrectly orientated breakwater.	**C**
Lamberts Bay 32°5'9"S 18°18'17"E	Sheltered location due to Bird Island.	**C**
Elands Bay 32°18'59"S 18°19'12"E	Perfectly orientated point, but no breakwater infrastructure.	**C**
Port Owen 32°46'5"S 18°8'36"E	Breakwater sheltered by Cape Columbine and potential sedimentation impacts at Berg River mouth.	**C**
Sandy Point 32°44'30"S 18°1'14"E	Well orientated breakwater, but sheltered due to Cape Columbine.	**B**
Saldanha 33°2'50.31"S 17°58'9.29"E	Correctly orientated jetty and artificial beach with ShoreSWEC retrofitting potential and good resource.	**A**
Yzerfontein 33°20'42"S 18°8'55"E	Short, incorrectly orientated breakwater, but significant resource available.	**C**
Koeberg 33°40'43.1"S 18°25'31.1"E	Correctly orientated long, rubble breakwater and good resource.	**A**
Granger Bay 33°53'56.95"S 18°24'54.58"E	Planned development that would require perfectly orientated caisson breakwater.	**A**
Hout Bay 34°3'5"S 18°21'1"E	Well orientated concrete block breakwater.	**B**
Simons Town 34°11'5"S 18°26'16"E	Sheltered location in False Bay	**C**
Kalk Bay 34°7'42"S 18°27'5"E	Sheltered location in False Bay	**C**
Gordons Bay 34° 9'48.09"S 18°51'30.42"E	Sheltered location in False Bay	**C**
Hermanus 34°26'0.48"S 19°13'40.46"E	Correctly orientated breakwater with good resource.	**A**
Gans Bay 34°35'7"S 19°20'25"E	Incorrectly orientated breakwater.	**C**
Mossel Bay 34°10'30"S 22°8'48"E	Breakwater of armour units in shallow water location.	**B**
Port St Francis 34°10'59"S 24°51'8"E	A short, well orientated breakwater.	**B**

Port Elizabeth 33°57'18"S 25°38'20"E	Correctly orientated quay wall of container terminal, but very sheltered location.	**B**
Port of Ngqura 33°49'5.78"S 25°41'37.01"E	Correctly orientated composite vertical breakwater.	**A**
East London 33°1'41"S 27°55'30"E	Shallower water location and potential impact on sedimentation.	**B**

Appendix B: Wave conditions in Table Bay

The frequency of occurrence of combinations of wave height, period and direction for NCEP data at 34S 17.4ºE is presented in Table B-1, Table B-2 and Table B-3.

Table B-1: Frequency of occurrence of concurrent wave height and wave period

Hm0 (m)		Peak wave period (s)																	
>=	<	3	4	5	6	7	8	9	10	11	12	13	14	15	16	17	18	19	Total
0.5	1.0			0			0	0	0										0
1.0	1.5		0	0	0	0	0	0	0	0	0	0	0	0	0				1
1.5	2.0	0	0	0	0	0	1	2	3	2	1	0	0	0	0	0	0		9
2.0	2.5		0	1	1	0	1	2	**5**	**6**	3	1	0	0	0	0	0		21
2.5	3.0			0	2	1	1	1	4	**7**	**6**	2	0	0	0	0	0		24
3.0	3.5			0	1	1	0	1	2	**5**	**5**	3	1	0	0	0	0		18
3.5	4.0				0	0	0	0	1	2	3	2	1	0	0	0	0		11
4.0	4.5				0	0	0	0	1	1	2	2	1	0	0	0			7
4.5	5.0					0	0	0	0	1	1	1	0	0	0	0			4
5.0	5.5					0	0	0	0	0	1	1	0	0	0				2
5.5	6.0							0	0	0	0	0	0	0	0	0			1
6.0	6.5						0		0	0	0	0	0	0	0				1
6.5	7.0								0	0	0	0	0	0	0				0
7.0	7.5									0	0	0	0	0	0				0
7.5	8.0									0	0	0	0	0	0				0
8.0	8.5										0	0	0	0					0
8.5	9.0												0	0					0
9.0	9.5											0		0					0
9.5	10.0													0					0
10.0	10.5											0		0					0
10.5	11.0												0						0
		0	0	1	4	3	3	7	16	26	22	12	4	1	0	0	0	0	

Table B-2: Frequency of occurrence of concurrent wave height and wave direction

Hm0 (m)		Peak wave direction (s)																
>=	<	0	22.5	45	67.5	90	112.5	135	157.5	180	202.5	225	247.5	270	292.5	315	337.5	Total
0.5	1.0						0	0		0	0	0	0					0
1.0	1.5	0					0	0	0	0	0	0	0	0	0	0		1
1.5	2.0	0					0	0	0	1	1	**5**	2	0	0	0	0	9
2.0	2.5	0	0				0	1	1	1	2	**12**	3	0	0	0	0	21
2.5	3.0	0					0	1	1	1	3	**14**	4	0	0	0	0	24
3.0	3.5	0					0	1	1	0	3	**11**	3	0	0	0	0	18
3.5	4.0							0	0	0	1	**7**	2	0	0	0	0	11
4.0	4.5	0						0	0	0	1	4	1	0	0	0	0	7
4.5	5.0								0	0	0	2	1	0	0	0	0	4
5.0	5.5								0	0	0	1	1	0	0	0	0	2
5.5	6.0									0	0	1	0	0	0	0		1
6.0	6.5										0	0	0	0		0		1
6.5	7.0										0	0	0	0				0
7.0	7.5										0	0	0	0				0
7.5	8.0										0	0	0	0				0
8.0	8.5											0	0	0				0
8.5	9.0											0						0
9.0	9.5											0	0					0
9.5	10.0											0						0
10.0	10.5											0	0					0
10.5	11.0											0	0					0
		0	0	0	0	0	0	3	4	3	12	58	17	1	1	1	0	

Table B-3: Frequency of occurrence of concurrent wave direction and wave period

	Peak wave period (s)																	
Dp	**3**	**4**	**5**	**6**	**7**	**8**	**9**	**10**	**11**	**12**	**13**	**14**	**15**	**16**	**17**	**18**	**19**	**Total**
0		0	0	0														**0**
22.5			0															**0**
45																		**0**
67.5																		**0**
90																		**0**
112.5			0	0	0	0	0	0			0							**0**
135			0	1	1	1	0	0	0	0	0	0						**3**
157.5	0	0	0	2	1	0	0	0	0	0	0							**4**
180		0	0	0	0	0	1	1	0	0	0	0						**3**
202.5			0	0	0	0	2	2	3	3	1	1	0	0	0	0		**12**
225			0	0	0	1	3	**10**	**18**	**15**	**8**	3	1	0	0	0		**58**
247.5		0	0	0	0	0	1	3	4	4	2	1	0	0	0	0		**17**
270		0	0	0	0	0	0	0	0	0	0	0						**1**
292.5	0	0	0	0	0	0	0	0			0	0						**1**
315	0	0	0	0	0	0	0						0	0				**1**
337.5		0	0	0	0	0	0											**0**
	0	**0**	**1**	**4**	**3**	**3**	**7**	**16**	**26**	**22**	**12**	**4**	**1**	**0**	**0**	**0**	**0**	

The average wave height per combination of wave period and direction is presented in Table B-4.

Table B-4: Average wave height for each combination of wave period and wave direction

	Peak wave period (s)																
Dp	**3**	**4**	**5**	**6**	**7**	**8**	**9**	**10**	**11**	**12**	**13**	**14**	**15**	**16**	**17**	**18**	**19**
0	1.00	1.24	1.98	2.74	1.00	1.00	1.00	1.00	1.00	1.00	1.00	1.00	1.00	1.00	1.00	1.00	1.00
22.5	1.00	1.00	2.04	1.00	1.00	1.00	1.00	1.00	1.00	1.00	1.00	1.00	1.00	1.00	1.00	1.00	1.00
45	1.00	1.00	1.00	1.00	1.00	1.00	1.00	1.00	1.00	1.00	1.00	1.00	1.00	1.00	1.00	1.00	1.00
67.5	1.00	1.00	1.00	1.00	1.00	1.00	1.00	1.00	1.00	1.00	1.00	1.00	1.00	1.00	1.00	1.00	1.00
90	1.00	1.00	1.00	1.00	1.00	1.00	1.00	1.00	1.00	1.00	1.00	1.00	1.00	1.00	1.00	1.00	1.00
112.5	1.00	1.00	0.99	1.69	1.56	1.87	1.69	2.03	1.00	1.00	1.86	1.00	1.00	1.00	1.00	1.00	1.00
135	1.00	1.00	2.01	2.28	2.58	2.57	2.42	1.88	2.16	2.10	2.25	2.13	1.00	1.00	1.00	1.00	1.00
157.5	1.27	1.51	1.91	2.52	2.95	2.78	2.37	2.01	2.40	2.52	2.65	1.00	1.00	1.00	1.00	1.00	1.00
180	1.00	1.47	1.88	2.32	2.27	2.00	2.28	2.67	3.23	3.36	1.88	4.37	1.00	1.00	1.00	1.00	1.00
202.5	1.00	1.00	1.33	2.19	2.18	2.09	2.22	2.47	2.76	3.21	3.46	3.94	4.09	3.68	3.24	2.47	1.00
225	1.00	1.00	1.43	1.65	1.89	2.12	2.10	2.34	2.65	3.03	3.42	3.93	4.07	3.93	3.43	2.69	1.00
247.5	1.00	1.94	1.13	1.75	2.12	2.52	2.32	2.41	2.69	3.16	3.54	3.72	4.02	3.48	2.76	2.44	1.00
270	1.00	1.18	1.55	2.29	2.77	3.25	2.84	3.60	3.82	3.51	3.92	5.99	1.00	1.00	1.00	1.00	1.00
292.5	1.39	1.47	1.82	2.41	3.19	3.68	4.23	4.69	1.00	1.00	1.07	1.12	1.00	1.00	1.00	1.00	1.00
315	1.43	1.58	1.97	2.86	3.46	4.34	5.11	1.00	1.00	1.00	1.00	1.00	1.52	1.05	1.00	1.00	1.00
337.5	1.00	1.70	2.04	2.93	3.42	4.36	4.04	1.00	1.00	1.00	1.00	1.00	1.00	1.00	1.00	1.00	1.00

The γ and m-values used in the SWAN simulations based on measured data are presented in Table B-5 and Table B-6.

Table B-5: γ-values for each combination of wave period and wave direction

	Peak wave period (s)																
Dp	**3**	**4**	**5**	**6**	**7**	**8**	**9**	**10**	**11**	**12**	**13**	**14**	**15**	**16**	**17**	**18**	**19**
0	4.0	3.5	2.8	2.1	2.4	2.0	1.5	1.1	1.0	1.0	1.0	1.0	1.0	1.0	1.0	1.0	1.0
22.5	1.6	1.6	1.6	1.5	1.5	1.4	1.4	1.3	1.3	1.3	1.2	1.2	1.1	1.1	1.1	1.0	1.0
45	1.6	1.6	1.5	1.5	1.5	1.4	1.4	1.3	1.3	1.3	1.2	1.2	1.1	1.1	1.1	1.0	1.0
67.5	1.6	1.6	1.5	1.5	1.5	1.4	1.4	1.3	1.3	1.3	1.2	1.2	1.1	1.1	1.1	1.0	1.0
90	1.6	1.6	1.5	1.5	1.5	1.4	1.4	1.3	1.3	1.3	1.2	1.2	1.1	1.1	1.1	1.0	1.0
112.5	1.6	1.6	1.5	1.6	1.5	1.5	1.4	1.4	1.3	1.3	1.3	1.2	1.1	1.1	1.1	1.0	1.0
135	1.6	1.6	1.6	1.6	1.6	1.6	1.5	1.4	1.4	1.4	1.3	1.3	1.1	1.1	1.1	1.0	1.0
157.5	1.6	1.6	1.6	1.6	1.6	1.6	1.5	1.4	1.4	1.4	1.4	1.2	1.1	1.1	1.1	1.0	1.0
180	1.4	1.5	1.5	1.6	1.6	1.6	1.6	1.7	1.7	1.8	1.7	1.9	1.6	1.6	1.7	1.7	1.7
202.5	1.5	1.5	1.6	1.8	1.8	1.8	1.9	2.0	2.1	2.2	2.2	2.3	2.4	2.4	2.4	2.4	2.4
225	1.8	1.9	1.9	2.0	2.1	2.1	2.2	2.2	2.3	2.4	2.4	2.5	2.6	2.6	2.6	2.7	2.7
247.5	2.0	2.1	2.1	2.1	2.2	2.2	2.2	2.3	2.3	2.4	2.4	2.4	2.5	2.5	2.5	2.5	2.5
270	1.8	1.9	1.9	2.0	2.0	2.1	2.1	2.2	2.2	2.2	2.2	2.4	2.0	2.0	2.0	2.0	2.0
292.5	1.0	1.2	1.3	1.5	1.8	2.0	2.2	2.4	2.1	2.3	2.4	2.6	2.7	2.9	3.0	3.2	3.2
315	1.7	1.8	1.9	2.1	2.3	2.5	2.6	2.1	2.2	2.3	2.3	2.4	2.6	2.6	2.6	2.7	2.7
337.5	4.0	3.3	2.8	2.0	1.4	1.0	1.0	1.1	1.0	1.0	1.0	1.0	1.0	1.0	1.0	1.0	1.0

The directional distribution function is $\cos^m(\theta - \theta_{peak})$ and was therefore prescribed in terms of the power *m*.

Table B-6: *m*-values for each combination of wave period and wave direction

	Peak wave period (s)																
Dp	3	4	5	6	7	8	9	10	11	12	13	14	15	16	17	18	19
0	3	3	3	4	3	4	4	4	4	5	5	5	5	6	6	7	7
22.5	17	15	15	12	11	10	10	9	8	7	7	6	6	6	5	5	5
45	17	15	14	12	11	10	10	9	8	7	7	6	6	6	5	5	5
67.5	17	15	14	12	11	10	10	9	8	7	7	6	6	6	5	5	5
90	17	15	14	12	11	10	10	9	8	7	7	6	6	6	5	5	5
112.5	17	15	14	13	12	11	10	10	8	7	7	6	6	6	5	5	5
135	17	15	15	14	13	12	11	9	9	8	8	7	6	6	5	5	5
157.5	17	16	15	14	13	12	11	10	9	8	8	6	6	6	5	5	5
180	5	5	5	5	5	5	5	5	5	5	4	5	3	3	3	3	3
202.5	1	2	2	2	3	3	3	4	4	5	6	8	10	11	12	11	11
225	2	2	2	3	3	3	3	4	4	5	6	7	7	8	8	8	8
247.5	2	2	2	2	3	3	3	3	4	4	5	6	6	6	6	7	7
270	2	2	2	3	3	3	3	4	4	4	4	6	4	4	4	4	4
292.5	3	3	3	3	3	3	3	3	3	3	3	3	3	3	3	3	3
315	2	2	2	3	3	4	4	2	2	2	2	2	3	3	3	3	3
337.5	3	3	3	4	4	5	5	4	4	5	5	5	5	6	6	7	7

Model correlation with virtual buoy data

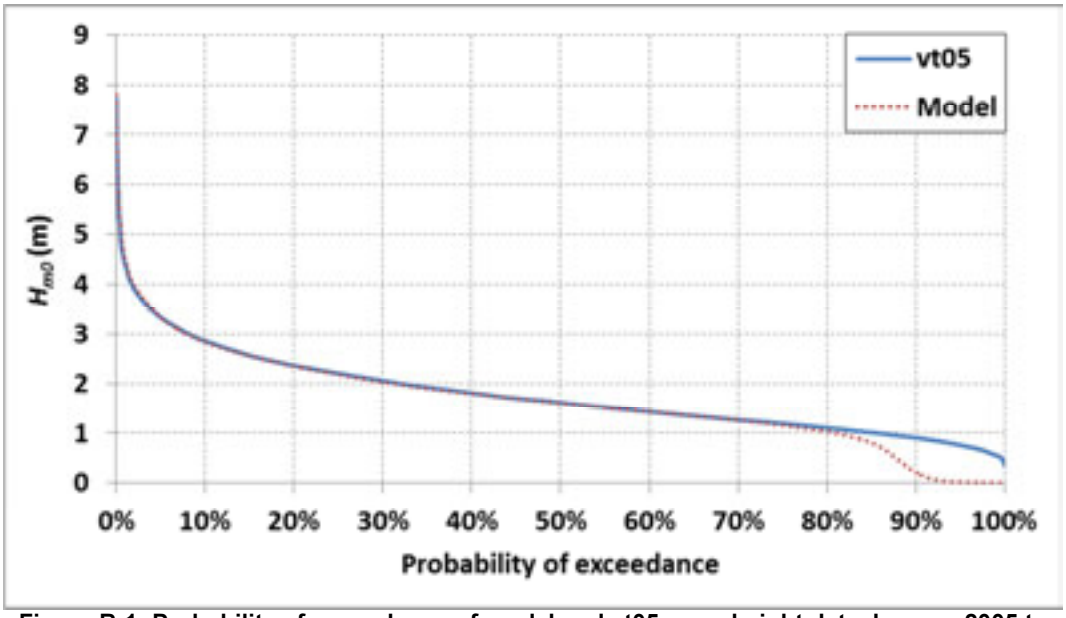

Figure B-1: Probability of exceedance of model and vt05 wave height data January 2005 to August 2008

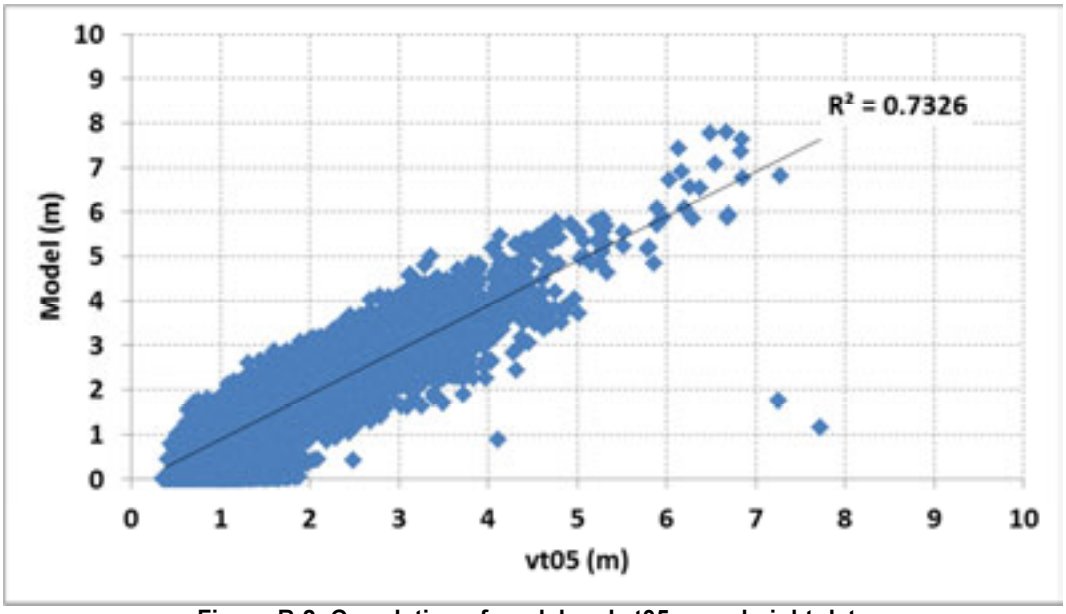

Figure B-2: Correlation of model and vt05 wave height data

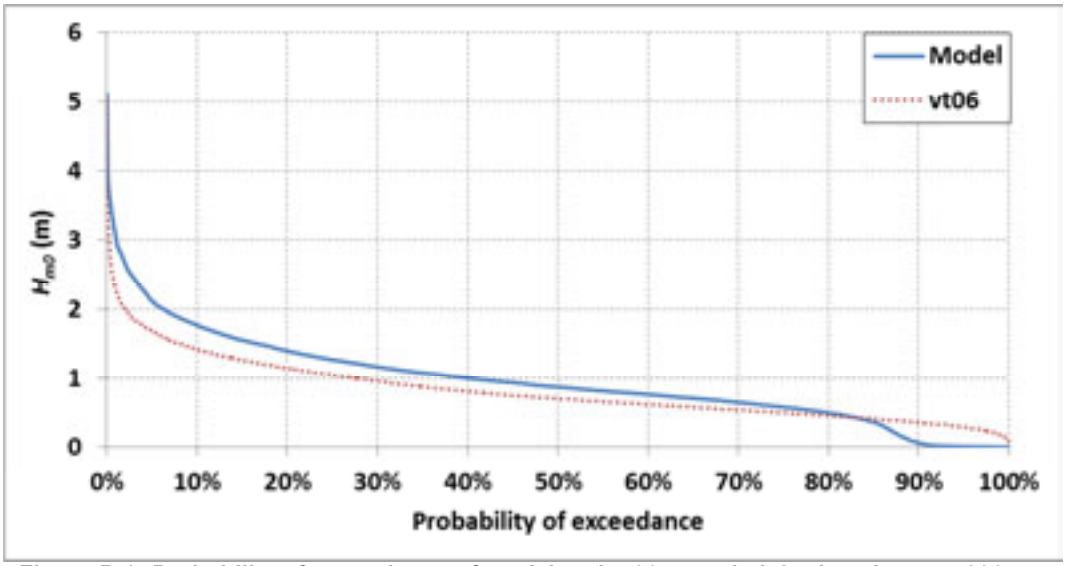

Figure B-3: Probability of exceedance of model and vt06 wave height data January 2005 to August 2008

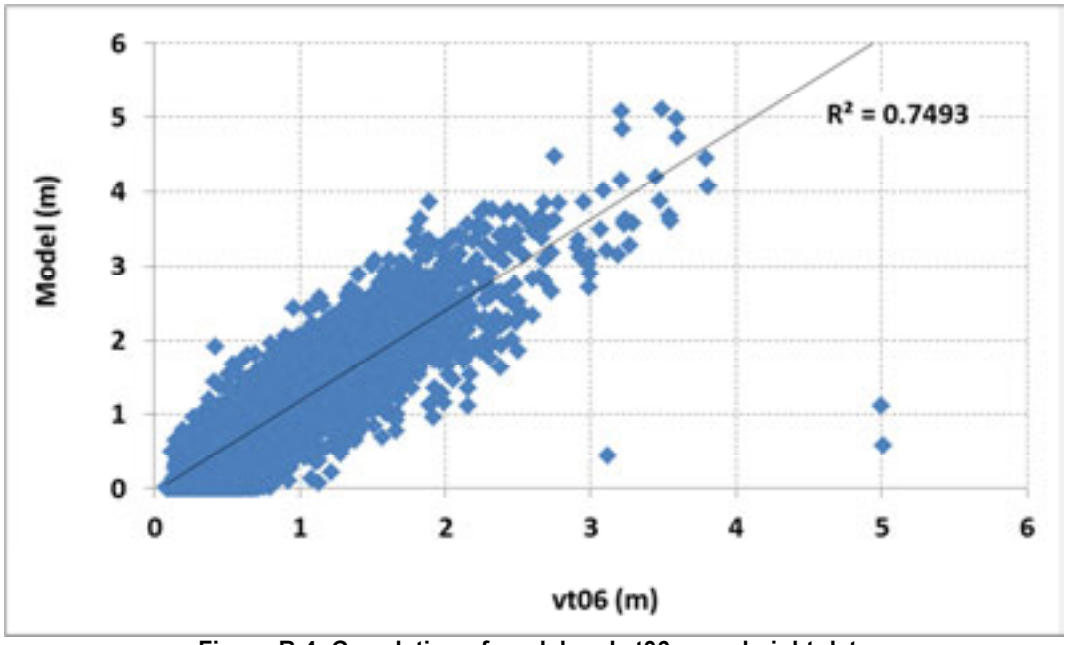

Figure B-4: Correlation of model and vt06 wave height data

SWAN input file example

An example of a typical SWAN input file for the initial run is presented.

```
$*************HEADING*************************************
PROJ 'Run' '1'
$

$TIDE
SET 2.0
COORD CART
$***********MODEL INPUT**********************************
$
CGRID REG 205000 6178500 0.0 65000.0 140000.0 260 560 CIR 72 0.033 1.0 40

$
INPGRID BOTTOM REG 205000 6178500 0.0 260 560 250.0 250.0
READINP BOTTOM 1. 'Grid1.dat'  4 0 FREE

$WAVES
BOUN SHAP JON  2.4 PEAK DSPR POW
$NORTHBOUND
BOUN SIDE N CON PAR  3.03 12 45 5
$WESTBOUND
BOUN SIDE W CON PAR  3.03 12 45 5
$SOUTHBOUND
BOUN SIDE S CON PAR  3.03 12 45 5
$EASTBOUND
BOUN SIDE E CON PAR  3.03 12 45 5

$DIFFRAC 1

NUM ACCUR 0.02 0.02 0.0  90. 20
$
$OFF BREA
$OFF WCAP
OFF QUAD
$
$************ OUTPUT REQUESTS *************************

GROUP 'Table1' 0 260 0 560
$OUT
Table 'Table1' HEAD 'Run1-SW-Tp 12.dat' XP YP DEP HS PDIR RTP DSPR


$NEST
NGRID 'Site' 255000 6243500 0 15000 14750 300 295
$NESTFILE
NESTOUT 'Site' 'Nest1-SW-Tp 12.txt '

$
TEST 0,0
COMPUTE
STOP
```

Appendix C: Stability analysis – example calculations

Detail of the stability analysis in Chapter 5 is presented by means of example calculations for the vertical wall structure (refer to §5.4.7) based on Goda's (1974) formulae and CEM (2006). Refer to the input parameters and calculated values as presented in the definition sketch of Figure C-1 and Table C-1.

Table C-1: Input data for stability analysis

H_{m0}	H_{design}	T	h_b	L	β
4.94	8.89 m	17 s	14 m	192 m	70°

In order to determine the wave induced pressures underneath the structure and on its front wall (p_u, p_1, p_2 and p_3) the coefficients α_1, α_2 and α_3 must first be calculated from the following equations.

Coefficients

$$\alpha_1 = 0.6 + 0.5\left[\frac{4\pi h_s / L}{\sinh(4\pi h_s / L)}\right]^2 \qquad \textbf{(C. 1)}$$

where h_s is the total water depth and L is the wavelength as determined for the given design wave period and water depth.

$$\alpha_2 = \text{smallest of}\left[\frac{(h_b - h_r)}{3h_b}\left(\frac{H_{design}}{h_r}\right)^2\right] \text{and} \frac{2h_r}{H_{design}} \qquad \textbf{(C. 2)}$$

where h_b is the water depth five H_{design} seaward of the vertical wall and h_r is the depth at the armour rock.

$$\alpha_3 = 1 - \frac{h_w - h_c}{h_s}\left[1 - \frac{1}{\cosh(2\pi h_s / L}\right] \qquad \textbf{(C. 3)}$$

where h_w is the total caisson structure height and h_c is the freeboard.

Pressures

The horizontal pressure at SWL is calculated from:

$$p_1 = 0.5(1 + \cos\beta)(\lambda_1\alpha_1 + \lambda_2\alpha_* \cos^2\beta)(\rho_w g)H_{design} \qquad \textbf{(C. 4)}$$

where $\alpha^* = \alpha_2$

The horizontal pressure at the top of the front wall is given by:

$$p_2 = \begin{cases} \left(1 - \frac{h_c}{\eta^*}\right) p_1 \text{ for } \eta^* > h_c \\ 0 \qquad\qquad \text{for } \eta^* \le h_c \end{cases} \quad \textbf{(C. 5)}$$

where η^* is the theoretical height of the pressure distribution above the vertical wall calculated from:

$$\eta^* = 0.75(1+\cos\beta)\lambda_1 H_{design} \quad \textbf{(C. 6)}$$

The pressure at the bottom of the seaward side of the structure is:

$$p_3 = \alpha_3 p_1 \quad \textbf{(C. 7)}$$

For this example it was assumed that the uplift pressure in the pores of the foundation material is fully developed underneath the entire base of the structure and was calculated from:

$$p_u = 0.5(1+\cos\beta)\lambda_3\alpha_1\alpha_3(\rho_w g)H_{design} \quad \textbf{(C. 8)}$$

where is ρ_w is the density of seawater.

Forces

The total horizontal and uplift force is determined by integrating the pressure distribution. CEM (2006) recommends an added value of bias and uncertainty for both these forces and the resulting moments as well. The horizontal force is defined as:

$$F_H = U_{F_H}\left[\frac{1}{2}(p_1 + p_2)h_c + \frac{1}{2}(p_1 + p_3)h'\right] \quad \textbf{(C. 9)}$$

where U_{F_H} is the stochastic variable signifying the bias and uncertainty related to the horizontal force and *h'* is the structure submerged depth. The uplift force is determined from:

$$F_U = U_{F_U}\frac{1}{2}\rho_u B \quad \textbf{(C. 10)}$$

where U_{F_U} is the stochastic variable signifying the bias and uncertainty related to the uplift force, *h'* is the structure submerged depth and *B* is the assumed width of the vertical structure to resist the applied force through its weight. The resistance force of the structure is made up of its concrete and sand weight minus the effect of buoyancy as shown:

$$F_G = \rho_c g B h_w - \rho_w g B h' \quad \textbf{(C. 11)}$$

where ρ_c is the concrete density.

Moments
The overturning moment due to the horizontal force is:

$$M_H = U_{M_H}\left[\frac{1}{6}(2p_1 + p_3)h'^2 + \frac{1}{2}(p_1 + p_2)h'h_c + \frac{1}{6}(p_1 + 2p_2)h_c^2\right] \quad \textbf{(C. 12)}$$

where $U_{M_H}$is stochastic variable signifying the bias and uncertainty of the horizontal moment.

The overturning moment of the uplift force is given by:

$$M_U = U_{M_U}\frac{1}{3}p_u B^2 \quad \textbf{(C. 13)}$$

where $U_{M_U}$is stochastic variable signifying the bias and uncertainty of the uplift moment.

The resistant moment of the net structural weight:

$$M_G = \frac{1}{2}B^2 g\left(\rho_c h_w - \rho_w h'\right) \quad \textbf{(C. 14)}$$

In the final stage of the stability analysis, the sliding and overturning load was determined and a caisson width wide enough to ensure adequate resistance to these failure modes was selected.

Sliding
The stability of the structure was checked against sliding between the base and its rubble foundation. A friction coefficient, μ, of 0.6 was assumed as recommended by CEM (2006) and BSI (1991). Therefore:

$$(F_G - F_u)\mu > F_H$$

A conservative safety factor of 1.5 was assumed as recommend by BSI (1991).

Overturning
The factor of safety against overturning about the heel of the structure is defined as:

$$M_G/(M_u + M_H)$$

Lastly, the safety against heel bearing pressure failure is evaluated.

Heel bearing pressure (P_e)
The net vertical force (W_e) and moment about the heel of the structure was determined and the moment's lever arm (t_e) was calculated. A trapezoidal bearing pressure distribution is assumed with:

$$P_e = \frac{2W_e}{B}\left(2 - 3\frac{t_e}{B}\right)$$

Furthermore it was assumed that the seafloor consists of dense sand and the core material of the foundation is of good bearing capacity. The calculated output values as determined for this stability analysis from the presented equations and formulae is shown in Table C-2, Figure C-1 and Table 5-4.

Table C-2: Calculated output values from stability analysis

Calculated values					
α_1	α_2	α_3	η^*	P_e	β
0.99	0.07	0.92	8.9	317kPa	70°

A 12.4 m wide ballast chamber was found to provide sufficient stability to the ShoreSWEC under these design pressure, force and moment conditions.

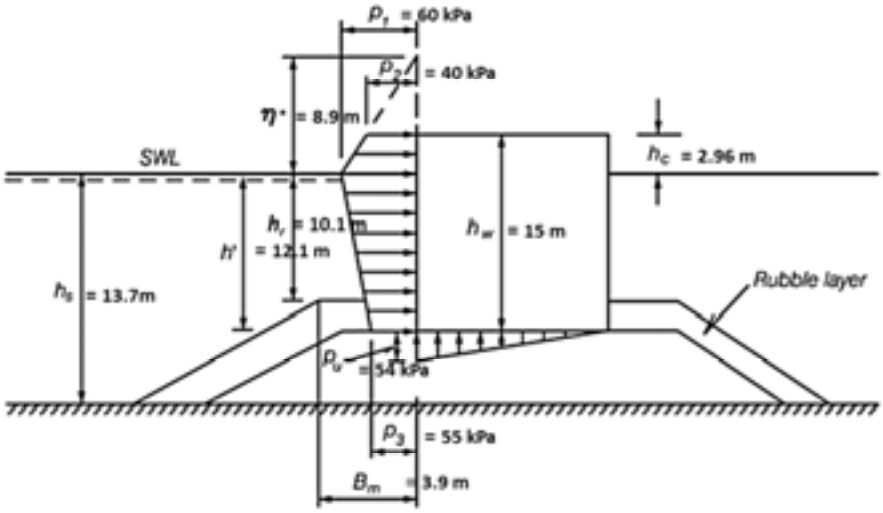

Figure C-1: Distribution of design pressures (CEM, 2006c)

Appendix D: Experimental setup

The main features of the experimental setup are presented in Figure D-1, Figure D-2 and Figure D-3.

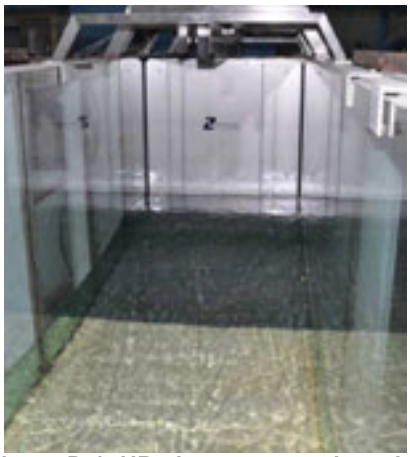

Figure D-1: HR piston wavemaker with dynamic wave absorption

Figure D-2: Absorption beach comprising of rubble, model armor units and hollow bricks

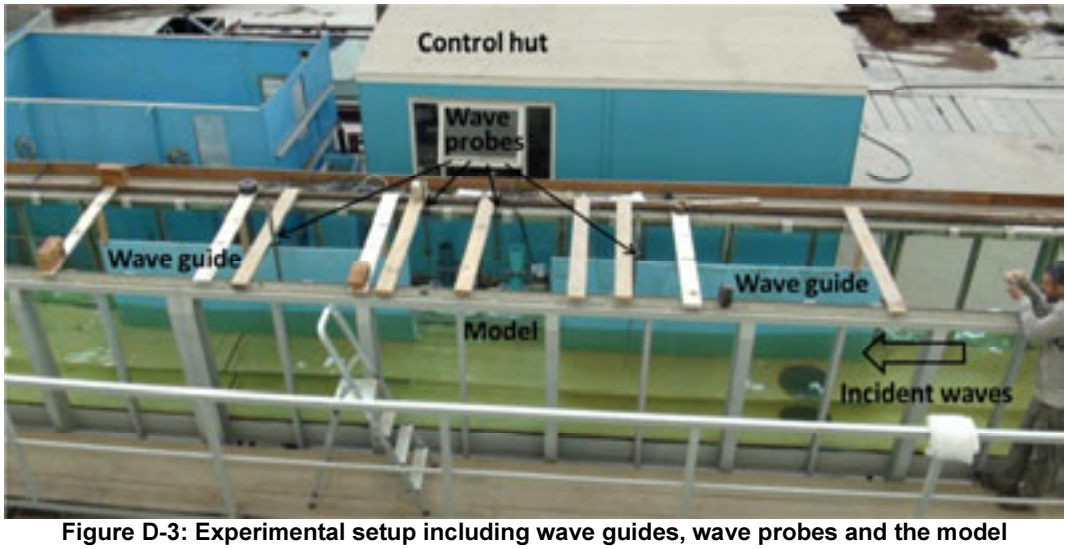

Figure D-3: Experimental setup including wave guides, wave probes and the model

The real and scaled experimental wave conditions tested are presented in Table D-1.

Table D-1: Real and model scale water depth, wave height and period

Real					Model scale				
d **(m)**	***H*** **(m)**	***T*** **(s)**	**CD *L*(m)**	**MSL *L*(m)**	***d*** **(m)**	***H*** **(m)**	***T*** **(s)**	**CD *L* (m)**	**MSL *L* (m)**
11	0.5	6	49.7	50.7	0.44	0.02	1.2	2.0	2.0
11.98	1.0	7	61.8	63.5	0.48	0.04	1.4	2.5	2.5
	1.5	8	73.5	75.8		0.06	1.6	2.9	3.0
	2.0	9	84.9	87.9		0.08	1.8	3.4	3.5
		10	96.2	99.7			2.0	3.9	4.0
		11	107.3	111.3			2.2	4.3	4.5
		12	118.3	122.8			2.4	4.7	4.9
		13	129.1	134.2			2.6	5.2	5.4

Appendix E: Orifice calibration

The orifice in its chimney housing was calibrated in the Mechanical Engineering's wind tunnel which was designed, manufactured and operated by Mr. K.G Allen. High and low flow conditions were tested as well as reverse flow to ensure that the orifice can accurately measure the bi-directional flow of the device. The mass flow rate as a function of the pressure drop over the orifice presented in Figure E-1, showing that all three flow tests yield very similar correlation curves.

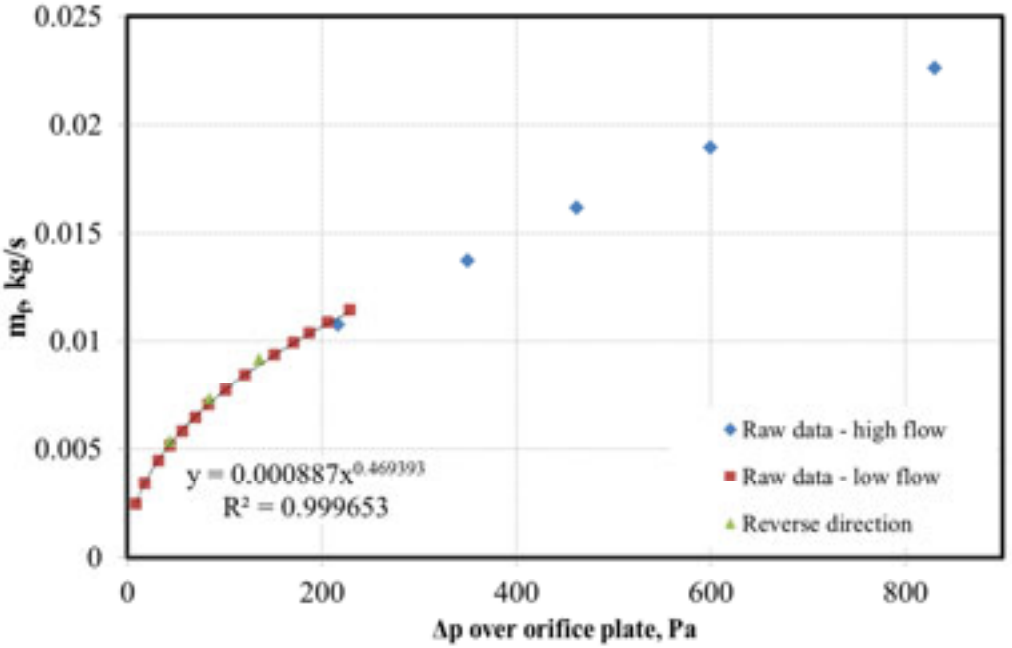

Figure E-1: Correlation curve of mass flow rate and pressure drop over the orifice

The relationship between the internal chamber pressure and volume flow rate through the orifice was further confirmed with the 3D CFD model. Figure E-2 shows the volume flow rate through the orifice as directly determined from the model and also the volume flow rate derived from the internal chamber pressure calculated by the model using the calibration equation.

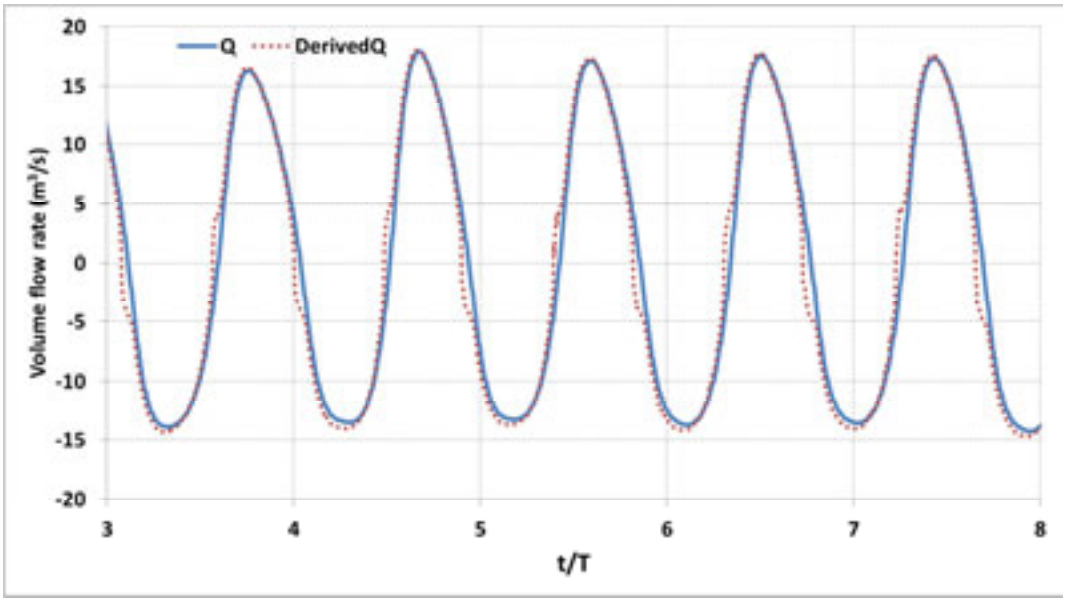

Figure E-2: Volume flow rate through the orifice as determined directly by the CFD model and calculated using the correlation equation

Appendix F: Additional Fluent output

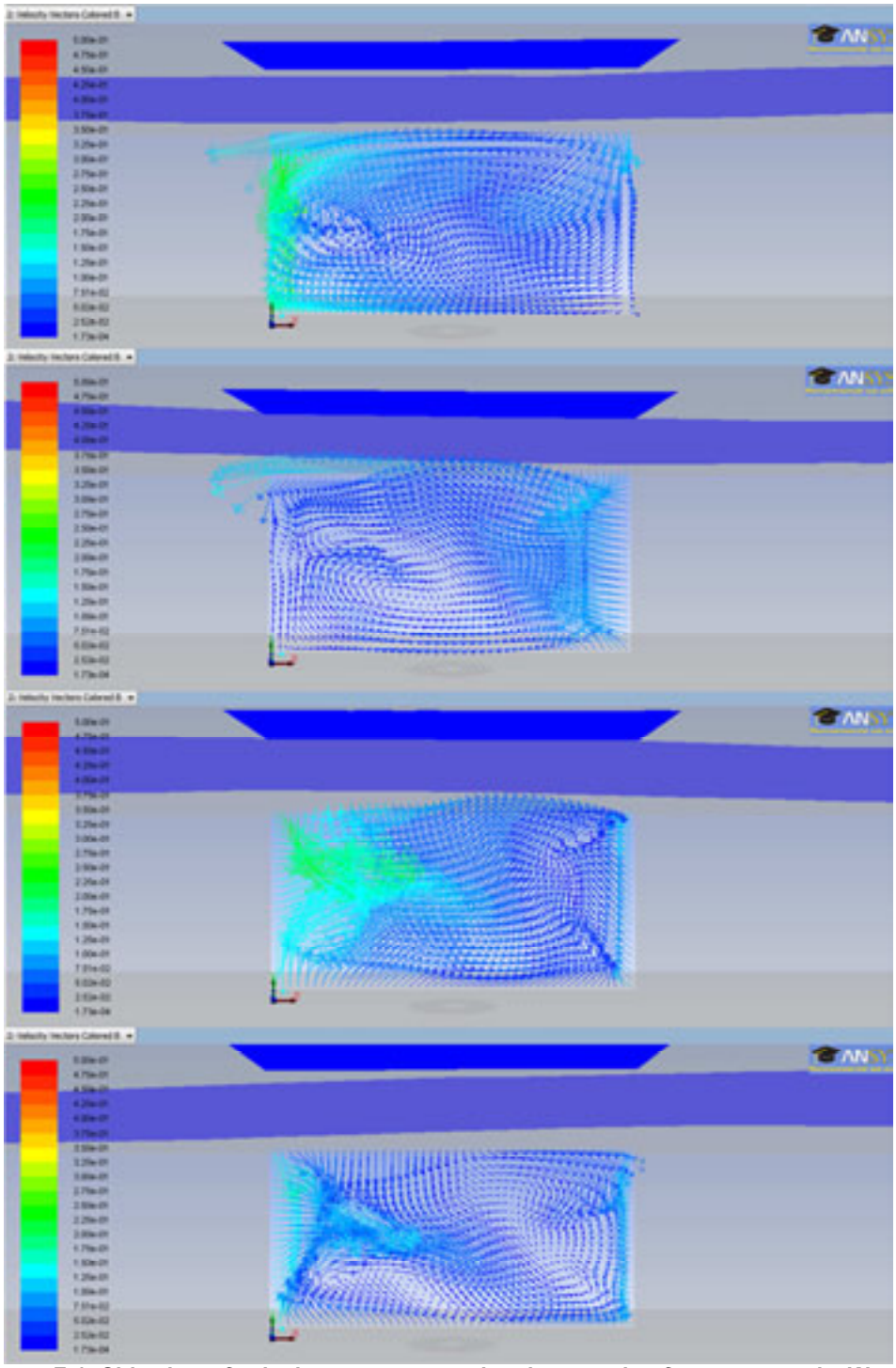

Figure F-1: Side view of velocity vectors over chamber opening for a wave cycle. Waves propagating from left to right.

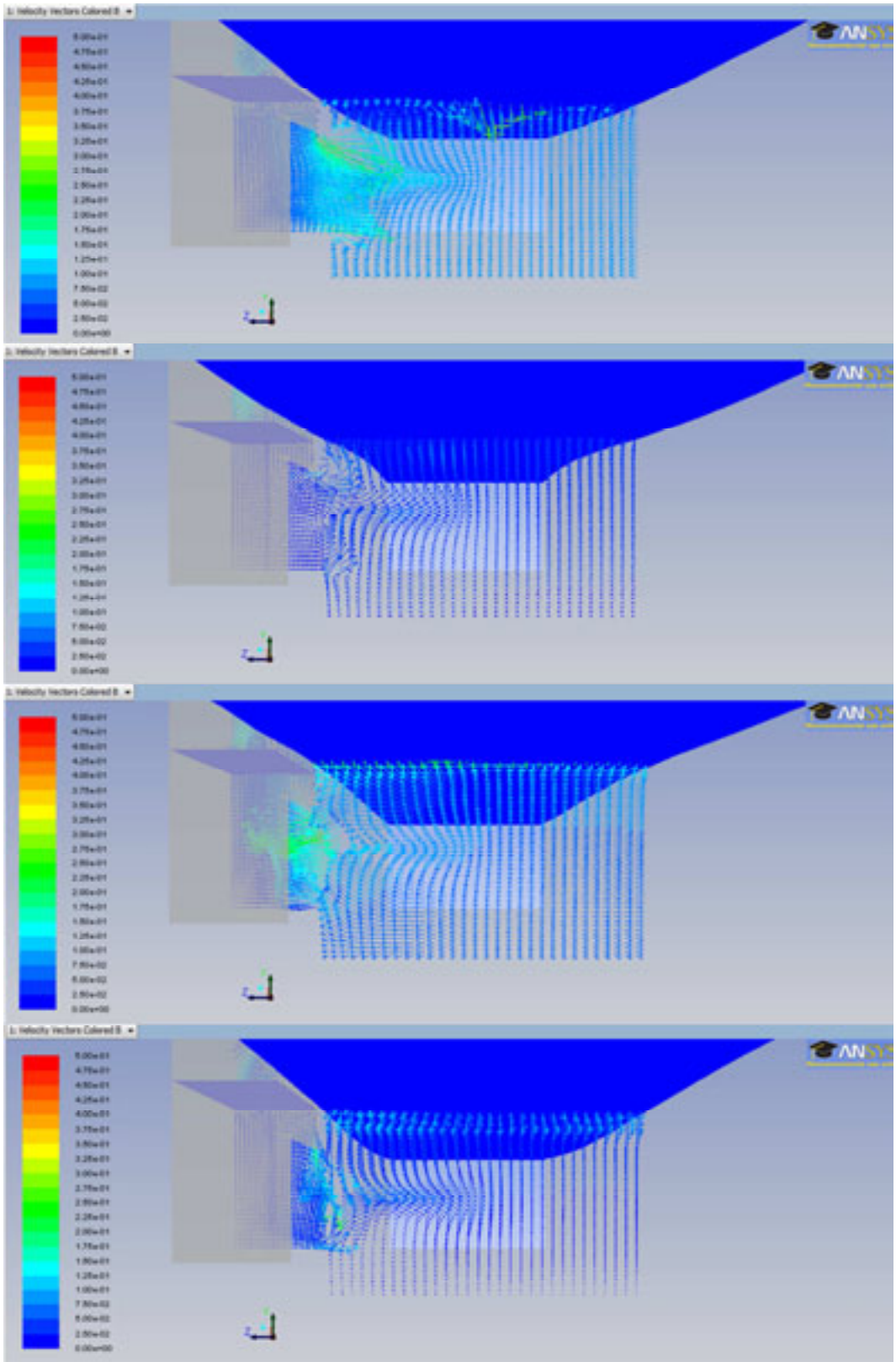

Figure F-2: Cross sectional view of model, looking towards the wavemaker, with velocity vectors for a typical wave cycle.

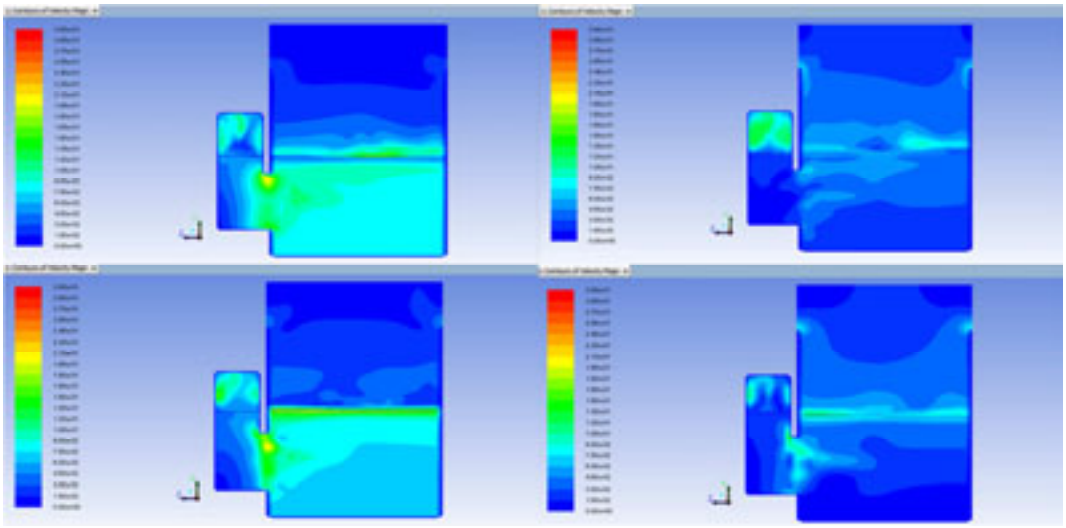

Figure F-3: Cross sectional view of 3D NWT and chamber showing velocity contours for a typical wave cycle. Sequence from left to right starting at the top left.

Appendix G: Fluent input

FLUENT
Version: 3d, pbns, vof, skw, transient (3d, pressure-based, VOF, standard k-omega, transient)
Release: 13.0.0

Models

Model	Settings
Space	3D
Time	Unsteady, 1st-Order Implicit
Viscous	k-omega turbulence model
Heat Transfer	Disabled
Solidification and Melting	Disabled
Species	Disabled
Coupled Dispersed Phase	Disabled
NOx Pollutants	Disabled
SOx Pollutants	Disabled
Soot	Disabled
Mercury Pollutants	Disabled

Material Properties

Material: aluminum (solid)

Property	Units	Method	Value(s)
Density	kg/m^3	constant	2719
Cp (Specific heat)	j/kg-k	constant	871
Thermal conductivity	w/m-k	constant	202.4

Material: air (fluid)

Property	Units	Method	Value(s)
Density	kg/m^3	constant	2719
Cp (Specific heat)	j/kg-k	constant	871
Thermal conductivity	w/m-k	constant	202.4
Viscosity	kg/m-s	constant	1.7894e-05
Molecular Weight	kg/kgmol	constant	28.966
Thermal Expansion Coefficient	1/k	constant	0
Speed of sound	m/s	none	#f

Material: water-liquid (fluid)

Property	Units	Method	Value(s)
Density	kg/m^3	constant	998.2
Cp (Specific heat)	j/kg-k	constant	4182
Thermal conductivity	w/m-k	constant	0.6
Viscosity	kg/m-s	constant	0.001003
Molecular Weight	kg/kgmol	constant	18.0152
Thermal Expansion Coefficient	1/k	constant	0
Speed of sound	m/s	none	#f

Cell Zone Conditions

Zones

Name	ID	Type
part-opening	11	fluid
part-solid	12	fluid
part-chimmid	90290	fluid
part-through_flume	13	fluid
part-bottom_box	14	fluid
part-chim2ndbot	90289	fluid
part-chim2ndtop	90293	fluid
part-middle_box	20053	fluid
part-top_box	15	fluid

Setup Conditions

part-opening

Boundary Conditions

Zones

Name	ID	Type
wall-part-solid	21	wall
wall-part-chim2ndbot	150514	wall
velocity_inlet	18	velocity-inlet
pressure_inlet	19	pressure-inlet
wall-part-opening	20	wall
wall-part-solid.1	130488	wall
wall-part-through_flume	22	wall
wall-part-bottom_box	23	wall
wall-part-chim2ndtop	90331	wall
wall-part-middle_box	20075	wall
wall-part-top_box	24	wall
pressure_outlet	110421	pressure-outlet

Setup Conditions

wall-part-solid – example of a wall boundary. All the other wall boundaries have the same conditions values.

Condition	Value
Enable shell conduction?	no
Wall Motion	0
Shear Boundary Condition	0
Define wall motion relative to adjacent cell zone?	yes
Apply a rotational velocity to this wall?	no
Velocity Magnitude (m/s)	0
X-Component of Wall Translation	1
Y-Component of Wall Translation	0
Z-Component of Wall Translation	0
Define wall velocity components?	no
X-Component of Wall Translation (m/s)	0

Y-Component of Wall Translation (m/s)	0
Z-Component of Wall Translation (m/s)	0
Wall Roughness Height (m)	0
Wall Roughness Constant	0.5
Rotation Speed (rad/s)	0
X-Position of Rotation-Axis Origin (m)	0
Y-Position of Rotation-Axis Origin (m)	0
Z-Position of Rotation-Axis Origin (m)	0
X-Component of Rotation-Axis Direction	0
Y-Component of Rotation-Axis Direction	0
Z-Component of Rotation-Axis Direction	1
X-component of shear stress (pascal)	0
Y-component of shear stress (pascal)	0
Z-component of shear stress (pascal)	0
Specularity Coefficient	0

velocity_inlet

Condition	Value
Velocity Specification Method	1
Reference Frame	0
Velocity Magnitude (m/s)	0
Supersonic/Initial Gauge Pressure (pascal)	0
Coordinate System	0
X-Velocity	(profile udf x_velocity::libudf)
Y-Velocity	(profile udf y_velocity::libudf)
Z-Velocity (m/s)	0
X-Component of Flow Direction	1
Y-Component of Flow Direction	0
Z-Component of Flow Direction	0
X-Component of Axis Direction	1
Y-Component of Axis Direction	0
Z-Component of Axis Direction	0
X-Coordinate of Axis Origin (m)	0
Y-Coordinate of Axis Origin (m)	0
Z-Coordinate of Axis Origin (m)	0
Angular velocity (rad/s)	0
Turbulent Specification Method	2
Turbulent Kinetic Energy (m2/s2)	1
Specific Dissipation Rate (1/s)	1
Turbulent Intensity (%)	5
Turbulent Length Scale (m)	1
Hydraulic Diameter (m)	0.07
Turbulent Viscosity Ratio	2
is zone used in mixing-plane model?	no

pressure_inlet

Condition	Value
Reference Frame	0
Gauge Total Pressure (pascal)	0
Supersonic/Initial Gauge Pressure (pascal)	0
Direction Specification Method	1
Coordinate System	0
X-Component of Flow Direction	1
Y-Component of Flow Direction	0
Z-Component of Flow Direction	0
X-Component of Axis Direction	1

Y-Component of Axis Direction	0
Z-Component of Axis Direction	0
X-Coordinate of Axis Origin (m)	0
Y-Coordinate of Axis Origin (m)	0
Z-Coordinate of Axis Origin (m)	0
Angular velocity (rad/s)	0
Turbulent Specification Method	2
Turbulent Kinetic Energy (m2/s2)	1
Specific Dissipation Rate (1/s)	1
Turbulent Intensity (%)	1
Turbulent Length Scale (m)	1
Hydraulic Diameter (m)	0.1
Turbulent Viscosity Ratio	2
is zone used in mixing-plane model?	no

pressure_outlet

Condition	Value
Gauge Total Pressure (pascal)	0
Backflow Direction Specification Method	1
Coordinate System	0
X-Component of Flow Direction	1
Y-Component of Flow Direction	0
Z-Component of Flow Direction	0
X-Component of Axis Direction	1
Y-Component of Axis Direction	0
Z-Component of Axis Direction	0
X-Coordinate of Axis Origin (m)	0
Y-Coordinate of Axis Origin (m)	0
Z-Coordinate of Axis Origin (m)	0
Turbulent Specification Method	3
Backflow Turbulent Kinetic Energy (m2/s2)	1
Backflow Specific Dissipation Rate (1/s)	1
Backflow Turbulent Intensity (%)	5
Backflow Turbulent Length Scale (m)	1
Backflow Hydraulic Diameter (m)	0.104
Backflow Turbulent Viscosity Ratio	10
is zone used in mixing-plane model?	no
Radial Equilibrium Pressure Distribution	no

Solver Settings

Equations

Equation	Solved
Flow	yes
Volume Fraction	yes
Turbulence	yes

Numerics

Numeric	Enabled
Absolute Velocity Formulation	yes

Unsteady Calculation Parameters

Time Step (s)	0.0099999998
Max. Iterations Per Time Step	40

Relaxation

Variable	Relaxation Factor
Pressure	0.4
Density	1
Body Forces	1
Momentum	0.5
Turbulent Kinetic Energy	0.5
Specific Dissipation Rate	0.8
Turbulent Viscosity	1

Linear Solver

Variable	Solver Type	Termination Criterion	Residual Reduction Tolerance
Pressure	V-Cycle	0.1	
X-Momentum	Flexible	0.1	0.7
Y-Momentum	Flexible	0.1	0.7
Z-Momentum	Flexible	0.1	0.7
Turbulent Kinetic Energy	Flexible	0.1	0.7
Specific Dissipation Rate	Flexible	0.1	0.7

Pressure-Velocity Coupling

Parameter	Value
Type	PISO
Skewness-Neighbour Coupling	no
Skewness Correction	0
Neighbour Correction	0

Discretization Scheme

Variable	Scheme
Pressure	Body Force Weighted
Momentum	Second Order Upwind
Volume Fraction	Geo-Reconstruct
Turbulent Kinetic Energy	First Order Upwind
Specific Dissipation Rate	First Order Upwding

Solution Limits

Quantity	Limit
Minimum Absolute Pressure	1
Maximum Absolute Pressure	5e+10
Minimum Temperature	1
Maximum Temperature	5000
Minimum Spec. Dissipation Rate	1e-20
Maximum Turb. Viscosity Ratio	100000